Universidad de Valencia
Instituto de Ciencia Molecular

Università degli studi di Perugia
Dipartimento di Chimica, Biologia e Biotecnologie

Doctoral Thesis

Modeling the Interaction of Light Gases with Graphene: From Coupled Cluster Calculations to Molecular Dynamics Simulations

---

Author:
Jelle Vekeman

Supervisors:
Alfredo Sánchez de Merás
Noelia Faginas-Lago
Inmaculada García Cuesta

Tutors:
José Sánchez Marín
Inmaculada García Cuesta

A thesis submitted in fulfillment of the requirements
for the degree of Doctor of Philosophy

in

Theoretical Chemistry and Computational Modeling

April 2, 2019

Abstract

The adsorption of gases on graphene has seen a major increase of interest recently for applications such as energy storage, gas sensors and gas separation. Small gases, such as methane, nitrogen, carbon monoxide and water interact with graphene via non-covalent interactions, which, due to their small size and nature, are still difficult to describe accurately by theoretical methods. This doctoral thesis tries to obtain simple, but very reliable potentials to model gas adsorption on graphene and test them in simulations of systems relevant for industrial applications.

First, the behavior of methane, nitrogen, water and carbon monoxide in contact with graphene is studied with high-level calculations at DFT and CCSD(T) level, whereby it is shown that the used B97-D density functional well describes the interactions of interest. The important adsorption sites and attacking geometries are identified and discussed for the different systems and it is found that for all molecules the attacking geometry is of larger importance than the positioning over the graphene sheet. This information is then used to build accurate, but simple molecular models to describe the involved dimer interactions. United-atom models are used to provide very cheap potentials that describe accurately the involved interactions as an average over the possible geometries, while atomistic potentials are used to explicitly take the orientation dependence of the interactions into account. The molecular models are then fitted to high-level dimer interaction energies to provide the correct behavior at short, intermediate and long distance ranges. Potentials are developed based on the Improved Lennard-Jones potential, a more accurate variant of the well-known Lennard-Jones potential, whereby the influence of electrostatic interactions, through a simple Coulombic sum, is investigated via the study of different charge schemes. A large number of potentials is then obtained and benchmarked against high-level calculations, allowing the comparison of different potentials and molecular models. A macromolecular property, the diffusion coefficient is calculated to allow comparison with experiment and thus the selection of a small amount of well-performing potentials for further use. For methane, nitrogen and CO we show that the selected potentials are well-capable of reproducing the DFT interaction energies and diffusion coefficient, whereby the atomistic models behave better at a larger computational cost in comparison to the united-atom models. For the water molecule, the situation was slightly more complicated because of the complex nature of hydrogen bonds and we thus propose two different sets of potentials depending on the conditions of the system.

The selected potentials were then used for molecular dynamics and grand canonical Monte Carlo simulations in systems important for real-world applications. The methane/nitrogen and methane/hydrogen mixtures were investigated as well as the pure methane, nitrogen, hydrogen, water and carbon monoxide gases, specifically looking at the storage and separation possibilities of graphene. In the molecular dynamics simulations, the inclusion of flexibility in graphene — through intramolecular force fields from the literature — were the prime focus in order to assess its influence on adsorption. The inclusion of intramolecular terms in the graphene sheet does clearly lead to different adsorption behavior, whereby introduction of a torsional term provided the most realistic description with good agreement with experimental results. Furthermore, it is shown that the flexibility significantly improves the performance when using a cheaper united-atom model for molecules where directionality is of major importance. Specifically, for methane this effect was found to be strong, leading to larger adsorption rates. For nitrogen and CO on the other hand, the amount of molecules adsorbed lowered upon introduction of flexibility. More generally, we have confirmed the strong promise of graphene to act as a separating membrane for the methane/nitrogen mixture showing high selectivities for the former — again dependent on the introduced flexibility in the graphene sheet. On the other hand, it was the first time the Improved Lennard-Jones potential was used for grand canonical Monte Carlo simulations, so this part of the work is intended as a proof-of-principle.

Resumen

El estudio de la adsorción de gases sobre grafeno ha suscitado gran interés debido a sus aplicaciones en el almacenamiento de energía, sensores gaseosos y separación de gases. Los gases ligeros interactúan con el grafeno mediante interacciones no covalentes, las cuales, debido a su débil naturaleza y corto alcance, son aún difíciles de describir con precisión por los métodos teóricos. La presente Tesis Doctoral está dedicada a obtener potenciales simples, pero muy fiables, para modelizar la adsorción de gases sobre grafeno, para posteriormente evaluarlos en simulaciones de sistemas relevantes para aplicaciones industriales.

En primer lugar, se estudió con metodologías de alta nivel (DFT y CCSD(T)) el comportamiento de metano, nitrógeno, agua y monóxido de carbono en contacto con grafeno para identificar y analizar los sitios de adsorción y geometrías de ataque, demostrando que el funcional B97-D describe correctamente las interacciones de interés. Se han identificado y discutido los sitios de adsorción y geometrías de ataque más importantes para los diferentes sistemas, encontrándose que para todas las moléculas la geometría de ataque tiene una mayor relevancia que su posicionamiento sobre las láminas de grafeno. Esta información se ha utilizado posteriormente para construir potenciales de interacción simples pero precisos, capaces de describir las interacciones que nos ocupan. En ambos casos, los potenciales de interacción se construyeron a partir del ajuste de las energias de interacción B97D de dimeros a un potencial del tipe "Improved Lennard-Jones", una variante más precisa del conocido potencial de Lennard-Jones, el cual proporciona el compartamiento correcto en todo el rango de distancias. La influencia de las interacciones electrostáticas ha sido evaluada mediante el estudio de diferentes esquemas de carga a través de una simple suma coulómbica. De esta forma, se ha obtenido un gran número de potenciales que han sido a su vez contrastados con cálculos de alto nivel, permitiendo así la comparación de los diferentes potenciales y modelos moleculares. Una propiedad molecular, en concreto el coeficiente de difusión, se ha calculado posteriormente para comparar directamente los resultados teóricos con los resultados experimentales. Para metano, nitrógeno y monóxido de carbono demostramos que los potenciales seleccionados son capaces de reproducir las energías de interacción y los coeficientes de difusión obtenidos con DFT, mientras que los modelos atomísticos se comportan mejor a costa de un mayor coste computacional con respecto a los modelos del átomo unido. Para la molécula de agua, la situación fue ligeramente más complicada debido a la compleja naturaleza de los enlaces de hidrógeno y, por lo tanto, proponemos dos conjuntos de potenciales diferentes dependiendo de las condiciones del sistema.

Los potenciales escogidos fueron empleados en simulaciones de dinámica molecular y de Monte Carlo sobre sistemas relevantes en aplicaciones del mundo real. Se estudiaron mezclas metano/nitrógeno y metano/hidrógeno, así como metano, nitrógeno, hidrógeno, agua y monóxido de carbono puros, haciendo especial hincapié en las capacidades de almacenamiento y de separación del grafeno. Uno de los objetivos principales de las dinámicas moleculares fue estudiar la influencia que la flexibilidad del grafeno – incluida a través de campos de fuerza intramoleculares obtenidos de la bibliografía – tiene en la adsorción de estos gases. La inclusión de términos intramoleculares en la lámina de grafeno claramente lleva a un comportamiento diferente en la absorción. En particular, la introducción de un término torsional proporcionó la descripción más realista, según los resultados experimentales. Además, en aquellos casos donde la direccionalidad es de gran importancia, se demostró que el aumento de la flexibilidad mejora significativamente el rendimiento cuando se usa en combinación con un modelo de átomo unido más barato. Más concretamente, se encontró que este efecto es particularmente significativo, dando lugar a una mayor adsorción. Por otro lado, para nitrógeno y CO, la cantidad de moléculas adsorbidas decrece con la introducción de flexibilidad. En general, hemos confirmado que el grafeno puede actuar como membrana separadora para mezclas de metano/nitrógeno, mostrando altas selectividades para el primero — de nuevo dependientes de la flexibilidad introducida en las láminas de dicho material. Por otro lado, la presente Tesis supone el primer uso del potencial Improved Lennard-Jones en simulaciones Monte Carlo, sirviendo para probar su validez en este tipo de simulaciones.

Astratto

L'assorbimento di gas sul grafene ha visto un notevole aumento di interesse per applicazioni in ambito di stoccaggio di energia od il loro utilizzo come sensori e separatori di gas. I piccoli gas interagiscono con il grafene tramite interazioni non covalenti, che, a causa delle loro piccole dimensioni e natura, sono ancora molto difficili da descrivere con precisione attraverso metodi teorici. Questo lavoro cerca di ottenere potenziali semplici ma molto affidabili per modellare l'assorbimento di gas sul grafene e testarli in simulazioni di sistemi rilevanti per applicazioni industriali.

In primo luogo si è studiato il comportamento di metano, azoto, acqua e monossido di carbonio a contatto con la superficie di grafene tramite calcoli basati sulla DFT e CCSD(T), in cui si dimostra che il funzionale di densità B97-D usato descrive accuratamente le interazioni che caratterizzano questi sistemi. I siti di adsorbimento più importanti e le geometrie di attacco sono identificati e discussi per i diversi sistemi ed è stato trovato che per tutte le molecole, la geometria di attacco ha un'importanza maggiore rispetto al posizionamento sulla superficie di grafene. Le informazioni ricavate vengono utilizzate per costruire modelli molecolari semplici, ma accurati. Da una parte si sono utilizzati modelli basati su una descrizione dell'atomo unificato che forniscono potenziali molto economici (in termini computazionali) e descrivono accuratamente le interazioni coinvolte grazie ad una media sulle possibili geometrie, d'altra parte si sono usati potenziali atomistici che considerano esplicitamente la dipendenza delle interazioni dall'orientamento relativo delle speci coinvolte. Questi modelli molecolari sono stati parametrizzati sulle energie di interazione fra dimeri e superficie ottenute ad un alto livello di teoria così. I potenziali sviluppati in questo lavoro si basano sul modello "Improved Lennard-Jones", una variante più accurata del noto potenziale di Lennard-Jones, con la quale l'influenza delle interazioni elettrostatiche viene studiata attraverso una semplice somma di cariche Coulombiane, è studiata tramite l'uso di diversi schemi per ottenere le cariche. Un gran numero di potenziali è stato quindi ottenuto e confrontato con calcoli di alto livello, consentendo il confronto di diversi potenziali e modelli molecolari. È stata inoltre calcolata una proprietà macromolecolare, il coefficiente di diffusione, per consentire il confronto con dati sperimentali. Per metano, azoto e CO mostriamo che i potenziali selezionati sono in grado di riprodurre le energie di interazione DFT e il coefficiente di diffusione, per i quali i modelli atomistici si comportano meglio e ad un costo computazionale maggiore rispetto ai modelli ad atomo unito. Per la molecola d'acqua, la situazione era leggermente più complicata a causa della natura complessa dei legami a idrogeno e quindi proponiamo due diversi gruppi di potenziali a seconda delle condizioni del sistema.

I potenziali selezionati sono stati utilizzati per simulazioni di dinamica molecolare e di tipo "grand-canonical Monte Carlo" in sistemi importanti per applicazioni nel mondo reale. Sono state studiate le miscele metano/azoto e metano/idrogeno nonché i gas puri di metano, azoto, idrogeno, acqua e monossido di carbonio, in particolare considerando le proprietà di stoccaggio e separazione del grafene. Nelle simulazioni di dinamica molecolare, è stata inoltre introdotta la flessibilità nel grafene — attraverso campi di forza intramolecolari disponibili in letteratura — ponendosi come obiettivo principale di valutare la sua influenza sulle proprietà di assorbimento. L'inclusione di termini intramolecolari nella descrizione della superficie di grafene porta chiaramente ad un comportamento di adsorbimento diverso, nel quale l'introduzione di un termine di torsione fornisce la descrizione più realistica ed essendo in buon accordo con i risultati sperimentali. Inoltre, si è dimostrato che la flessibilità migliora significativamente le prestazioni quando si utilizza un modello più economico ad atomo unito per le molecole in cui la direzionalità è di grande importanza. Specificamente, questo effetto è risultato essere importante per il metano, portando ad un maggiore adsorbimento da parte del grafene. Nel caso dell'azoto e la CO invece, la quantità di molecole adsorbite è risultata ridotta con l'aggiunta della flessibilità. Più in generale, con questi studi abbiamo confermato il potenziale del grafene come membrana separatrice per la miscela di gas metano/azoto, mostrando un'elevata selettività per il primo — ancora una volta dipendente dalla flessibilità introdotta nella superficie grafene. Inoltre, per la prima volta, il potenziale "Improved Lennard-Jones" è stato utilizzato per simulazioni di tipo "grand-canonical Monte Carlo", esplorando quindi in questa parte di lavoro nuovi metodi di simulazione.

Acknowledgements

I would like to start this section with acknowledging the people that have supported my scientific work during the last three years. Starting off with the support I received in my main host institution, the university of Valencia, I would like to thank my supervisors prof. dr. Alfredo Sánchez de Merás and prof. dr. Inmaculada Garcia Cuesta for showing me how to perform a research at a high level, combining ideas and enthousiastic generation of results with meticulous and careful analysis afterwards. Their habit of not resting before a given problem was fully understood, has been an life-lesson. I also thank them for their general friendliness outside of work and interest in me and my family. Aside from our scientific discussions, I am strongly indebted to my tutor prof. dr. José Sánchez Marín who has been a huge support in the bureaucratic work surrounding in a cotutelle project abroad. But even more than that, I have enjoyed his general wisdom on all sides of life and I wish him all the best after his recent retirement. Moving to my second host institution, the university of Perugia, I would like to acknowledge my supervisor dr. Noelia Faginas-Lago for her enthousiasm in and out of the office and actively showing me and my family the way in Italian daily life and Perugia specifically. Finally, I would like to thank prof. dr. Lourdes Vega for the warm welcome at AlyaTech during my secondment. A special thanks goes to all the above mentioned supervisors for their flexibility and support during the pregnancy of my girlfriend and the first months after our son was born.

This project was part of the European Union's Horizon 2020 research and innovation programme under the Marie Sklodowska-Curie grant agreement No 642294, for which I gratefully acknowledge the funding. The construction of this large programme and netwerk around it is an enormous task and therefore I am very thankful to prof. dr. Manuel Yañez Montero, prof. dr. Otilia Mó, dr. Wilson Rodriguez and their team. This very specific PhD programme has been tremendously interesting and I have no doubt it has prepared me well for the remainder of my professional career.

Next, I would like to thank a number of colleagues that have helped me to develop to the scientist as well as the person I am now through endless interesting scientific discussions on one hand and other social interactions on the other. In Valencia they were dr. Antonio Francés, dr. Joaquin Calvo Roig, Jake Wilson, Ahmad Huran, dr. Benedikt Daenekamp, dr. Juan Aragó, dr. Daniel Roca Sanjuán and Sebastian Sitkiewicz, at AlyaTech dr. Patricia Ruiz, dr. Ewa Szlapa and Laura Dorado and at the university of Perugia dr. Stefano Battaglia and dr. Carles Martí. Of course I should mention the remaining 14 ESR's that were with me, spread out over Europe, during the last three years and with whom I have spent multiple workshops, courses and conferences. Some of them have become friends and treasured colleagues that will definitely reappear from time to time in both my professional and personal future.

Moving and working abroad for three years would not have been so easy without the continued support from my family and old friends from home. Knowing that they were there whenever I needed to go back to basics gave me the necessary calmness and confidence to continue my work and explore new personal objectives. I would like to mention especially my mother, Griet Soetaert, and my father, Dirk Vekeman, my brothers, Seppe and Josse Vekeman, and my sisters, Sanne and Lore Vekeman. Furthermore, some of my oldest friends deserve a special thanks: Brecht Mertens and Edine Barbier, Cédric Gazulla, Thomas Torck and Valerie Van Hastel, Aïcha Naesen and Sietske Kneuvels. Further thanks to my old study mates at Ghent University for the ongoing support and friendship.

Finally and most importantly, I would like to thank my girlfriend, Maike van den Hoven. Aside from her continued interest in my work, totally unrelated to her fields of interest, she has been a strong support during this PhD. Aside from spending two years at long distance, while working in Belgium, she moved with me to Italy with our first-born, Fons, to who she had given birth briefly before. Living in a small town in Italy, without speaking the language and taking care of a new born baby, effectively putting aside her personal ambitions for one year, was not always easy for her. I am duely aware of that and could not be more grateful.

Contents

List of Figures

List of Tables

Chapter 1

Introduction

Experiments have led the way forward in chemistry — and science in general — for centuries and they still are the yardstick for scientific advances. However, the availability of increasing computational power in the last decades has provided the tools for a complementary route to work alongside experiment. In its early stages, computational chemistry has helped gaining insights into theoretical principles underlying chemistry, but now it is rising to a level where the behavior of real-life applications can be accurately described and even predicted on a routine basis. It is clear that theory should not try to replace experiment, but does have some considerable advantages over experimental chemistry that make it a worthy tool alongside experiment [1].

A first major advantage is that new materials are only a couple of mouse clicks away on a computer as opposed to the sometimes cumbersome synthesis processes that precede experiments [2]. For example, graphene, discovered in 2004 only [3, 4], has been studied theoretically since the late forties [5–8]. Especially in areas where a small amount of simple building blocks allow for a plethora of final materials — all with their own characteristics — this can be a considerable advantage. Going trough the synthesis of all these possible materials would in some cases be impossible, or at least impractical, due to time constraints while they can be accurately modeled within realistic time frames on computers. Molecular modeling can then play a guiding role for experimental chemistry in two ways. Firstly, fast calculations can point in the direction of promising materials with the right characteristics for a given application of interest or, indeed, indicate which directions should be avoided. Experimentalists can then try to synthesize this more limited set of materials or molecules and study their experimental features, a procedure that is often used for materials derived from graphene [9, 10]. Secondly, trends and characteristics of specific building blocks and their combinations can be identified leading to guidelines in the development of new materials. An example relevant for this work is the large amount of different nanocarbon materials that can be formed. Theoretical prescreening and characterization can lead the way to succesful materials for different applications [11].

A second major advantage of theoretical chemistry is the molecular view it provides on materials and processes of interest. Whereas experiments typically treat a large amount of molecules at mole scale, theoretical calculations and simulations allow for zooming in into the level of single molecules. Indeed, very often it is not even possible to study more than a couple of hundreds of molecules and at this scale, it is often easier to identify the reason for certain effects of interest and the influence of different relevant conditions [12]. As such, theoretical chemistry can not only lead the way to new materials, but also gain important insights into the very reasons of their success.

In particular, a strong interest has arisen in the adsorption of small gases, whereby adsorption refers to the phenomenon of gas molecules being attracted to a surface through non-covalent interactions. Physisorption, as it is also called, is of high-interest because of its promise for a number of applications, such as the storage and separation of gas molecules. There are a multitude of gas mixtures that need separation before or after use in industrial processes, while other applications require their storage and/or transportation. Specifically for the latter, the traditionally used procedures are expensive, difficult and sometimes dangerous [13]. Indeed, gas storage and transportation is usually done in containers that need to be cooled to very low temperatures and are under high pressure in order to store a feasible amount of gas [14, 15]. The procedure of adsorbing gas into a solid material with strong affinity for the gas of interest would take away a lot of the disadvantages that come with the storage in containers [16, 17]. Furthermore, depending on the properties of the surface and the gas molecule, the electronic properties of the former could be altered upon adsorption. If a suitable way can be found to detect the altered property, the surface becomes a potential gas detector with extreme sensitivity, in some cases detection of a single molecule is within reach [18, 19]. For these reasons, gas adsorption on a plethora of materials was considered [9, 20]. Among them, the most popular are MOFs [2, 21–24], zeolites [25, 26], activated carbon [17, 27, 28], graphite [29, 30] and nanocarbon materials like graphene and carbon nanotubes [31–34].

Especially, graphene, with its specific 2D structure and electronic properties, has shown a strong promise as an adsorbent for gas adsorption through van der Waals interactions ever since its discovery [35–41]. Indeed, the remarkable two dimensional nature of graphene with its sp^2 carbon atoms covalently bound in a hexagonal lattice and π-electron clouds on either side of the sheet, have shown a strong affinity for the adsorption of small gas molecules [11]. Many derivatives of it have been studied such as graphene sheets containing defects in all kinds of shapes [42, 43], doped with atoms like nitrogen [44], lithium [45], aluminium [19], boron [44] or oxidized to graphene oxide [11, 46]. Also, more complicated materials have been built containing constructions of graphene and carbon nanotubes [47, 48] or graphene derivatives where benzene rings were removed to obtain ordered pores for molecular sieving, such as graphtriyne [49]. In this context, the main goal of the work presented in this thesis is, precisely, the theoretical characterization of the adsorption of small gases on graphene. To this end, a multi-scale study going from CCSD(T) and DFT modeling to molecular dynamics and grand canonical Monte Carlo simulations has been carried out.

The non-covalent interactions leading to gas adsorption are by default very weak and therefore hard to study at both the theoretical and experimental level [50]. Proper representation by theoretical simulations can thus provide important insights in the way these interactions work at the molecular level and provide pathways to tune and modify materials to maximize the effects of interest [51, 52]. Such a theoretical approach faces two important difficulties: firstly, the intermolecular interactions appearing in the systems of interest are, in most cases, of dispersion type and, consequently, their adequate description requires the use of highly accurate — and expensive — quantum methods. In fact, dispersion interactions are caused by instantaneous changes in the electron clouds of the interacting partners and are, therefore, non-local, requiring the use of methods that explicitly take non-local electron correlation into account, such as coupled cluster calcuations, preferably of the CCSD(T) type [53, 54]. Secondly, for the theoretical predictions to correctly represent the macroscopic aspects of adsorption, it is important to study a large amount of molecules in their behavior through time. Systems of these sizes are not computationally viable for study through accurate quantum chemical methods and therefore, simplified analytical expressions are used considering the always important balance between accuracy and computational cost [55]. The first aim of this work is then to design a set of accurate, yet simple analytical expressions, specifically for adsorption of small gases on graphene, that can be implemented in fast simulation protocols allowing the study of a large number of molecules [56].

An important feature of dispersive interactions, inherently related to instantaneous fluctuations of the electron density and resulting dipoles, is that they are always attractive, but not isotropic. The relative orientation of molecules towards each other may thus be of primary importance [57] calling for models that are orientation-dependent for accurate results [41, 58]. On the other hand, the large amount of molecules and the statistical treatment within the simulation techniques allow for analytical expressions that treat the interactions in an average fashion, leading to a significant speed-up. In these more simple model-types, the orientation dependence of the model is treated in an average fashion instead of implicitly built in [29, 59].

Previously, similar force fields have been designed, often via fitting of a suitable potential against experimental data [60, 61]. The transferability of these kinds of force fields is questionable and needs to be approached with care. In this work, however, the potentials are specifically developed for gas adsorption on graphene from fitting to theoretical reference data of very high quality. Intermolecular interaction energies were calculated using the B97-D DFT functional, proven to accurately describe similar systems [62–64]. The interaction energies obtained, were then used as a database for fitting of well-chosen analytical expressions to capture the average behavior over a large amount of geometries. On the other hand, the high level interaction energies also allow for identifying directional behavior within the adsorption process such as preferences for specific sites or orientations of the gas molecule.

The analytical expression that is very often used to combine the requirements described in previous paragraphs, is the Lennard-Jones (LJ) potential [58, 65–67]. It has been developed in the early stages of theoretical chemistry and has known a large success in the world of simulations [55, 68]. Through time, however, it has become clear that there are important shortcomings in the potential related to its mathematical simplicity, which, in itself, is the very reason for its success. Many attempts have been performed to develop better potentials that add more physical relevance without losing the mathematical simplicity and thus computational cheapness. One of these attempts that has shown particular promise, is the so-called Improved Lennard-Jones (ILJ) potential which, through one extra physical parameter, adds extra flexibility in the expression to account for the shortcomings of the LJ potential [56, 69–73]. It is this potential that will be the workhorse during this thesis where it will first be used to obtain an accurate and simple set of intermolecular force fields for the systems under study, which will then be implemented in different simulation techniques to study the behavior at a molecular level [59, 73, 74]. Aside from this potential, the Coulombic sum will be used to study the influence of electrostatic interactions on the ILJ potential and their compatibility [22, 34, 75, 76]. It is important to note here, that, although obtaining very accurate potentials is not too hard for the systems under study, the focus is here on finding very simple potentials that allow for fast calculation of large systems.

The potentials that have thus been obtained and benchmarked are then used in simulation techniques such as molecular dynamics (MD) and grand canonical Monte Carlo (GCMC) to study the adsorption of pure gases and the separation of their mixtures on graphene. In molecular dynamics, the systems of interest are propagated through time allowing for the calculation of interesting properties like temperature, energy, but also more qualititative behavior like z-density profiles as an average over time. GCMC simulations on the other hand roam phase space via the introduction of random movements in the system allowing states that would take very long or even be impossible to reach in MD. The properties of interest are then calculated as an average over random moves through phase space. Since the ILJ potential was not used before in GCMC simulations, its implementation and a proof-of-concept of the combination of this potential and simulation technique was also of interest. It is worthy to stress that in most of previous studies, the graphene sheet or related structure, is modeled as a rigid entity without internal movements. However, it has been shown that wrinkles in the graphene sheet may influence its surface area and electronic properties [77], which may have a further impact on its abilities as an adsorbent. Furthermore, the curvature in fullerenes and carbon nanotubes was shown to strongly affect gas adsorption [78]; curvature, which may be expected to be introduced locally into the graphene sheet by internal movements of the constituting carbon atoms in a concerted fashion. In this work, we have then applied different intramolecular force fields from the literature to model the inherent flexibility of the graphene sheet and its influence on gas adsorption [79–82].

A first gas molecule that was studied in this work is methane, highly relevant due to its promise as a midterm replacement for fossil fuels on one hand and, ironically, for its destructive influence on the environment on the other [45, 83]. Methane gas is fairly easy won from natural gas — whereby it needs to be separated from nitrogen gas — and has a relatively high energetic value leading to possible uses as fuel. What makes it so interesting is the fact that it is on one hand cleaner and more abundant on earth than traditional fossil fuels, while on the other hand being directly applicable into existing applications [38, 84]. On a long term, current society will have to change its industry away from traditional fuels because of the high environmental cost and the dwindling of available resources [85]. While new technologies are being developed and implemented, methane can serve as a transition fuel allowing for a cleaner combustion without the major price issues related to a complete conversion that comes with a radically different fuel [86, 87]. Adsorption of methane on solids allows then for a clean and safe storage and transportation of methane for use as a transition fuel. Aside from this and although CO_2 is usually more focused on as the most important greenhouse gas due to its larger emissions, methane is actually a larger contributor to the greenhouse effect per molecule [88]. It is thus of primary importance to separate methane gas from combustion exhausts before release in the atmosphere [25, 89].

In experimental chemistry, one of the first steps in characterizing a new adsorption material is determination of the pore volume, often done with nitrogen gas [57, 90, 91]. The inert nature of N_2 and the absence of strong intermolecular interactions with most materials, makes it a particularly suited molecule for this purpose [23, 90]. It is assumed that nitrogen barely interacts with the material and therefore the gas behaves as bulk gas within the adsorbent, the amount of gas entering the material is then a direct measure for its pore volume [92]. As a first test for a theoretical model of a material, the simulations need to reproduce these experimental measurements on the pore volume, while newly predicted materials need a trustworthy pore volume upon which decisions towards the synthesis of the material can be based. For these reasons, accurate models for nitrogen are very important. Furthermore, it was shown that nitrogen has a strong influence on extracting methane from clathrate reservoirs by aiding the dissociation of the methane hydrates [93]. Yet another interesting application has been suggested by Ohba et al. whereby the amount of nitrogen adsorbed on graphene was used to estimate the amount of graphene layers that was present in the surface [94].

It goes without saying that water is one of the most studied molecules in chemistry because of its omnipresence in chemical and biological processes. Specifically for this work, it is mostly important because of its presence in a variety of processes as an impurity [95]. In pre- and post-combustion mixtures, there is often at least some water present which may substantially influence the behavior of the mixture [96–98], especially through its very specific behavior when confined into ordered nanomaterials [99, 100]. Furthermore, water itself has shown promise for gas storage through the formation of clathrates [101], while other important applications include the elimination of water after alcohol production for biofuels [102] as well as the purification of water itself to eliminate contaminants as Ibuprofen [103]. Finally, the wetting properties of ordered carbon nanomaterials like graphene are also under research because of possible applications on a variety of processes like seawater desalination or DNA-sequencing [104–107].

Another important gas in industry is carbon monoxide as it is, among others, an important component of the Fischer-Tropsch process [108] and of the synthesis of methanol. Furthermore, it is known to poison catalysts and fuel cells after contaminating hydrogen gas, removing the gas before the start of the process is thus very important [109]. As known, carbon monoxide can be very dangerous when inhouse combustion processes go wrong and sensitive CO sensors can thus be life-saving in certain situations [19].

Hydrogen on the other hand shows promise for a whole new energy paradigm based on fuel cells without environment damaging exhaust gases [13]. Transportation and storage is of particular importance here, since the gas is highly explosive in the conditions needed for efficient storage. Once again, adsorption on the right material is vital [14].

Finally, two binary gas mixtures — important for industrial applications — are investigated in this work. The first is the methane/nitrogen gas mixture, important since nitrogen is often found as an unwanted impurity in natural gas [26, 110]. Furthermore, post-combustion gases often contain both nitrogen and methane whereby it is important to eliminate the latter before releasing the harmless nitrogen into the atmosphere [74, 97, 111–113]. The methane/hydrogen mixture, on the other hand, is of interest since methane is an unwanted byproduct of hydrogen gas production [114]. Finally, it was found that introduction of hydrogen in methane gas, leading to hythane, gives a more efficient energy source than methane in itself under certain conditions [115, 116].

In chapter 2, the theoretical methods used in this work will be discussed, while in chapter 3, the development of the force fields needed to describe the adsorption of methane, nitrogen and water on graphene will be discussed in detail and, furthermore, the treatment of orientation effects will be exemplified by a theoretical investigation of the different gas dimers. In chapters 4 and 5, the implementation and application of the potentials in MD and GCMC will be discussed and illustrated mainly by studying the possibility of separations of mixtures of methane and nitrogen and methane and hydrogen, respectively. Finally, chapter 6 will present the main conclusions of this work.

Chapter 2

Theoretical Methods

A plethora of methods has been developed for the theoretical study of chemical systems, some of which have become standardized, while others have been less used or are still in development. This section aims to provide an overview of the methods that were relevant for this thesis. Generally, two types of methods have been used throughout this work: quantum mechanics and classical molecular dynamics. The first refers to methods that aim at calculating a single state of a system with very high accuracy using the concepts of quantum theory. The second introduces time and space in an intent to follow the behavior of the system through time. The large amount of calculations that is needed for this, often forces the use of classical descriptions that include quantum effects only implicity. This section has been written with the aid of some standard text books that deserve a mention here, specifically the work by Jensen [117] on computational chemistry and the "bible" by Szabo and Ostlund [118] were used for the quantum mechanical part, the work by Smith [119] was used for the molecular dynamics part and the work by Landau et al. [120] was used for the Grand Canonical Monte Carlo part. Further references will be cited in the text as conventional.

2.1 Quantum Mechanical Methods

In quantum mechanics, the main goal is to solve the time-dependent Schrödinger equation

$$\hat{H}(\vec{r},t)\Psi(\vec{r},t) = \frac{\delta\Psi(\vec{r},t)}{\delta t} \quad , \tag{2.1}$$

whereby $\hat{H}(\vec{r},t)$, the Hamiltonian operator, is formed by the summation of the kinetic and potential energy operators

$$\hat{H}(\vec{r},t) = \hat{T}(\vec{r},t) + \hat{V}(\vec{r},t) \quad . \tag{2.2}$$

The solution of this equation gives the wave function, $\Psi(\vec{r},t)$, as a function of time and describes the probability of finding a particle at position, $\vec{r}$, and time, t. When the potential energy operator is independent of time, the Hamiltonian becomes independent of time as well, yielding the total energy when acting on the wave function

$$\hat{H}(\vec{r})\Psi(\vec{r},t) = E(\vec{r})\Psi(\vec{r},t) \quad . \tag{2.3}$$

This makes it possible to separate the time and space variables of the wave function, showing that the time-dependence of the wave function can be written as the spatial wave function mutiplied by a phase factor. The latter can be ingored for time-independent problems, leading to the time-independent Schrödinger equation

$$\hat{H}(\vec{r})\Psi(\vec{r}) = E(\vec{r})\Psi(\vec{r}) \quad . \tag{2.4}$$

As the main interest in this part is the single point calculation, it is this time-independent Schrödinger equation that we want to solve. For most systems, however, this is not possible analytically and multiple approximations exist to overcome this problem. We will not make an attempt to discuss all of them, but merely give an overview of the methods that were used during this work and motivate those choices. All described methods fall within the Born-Oppenheimer approximation, which will be assumed known and applicable throughout this work.

2.1.1 Wavefunction Based Methods

Looking at the time-independent Schrödinger equation (equation 2.4), it is clear that, in order to find the energy, $E(\vec{r})$, we need to know the expressions for the wave function, $\Psi(\vec{r})$. This expression, however, is not known on beforehand and needs to be found together with the energy, which is done via an iterative process, called the self-consistend field (SCF) procedure. In this process, a trial wave function (in practice, this will be a set of coefficients, see later) is entered into equation 2.4 and the energy is minimized. The minimization gives rise to a new wave function (set of coefficients) for which the energy is again minimized leading to a new wave function (set of coefficients), this procedure is repeated until convergence of the energy. In principle, this is a minimization problem whereby the energy is minimized in function of a set of parameters (coefficients) that determines the trial wave function. The variational principle — stating that any approximate wave function can never have an energy lower than the ground state wave function — guarantees that the end result will be very close or equal to the ground state wave function and the corresponding energy as long as the starting geometry is sufficiently close to equilibrium. This procedure is termed the self-consistent field (SCF) procedure because it leads to an expression that is 'self-consistent' with itself in the sense that, after convergence, minimizing the energy will lead to an unchanged wave function.

2.1.1.1 The Hartree-Fock Approximation

The most widely used approximation to solve the electronic Schrödinger equation, is the Hartree-Fock (HF) approximation, stating that the ground state of an N-electron system can be described by a single Slater type determinant [1]

$$\psi(\vec{x}_1, \vec{x}_2, ..., \vec{x}_n) = \frac{1}{\sqrt{N!}} \begin{vmatrix} \chi_1(\vec{x}_1) & \dots & \chi_j(\vec{x}_1) & \cdots & \chi_n(\vec{x}_1) \\ \chi_1(\vec{x}_2) & \dots & \chi_j(\vec{x}_2) & \cdots & \chi_n(\vec{x}_2) \\ \vdots & \ddots & \vdots & \ddots & \vdots \\ \chi_1(\vec{x}_n) & \dots & \chi_j(\vec{x}_n) & \cdots & \chi_n(\vec{x}_n) \end{vmatrix} \quad , \tag{2.5}$$

where N is the number of electrons in the system, $\chi_n(\vec{x}_n)$ is a molecular spin orbital depending on $\vec{x}_n = (\vec{r}_n, s_n)$ where $\vec{r}_n$ is the position vector of the n^{th} electron and s_n its spin. Description of the system by such a wave function, guarantees the fulfillment of the Pauli principle because of its antisymmetric nature. The mathematical expression for the variational principle mentioned before states, in other words, that the best possible wave function of the chosen form, is the one that leads to the lowest possible energy

$$E_0 = \langle \Psi_0 | \hat{H} | \Psi_0 \rangle \quad , \tag{2.6}$$

where $\hat{H}$ is the electronic Hamiltonian and is given by

$$\hat{H}_{\text{elec}}(\vec{r}; \vec{R}) = -\frac{1}{2} \sum_{i=1}^{N} \nabla_i^2 - \sum_{\alpha=1}^{M} \sum_{i=1}^{N} \frac{Z_a}{|\vec{r}_i - \vec{R}_\alpha|} + \sum_{i=1}^{N} \sum_{j>i}^{N} \frac{1}{|\vec{r}_i - \vec{r}_j|} \quad . \tag{2.7}$$

Given the form of the wave function, this can be converted to a more convenient form, called the Fock operator

$$\hat{f}(k) = \hat{h}(k) + 2 \sum_{j}^{\frac{N}{2}} [\hat{J}_j(k) - \hat{K}_j(k)] \quad . \tag{2.8}$$

Here, $\hat{h}(k)$ is defined as the one-electron operator containing the kinetic energy and the electron-nucleus potential of electron k moving in the field of all the nuclei. On the other hand, $\hat{J}_j(k)$ and $\hat{K}_j(k)$ are the Coulomb and exchange operators respectively and as such describe the repulsion of the electron to all other electons present. The Coulomb operator is given by

$$\hat{J}_j(k) = \left\langle \chi_j(m) | \frac{1}{r_{mk}} | \chi_j(m) \right\rangle \quad , \tag{2.9}$$

while the latter can only be written down applied to a (spin) orbital

$$\hat{K}_j(k) \chi_i(k) = \left\langle \chi_j(m) | \frac{1}{r_{mk}} | \chi_i(m) \chi_j(k) \right\rangle \quad . \tag{2.10}$$

The Coulomb operator represents the classical repulsion between two charge distributions, while the exchange operator arises from the antisymmetry principle although it cannot be explained classically. Together, however, they constitute the

---

[1] or by a simple spin-symmetry determined linear combination of determinants forming a single configuration state function

electron-electron interaction of the system as the interaction between a given electron with the averaged interaction of the remaining electrons combined.

As explained in section 2.1.1, the best possible wave function of this type can now be found by minimizing the energy with respect to the molecular orbitals. However, in this minimization, the orthogonality and normalization of the molecular orbitals should be maintained. Such a constrained minimization can be performed by using Lagrangian multipliers,

$$L = E - \sum_{ij}^{N} \lambda_{ij} \left(\langle \phi_i | \phi_j \rangle - \delta_{ij} \right) \quad , \tag{2.11}$$

and setting the condition that the Langrange function should not change upon a small variation of the molecular orbitals

$$\delta L = \delta E - \sum_{ij}^{N} \lambda_{ij} \left(\langle \delta\phi_i | \phi_j \rangle - \langle \phi_i | \delta\phi_j \rangle \right) = 0 \quad . \tag{2.12}$$

Solving this, imposing the orthonormality restriction, $\langle \chi_i | \chi_j \rangle = \delta_{ij}$, the eigenvalues and eigenvectors for the Fock operator can be found, corresponding to the spin orbitals and energies

$$\hat{f} \chi_i(\vec{x}_i) = \epsilon_i \chi_i(\vec{x}_i) \quad , \tag{2.13}$$

where, furthermore, a linear transformation of the spin-orbitals has been carried out to diagonalize the λ-matrix, the ϵs being the corresponding eigenvalues. According to the linear combination of atomic orbitals (LCAO) approximation, the molecular spin orbital can be further expressed as

$$\chi_i(\vec{x}_i) = \sum_{\mu=1}^{N} c_{i\mu} \phi_\mu(\vec{x}_i) \quad , \tag{2.14}$$

whereby, ϕ_μ, are atomic functions of chosen form (see section 2.1.3) that do not change and $c_{i\mu}$ are the corresponding coefficients which need to be optimized in the minimization procedure. Assuming that an infinite amount of atomic orbitals is included, the obtained energy will be exact within the HF limit. Since, the form of the atomic orbitals is chosen and unchanged after, the minimization is now reduced to minimization of the energy as a function of the orbital coefficients $c_{\mu i}$, written in matrix notation as

$$FC = SC\epsilon \quad . \tag{2.15}$$

These so-called Roothaan-Hall equations contain the following matrix elements

$$F_{ij} = \left\langle \chi_i | \hat{f} | \chi_j \right\rangle \tag{2.16}$$

and from this it is clear that the Fock operator used to minimize the energy with respect to the spinorbitals depends itself on those very same spinorbitals. An iterative procedure is thus needed to find the coefficients for the atomic orbitals in equation 2.14 as was explained in section 2.1.1.

A consequence of representing the trial wave function by a single Slater determinant is that the interaction of any electron with the other electrons is taken into account by assuming that their spatial distribution is described by a set of orbitals. This effectively means that the interaction with the other electrons is represented as a system-average and the method is therefore called a mean-field approximation. Although this approach retains a very large part of the total energy (up to 99%) many of the chemically relevant phenomena have their origin in the remaining 1% that is not retained in the HF approximation. More specifically, the part that is lacking in the HF picture is the Coulomb correlation, the correlation between electrons of different spins, while the Fermi correlation, correlation between electrons of parallel spin, is adequately described. Since the part that is missing from the HF approximation is related to the correlated motion of electrons in the system, the missing part is often refferred to as the correlation energy

$$E_{\mathrm{corr}} = E_{\mathrm{total}} - E_{\mathrm{HF}} \quad . \tag{2.17}$$

By construction, HF gives the best possible description of the system a single Slater determinant can give. It is therefore clear that to further improve the picture, more Slater determinants need to be added to the initial trial wave function. Since HF retains up to 99% of the total energy, it is often used as the starting point for further improvements and different ways of thinking exist to implement these improvements. Only two will be discussed here as they were used during this work. The first one consists in adding extra Slater-type determinants representing excitations from electrons from their ground state orbital to higher level orbitals, this will be discussed in the next section on electron correlation methods. The second method changes the picture drastically and focuses on the electron density instead of the wave function, density functional theory (DFT) will be covered in section 2.1.2.

2.1.1.2 Coupled Cluster

Just as the molecular orbitals were described as a linear expansion of atomic orbitals (see equation 2.14), we can use a linear expansion of single determinant wave functions to describe a multi-determinant wave function

$$\Psi = a_0 \Phi_{\mathrm{HF}} + \sum_{i=1} a_i \Phi_i \quad . \tag{2.18}$$

The new set of determinants, Φ_i can be obtained by using the HF single-Slater determinant and exchanging occupied and unoccupied molecular orbitals. This way a set of determinants can be constructed where one occupied and unoccupied molecular orbital were interchanged, another set where two were interchanged and so on. These determinants are referred to as singly, doubly, ... excited and the number of possible excitations depends on the size of the basis set as will be explained in detail later on. All the electron correlation in the system can be retained by including all possibe excitations in the system, meaning that for the complete basis set limit, the Schrödinger equation is solved exactly within the Born-Oppenheimer and non-relativistic frameworks. However, the inclusion of all possible excitations is very expensive and many ways are introduced to lower the computational cost. Since chemical phenomena of interest involve mostly the valence electrons, an often used approach is to exclude the non-valence electrons, e.g. the core electrons, from the excitations. Such an approach is called a frozen-core approximation. The approach is valid for calculation of energy differences, because the correlation of the frozen electron is a constant for a given system. Different approaches exist to calculate the electron correlation, the main ones are Configuration Interaction, the Many-Body Perturbation Theory and Coupled Cluster. In this work, Coupled Cluster was used, so the discussion will be limited to this method.

Referring to equation 2.18, we can define an excitation operator,

$$\hat{T} = \hat{T}_1 + \hat{T}_2 + \hat{T}_3 + ... + \hat{T}_N \ , \tag{2.19}$$

such that the operator T_i acting on the HF wave function gives the Slater determinants excited to the i^{th} order

$$\hat{T}_1 \Phi_0 = \sum_{i}^{\text{occ}} \sum_{a}^{\text{vir}} t_i^a \Phi_i^a \tag{2.20}$$

and

$$\hat{T}_2 \Phi_0 = \sum_{i<j}^{\text{occ}} \sum_{a<b}^{\text{vir}} t_{ij}^{ab} \Phi_{ij}^{ab} \ , \tag{2.21}$$

where t_i^a are expansion coefficients, which in this context are often referred to as amplitudes. The coupled cluster wave function is now defined as

$$\Psi_{\text{CC}} = e^{\hat{T}} \Phi_0 \ , \tag{2.22}$$

whereby $e^{\hat{T}}$ can be expanded in a Taylor series as

$$e^{\hat{T}} = 1 + \hat{T} + \frac{1}{2}\hat{T}^2 + \frac{1}{6}\hat{T}^3 + ... = \sum_{k=0}^{\infty} \frac{1}{k!} \hat{T}^k \ . \tag{2.23}$$

The Schrödinger equation now becomes

$$\hat{H} e^{\hat{T}} \Phi_0 = E e^{\hat{T}} \Phi_0 \ . \tag{2.24}$$

This equation can be evaluated via the variational principle, but this leads to terms up to order N and, thus, to an enormous compuational cost. Therefore, usually, the coupled cluster Schrödinger equation is projected onto the reference HF wave function as follows

$$\left\langle \Phi_0 | \hat{H} e^{\hat{T}} | \Phi_0 \right\rangle = E_{\mathrm{CC}} \left\langle \Phi_0 | e^{\hat{T}} | \Phi_0 \right\rangle \quad . \tag{2.25}$$

Plugging in equation 2.23, gives

$$\left\langle \Phi_0 | \hat{H} e^{\hat{T}} | \Phi_0 \right\rangle = E_{\mathrm{CC}} \left\langle \Phi_0 | 1 + \hat{T}_1 + \hat{T}_2 + ... | \Phi_0 \right\rangle \quad . \tag{2.26}$$

After which the coupled cluster energy is given as

$$E_{\mathrm{CC}} = \left\langle \Phi_0 | \hat{H} e^{\hat{T}} | \Phi_0 \right\rangle \quad . \tag{2.27}$$

Using the expansion of $e^{\hat{T}}$ from equation 2.23 and the definition of the Hamiltonian operator in equation 2.7, containing only one-and two-electron operators, we get

$$E_{\mathrm{CC}} = \langle \Phi | \hat{H} \left(1 + \hat{T}_1 + \hat{T}_2 + \frac{1}{2} \hat{T}_1^2 \right) | \Phi_0 \rangle \quad , \tag{2.28}$$

leading to

$$E_{\mathrm{CC}} = \langle \Phi_0 | \hat{H} | \Phi_0 \rangle + \langle \Phi_0 | \hat{H} | \hat{T}_1 \Phi_0 \rangle + \langle \Phi_0 | \hat{H} | \hat{T}_2 \Phi_0 \rangle + \frac{1}{2} \langle \Phi_0 | \hat{H} | \hat{T}_1^2 \Phi_0 \rangle \tag{2.29}$$

and

$$E_{\mathrm{CC}} = E_0 + \sum_{i}^{\mathrm{occ}} \sum_{a}^{\mathrm{vir}} t_i^a \langle \Phi_0 | \hat{H} | \Phi_i^a \rangle + \sum_{i<j}^{\mathrm{occ}} \sum_{a<b}^{\mathrm{vir}} \left(t_{ij}^{ab} + t_i^a t_j^b - t_i^b t_j^a \right) \langle \Phi_0 | \hat{H} | \Phi_{ij}^{ab} \rangle \quad . \tag{2.30}$$

The infinite expansion of the expansion operator now leads to a highest order term of only second order instead of order N. A further advantage is that the use of HF orbitals for construction of the Slater determinants leads to the vanishing of the first matrix elements, due to the Brillouin theorem, and the second matrix element reducing to two-electron integrals over the molecular orbitals

$$E_{\mathrm{CC}} = E_0 + \sum_{i<j}^{\mathrm{occ}} \sum_{a<b}^{\mathrm{vir}} \left(t_{ij}^{ab} + t_i^a t_j^b - t_i^b t_j^a \right) \left(\langle \phi_i \phi_j | \phi_a \phi_b \rangle - \langle \phi_i \phi_j | \phi_b \phi_a \rangle \right) \quad . \tag{2.31}$$

The coupled cluster energy is thus defined in terms of the singles and doubles amplitudes and the two-electron molecular orbital integrals. However, the amplitudes are still unkown at this point and can be obtained by projecting the Schrödinger equation onto the space of single, double, ... excited determinants, often done via a similarity transformation of the Hamiltonian operator. Starting from equation 2.24 and multiplying on the left with a deexcitation operator, working on the function to the left, we get

$$e^{-\hat{T}} \hat{H} e^{\hat{T}} \Phi_0 = E_{\mathrm{CC}} \Phi_0 \quad , \tag{2.32}$$

which after multiplication with Φ_0^* from the left and integration, leads to

$$E_{\text{CC}} = \langle \Phi_0 | e^{-\hat{T}} \hat{H} e^{\hat{T}} | \Phi_0 \rangle \ . \tag{2.33}$$

Since the deexcitation operator tries to deexcite the reference wave function in this equation, it is essentially equal to equation 2.27. To obtain equations for the amplitudes, we need to multiply with a respective excited state

$$\langle \Phi_m^e | e^{-\hat{T}} \hat{H} e^{\hat{T}} | \Phi_0 \rangle = 0 \tag{2.34}$$

for the single excitation amplitude and

$$\langle \Phi_{mn}^{ef} | e^{-\hat{T}} \hat{H} e^{\hat{T}} | \Phi_0 \rangle = 0 \tag{2.35}$$

for the double excitation amplitude and so on. It should be stressed that, because of the two-electron nature of the Hamiltonian, no more than quartic equations need to be solved, regardless of the chosen excitation level.

So far, if all possible excitation operators are included, an exact calculation is again performed within the assumed approximations which is computationally prohibitive for most systems. For this reason, a truncation is performed after a chosen excitation operator. Truncating after the first excitation operator, gives no improvement to the HF energy and thus at least doubly excited states need to be included. The resulting CCD level reduces to MP2 if the amplitudes are calculated as

$$t_{ij}^{ab} = -\frac{\langle \Phi_{ij}^{ab} | \hat{H} | \Phi_0 \rangle}{\epsilon_a + \epsilon_b - \epsilon_a - \epsilon_b} \ , \tag{2.36}$$

where ϵ_i is the energy of orbital i. Since including the singles as well adds very little to the computational cost, an often used approach is the CCSD approximation, scaling as N_{basis}^6. A further improvement to the level of CCSDT scales as N_{basis}^8 and is computationally prohibited for all but the smallest system. In a way to find middle ground between these two methods, there are several hybrid methods whereby the CCSD method is used and the triple excitations are then added as evaluated by perturbation theory. The most commonly used variation is the CCSD(T) method which is indeed regarded as the current "gold standard" of quantum chemistry. The CCSD(T) energy can be written as an energy correction on CCSD energy [121]

$$E_{\text{CCSD(T)}} = E_{\text{CCSD}} + \Delta E_{\text{CCSD(T)}} \tag{2.37}$$

and the correction is then given as

$$\Delta E_{\text{CCSD(T)}} = \sum_{ai} \bar{t}_i^{a\,*} \hat{T}_i^a + \sum_{abij} \bar{t}_{ij}^{ab\,*} \hat{T}_{ij}^{ab} \ . \tag{2.38}$$

Here, $\bar{t}_i^a$ and $\bar{t}_{ij}^{ab}$ are expressed in terms of the CCSD amplitudes, t_i^a and t_{ij}^{ab}, while

$$\hat{T}_i^a = \sum_{cdkl} \left({}^{*}t_{ikl}^{acd(2)} - {}^{*}t_{lki}^{acd(2)} \right) L_{kcld} \tag{2.39}$$

and

$$\hat{T}_{ij}^{ab} = \sum_{cdk} \left({}^{*}t_{ijk}^{acd(2)} L_{bckd} - {}^{*}t_{kji}^{acd(2)} \left(kd|bc\right) \right) - \sum_{ckl} \left({}^{*}t_{ikl}^{abc(2)} L_{kjlc} - {}^{*}t_{lki}^{abc(2)} \left(kj|lc\right) \right) \quad , \tag{2.40}$$

with

$$L_{kcld} = 2\left(kc|ld\right) - \left(kd|lc\right) \quad . \tag{2.41}$$

The second order triple amplitudes are then obtained from the CCSD amplitudes, t_{ij}^{ab} via perturbation theory as follows

$$^{*}t_{ijk}^{abc(2)} = -\hat{P}_{ijk}^{abc} \left(\left(\sum_{d} t_{ij}^{ad} \left(ck|bd\right) - \sum_{l} t_{il}^{ab} \left(ck|lj\right) \right) D_{ijk}^{abc} \right) \quad , \tag{2.42}$$

whereby the operator, $\hat{P}_{ijk}^{abc}$, generates the sum of all permutations of ai, bj, ck. D_{ijk}^{abc}, on the other hand, is

$$D_{ijk}^{abc} = \frac{1}{\epsilon_a + \epsilon_b + \epsilon_c - \epsilon_i - \epsilon_j - \epsilon_k} \tag{2.43}$$

and can be simplified via the Cholesky decomposition to

$$D_{ijk}^{abc} = \frac{1}{\epsilon_a + \epsilon_b + \epsilon_c - \epsilon_i - \epsilon_j - \epsilon_k} = \sum_{n=1}^{N_\delta} d_{aij}^{n} d_{ckb}^{n} \quad , \tag{2.44}$$

where N_δ is the number of Cholesky vectors included in the calculation and can analytically be calculated as

$$d_p^n = \frac{\sqrt{2\omega_{Jn}}}{\omega_p + \omega_{Jn}} \prod \left(\frac{\omega_p - \omega_{Jm}}{\omega_p + \omega_{Jm}} \right) \quad . \tag{2.45}$$

The use of this Cholesky decomposition reduces the scaling of the CCSD(T) calculations from N^7 to N^6 [121]. It is this level of theory that is used in this work as a benchmark to validate the routinely used lower level methods as well as the resulting potentials that were developed.

2.1.2 Density Functional Methods

Hohenberg and Kohn have first proven that the ground state electronic energy is, apart from a constant, completely determined by the electron density ρ, leading to DFT [122]. This constitutes a major advantage compared to a wave function approach. While the latter uses $4N$ variables, three spatial and one spin coordinate per electron — N being the total number of electrons — DFT depends only on three spatial coordinates independent of the amount of electrons in the system. However, although it can be proven that there exists a functional yielding the ground state energy from the electron density, there is no information available regarding the shape of this functional.

2.1.2.1 Kohn-Sham Theory

Multiple varieties exist of DFT, but the Kohn-Sham variant is by far the most succesful. Kohn and Sham suggested to represent the electron density in terms of one electron functions from a hypothetical system of non-interacting electrons

$$\rho = \sum_{i=1}^{N} |\phi_i|^2 \quad . \tag{2.46}$$

This allows the largest part of the electron kinetic energy to be calculated exactly, leaving just a smaller correction term that is to be added later. The part that can be calculated exactly is very similar to the known HF energy. It represents the kinetic energy under the assumption that the electrons are not interacting and, thus, the correction term implicitly introduces the electron correlation that was lacking in HF. The cost of this procedure is the reintroduction of orbitals which rescales the problem again to $3N$ instead of just the three variables needed for orbital-free densities, but the gain is that the simple procedures for HF can be applied on DFT.

The DFT energy can then be written as a summation of the nucleus-electron attraction, $E_{\mathrm{ne}}[\rho]$, the electron-electron repulsion, $E_{\mathrm{ee}}[\rho]$ and the kinetic energy, $T[\rho]$,

$$E_{\mathrm{DFT}} = E_{\mathrm{ne}}[\rho] + E_{\mathrm{ee}}[\rho] + T[\rho] \quad . \tag{2.47}$$

The first term, $E_{\mathrm{ne}}[\rho]$, is directly available as a classical expression

$$E_{\mathrm{ne}}[\rho] = -\sum_{a}^{N_{\mathrm{nuclei}}} \int \frac{Z_a(\vec{R}_a)\rho(\vec{r})}{|\vec{R}_a - \vec{r}|} d\vec{r} \quad , \tag{2.48}$$

while the second term, E_{ee}, contains a classical Coulombic part, $J[\rho]$,

$$J[\rho] = \frac{1}{2} \int \int \frac{\rho(\vec{r})\rho(\vec{r}')}{|\vec{r} - \vec{r}'|} d\vec{r} \quad , \tag{2.49}$$

with a remaining exchange part $K[\rho]$ that cannot be exactly defined and will be treated later. As mentioned before, the core idea of the Kohn-Sham theory is to divide the third term, the kinetic energy, $T[\rho]$, which is poorly represented by other methods, into two parts. The first part being the kinetic energy of the system assuming non-interacting electrons, which can be represented as an exact functional

$$T_{\mathrm{S}} = \sum_{i=1}^{N_{\mathrm{elec}}} \left\langle \phi_i \right| - \frac{1}{2}\nabla^2 \left| \phi_i \right\rangle \quad . \tag{2.50}$$

The correlation, the kinetic energy coming from the fact that the electrons do interact, is the second part and is defined as a correction energy since it cannot be defined exactly. It is grouped together with the previously mentioned exchange functional into the so-called exchange-correlation (XC) functional. In short, Kohn-Sham DFT divides the total energy in a part that can be exactly calculated, equivalent to the HF energy, and a part that cannot be exactly defined. The DFT energy can then be written as

$$E_{\mathrm{DFT}} = T_{\mathrm{S}}[\rho] + E_{\mathrm{ne}}[\rho] + J[\rho] + E_{\mathrm{xc}}[\rho] \ , \tag{2.51}$$

which now by itself defines the XC term via equation 2.47

$$E_{\mathrm{xc}}[\rho] = (T[\rho] - T_{\mathrm{S}}[\rho]) + (E_{\mathrm{ee}}[\rho] - J[\rho]) \ . \tag{2.52}$$

2.1.2.2 Parametrizations of the XC Functional

Although it has been proven that the XC potential is a unique functional valid for all systems, it has been impossible to define its shape and the difficulty is then to find accurate approximations. By obliging candidate functionals to obey certain restrictions and/or by fitting candidate functionals to experimental data, it is possible to find approximations that give reasonable to accurate results [123]. Unfortunately and contrary to wave function based methods, there is no clear criterion to define a systematic improvement of the available methods, meaning that the performance of a specific functional may be very dependent on the system upon which it is applied. For this reason, benchmarking the used DFT functional for a specific application is highly recommended. The well-known "Jacobs-ladder", however, tries to classify the existing types of functionals in a more or less systematic way. In the following, the rungs of the ladder, relevant to this work, will be covered briefly.

On the first rung sits the local density approximation (LDA) where it is assumed that the electron density can locally be represented as a uniform electron gas and thus varies only slowly through space. The Dirac formula gives the corresponding exchange energy

$$E_{\mathrm{x}}^{\mathrm{LDA}}[\rho] = -C_{\mathrm{x}} \int \rho^{\frac{4}{3}}(\vec{r})d\vec{r} \ , \tag{2.53}$$

while the correlation energy can be determined with high precision, numerically. For DFT calculations, an analytical form is needed and multiple interpolation formulae have been proposed in the literature. Although this is a very crude approximation for molecules, the obtained results are remarkably good and come close to HF results; for the specific case of a uniform electron gas, this functional is exact. Even though it is still used in the physics community to describe extended systems, it is not accurate enough to do relevant chemistry as bond strenghts are overstimated by values up to 24 kcal mol^{-1}.

A logical next step (rung 2) is to move from a uniform electron gas to a non-uniform electron gas. This can be done by making the exhange-correlation functional dependent not only on the local density, but also on its gradient. Important is the inclusion of the restriction that the Fermi and Coulomb holes integrate to -1 and 0, respectively, a requirement that is inherent to LDA. A failure to fulfill this restriction will lead to results worse than LDA. The resulting methods are called generalized gradient approximations (GGA) and can reduce the error in the exchange energy by almost two orders of magnitude.

After including the first derivative of the density, it seems logical to add higher-order derivatives to go to the third rung, the meta-GGA functionals. However, it has been shown that including derivatives higher than the second order improves the functional little. Furthermore, the second derivative of the density contains essentially the same information as the orbital kinetic energy density. Since the latter is numerically more stable, usually the functional is made dependent on this term. Also other functionals that make use of orbital information may be positioned on this rung.

In hybrid methods (fourth rung) the idea is to mix a part of the exact exchange energy for the non-interacting (no correlation energy) reference system, calculated at HF level, in the functional to improve the picture. Because of this mixing of two different methods, they are termed hybrid functionals. The exact way and extent to which the two methods are mixed is determined by fitting to experimental data. From the large amount of functionals that are available, in this work a reparametrized version (see below) of the B97 functional was used for the DFT calculations [124].

The B97 functional contains two parts, the exchange part and the correlation part, the former of which is approximated by the common GGA form

$$E_{\mathrm{x}}^{\mathrm{GGA}} = \sum_{\sigma} \int e_{\mathrm{x}\sigma}^{\mathrm{LDA}} \left(\rho_{\sigma}\right) g_{\mathrm{x}\sigma} \left(s_{\sigma}^{2}\right) d^{3}\vec{r} \ , \tag{2.54}$$

where $e_{\mathrm{x}\sigma}^{\mathrm{LDA}}$ is the σ-spin exchange energy density per unit of volume at the LDA level. The factor $g_{\mathrm{x}\sigma}$ corrects this exchange term towards a non-uniform electron gas depending on the spin-density gradient, s_{σ}^{2}. To this term, a dynamical correlation factor, $E_{\mathrm{c}}^{\mathrm{GGA}}$, is then added

$$E_{\mathrm{c}}^{\mathrm{GGA}} = E_{\mathrm{c}\alpha\beta}^{\mathrm{GGA}} + \sum_{\sigma} E_{\mathrm{c}\sigma\sigma}^{\mathrm{GGA}} \ , \tag{2.55}$$

with $E_{\mathrm{c}\alpha\beta}^{\mathrm{GGA}}$ the contribtion of opposite spins

$$E_{\mathrm{c}\alpha\beta}^{\mathrm{GGA}} = \int e_{\mathrm{c}\alpha\beta}^{\mathrm{LDA}} \left(\rho_{\alpha}, \rho_{\beta}\right) g_{\mathrm{C}\alpha\beta} \left(s_{\mathrm{avg}}^{2}\right) d^{3}\vec{r} \ , \tag{2.56}$$

with $s_{\mathrm{avg}}^{2} = \frac{1}{2}\left(s_{\alpha}^{2} + s_{\beta}^{2}\right)$ and, $E_{\mathrm{c}\sigma\sigma}^{\mathrm{GGA}}$, the contribution for parallel spins

$$E_{\mathrm{c}\sigma\sigma}^{\mathrm{GGA}} = \int e_{\mathrm{c}\sigma\sigma}^{\mathrm{LDA}} \left(\rho_{\sigma}\right) g_{\mathrm{c}\sigma\sigma} \left(s_{\sigma}^{2}\right) d^{3}\vec{r} \ . \tag{2.57}$$

For the LDA contributions the parameterization by Perdew and Wang was used [125], while, to finalize the current approach, the $g_{\mathrm{x}\sigma\sigma}$, $g_{\mathrm{c}\alpha\beta}$ and $g_{\mathrm{c}\sigma\sigma}$ need to be systematically optimized to representative experimental data.

Via the transformation of the semi-infinite variable, s^{2}, to the more convenient and finite variable u

$$u = \frac{\gamma s^{2}}{1 + \gamma s^{2}} \ , \tag{2.58}$$

whereby γ is an empirical parameter [126], we obtain

$$g_{\mathrm{x}\sigma\sigma} = 1 + 0.967 u_{\sigma} \quad , \tag{2.59}$$

$$g_{\mathrm{c}\alpha\beta} = 1 - u_{\mathrm{c}\alpha\beta} \tag{2.60}$$

and

$$g_{\mathrm{x}\sigma\sigma} = 1 - u_{\mathrm{c}\sigma\sigma} \quad , \tag{2.61}$$

which can be expanded in a polynomial series according to

$$g = \sum_{i=0}^{m} c_i u^i \quad . \tag{2.62}$$

As the functional is of the hybrid type, an exactly computed exchange term is included in the fitting such that the full XC functional looks like

$$E_{\mathrm{xc}} = E_{\mathrm{x}}^{\mathrm{GGA}} + E_{\mathrm{c}}^{\mathrm{GGA}} + C_{\mathrm{x}} E_{\mathrm{x}}^{\mathrm{exact}} \quad . \tag{2.63}$$

The coefficients, c_i, up to an expansion of second order, are then to be determined via a fitting to accurate thermochemical data together with the C_{x} parameter — determining the amount of exact exchange — leading to ten parameters in total.

As stated before, dispersion interactions, of major importance for the non-covalently bound systems in this work, come from instantaneous fluctuations of the density. Single determinant methods as DFT are inherently unable of providing a realistic picture of these effects and alternative procedures are needed to include them [53]. Given the lack of a definite criterion to improve such picture, probably the most efficient way of including dispersion effects is the explicit introduction of an empirical correction term imposing the correct behavior

$$E_{\mathrm{tot}} = E_{\mathrm{DFT}} + E_{\mathrm{disp}} \quad , \tag{2.64}$$

whereby the dispersion energy is given as

$$E_{\mathrm{disp}} = -\sum_{A,B} f(R_{AB}) \frac{C_6^{AB}}{R_{AB}^6} \quad , \tag{2.65}$$

where C_6 is the dispersion coefficient and is specific for the combination of interacting bodies, A and B. $f(R_{AB})$ is a damping function that mixes a correct amount of dispersion correction into the energy depending on the intermolecular distance, whereby the function goes to one at large distances and to zero at small distances. Damping is important because DFT does account natively for local correlation effects and, therefore, only non-local effects need to be introduced. This approach assumes that the dispersion energy is pairwise additive and can thus be calculated as a sum over all atom pairs AB. Methods following this scheme are called DFT-D approaches and are very often used because of their computational efficiency.

The functional used in this work, as mentioned before, is the B97 functional to which this dispersion correction term was added, leading to the B97-D functional. It is important to note that the parameters of this functional were explicitly reparametrized for use with the dispersion correction by Grimme and are therefore different from the parameters for the original B97 functional [62]. The damping function used is slightly different from the one in equation 2.65, because of the introduction of a scaling factor, s_6,

$$E_{\text{disp}} = -s_6 \sum_{A,B} f(R_{AB}) \frac{C_6^{AB}}{R_{AB}^6} \quad , \tag{2.66}$$

whereby the scaling factor depends on the density functional of choice. The damping function is given by

$$f(R_{AB}) = \frac{1}{1 + e^{-d\left(\frac{R_{AB}}{R_r - 1}\right)}} \quad . \tag{2.67}$$

where R_r is the sum of atomic Van der Waals radii. This new parametrization ensures that double counting of correlation effects is avoided in the sense that local correlation is represented by the functional itself, while medium and long-range correlation effects are taken care of by the dispersion correction.

2.1.3 Basis Sets

Most *ab initio* methods make use of the expansion of unknown functions — often molecular orbitals — into functions that are well known and easy to compute, usually referred to as basis functions. This procedure would be exact if the expansion consisted out of an infinite amount of basis functions which of course is not feasible in practical calculations. The expansion will thus be truncated, introducing an approximation whereby computational efficiency needs to be balanced with desired accuracy.

Two things are important when deciding on the type of function to use as basis functions. On one hand, the closer a single basis function represents the original function of interest, the less basis functions are needed to give an accurate representation. On the other hand, the computational efficiency of these integrals is an important consideration since the expansion will lead to a large amount of integrals to be calculated over the chosen basis functions. In practice, two types of basis functions are routinely used, Slater Type Orbitals (STO) and Gaussian Type Orbitals (GTO), which are represented respectively as follows

$$\chi^{\text{STO}}_{\zeta,n,l,m}(r,\theta,\phi) = N Y_{l,m}(\theta,\phi) r^{n-1} e^{-\zeta r} \tag{2.68}$$

and

$$\chi^{\mathrm{GTO}}_{\zeta,n,l,m}(r,\theta,\phi) = NY_{l,m}(\theta,\phi)r^{2n-2-l}e^{-\zeta r^2} \quad , \tag{2.69}$$

where N is a normalization constant and $Y_{l,m}$ are spherical harmonic functions. The advantage of STOs is that they are exact for the hydrogen atom and thus very accurate in general, but unfortunately it is not possible to calculate them analytically. The GTO's on the other hand, have the disadvantage of a zero slope at the nucleus instead of a cusp like the STOs — and indeed the actual molecular orbital — and thus give a poor representation near the nucleus. Furthermore, the representation far away of the nucleus is poor because the tail falls off too quickly. As mentioned before, this can be solved by including more GTO's into the expansion and roughly three times as many GTO's are needed to reach a similar accuracy as with STO's.

2.1.3.1 Types of Basis Sets

A next important consideration is the amount of basis functions to be included. When just enough basis functions are included to accomodate all electrons, this is called a minimal basis set. However, usually this is by far not enough to reach a decent accuracy. To improve the accuracy, the amount of basis functions is doubled (double zeta (DZ)) or tripled (triple zeta (TZ)) allowing more flexibility in the representation of the orbitals. In order to save computation time, often only the valence electrons are given doubled or tripled basis functions, while the core electrons are designated only one basis function; this procedure is called a split valence double zeta (VDZ) or split valence triple zeta (VTZ). A further improvement to the basis set can be done by adding higher angular momentum functions, called polarization and diffusion functions. The former are introduced to give more flexibility to the basis set to describe the polarization of the atomic orbital and introduce necessary asymmetry. Just as for the previous case, these functions can be doubled for further improvement of the accuracy which gives rise to TZV2P type basis sets. Diffusion functions on the other hand are mainly important for methods including electron correlation: to correctly describe the electrons avoiding each other, multiple functions of the same type, but with different exponents are needed.

For reasons of computational efficiency, basis sets are often contracted. This means that a specified number of basis functions is written as a fixed linear combination, leaving only one coefficient to be optimized during the SCF procedure, saving considerable computation time. This is usually done for the basis functions describing the chemically less relevant inner region of the atom of interest. The contraction of basis functions can be done in different ways depending on the application of interest. Two contraction types are used during this work and thus they are the only two that will be discussed here.

The first of those contractions was performed by Ahlrich and coworkers who have designed various basis sets of DZ, TZ and QZ level. More specifically, they have produced a TZV basis set that was later on extended to a TZV2P basis set suitable for the DFT calculations throughout this work [127]. The basis set is designed to well describe the inner part of the atom while allowing large flexibility in the valence region. This is very important for our calculations since we are aiming to capture very small interaction energies far away from the nucleus. Furthermore, the basis set includes two sets of polarization functions which are necessary to capture the weak bonding interactions that are of interest here. Finally, Grimme has recommended the use of the TZV2P basis functions in combination with his B97-D density functional [62].

A second type of contracted basis function is the correlation consistent type which are specifically designed to recover the correlation energy of the valence electrons. They do this by introducing functions that contribute a similar amount of correlation together, independent of the type of the function. For example a second d-function is always introduced with a first f-function because of their equal contribution to the correlation energy. The basis sets are named after the final number of contracted functions and the possible inclusion of polarization and/or diffusion functions. The basis set used for our CCSD(T) calculations is the aug-cc-pVTZ basis set.

2.1.3.2 Basis Set Superposition Error

An important note to be added here is the notion of basis set superposition error (BSSE). This error arises when the interaction energy is calculated between two non-bonded molecules. Since most basis sets are atom centered, the basis set used when calculating the total system will be larger than the ones used for the separate molecules. The larger basis set for the total system is more flexible and can thus artificially lower the energy relative to the monomer energies, thus overestimating the interaction energy. This phenomenon is especially important for the calculation of very weak interaction energies such as the dispersion interaction of interest in this work. The obvious solution — enlarging the basis set until the error disappears — is computationally cumbersome if not prohibited and, therefore, the approach usually applied is to try and limit the error by using the basis set of the entire system for the calculation of the monomers. In essence this means that the separate molecules are calculated using the basis set of the complete system by introducing ghost atoms and corresponding basis functionas at the correct positions. This procedure is referred to as the Counterpoise correction and was introduced by Boys et al. [128].

2.1.3.3 Midbond Functions

Aside from the BSSE, non-covalently bound systems are sensitive to other errors resulting from too small a basis set as the weakly correlated electrons need a large amount of functions. At higher levels of theory, for example CCSD(T), these large basis sets are often not computationally feasible and other ways are needed to include extra flexibility in the basis set. One procedure that is often used is the implementation of midbond functions in the basis set, whereby extra basis functions are allocated to a point halfway between the interacting dimers [129]. The idea is that the extra basis functions are used to describe the electrons that are weakly interacting with the nuclei whereby the exact position of the functions seems to be of minor importance [130]. It has been shown that inclusion of these midbond functions can lift the performance of a double zeta basis set to almost the level of a triple zeta basis set and that it significantly reduces the BSSE [131]. In this work we have made use of 3s3p2d1f1g midbond functions as suggested by Tao et al. [129].

2.2 Classical Methods

Until now, we have only discussed single-point calculation methods, calculating with high precision the electronic energy of a system as a function of a given set of nuclear coordinates frozen in time and space. In reality, however, chemical systems are dynamic, showing vibrations, rotations and other types of movement and to capture this behavior, we need methods that allow the system to change its shape and behavior through time. In principle, we can in this way simulate what would happen to a system in a real-life experiment and these methods are also capable of connecting the properties at molecular level to observables at bulk scale. We will use two different approaches to do this throughout this work. One approach, called molecular dynamics (MD), introduces time via some time-dependent equations of motion, while a second approach, grand canonical Monte Carlo (GCMC) simulations, introduces system dynamics via a stochastic process. The biggest difference between the two is the sampling technique, in the first there is a sampling over long periods of time, called Boltzmann averaging, while the second samples over a large amount of distinct, but equivalent replicas of the same system, called Gibbs averaging. Both will be discussed in detail later on, but before we can go into the details of both methods, we need to adress another problem.

To capture the correct dynamics and to allow relevant comparison to experiment, we need to model a large amount of molecules. Such a large system prohibits the use of the accurate quantum methods that were described in section 2.1 and, therefore, we will use simple analytical expressions and try to capture as much of the correct behavior as possible in there. Such a set of analytical expressions, describing the behavior of a certain system, is called a force field and it is the subject of the next section (section 2.2.1). Afterwards, MD and GCMC will be discussed in detail in sections 2.2.2 and 2.2.3, respectively.

2.2.1 Force Fields

As said, a force field is a set of simple analytical functions that defines a given potential energy surface and allows for very fast energy calculations. The analytical expression usually contains a limited set of parameters with physical relevance that are obtained by fitting to higher-level calculations or experimental results. Furthermore, the system is very often considered to be classical, meaning that quantum effects are ignored and the interacting atoms are described as hard spheres interacting as springs, whereby the parameters of the force field describe the behavior of the springs. One of the main reasons for the use of force fields is the fact that many molecules exist out of similar subgroups of atoms that behave in similar ways across different systems. A classic example is the C-H bond, which has the same attributes in a large amount of different systems. The strength of a force field is then that parameters obtained for a specific system can, within well defined constraints, be transferred to other systems having similar traits. As such, in the literature many force fields have been proposed for multiple general purposes, listing parameters for atoms and functional groups to be used across different molecular species and chemical phenomena. However, the transferability of these general-purpose force fields is often questionable and, therefore, in this work, a new force field was proposed specifically for use in gas adsorption on graphene and similar structures.

The energy calculated by a force field is assumed to be composed of different contributions that are independent of each other, whereby each term gives the change in energy following a specific disturbance of the molecule

$$E_{\text{FF}} = E_{\text{str}} + E_{\text{bend}} + E_{\text{tors}} + E_{\text{vdw}} + E_{\text{elec}} + E_{\text{cross}} \quad . \tag{2.70}$$

Not all these terms are equally important for all systems and very often only some of them are included in the force field. Indeed, the force fields developed in this work will not consider intramolecular terms (E_{str}, E_{bend} and E_{tors}) since we will consider the small gas molecules to be rigid. However, these three terms will be used in the intramolecular force field for graphene taken from the literature and we will thus briefly clarify them. The Van der Waals energy term, E_{vdw} and the electrostatic energy term, E_{elec} are of major importance in this work and will be discussed in separate sections below. The cross term, E_{cross}, is only used in some force fields to cover couplings between some of the other terms, but will not be used anywhere in this work.

The stretching term, E_{str}, describes the energy in function of the distance between a pair of atoms as a simple spring vibrating around an equilibrium distance

$$E_{\text{str}} = k_{\text{str}} \Delta R^2 \quad , \tag{2.71}$$

whereby ΔR is the distance between involved atoms and k_{str} is the force constant difining the 'stiffness' of the spring. The bending energy, E_{bend}, describes the energy associated with distorting the angle between three atoms of the molecule and is defined as

$$E_{\text{bend}} = k_{\text{bend}} \Delta \Theta^2 \quad , \tag{2.72}$$

where k_{bend} is again a force constant and $\Delta\Theta$ is the deviation from the natural angle. As the stretching energy, the bending energy is thus easiest described by a harmonical function. The torsional energy, E_{tors}, describes the energy change associated to rotation around a bond. Because of this rotation, the describing function should be periodic in the angle ω and is given as a Fourier series

$$E_{\text{tors}} = \frac{1}{2} V_n \cos(n\omega) \quad , \tag{2.73}$$

where V_n is the barrier associated with rotation around the bond of interest for a given n, the latter indicating periodicity by $\frac{360}{n}$ degrees. The values of n that enter the equation depend strongly on the system type that is to be represented.

2.2.1.1 Van der Waals Energy

Together with the electrostatic energy, the Van der Waals energy constitutes the interaction between two non-bonded partners. The Van der Waals interaction can be explained by the balancing of two different phenomena, one repulsive and the other attractive. The former originates in the overlap of the negatively charged electron clouds of the different species, an effect that dominates the term at short distances, while the attractive part is the result of instantaneous movement of electrons in otherwise neutral species. This movement creates very short-lived multipoles that attract each other at medium distances and the resulting force is denoted as the London or dispersion force [132]. Although the Van der Waals interactions are very weak, they constitute the main (and sometimes sole) interaction between non-polar molecules. The attractive part of the Van der Waals interaction can theoretically be derived to decay with distance as a power of 6, while it has been proven impossible to theoretically derive the functional form of the repulsive part. It is clear, however, that it should dominate the attractive part at short distance and decay to zero at longer distance. As such, there will be a distance where both interactions balance each other exactly, the point of lowest energy, called the equilibrium distance and the associated energy constitutes the well depth of the potential.

A very popular functional representation of the Van der Waals interaction is the Lennard-Jones (LJ) potential

$$E_{\text{LJ}}(R) = \epsilon \left[\left(\frac{r_0}{R} \right)^{12} - 2 \left(\frac{r_0}{R} \right)^{6} \right] \quad , \tag{2.74}$$

where ϵ and r_0 are the well depth and equilibrium distance as described before, while R is the interspecies distance. The LJ potential does indeed have an attractive part that decays with a factor of 6 with the distance, while the repulsive part was historically chosen to be 12. This choice was made at a time of limited computing power where the simple doubling of the attractive exponent proved a major save on computational cost, while statisfying the necessity to dominate the attractive part at short distance and to quickly decay to zero. It has been shown, however, that problems arise with the LJ potential at short and long distances [133] due to the use of only two parameters defining the position and value of the point of lowest energy and thus drastically limiting its flexibility in the other parts of the potential. It has been shown, for example, that the repulsive wall is too hard and that a decay by a factor of 9 or 10, gives better results. Although attempts have been made to do better than the LJ potential, the original, cheap and convenient formulation is still very widely used in the field because of its computational efficiency and the availability of parameters for a wide range of systems.

At the university of Perugia, one out of two academic partners of this project, a large amount of work has been done on an improvement of the LJ potential denoted as the Improved Lennard-Jones (ILJ) potential [69, 70]

$$V_{\text{ILJ}}(R) = \epsilon \left[\frac{m}{n(R) - m} \left(\frac{r_0}{R} \right)^{n(R)} - \frac{n(R)}{n(R) - m} \left(\frac{r_0}{R} \right)^{m} \right] \; , \tag{2.75}$$

where

$$n(R) = \beta + 4 \left(\frac{R}{r_0} \right) \; , \tag{2.76}$$

whereby ϵ and r_0 are the well depth and its position just as in the LJ potential, while β is an extra parameter adding needed flexibility. As can be seen from equation 2.75, the repulsive part is no longer decaying by a factor of 12, but the decay is instead made dependent on the reduced intermolecular distance,$\frac{R}{r_0}$. This way, the potential retains the accurate description of the LJ potential in the equilibrium region, while allowing for flexibility in the long and short range of the potential. The β parameter is loosely related to the hardness of the interacting species and is usually chosen in an interval between 7 and 9 for purely dispersive interactions. In recent years, the potential has been extensively tested on different systems in molecular dynamics simulations in comparison with experimental data [59, 72, 101, 134, 135].

In most force fields, interaction parameters are obtained for individual atom types and they are then combined to get interaction parameters for different atom pairs via mixing rules. The Lorentz-Berthelot mixing rules are the most commonly used

$$r_0^{AB} = r_0^A + r_0^B \tag{2.77}$$

for the equilibrium distance and

$$\epsilon^{AB} = \sqrt{\epsilon^A \epsilon^B} \tag{2.78}$$

for the well depth. These mixing rules assume that the interacting parameters are very similar in nature, wich is not always the case and can lead to considerable problems in the resulting potentials. Therefore, in this work, we will not use mixing rules and instead, interaction parameters will be obtained specifically for interspecies interactions.

It is important to note that potentials of the LJ type are pairwise potentials assuming that all interactions present in the system can be represented by two-body interactions. However, the parameters are usually fitted to experimental data consisting of multiple molecules and thus automatically implicitly include at least partly possible many-body contributions. The fact that the potentials are pairwise means that interaction centres need to be defined between which the interaction is computed. The most simple way is to attach an interaction centre to the centre of mass of the molecule, an approach that is mostly valid for small, symmetrical molecules like methane. This approach, called the united-atom approach, does however, completely neglect the orientation dependence of the Van der Waals interactions. This can be remedied by the positioning of interaction centres on multiple positions in a molecule. Indeed, force fields have been proposed with interaction centres on bonds, or where chemical groups within larger molecules were combined into a united-atom. The most thorough strategy, however, is to attach interaction centres to all atoms of the molecule, thus effectively considering the Van der Waals interactions through the atomic polarizabilities within the molecule.

2.2.1.2 Electrostatic Energy

Different atom types within molecules have different electronegativities causing the electron cloud to divide itself over the molecule in a non-symmetric way. Contrary to the movements described in the section on Van der Waals interactions, the distribution differences now have a permanent average character and thus lead to positions in the molecule with more and others with less electrons than would be the case in stand-alone atoms. This gives rise to the concept of molecular charges which are assigned to individual atoms within a molecule, leading to formation of permanent dipoles, quadrupoles and higher-order multipoles. The resulting electrostatic interactions can be described in different ways. The simplest one is taking a Coulombic sum over the assigned atomic charges where it is important to note that these charges have no true physical meaning and are always arbitrary to some extent. Alternatively, the interactions can be described via the interactions between dipoles, quadrupoles and so on. The Coulombic sum is given by

$$E_{\mathrm{elec}} = E_{\mathrm{Coul}} = \sum_{A,B} \frac{q_A q_B}{R_{AB}} \quad , \tag{2.79}$$

where q_A denotes the atomic charge assigned to atom A and the sum is taken over all atoms present in the molecule. The dipole-dipole interaction can be represented as follows

$$E_{\mathrm{elec}} = E_{\mu\mu} = -\frac{\mu_A \mu_B}{R^3} \left(2\cos\theta_A \cos\theta_B - \sin\theta_A \sin\theta_B \cos\phi \right) \quad . \tag{2.80}$$

It is worthy to note that electrostatic interactions are often small in non-polar systems and are therefore neglected in a large portion of the force fields in the literature for molecules like hydrocarbons.

Finally, it is important to remark that most force fields obtain their parameters by inclusion of physically relevant phenomena via the fitting to experimental values for the spicific phenomenon. It is then important to include all effects in an explicit way, in order to obtain a complete picture. This is distincly different from the approach used in this work as we fit our parameters to *ab initio* data including all effects within the approximations of the method, meaning that all present effects are implicitly accounted for in the parameters. There is no need for explicitly covering all the possible interaction types and, thus, when we introduce concepts like partial charges to improve the accuracy, physical meaning is welcomed, but not of first concern. Principally, we are just looking to get a mathematical fitting that reproduces as accurate as possible the interaction energies obtained from *ab initio* calculations.

2.2.2 Molecular Dynamics

As mentioned in the introduction, molecular dynamics aims at introducing time evolution into the system by applying the laws of classical mechanics, usually via use of Newtons equations of motion. Since an analytical expression is unfeasible for a large amount of atoms, the process is essentially numerical and system properties are obtained at well-defined time steps. Therefore, discrete forms of the equations of motion are needed to calculate the system composition at a certain time step and — using the knowledge of the current and previous time step — the equations of motion can be used to calculate new positions. The large amount of data that comes out of this procedure, is then processed statistically in order to gain insights into the system. In classical MD — as opposed to *ab initio* MD — the interaction between the different species in the system are calculated by the classical force fields that were explained in section 2.2.1. These potentials, aside from determining the energy of the system at a given time step, also lead to forces acting on the different interaction centres. Here, we will only discuss in details forces depending on distances and not on angles or dihedrals, since the latter are not of prime concern in this work. The forces, $\vec{f}_{ij}\left(R_{ij}\right)$, are calculated as the derivative of the potential to the relevant distance for the interacting pair

$$\vec{f}_{ij}\left(R_{ij}\right) = -\left(\frac{1}{R_{ij}}\right)\left(\frac{d}{dR_{ij}}\Phi\left(R_{ij}\right)\right)\vec{R}_{ij} \ , \tag{2.81}$$

where $\Phi\left(R_{ij}\right)$ is the potential acting on the particle. A certain atom will feel a force coming from all other atoms that it interacts with and are located within a chosen cut-off distance, the net force will thus be defined as

$$\vec{f}_j = \sum_{i \neq j}^{R_{ij} < R_{\text{cut}}} \vec{f}_{ij}\left(R_{ij}\right) \tag{2.82}$$

and the force is as such the negative gradient of the potential energy surface (PES) predefined in the force field

$$\vec{f}_j = \nabla_j E(R_1, R_2, ..., R_j) \quad . \tag{2.83}$$

Now that the positions of and the forces acting on all atoms of the system are known, Newton's equations of motion can be applied to determine new positions and velocities at time step $t + \Delta t$

$$\frac{d\vec{v}_j}{dt} = \frac{1}{m_j}\vec{f}_j \tag{2.84}$$

for the velocity and

$$\frac{dR_j}{dt} = \vec{v}_j \tag{2.85}$$

for the position, where m_j is the mass of atom j and $\vec{R}_j$ is the position vector of atom j. A crucial part of this, is the selection of an appropriate time step, dt. Too large a time step may lead to unstable systems because of growing inaccuracies in the integration procedure, while too short a time step makes the calculation very expensive. Time steps of 1 fs or 2 fs are typically used and current computational power thus allows simulations on time scales up to several microseconds.

As mentioned before, these analytical expressions need to be discretized before use. Many ways exist to do this, but we restrict this discussion to the most simple one, the leapfrog algorithm, which is also the one applied by default in DL_POLY v2.2 [136], the software used for MD in this work. A typical feature of this procedure is that half time steps are used in the time propagation. More specifically, the calculation of the velocity, uses the force exerted at the current time step t and the velocity at $t - \frac{1}{2}$ to calculate the velocity at $t + \frac{1}{2}$

$$\vec{v}_j\left(t + \frac{1}{2}\right) = \vec{v}_j\left(t - \frac{1}{2}\right) + \frac{\Delta t}{m}\vec{f}_j(t) \quad . \tag{2.86}$$

On the other hand, the position at time $t + 1$ is determined using the position at time t and the velocity at time $t + \frac{1}{2}$

$$\vec{R}_j(t+1) = \vec{R}_j(t) + \Delta t \vec{v}_j\left(t + \frac{1}{2}\right) \quad . \tag{2.87}$$

Before a simulation is started, a starting configuration is set up by the user. Usually, this configuration will be nowhere near a representative state of the system and therefore the system needs to be propagated for some time to relax to a dynamic equilibrium state. Indeed, thermodynamics imposes that this will happen if enough time is allowed. It is important to make sure that equilibrium is obtained before sampling results from the simulation and monitoring of system properties like temperature and kinetic and configurational energy can give good indications. Ideally no systematic drift is seen through time, only 'small' fluctuations around a fixed average value should be visible. When equilibration is confirmed, properties of interest can be calculated, but, even at equilibrium, the system is dynamic and we therefore need to sample a lot of configurations in order to obtain statistically relevant data.

Many properties can be calculated and only the ones that are of specific interest for this work will be discussed. One of the primary properties of interest for a given chemical system is the temperature, which can be calculated from the system average kinetic energy,

$$T = \frac{2}{3k_{\mathrm{B}}} \langle K \rangle \quad , \tag{2.88}$$

where k_{B} is the Boltzmann constant and $\langle K \rangle$ is the average system kinetic energy. The latter is calculated for a specific configuration as follows

$$K = \frac{1}{2} \sum_{i=1}^{N} m_i \left(\frac{d\vec{R}_i}{dt} \right)^2 \quad , \tag{2.89}$$

which is also an important feature to monitor, just like the configuration energy, E_{conf},

$$E_{\mathrm{conf}} = \sum_{i=2}^{N} \sum_{j<i} \Phi_{ij} \left(R_{ij} \right) \quad , \tag{2.90}$$

where Φ_{ij} represents an appropriate pair potential.

Another important property that will be calculated in this work is the mean-squared displacement, an expression that quantifies the movement of an atom or molecule of interest through the system as the particle moves randomly as a consequence of collisions with other particles. This movement can be represented by allocating a position vector to the particle at time zero, $\vec{R}_i(0)$, and comparing it to its position vector at time t, $\vec{R}_i(t)$. Squaring this difference and taking the ensemble average, gives the mean squared displacement

$$\langle R^2(t) \rangle = \left\langle \frac{1}{N} \sum_{i=1}^{N} |\vec{R}_i(t) - \vec{R}_i(0)|^2 \right\rangle \quad , \tag{2.91}$$

where N is the number of particles in the system. This expression is directly related to the diffusion coefficient obtainable from experiment via the following Einstein equation

$$\langle R^2(t) \rangle = 6Dt + C \quad , \tag{2.92}$$

whereby D is the diffusion coefficient and C a constant. This relation is valid at large t and shows that the mean squared distance is a linear function of time with slope $6D$. Unfortunately, this relation has been shown to be very sensitive to statistical variance and it is thus important to use a good sampling technique. Specifically, it has been shown that a lot of time origins are needed in order to get trusthworthy results. This will be taken care of at the appropriate moment in the results section.

Finally, in order to fully understand the process of molecular dynamics, a few remaining principles need to be explained, the periodic boundary condition, the potential cut-off and the concept of ensembles.

Often when doing molecular dynamics simulations, the properties of interest to be simulated are bulk properties meaning that a very large amount of molecules is needed to avoid edge, wall, surface or other effects due to the uncorrect truncated representation of the system. A way to circumvent this problem is the use of periodic boundary conditions, whereby the system is represented by a smaller amount of molecules which are then replicated through space in one, two or three dimensions depending on the specific system of interest. The replicas on all sides are exact copies of the main box, which is the only one that is actually propagated through time. When a molecule is set to leave the simulation box, it will re-enter on the other side as if it has just crossed the box wall and entered from the replica on the other side.

The pair potentials as described in section 2.2.1 tend to zero at infinite distance, which is impossible to calculate for computational reasons. It is therefore necessary to set a cutoff after which the potential is no longer calculated and as such a specific atom pair is assumed to be non-interacting when they are separated by a distance larger than the chosen cutoff. Furthermore, care needs to be taken to choose a cut-off that is smaller than the size of the box when periodic boundary conditions are used. If the cut-off is larger, a molecule may interact with more than one image of the same molecule and unphysical interactions will disturb the system. This procedure, whereby only one single copy is considered during calculation of the interactions, is called the minimum image convention.

In molecular dynamics different types of ensembles are used, defined by the system properties that are set and controlled by the user. A first commonly used ensemble is the microcanonical ensemble (NVE) where the amount of atoms, the volume and the total energy are conserved throughout the whole simulation. The second ensemble that is often used is the canonical ensemble (NVT) where the amount of atoms, the volume and the temperature are set and conserved all the way through. In order to maintain the temperature throughout, a thermostat has to be chosen in order to rescale the velocities of the atoms in the system to avoid deviations from the chosen temperature. The NVT calculations in this work use the Nosé-Hoover thermostat to rescale the velocities to the set temperature and the Newton equations presented earlier are then changed to the following form

$$\frac{d\vec{r}_i}{dt} = \frac{\vec{p}_i}{m_i} \tag{2.93}$$

for the velocities and

$$\frac{d\vec{f}_i}{dt} = \vec{f}_i\left(\{\vec{r}_i\}\right) - \zeta\vec{p}_i \tag{2.94}$$

for the force, with

$$\frac{d\zeta}{dt} = \frac{1}{Q}\left[\sum_{i=1}^{N}\frac{p_i^2}{m_i} - N_\mathrm{f}k_\mathrm{B}T_0\right] \quad , \tag{2.95}$$

where $\vec{r}_i$ and $\vec{f}_i$ are the position and momentum vectors of atom i, T_0 is the selected system temperature and k_{B} is the Boltzmann constant. N_{f} is the number of degrees of freedom and Q is a thermal inertia parameter determining the rate of the heat transfer. Finally, ζ is a time dependent variable that controls the temperature.

2.2.3 Grand Canonical Monte Carlo Simulation

The term "grand canonical Monte Carlo simulation" holds in its name two new terms that need introducing. The first is grand canonical (GC), which refers to the ensemble that is used as opposed to the canonical (NVT) and microcanonical (NVE) ensembles discussed in the previous section, while the second term is Monte Carlo (MC) which refers to the way of moving through phase space and is opposed to the time-dependent movement through phase space in MD.

Contrary to MD, the time dependence of the system is not directly introduced in a Monte Carlo simulation. Instead, a series of random numbers generates different samples of the same system that converges to a statistically significant simulation. The randomness that is introduced allows the system to jump the time scale and reach configurations that would take very long by direct time-dependent methods. Different algorithms exist to perform MC simulations, but one of the most popular ones is the Metropolis algorithm. In this procedure, a new configuration is generated randomly according to some standard, whereby the new configuration is accepted depending on the energy difference between the old and the newly generated states via a previously defined probability density. When a new state is created from a previous state repeatedly, a chain of states is generated that is denoted as the Markov chain of states.

Contrary to the canonical and microcanonical ensembles, the grand canonical ensemble allows the number of particles to change during the simulation. The controlled independent variables are then, the chemical potential, μ, the volume, V and the temperature, T. It is now possible to simulate adsorption experiments where an adsorbent is brought into contact with a gas reservoir allowing the transfer from molecules from the reservoir into the adsorbent. It is an example from a simulation that mimicks closely the experimental setup. The GC partition function can be written as follows

$$\begin{aligned} Y(\mu, V, T) = \sum_{N=0}^{\infty} \frac{1}{N!} \Bigg(\left(\frac{V}{\Lambda^3} \right)^N \exp\left(\frac{\mu N}{k_{\mathrm{B}} T} \right) \\ \int d\vec{s}_1, \ldots, \int d\vec{s}_N \exp\left(\frac{-U\left(\vec{s}_1, \ldots, \vec{s}_N\right)}{k_{\mathrm{B}} T} \right) \Bigg) \quad , \end{aligned} \tag{2.96}$$

where $\vec{s}_i$ represents the scaled coordinates of particle i. If we consider a three dimensional box, we get the probability density as

$$\mathcal{N}_{\mu VT}\left(\vec{s}_1,...,\vec{s}_N,N\right) \propto \frac{1}{N!}\left(\frac{V}{\Lambda^3}\right)^N \exp\left(\frac{-\left(U\left(\vec{s}_1,...,\vec{s}_2\right)-\mu N\right)}{k_\mathrm{B}T}\right) \quad , \tag{2.97}$$

which can be sampled via a Metropolis MC method as described before. There are now three different trial moves, the first of which is the displacement of particles, described by

$$W\left(r_i - r_i'\right) = \min\left(1, \exp\left(\frac{-\Delta U}{k_\mathrm{B}T}\right)\right) \quad . \tag{2.98}$$

This represents the acceptance probability for selecting a particle i at random and displacing it randomly by d to a new position, $\vec{r}_i' = \vec{r}_i + \vec{d}$, whereby $\vec{d}$ is selected from a volume region, ΔV, such that the probability of acceptance equals a previously set value. In a similar fashion, acceptance ratios can be formulated for the insertion or removal of a random particle i. For insertion the probability is

$$\begin{aligned} W\left(N \rightarrow N+1\right) = \min\Bigg(1, &\frac{V}{\Lambda^3\left(N+1\right)} \\ &\exp\left(\frac{-\left(U\left(\vec{s}_1,...,\vec{s}_{N+1}\right)-U\left(\vec{s}_1,...,\vec{s}_N\right)-\mu\right)}{k_\mathrm{B}T}\right)\Bigg) \end{aligned} \tag{2.99}$$

and the removal of a random particle i has a probability density of

$$\begin{aligned} W\left(N \rightarrow N-1\right) = \min\Bigg(1, &\frac{\Lambda^3 N}{V} \\ &\exp\left(\frac{-\left(U\left(\vec{s}_1,...,\vec{s}_N\right)-U\left(\vec{s}_1,...,\vec{s}_{N-1}\right)-\mu\right)}{k_\mathrm{B}T}\right)\Bigg) \quad . \end{aligned} \tag{2.100}$$

When a simulation is run, the steps do not refer to a propagation through time as in molecular dynamics, but to an execution of one of the three trial moves. As more steps are carried out, the system will converge towards a situation where the chemical potential of the gas reservoir and the simulation box of interest are equilibrated. When this equilibration is reached, information can be sampled in order to calculate the system properties of interest.

Chapter 3

Force field development for the adsorption of gases on graphene

As explained in chapter 2, accurate quantum mechanic calculations are not feasible for the simulation of medium-sized to large systems. Simulations of large system thus require the development of a force field consisting out of simple analytical expressions that contain the relevant quantum and other effects in an average fashion. The idea is then to capture the complex chemistry behind the system in an expression that is as simple as possible. Two ways of thinking can be used to construct those expressions, a physical representation of the involved interactions or a purely mathematical fitting to data of interest. In the first, the goal is to decompose the interaction into physically relevant contributions and then represent these as realistic as possible via separate additive expressions. The advantage is that — when performed well — the parameters have a physical meaning leading to further insights on the system, while allowing for their calculation from experimental or theoretical data. A disadvantage is that if not all constituting parts of the interaction are accounted for, they are also not present in the calculation leading to errors in the potential energy surface. A second strategy is selecting accurate data and performing a pure mathematical fitting as accurate as possible. In this case, a potential is selected that contains enough flexibility to fit the data, but may have parameters that are physically meaningless. The advantage is that the mathematical representation of the interaction energy is very good and that, by definition, all possible interfering interactions are implicitly taking into account. The downside is that little to no physical understanding can be gained from the potential parameters. It is this second approach that has priority in this work, although we use expressions that have the potential for physically meaningful parameters, this is not of prime concern. We will fit potentials of different types to first principles calculations, which ensures that all relevant physics is in the training data and thus, the potential that fits this data most closely is then the one representing best the total physical interaction.

This chapter aims to provide a protocol that can be followed to create force fields for different kinds of neutral gas molecules of interest and their interaction with a surface. Starting from a large amount of static interaction energy calculations at a carefully benchmarked DFT level, different potentials are fit to this data to obtain different force fields. The force fields are then benchmarked themselves and tested by calculation of macromolecular properties directly comparable to experiment. In section 3.1, the methodology will be described in detail, after which the protocol will be applied to the following gases and their interactions with graphene: methane (section 3.2), nitrogen (section 3.3), water (section 3.4) and carbon monoxide (section 3.5). Section 3.6 will discuss the force fields developed for gas mixtures, while section 3.7 will discuss the intramolecular force fields from the literature that were used to model the flexibility of the graphene sheet. Finally, section 3.8 will discuss an alternative, faster way to obtain interaction parameters from atomic and molecular polarizabilities.

3.1 Methodology

The systems studied in this work consist of neutral gas molecules in direct contact with a graphene sheet, meaning that the interactions will be primarily of dispersive nature. However, some molecules, like water, are known to have strong electrostatic interactions depending on the specific orientation of the molecule. We will try to catch some of the physics behind these interactions by using the ILJ potential to represent the dispersive part and a Coulombic sum for the electrostatic part. Note, however, that although this kind of partition is very frequently used in chemistry, it contains a certain degree of arbitrariness since its components are not true quantum obeservables. Therefore, these mathematical expressions should not be seen as exact representations of the respective counterparts of the energy. We merely introduce these terms to give the potential the flexibility to accurately represent the interaction of interest.

3.1.1 The Problem of Molecular Orientation

An important aspect of molecular interactions is the dependence on the orientation of the interacting partners, which can sometimes be significant as will be shown later on in this chapter. Since potentials like LJ and ILJ are pairwise — and thus describe the interaction between two chosen interaction centres — the orientation dependence can be introduced via a proper allocation of interaction centres. However, often in the literature, this orientation dependence is ignored by placing an interaction centre on the centre of mass of the molecule, considering it as a united-atom and effectively reducing the molecule to a sphere with the same molecular polarizability as the original molecule. Due to the averaging nature of statistical methods like MD and GCMC, these models often perform well, especially for molecules that are highly symmetrical. Although this model has the advantage of being cheap, problems may arise since there is no orientation dependence included in the model and therefore, during simulations, these models have no constraints on the amount of rotational energy that can be stored in the molecules. Note that orientation dependence may be reintroduced via addition of partial charges and for molecules with strong electrostatic interactions, like water, this leads to very good results. However, at the very least an attempt should be made to include the orientation dependence in the potentials and compare the results to the united-atom approach in order to justify the approximated molecular structure.

Pirani et al. have proposed a model whereby interaction centres were placed on molecular bonds instead of on the centre of mass [69, 137]. In fact they treated the assymetry of the polarizabilty of such a bond by introducing a parallel and an orthogonal component with their own parameters, which were then mixed according to the Jacobi angles between the two bonds of interest. Although they used this model with success, it requires the determination of two sets of parameters for all interaction types which is not complementary with the fast and simple approach that we are aiming for. We have, however, in a preliminary study, tried to include orientation dependence in the hydrogen dimer via interaction centres on the molecular bonds and their angular dependence.

Considering the parallel hydrogen dimer there are only two rotations that can change the geometry of the dimer — rotation along the x- and y-axes — due to the symmetry of the hydrogen molecule: a rotation around the z-axis does not change the dimer. We therefore calculated the interaction energies of the dimers by systematically rotating one out of two monomers around the x-axis in a first set of calculations and around the y-axis in a second set of calculations. The rotations were done for 90° in steps of 10°, as further rotations will give the same interaction energies, leading to a repetitive interaction energy with the rotation angle as shown for the rotation around the x-axis in the left panel of figure 3.1, the rotation around the y-axis showing very similar results. We have then fitted these calculated results with a simple cosine function as shown in the same figure.

As the intermolecular distance becomes larger, the orientation dependence of the interaction energy diminishes because the interaction energy as a whole decreases. To take this into account, we have done a scan over the distance for all the considered dimers up to 20 Å and averaged the interaction energies for every single angle. This allowed us to fit an exponential function to the decaying interaction energies to damp the cosine function introduced before. Combining the cosine function with the exponential function allowed us to recalculate the interaction energies very well for a single rotation around the respective axes. However, to be useful for application in a simulation procedure, the two rotations need to be combined and for this we scanned the interaction energy over the two angles, systematically for rotations of 180° around both axes. To these results, we fitted the summation of two cosine functions as shown in figure 3.1.

Although the performance of the fit was quite good, it proved hard to reproduce interaction energies of randomized hydrogen dimer geometries. Furthermore, it can be expected that for less symmetric molecules, where a rotation around the z-axis needs to be included as well, the situation will become even more complicated. Finally, the fact that we were straying from the path to fast and simple interaction

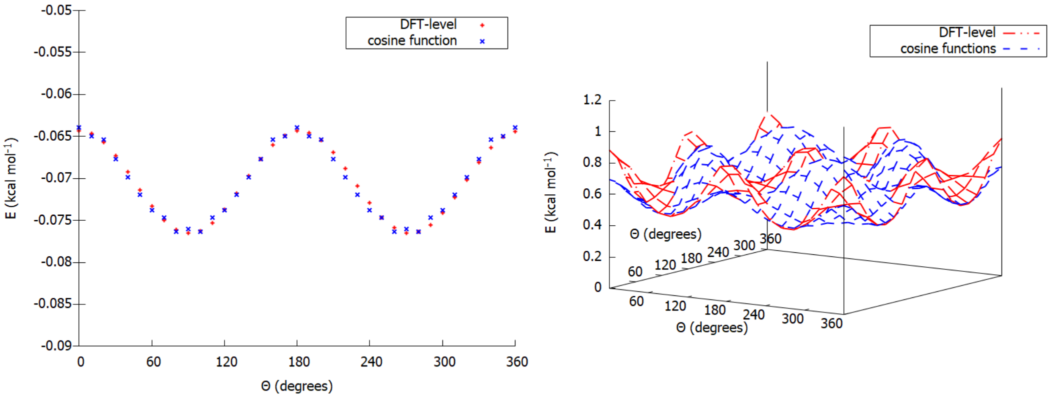

single rotation

double rotation

FIGURE 3.1: The dependence of the interaction energy of the hydrogen dimer on the rotation of a single monomer around the x-axis (left) and the rotation around both the x- and y-axes (right) at the DFT level (red) and with the fitted cosine function (blue).

potentials led us to the decision to leave this approach and focus on potentials dependent on interspecies distances only. Note that the calculation of angles during simulations is no trivial task and the computational cost would be signifiantly increased.

An easier way to include explicitly the orientation dependence, without the need for calculating angles, is the assignment of interaction centres to the individual atoms of the molecule leading to a full atomistic potential. The nonelectrostatic part of the energy will then be composed out of a summation of ILJ potentials taking explicitly into account all the interatomic distances and the resulting interaction energies. Models like this are capable of distinguishing different dimer orientations based on their energy, but at a computational cost since all the interatomic distances need to be calculated instead of just the intermolecular one. We will use this approach to account for the orientation dependence in our models and make the comparison with the united-atom models.

3.1.2 Three-Body Interactions

As said, LJ and ILJ potentials are pairwise potentials and thus, by construction, do not include possible three-body, four-body, ... interactions. When the potentials are fit to experimental data of a bulk system, it is often argued that three-body interactions are implicitly taken into account. In this work, however, we will fit to dimer interaction energies only and we can thus not just assume that three-body interactions are taken care of in these poentials. To assure us that the pairwise potentials of use are suitable, we have investigated, in a preliminary study, the behavior of all possible trimers of methane and hydrogen. We will outline the procedure for just the H_2-H_2-H_2 trimer for simplicity, but very similar results were obtained for the CH_4-H_2-H_2, CH_4-CH_4-H_2 and CH_4-CH_4-CH_4 trimers.

First we calculated the interaction energies at DFT level for 1000 random trimers with varying intermolecular distances. A potential consisting out of three pairwise ILJ potentials was fit to these interaction energies and the obtained potentials were used to recalculate the 1000 trimer energies. Then we introduced a screened harmonic three-body term in the potential as follows

$$E_{\text{three-body}} = \frac{k}{2}\left(\Theta_1 - \Theta_0\right)^2 e^{\left(-\frac{R_1}{\rho_1}-\frac{R_2}{\rho_2}\right)} \ , \tag{3.1}$$

where Θ_1 is the angle between the z-axes of the respective monomers and R_1 and R_2 are the intermolecular distances between the monomers. Θ_0, ρ_1, ρ_2 and k are parameters that need fitting. The resulting potential, including three pairwise ILJ terms and the three-body term, was then fitted to the DFT data and again the 1000 interaction energies for the trimers were calculated using this potential. From the comparison in figure 3.2, it is seen that the interaction energies calculated using the three different methods correlate well. Most importantly, the correlation between the potential including the three-body potential and the one without is extremely well. The differences that are seen come from deviations between the fitted models with the DFT energies, but not from deviations between the fitted potentials themselves. From this we conclude that contributions from three-body interactions are very small in these kinds of systems and thus need not to be included in most of the remainder of this work. However, as discussed in section 3.4, some complications related to hydrogen bonds will appear in the case of water complexes.

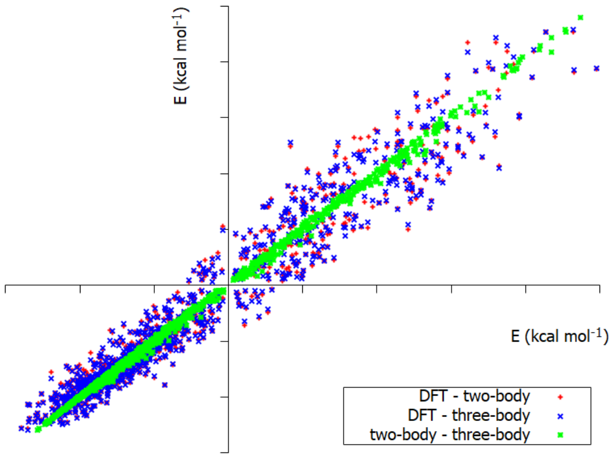

FIGURE 3.2: Comparisons between the interaction energies calculated at the DFT-level and the fitted potentials with and without three-body term for the H_2-H_2-H_2 trimer.

3.1.3 General Protocol

The fact that the main interaction for a lot of the systems we will study is from dispersive nature means that we need to be very careful when creating the training data set for the potentials. Dispersive interactions are very low in energy and it has been a challenge to accurately describe them using methods that allow for a large amount of routine calculations [138]. Lately, however, methods have been developed that allow accurate calculation of dispersive interactions using DFT at an affordable computational cost [63]. More specifically, we will use the B97-D functional [62] in combination with the TZV2P basis set [127] as the workhorse of this work to generate the data needed for the fitting. Although functionals have been developed that are more accurate, the B97-D/TZV2P combination strikes a very good balance between computational cost and accuracy allowing for the large amount of calculations needed for this work. More specifically, the functional recovers the dispersion interactions via an empirical term especially designed for capturing the electron correlation at large distances. But first, all monomers used in this work were optimized at the B3LYP/6-31G** [139, 140] level and were considered rigid from then on. All interaction energies at DFT level were calculated using Gaussian09 [141] and the ESML basis set exchange [142, 143], while at CCSD(T) level, the Dalton package was used [144, 145].

Although the B97-D functional in combination with the TZV2P basis set has been shown to accurately capture the dispersion interactions of interest in similar systems [56, 146], we cannot just assume that the performance will be as good in our systems. Therefore, we carefully benchmarked the interaction energies calculated at DFT level against CCSD(T) level interaction energies. For the gas dimers, we selected a number of symmetrical — for computational reasons — dimers for the molecule under study and calculated the interaction energy at the B97-D/TZV2P level and compared them to our own CCSD(T)/aug-cc-pVTZ level calculations and/or existing literature.

For computational reasons, it is unfeasible to consider large graphene sheets even at DFT level for the amount of static calculations needed here. Therefore, graphene has been represented by smaller, finite models like coronene ($C_{24}H_{12}$) for CCSD(T) calculations and circumcoronene ($C_{54}H_{18}$) for DFT calculations (see figure 3.3) as has often been done in the literature [11, 50, 147–153]. These molecules can be seen as small pieces of graphene capped of with dangling hydrogen atoms at the edges to avoid incomplete electronic structures. The addition of hydrogens does, however, influence the electron structure of the considered models, leading to effects that are not present in graphene: the electrons from the hydrogen atoms are pulled towards the more electronegative carbon atoms leading to a quadrupole moment because of positive partial charges on the hydrogens and negative partial charges above and below the plane of the molecule. The size of the quadrupole moment depends on the size of the polyaromatic hydrocarbon and can be expected to converge to the zero quadrupole moment of graphene with increasing size. Indeed, in our own lab, Wilson et al. [146] have shown the very fast convergence from the interaction energy between carbon monoxide and the series of benzene, coronene and circumcoronene, results that confirmed previous work by Haldar et al. [154]. Furthermore, Bin Yeamin et al. [56] have shown that the interaction energy predicted by molecular dynamics between coronene and hydrogen, closely resembles the interaction energy

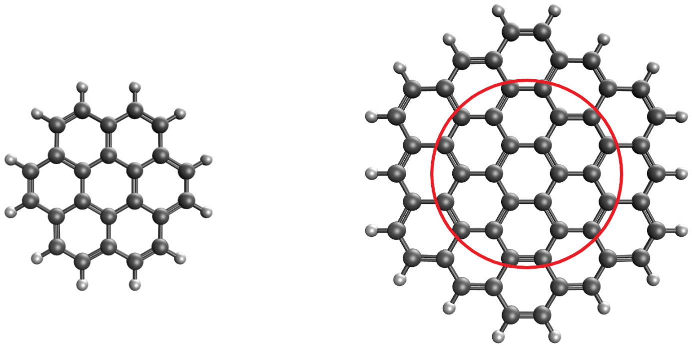

coronene circumcoronene

FIGURE 3.3: Structures of the coronene and circumcoronene molecules used as models for graphene in the static interaction energy calculations at CCDSD(T) and DFT levels, respectively. The red circle on circumcoronene indicates the circle where gas molecules are confined to for the randomized static interaction energy calculations.

predicted for the graphene-hydrogen system. Finally, Lazar et al. have confirmed this via DFT calculations using different functionals on a coronene molecule and an infinite graphene sheet using periodic boundary conditions [149].

Even though we use the coronene molecule instead of the circumcoronene molecule for benchmarking at CCSD(T) level, calculations using the triple zeta basis set are still unfeasible without severe approximations in the coupled cluster method equations [147]. Therefore, we calculated the coronene-gas interactions using a double zeta basis set augmented with midbond functions (3s3p2d1f1g) [129]. This type of basis set has been proven to perform almost at the same level of accuracy as a triple zeta basis set [155]. The CCSD(T)/aug-cc-pVDZ-mb level of theory is then used as a benchmark to study specific adsorption sites and attacking geometries of the gas molecule on coronene.

Once the B97-D/TZV2P level has been benchmarked, it can be used to generate the database of interaction energies for fitting the potentials. For the gas dimers this is done by randomly generating 99 different dimer geometries for each of which an interaction energy curve is calculated via a scan over the intermolecular distance. In these calculations, care was taken to sample more distances close to the equilibrium region in order to well capture this important part of the curve. Since the graphene sheet will be represented as an infinite sheet in the simulations, we are only interested in interaction of the gas molecules with the plane of the circumcoronene molecule. Situations where the gas molecule is positioned in the same plane as the circumcoronene molecule are thus not of interest and, therefore, as well as for computational reasons, we calculated only 10 geometries of the circumcoronene-gas system. The gas molecule was always randomly rotated and positioned above the plane of the circumcoronene molecule, whereby care has been taken to minimize the edge effects coming from truncation of the graphene to circumcoronene. More specifically, the gas molecule was positioned such that it falls within the circle made up by the first ring of benzene rings and the inner benzene ring as shown in figure 3.3.

Now that we have the data set that will be used for fitting, we need to define the potentials that will be used. For this, we will assume that the nonelectrostatic part and the electrostatic part of the energy can be treated independently. The nonelectrostatic part will then be represented by the ILJ potential, while the electrostatic part will be treated by a simple Coulombic sum

$$\begin{aligned} V_{\text{tot}}(R) &= V_{\text{nelec}}(R) + V_{\text{elec}}(R) \\ &= V_{\text{ILJ}}(R) + V_{\text{Coul}}(R) \ . \end{aligned} \tag{3.2}$$

Different charge schemes from the literature and from different types of population analyses are introduced in the Coulombic sum and then the ILJ parameters are fitted accordingly. This way, the influence of the charge schemes on the parameters is investigated with the final goal of getting the best possible mathematical fit to the calculated interaction energies. Note that the charge schemes used here belong to existing force fields from which we have only retained the charges and used them to obtain our own parameters. In most cases, we treat the electrostatic part as predefined in the sense that we decide on the charges by picking a certain charge scheme and then fit the parameters for the ILJ potential keeping the charges fixed. Deficiencies in the description of the electrostatic part will then be accounted for via adjustment of the nonelectrostatic part. However, in some cases, we have attempted to fit the charges as well: the largest charge present in the molecule is then introduced as a fitting parameter and the other charges are automatically updated accordingly. As such, our model types will have the following form

$$V_{\text{tot}} = \sum_{AB} V_{\text{ILJ}}^{AB} + \sum_{XY} \frac{q_X q_Y}{R_{XY}} \ , \tag{3.3}$$

whereby A and B refer to the ILJ interaction centres and X and Y to the partial charges positioned on the molecules.

Many more model types have been suggested: Pirani et al. have suggested placing interaction centres on the bonds of the molecules, making the interaction dependent on both the distance and the angles between the different bonds [69, 137]. Furthermore, polarizable models have been proposed in different varieties [68, 156]; the most simple example includes charges attached to the molecule by a harmonic function [157]. Although very accurate results can be obtained by some of these models, the goal of this work is to provide very simple potentials that allow for fast simulation of a large amount of molecules with good accuracy. For this reason, in this work, we will stick to the united-atom and the atomistic approaches where only intermolecular or interatomic distances need to be calculated.

For the gas molecules, we will develop two models, using both a united-atom approach and an atomistic approach with appropriate partial charges. This way, we can compare the performance of the cheaper, but in principle less accurate united-atom approach to the performance of the more expensive, but more accurate atomistic approach. For the graphene sheet, on the other hand, we will always use an atomistic approach by putting interaction centres on all carbon atoms allowing the accurate description of the spcific position of the gas molecules over the graphene sheet. Since an infinite graphene sheet has no hydrogens, we put no interaction centres on the hydrogen atoms when fitting the circumcoronene, the approximation this introduces is minimized by constraining the gas molecules to the inner part of the circumcoronene molecule as mentioned before.

As said in the theoretical part, the ILJ potential is an extension of the LJ potential and aims to outperform the latter specifically at the short and long range of the interaction. This effectively means that at equilibrium region, the two potentials are expected to behave very similar and for this reason, we will in this work regularly compare the ϵ and r_0 obtained for the ILJ potential to LJ-based force fields from the literature. Often, the LJ parameters are given as ϵ and σ instead of ϵ and r_0 and in these cases, the σ reported was converted to r_0 via the relation $r_0 = 2^{\frac{1}{6}}\sigma$ to allow direct comparison.

At this point, we have a number of different potentials for the gas molecule, using different charge schemes and suitable ILJ potentials for both the united-atom and the atomistic approach. In order to benchmark the used potentials, we compare them to the same CCSD(T) interaction energies that were used for benchmarking the DFT results. This gives an idea of the capability of the force field to reproduce the average interaction energies and, for the atomistic potentials, the ability to capture the orientation dependence within the dimers.

As a last step, in order to make a decision on which potential to use for each gas molecule during simulations, we calculate the diffusion coefficient from molecular dynamics. This property can be compared directly to experimental results, thus allowing an assesment of the performance of the force field. The diffusion coefficient was calculated by placing 100 molecules of the molecule of interest in an empty simulation box adjusted in size to reproduce the density of the molecule at ambient conditions (300K and 1 atm). The simulation was then run using timesteps of 1fs for 5,000,000 time steps, 3,000,000 of which for equilibration. The diffusion coefficient as calculated from a molecular dynamics simulation is very sensitive to statistical effects [158] and for this reason, we have divided the 2,000,000 time steps in half and calculated the diffusion coefficients as an average over 1,000,000 different time origins. More specifically, we calculated the diffusion coefficient over time steps 1 to 1,000,000, 2 to 1,000,001 and so on. We then repeated this procedure for five different starting geometries and the final average of these five simulations was taken as the diffusion coefficient.

3.2 Methane and Graphene-Methane interactions

Most common force fields treat methane as a united-atom using the LJ potential, thereby placing an interaction centre on the carbon atom and ignoring the presence of the hydrogens. This way, the molecule is treated as a sphere and no directionial effects are taken into account which is justified by the highly symmetrical nature of the methane molecule, reflected in the fact that its first non-zero electrical moment is the octupole. By far the most used methane model, coming from the TraPPE force field, is of this type and was specifically developed to reproduce liquid methane properties [159]. It includes no electrostatic interactions and numerous studies were carried out using this model: Bichoutskaia used the model to study methane adsorption in metal organic frameworks [24] as did Vandenbrande et al. [75], while Kaur et al. used it to study its influence on the nanostructuring of water and formation of nanobubbles [93]. Gomez-Gualdron et al. studied the storage and delivery of methane in nanoporous materials [160] and Liu et al. studied the temperature evolution of methane adsorption on graphite [161]. Duren et al. used the same model to explore new materials for methane adsorption [15] and Dundar et al. studied how methane melts in nanopores [67]. In general, this model performs very well for studies of liquid methane, but less so for methane in gas phase [162]. This can be understood by the notion (explained in chapter 2) that the LJ potential has important shortcomings at longer distances, which is very important for gas phase and only to a lesser extent for liquid methane. With the same reasoning, it can be understood that, although the force field performs well for high-pressure adsorption, deviations of up to 200 % have been found for adsorption uptake of low pressure methane in MOFs using the the TraPPE force field [163]. The parameters for this model and the other models from the literature discussed in the next paragraphs are collected in table 3.1.

There are a number of studies that use a model that deviates only slightly from the TraPPE force field and we therefore do not include the parameters here specifically, but the studies include the work of Blanco et al. who studied the pore size distribution of carbon monoliths via the adsorption of methane [27]. Albesa et al. studied the adsorption of methane on exfoliated graphene and graphite [29, 164], while Morales-Cas et al. studied the adsorption of methane and hydrogen on carbon cylindrical cavities [31]. Heuchel et al. studied adsorption on activated carbon [165] and Gatica et al. studied the adsorption on carbon nanohorns [166]. Kowalczyck et al. optimized slitlike carbon nanopores for hythane storage [115] as did Cracknell et al. for methane [167]. Sweatman et al. characterized porous materials for gas adsorption at ambient temperature and high pressure [168] and Shao et al. looked at methane adsorption on novel activated carbon beads [111]. Lucena et al. compared a slightly different united-atom model to other more complicated potential types and found it to perform reasonable taking into account the low cost of the method [55].

TABLE 3.1: Parameters for different methane force fields from the literature. Cm refers to the center of mass, C to the carbon atom, H to the hydrogen atom and M to the midbond-point of the CH bond.

	interaction	ϵ (kcal mol^{-1})	r_0 (Å)	β	q_C (e)	q_H (e)
united-atom						
TraPPE [159]	CmCm	0.294	4.187	-	-	-
Albertí et al. [59]	CmCm	0.335	4.06	9.000	-0.626	0.157
Stassen A [65]	CmCm	0.298	4.190	-	-	-
Faginas-Lago et al. [135]	CmCm	0.345	4.040	8.000	-	-
atomistic						
AIREBO [61]	CC	0.065	3.816	-	-	-
	CH	0.048	3.395	-	-	
	HH	0.035	2.975	-		
Sun et al. [169]	CC	0.109	3.816	-	-0.660	0.165
	CH	0.041	3.395	-		
	HH	0.016	2.974	-		
Stassen B [65]	CC	0.102	3.760	-	-	-
	CH	0.047	3.362	-		
	HH	0.017	3.157	-		
Stassen C [65]	CC	0.066	3.929	-	-0.240	0.060
	CH	0.044	3.367	-		
	HH	0.030	2.806	-		
Stassen D [65]	CC	0.066	3.929	-	-	-
	CH	0.044	3.367	-		
	HH	0.030	2.806	-		
Vela et al. [41]	CC	0.056	3.816	-	-	-
	CH	0.061	3.574	-		
	HH	0.066	3.326	-		
other approaches						
Stassen L [65]	HH	0.089	2.750	-	-	-
TraPPE-EH [159]	MM	0.030	3.72	-	-	-

Albertí et al. have studied the interaction of methane with benzene using a united-atom approach and the ILJ potential. The interaction parameters were derived from the molecular polarizability via semi-empirical correlation formulae and included charges of -0.626e on the carbon atom and 0.157e on the hydrogen atoms [59]. This method is closely related to the method described in section 3.8 of this work, albeit starting from experimental data. Also Faginas-Lago et al. have developed a united-atom model based on the ILJ potential and have used it to study methane ice formation [135], while the same force field was used by Albertí et al. for the study of methane hydrates [134]. By using the ILJ potential, they eliminated a large part of the issues related to LJ potenials, but the parameters were obtained from experimental data through semi-empirical formulae. In this work, the attempt was to obtain the parameters directly from DFT-level calculations to try and capture the accuracy of this method.

The AIREBO force field is an example of an atomistic potential, whereby the LJ potential was introduced into a reactive force field and adjusted accordingly [61]. The parameters were obtained by fitting the LJ parameters to experimental data for liquid methane and ethane and no partial charges were considered. This force field was used by Raghavan et al. [32] to study the separation of methane and hydrogen using nanoporous graphene, whereby they made no distinction between the hydrogen atoms from the methane molecules and the hydrogen atoms from the hydrogen molecules. Liu et al. [34] used an atomistic force field developed by Sun et al. [169] via calculation of solvation free energies, to study the behavior of methane (and carbon monoxide) on carbon nanotubes and disordered carbons. The same force field was used by Yaganegi et al. to study the behavior of methane in carbon nanotubes [170]. For the studies in this work, we are not interested in reactive force fields and we therefore have not used the AIREBO force field in the remainder of this work.

Stassen has performed a study comparing the behavior of a number of force fields for methane as a dense fluid [65]. He considered six different potentials based on the Lennard-Jones potential, three of which are atomistic, one is a united-atom approach and two consider only hydrogen-hydrogen interactions. Furthermore, he investigated seven models that were based on an exponentially repulsive potential. He found, first of all, that the LJ based potentials behaved better in reproducing experimental properties like the radial density. For this reason and because the parameters are not comparable with the parameters that will be developed in this work, the parameters of the exponentially repulsive potentials are not given here. Among the LJ potentials, they found that the atomistic models behave better than the model based on hydrogen interactions only and the united-atom approach. In conclusion, he recommends use of potentials Stassen B and Stassen C, see table 3.1, whereby we named the potential after the author, keeping the letter that was given to the respective potentials in the original work. Again, the force fields behave well for the simulation of dense liquid methane, but comparison later on in this work will show that LJ based force fields perform worse than ILJ based force fields for low-density gas phase methane.

Force fields are often developed by fitting a potential of choice to experimental data. The choice of the data heavily determines the possible uses and transferability of the parameters. A balance needs to be maintained between accuracy and transferability, since obtaining very accurate force fields for one specific application might make it useless for all other applications. If fitting is, for example, specifically done to experimental data for the liquid phase (as was done for most of the force fields discussed above), than this may be accurate for the liquid, but perform badly for the gas phase and vice versa. As is evident from the previous overview, little force fields are available for the specific modeling of methane gas. Fitting of the potentials to theoretical interaction energies, is, by definition, fitting to gas phase data and we will thus obtain models suitable for the simulation of methane molecules in gas phase.

3.2.1 CCSD(T) and DFT Interaction Energies

For benchmarking the B97-D functional for the methane dimer interactions, we have selected six symmetrical methane dimer geometries (see figure 3.4) and calculated their intermolecular equilibrium distance, R_e, and corresponding interaction energy, D_e at both DFT and CCSD(T) level. For this, we first selected the six geometries and then did a scan over the intermolecular distance, while all the other structural parameters were kept frozen, the results are shown in table 3.2. The small size of the interaction energies and the differences between the respective geometries confirm that the interaction is dominated by dispersive interactions and is orientation dependent. The CCSD(T) energies show an ordering in stability as A $>$ B $>$ D $\approx$ C $>$ E $>$ F for the six methane dimers considered, altough only the extremes A and F are clearly distinct in energy; the other geometries (B, D, C and E) are very similar and in the intermediate energy range.

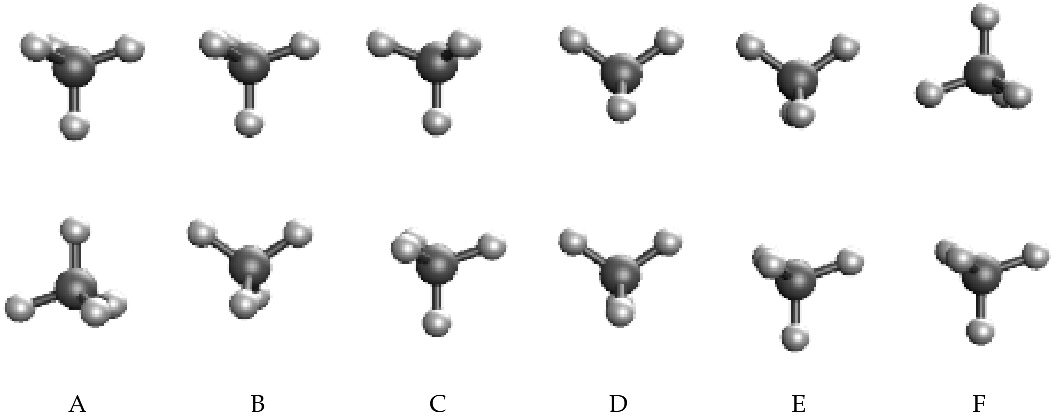

FIGURE 3.4: The six orientations of the methane dimers considered in this work for benchmarking purposes.

The DFT functional, B97-D, is well capable of distinguishing different energy regions in the sense that the most and the least stable conformations are clearly separated from each other and from the intermediate energy range. However, it has some trouble to differentiate the very close energies in the intermediate range, leading to the stability sequence A $>$ B $\approx$ D $>$ E $>$ C $>$ F. Analysis of the different ordering leads to the conclusion that the DFT functional has a problem with the representation of the interaction through the vertex of the tetrahedron as can be seen in conformations D and E. These are overestimated by an amount larger than the energy difference between the geometries, leading to the wrong ordering. Nevertheless, as said, the DFT functional is clearly able to differentiate the different energy ranges and we are thus confident that the performance is good enough to give trustworthy results for the current application. We would like to stress that the average DFT energy over the six dimers, 0.46 kcal mol^{-1}, is in excellent agreement with the average

TABLE 3.2: CH_4-CH_4 interaction energies, D_e, and equilibrium distances, R_e, for the structures (see fig 3.4) investigated in this work compared to previous theoretical and experimental studies

		D_e (kcal mol^{-1})		R_e (Å)	
	orientation	DFT	CCSD(T)	DFT	CCSD(T)
A	3H - 3H	0.558	0.548	3.8	3.7
B	3H - 2H	0.515	0.464	3.9	3.8
C	2H - 2H	0.474	0.424	4.0	4.0
D	3H - 1H	0.523	0.434	4.0	4.1
E	2H - 1H	0.499	0.357	4.3	4.3
F	1H - 1H	0.220	0.145	4.7	4.8

CCSD(T) energy of 0.40 kcal mol^{-1}. Furthermore, the results for the intermolecular distances are even better; for the different orientations, the errors are smaller than 0.1 Å , while the average bond distances (4.117 Å for both DFT and CCSD(T)) fall within the experimental, spectroscopic interval of 4.1152 Å - 4.2202 Å [171] .

The same DFT functional was used for the calculation of interaction energies on the circumcoronene-methane system and here benchmarking is also needed. However, since calculations on circumcoronene are not feasible at the CCSD(T) level, we have used coronene as a model. On the coronene molecule, three different adsorption sites were selected, the C, B and T site, as these locations have been identified as the main adsorption sites for small molecules on graphene [11]. The C site is the position at the centre of mass of the coronene molecule, while the B site is a position above the mid-bond point of a bond of the inner benzene ring and the T site is situated above a carbon of the same inner benzene ring, the positions can be seen in figure 3.5. Then, we have selected three 'attacking' geometries of the methane molecule, which we named according to the number of hydrogen atoms that are facing away from the coronene plane — H-up, 2H-up and 3H-up (see figure 3.5) — and calculated the interaction energies of the three geometries at the three different adsorption sites for a total of nine conformations. The intermolecular distances were optimized at the DFT level and then the CCSD(T) energies were calculated at this geometry since the size of the system prohibits optimization of the intermolecular distance at CCSD(T) level, results are shown in table 3.3.

The DFT results represent well the CCSD(T) energies reproducing the stability sequence for the three adsorption sites as well as for the three methane orientations. DFT does overestimate the binding of all geometries by about 0.5 kcal mol^{-1}, an overestimation that lowers as the number of $H_{methane}$-ring interactions increases. This is beneficial for our purpose, since these interactions are also lower in energy and thus of more influence during the simulations we want to perform. From the results, it can be deduced that the adsorption site is of little importance since their energies are quite comparable: the T and B site are very similar, while the C site is only slightly favored by about 0.2 kcal mol^{-1}. More important is the orientation of the

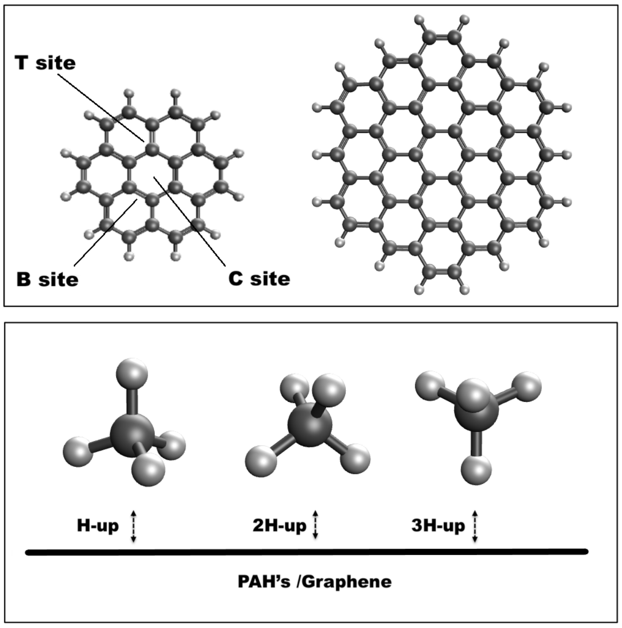

FIGURE 3.5: Structures of the coronene and circumcoronene molecules used as graphene models showing the different interaction sites of CH_4 on coronene considered for ab-initio calculations (top). The three different orientations of CH_4 relative to the graphene plane (bottom).

methane molecule where we see a preference for the H-up orientation over all three adsorption sites. Our results agree well with calculations done at the MP2/(T,Q) + ΔCCSD(T) and DFT/CC level, while BLYP-D3 gives slightly higher energies, in the upper range of the experimentally found values [172–174]. The latter result can be explained by an effect which causes larger graphene models to artificially gain extra interaction energy with methane, from wich some methods suffer [174]. The M06-2X energy, on the other hand, seems stabilized at 3.5 kcal mol^{-1} when increasing the size of the graphene model [175], rather above the experimental value.

Thierfelder et al. reported the same most stable geometry as us at the MP2/aTZ level, although they report a substantially higher interaction energy; it is known, however, that MP2 overestimates dispersion energy [40, 147]. The second most stable structure reported by Thierfelder et al. is the T site H-up configuration coinciding with our results. However, the fact that the three adsorption positions have very similar energies with differences below the precision of the method, causes different methods to obtain different minimum structures: Umadevi and Sastri found the B site H-up geometry to be the most stable at the M06-2X/6-31G*:AM1 level [175], while Smith and Parkowski found the T site H-up as the lowest energy geometry at the MP2/aDZ level [172]. All of the reported intermolecular distances fall within the experimental range, apart from the M06-2x value. Comparison between experimental findings and theoretical calculations provides again convincing evidence of the good behavior of the used method as the lowest DFT values we found, fall within the experimental range. It should be noted that the experimental value takes the lowest

TABLE 3.3: Coronene-CH_4 interaction energies, D_e, and equilibrium distances, R_e, for the structures investigated in this work (see figure 3.5) compared to previous theoretical and experimental studies

		D_e (kcal mol^{-1})		R_e (Å)
	orientation	DFT	CCSD(T)	DFT
C	H-up	2.928	2.584	3.4
	2H-up	2.810	2.312	3.4
	3H-up	2.539	2.018	3.6
T	H-up	2.908	2.571	3.3
	2H-up	2.605	2.177	3.5
	3H-up	2.228	1.652	3.7
B	H-up	2.887	2.446	3.3
	2H-up	2.683	1.905	3.3
	3H-up	2.293	1.713	3.7
other work		2.85[a] [172], 2.80[b] [173], 3.32[c] [174], 3.36[d] [172], 3.00[e] [40], 3.92[e] [40], 3.69[f] [40], 3.23[f] [40], 3.47[g] [175], 3.48[h] [175]		3.32[a] [172], 3.31[b] [173], 3.37[c] [174], 3.32[d] [172], 3.29[e] [40], 3.28[e] [40], 3.64[f] [40], 3.60[f] [40], 2.79[g] [175], 2.81[h] [175]
experiment[i] [176]		3.00 ± 0.23		3.45

[a] MP2/(T,Q) + ΔCCSD(T)/local-DZ, site T H-up
[b] DFT/CC (PBE/aQZ), site T H-up
[c] BLYP-D3/aTZ, site C H-up
[d] circumcoronene-CH_4, B3LYP-D3/aDZ, site T H-up
[e] graphene-CH_4, MP2/aTZ, site T H-up and site C H-up, respectively
[f] graphene-CH_4, vdW-DF(refPBE)/aTZ, site T H-up and site C H-up, respectively
[g] $C_{72}H_{24}$, M06-2X/6-31G*:AM1, site B H-up
[h] $C_{126}H_{36}$, M06-2X/6-31G*:AM1, site B H-up
[i] recommended experimental value of the zero-coverage adsorption well depth of methane on the (001) surface of graphite and the distance between the methane carbon and the surface

energy geometries more into account since they will be more likely to occur in reality. In conclusion, the DFT results are capable of capturing the orientation dependent, dispersive interactions in the methane dimer and the circumcoronene-methane system. This is convenient, since it is a level of theory that allows calculation of the large amount of interaction energies needed to fit the potentials.

3.2.2 Force Field for CH_4 and C-CH_4 Interactions

For the methane dimer, 99 random dimer orientations were generated and for all of them a scan over the distance was done between 3.2 Å and 20 Å to obtain 99 different interaction energy curves at DFT level. We thus calculated geometries at 39 distances for a total of 3861 calculations and used the resulting interaction energies to fit the trial potentials made up of different models considering both united-atom and atomistic approaches. A similar procedure was used for the circumcoronene-methane system: 10 random geometries of methane were generated over the surface of the circumcoronene molecule and interaction energies were calculated on distances between 3.2 Å and 20 Å for 32 intermolecular distances leading to a total of 320 calculations.

We now want to construct the potentials that will be fitted to the randomized DFT interaction energies. For the methane molecule, charge schemes are often omitted because of the symmetrical nature of the molecule and the clear dispersive character of its interactions. However, as seen in table 3.1, some authors did apply partial charges. The highest non-zero multipole in methane is the octupole which can be represented by following chemical intuition and applying a negative charge on the carbon atom and positive charges on the hydrogen atoms in such a way that the total charge is zero. To investigate the influence of the charges on the ILJ parameters, we have included different charge schemes. One was taken from the paper by Albertí et al. [59], where they specifically chose this scheme to reproduce the experimental octupole of the methane molecule. Furthermore, we have calculated different partial charge distributions via distinct population analysis methods such as Mulliken, atomic polar tensor (APT), Hirshfeld and natural population analysis (NPA).

Tsuzuki et al. have shown that, altough dispersion interactions are the most important component for the benzene-methane interaction, electrostatic interactions stabilize the 3H-up structure. However, on passing to polycyclic aromatic hydrocarbons (PAHs) the electrostatic part becomes neglegible [177], a conclusion that was supported by the energy decomposition analysis and CCSD(T) calculations on naphthalene-methane and pyrene-methane systems in the same article. Lazar et al. showed that interaction between graphene and organic molecules is mainly of dispersive nature [149] as was confirmed by Jenness et al. [153]. The electrostatic part is therefore assumed to be of little importance in the interaction between circumcoronene and methane[11] and is therefore ignored for this system in the remainder of this work.

Table 3.4 gives the parameters obtained from fitting the potentials for the methane dimer to the DFT interaction energies. Looking first at the results for the united-atom approach, it is seen that with growing electrostatic interactions — larger partial charges — the parameters change systematically: ϵ gets larger, while r_0 and β diminish. This change, however, is limited and only appears upon the introduction of relatively large charges. It thus seems that the introduction of partial charges is of limited influence on the parameters of the nonelectrostatic energy part as is evidenced in the literature by the routine use of united-atom models without partial charges for the methane molecule (see table 3.1). The interaction parameters for the united-atom approach can be compared to the parameters by Albertí et al., especially for our potential using their charge scheme [59]. They reported values of 0.345 kcal mol^{-1} and 4.04 Å for ϵ and r_0, respectively, while fixing β at 8, where we found values of 0.427 kcal mol^{-1}, 4.163 Å and 8.202 for ϵ, r_0 and β, respectively. Two major differences in approach are to be noted: first of all, they fixed the β value to 8, while we included β in the fitting and secondly and more importantly, they obtained the

TABLE 3.4: Parameters defining the ILJ potentials for the methane dimer from fitting to B97-D calculations. The various charge schemes and potential models described in the text are shown with the atomic charge on carbon (in e) between parentheses.

	ILJ parameters	no charges	APT (0.026)	Hirshfeld (-0.148)	Mulliken (-0.471)	Albertí (-0.626)	NPA (-0.823)
united-atom							
CmCm	ϵ (kcal mol^{-1})	0.421	0.421	0.421	0.424	0.427	0.431
	r_0 (Å)	4.169	4.169	4.168	4.165	4.163	4.159
	β	8.216	8.216	8.215	8.208	8.202	8.192
atomistic free							
CC	ϵ (kcal mol^{-1})	0.109	0.109	0.108	0.070	0.125	0.140
	r_0 (Å)	3.800	3.800	3.800	3.829	3.815	3.797
	β	8.027	8.027	8.024	8.149	7.464	7.421
CH	ϵ (kcal mol^{-1})	0.075	0.075	0.075	0.088	0.067	0.068
	r_0 (Å)	3.628	3.628	3.628	3.604	3.639	3.632
	β	4.932	4.933	4.941	4.798	5.414	5.490
HH	ϵ (kcal mol^{-1})	0.005	0.005	0.005	0.004	0.003	0.003
	r_0 (Å)	3.419	3.419	3.411	3.401	3.373	3.365
	β	4.363	4.363	4.364	4.437	4.938	4.989
atomistic restricted							
CC	ϵ (kcal mol^{-1})	0.198	0.198	0.198	0.196	0.195	0.194
	r_0 (Å)	4.141	4.141	4.139	4.122	4.106	4.077
	β	7.645	7.645	7.645	7.642	7.643	7.647
CH	ϵ (kcal mol^{-1})	0.047	0.047	0.047	0.047	0.048	0.048
	r_0 (Å)	3.368	3.368	3.370	3.389	3.404	3.426
	β	7.279	7.279	7.278	7.268	7.260	7.249
HH	ϵ (kcal mol^{-1}	0.013	0.013	0.013	0.013	0.013	0.013
	r_0 (Å)	2.610	2.610	2.610	2.608	2.607	2.606
	β	7.038	7.038	7.037	7.034	7.032	7.028

parameters via correlation formulae from experimental molecular polarizabilities. With this approach, they attempted to capture the true physics of the interaction in their potential with the disadvantage that possibly neglected parts of the interaction are not taken into account. Since we fit the potential to high-level interaction energy calculations, all possible effects are in principle taken care of implicitly.

The atomistic potentials give the fitting a lot of degrees of freedom, leading to sometimes unexpected results. We therefore tried introducing some limits into the fitting in order to stay closer to the physical meaning of the respective parameters. In a first attempt, however, the parameters were left free during the fitting, denoted as "atomistic free" in table 3.4. The introduction of charges in the atomistic models influences the parameters more than for the united-atom approach, although only above a certain treshold charge. The variation is found mostly in the ϵ of the C-C interaction and the β for all three interactions, while r_0, on the other hand, is barely influenced. One potential — the one using Mulliken charges — behaves unexpectedly since the parameters show strange behavior from a physical point of view. The well depth for the C-H interaction is higher than the one for the C-C interaction, which is contrary to chemical intuition. Dispersive interactions depend to a large extent on the polarizability which, in turn, depends on the size of the electron cloud. The larger cloud of the carbon atoms, would suggest a larger well depth for the C-C interaction than for the C-H interaction. The performance of some selected potentials is compared in figure 3.6.

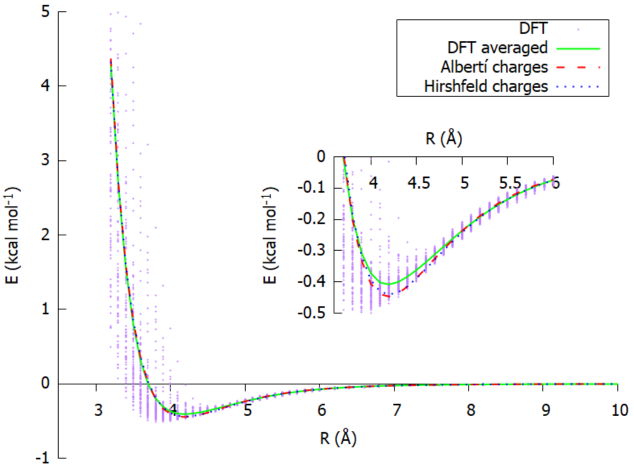

FIGURE 3.6: Comparison between the average energies at DFT level (continuous green line) and the potentials using Albertí's charges (dashed red line) and Hirshfeld charges (dotted blue line). Single point energy DFT calculations are given as small purple points.

The original goal of the ILJ potential was to use parameters with physical relevance, which is lost sometimes during our purely mathematical fittings. More specifically, in the original papers on the ILJ potential, the β is restricted in the interval between 7 and 9 [69, 70], because of the fact that the ILJ potential reduces to the LJ potential in the region where $R \approx r_0$ when β equals 8. The β values that were presented up till now, sometimes reach values as low as 4.5 which can be justified by two main arguments. Firstly, the ILJ potential is based on the concept of polarizability, which for an atomistic potential is an atomic polarizability deduced from the molecular one. The definition of atomic polarizabilities introduces an arbitrariness since the conversion from molecular properties into atomic properties is not necesarily unique and therefore a statistical fitting cannot be expected to reproduce this distribution. Secondly, the use of atomic charges via the Coulombic sum, introduces an incorrect behavior of the electrostatic part with the distance. The Coulombic sum decays with distance as R^{-1} , while the first non-zero term of the multipole expansion of the electrostatic interaction for the methane molecule is an octupole and such interactions reduce faster as R^{-7} . This wrong behavior is compensated for via the lowering of the β in the nonelectrostatic part of the potential. In an attempt to reintroduce physical meaning, we repeated the fitting adding constraints and weights to each fitting point related to the difference between the DFT-energy and the energy as predicted by the united-atom model. In the new fittings, we have thus restricted the β values to fall within the interval of 7 and 9 as originally intended. The parameters are denoted as "atomistic restricted" in table 3.4. A last set of fittings was attempted where also the ϵs and the r_0s were restricted within the recommended intervals. However, their performance compared to the DFT results was very poor and they were thus discarded.

Vela et al. have used an atomistic model that is comparable to ours, although they have used the LJ potential [41]. They reported following values of ϵ = 0.056 kcal mol^{-1}, r_0 = 3.82 Å for the C-C interaction, ϵ = 0.061 kcal mol^{-1}, r_0 = 3.57 Å for the C-H interaction and ϵ = 0.066 kcal mol^{-1}, r_0 = 3.33 Å for the H-H interaction. The r_0s are in good agreement with ours, while the ϵs are not; it is very surprising that their ϵs increase in the series C-C $<$ C-H $<$ H-H. As mentioned before, the dispersive interactions are expected to be stronger for larger polarizabilities and chemical intuition thus completely contradicts their parameters. It is especially important to note that they did not discriminate the C atom from the methane molecule from the carbon atoms within the carbon nanotube of interest, a choice, that has definitely influenced the resulting parameters. Stassen et al. used an atomistic model without electrostatic part, comparable to our atomistic model without charges [65]. Their parameters compare well with ours with their values of ϵ = 0.102 kcal mol^{-1} and r_0 = 3.76 Å for the C-C interaction, ϵ = 0.047 kcal mol^{-1} and r_0 = 3.36 Å for the C-H interaction and ϵ = 0.017 kcal mol^{-1} and r_0 = 3.16 Å for the H-H interaction.

In a last procedure, we have included the charges in the fitting to check what an optimal charge would be according to our methodology. For the united-atom approach, we obtained following parameters: ϵ = 0.467 kcal mol^{-1}, r_0 = 4.125 Å, β = 8.115 and q_C = -1.738e. This potential follows the trend observed previously whereby ϵ rises and $r0$ and β lower with rising charges, however the charge becomes way to high to bare any physical meaning. For the atomistic model, we obtained ϵ = 0.091 kcal mol^{-1}, r_0 = 3.755 Å and β = 7.764 for the C-C interaction, ϵ = 0.086 kcal mol^{-1}, r_0 = 3.591 Å and β = 5.240 for the C-H interaction and ϵ = 0.003 kcal mol^{-1}, r_0 = 3.406 Å and β = 4.548 for the H-H interaction with q_C = -0.917e. Although this latest result seems reasonable and follows the previously identified trends, we found that in general the inclusion of the charges in the fitting leads to a very dificult convergence process making the results dubious at best and we have thus decided to make no further use of this model.

Since electrostatic interactions were not considered for the circumcoronene molecule, only two models were considered as displayed in table 3.5. The first represents the methane molecule by a united-atom approach and the second by an atomistic approach. The united-atom parameters can be compared to the values by Albertí et al. who reported parameters for the interaction of benzene and a united-atom methane as 0.155 kcal mol^{-1} and 4.093 Å for ϵ and r_0 with a β fixed at 9.4. These values are in the same range as ours, especially considering that they introduced a second set of parameters explicitly considering the hydrogen atoms on the benzene and, again, they fixed the β to a value of choice, where we allowed it to relax. Furthermore, it should be noted that the interaction between benzene and methane is quite different from the interactions between PAHs and methane as will be discussed in more detail further on. We, then, also report values for the graphene-methane interaction using an atomistic methane model, which, to the best of our knowledge, has not been done before.

TABLE 3.5: Interaction parameters for the circumcoronene-CH_4 system using a united-atom apprach and an atomistic approach for the methane molecule. Cm refers to the centre of mass of methane, C_g to a carbon atom in graphene, C to a carbon atom in methane and H to a hydrogen atom in methane.

	ϵ (kcal mol^{-1})	r_0 (Å)	β
united-atom			
C_gCm	0.210	3.938	8.185
atomistic			
C_gC	0.195	3.671	7.745
C_gH	0.099	3.727	5.476

3.2.3 Benchmark of Obtained Force Fields

In order to assess the quality of the different force fields obtained for the methane dimer, we benchmarked them against the CCSD(T) calculations for the six symmetrical dimers presented previously in table 3.2 and figure 3.4, the results are given in table 3.6. Obviously, the united-atom model without charges gives the same energy for the six dimers since there is, by construction, no directionality in the model. A similar conclusion can be drawn for the models having small charges (APT and Hirshfeld), there is not enough directionality introduced to distinghuish the different dimers. Perhaps surprising is the observation that the introduction of large charges (Albertí and NPA) shows a completely wrong behavior and does not manage to correctly reproduce the stability sequence predicted by CCSD(T). It is especially striking that the NPA charges behave so badly, since it is currently the standard charge scheme used for static calculations. The poor performance of the larger charges, gives further evidence for the assumption that a sufficently flexible potential is needed to compensate the poorly described electrostatic interactions. Although the united-atom appraoch without charges is not capable of distinguishing the different dimers as expected, the average interaction energies are very statisfactory. The same goes for the intermolecular equilibrium distance, which, for the models with smaller charges coincides very well with the CCSD(T) results, while being overestimated by the models with larger charges. The models with relatively low charges can thus

TABLE 3.6: Interaction energies (D_e) in kcal mol^{-1} and intermolecular equilibrium distances (R_e) in Å, of the representative configurations of the methane dimer (see figure 3.4) as determined from the potential energy functions in Table 3.4

	A		B		C		D		E		F	
	D_e	R_e	D_e	R_e	D_e	R_e	D_e	R_e	D_e	R_e	D_e	R_e
CCSD(T)												
	0.548	3.660	0.464	3.849	0.424	3.992	0.434	4.106	0.357	4.341	0.145	4.811
united-atom												
no charges	0.417	4.197	0.417	4.197	0.417	4.197	0.417	4.197	0.417	4.197	0.417	4.197
APT	0.417	4.197	0.417	4.197	0.417	4.197	0.418	4.197	0.417	4.197	0.417	4.197
Hirshfeld	0.416	4.197	0.417	4.196	0.419	4.194	0.421	4.192	0.419	4.194	0.412	4.202
Mulliken	0.404	4.207	0.413	4.200	0.435	4.179	0.455	4.159	0.434	4.176	0.366	4.259
Albertí	0.394	4.217	0.411	4.204	0.472	4.144	0.515	4.088	0.453	4.163	0.326	4.309
NPA	0.377	4.232	0.405	4.210	0.473	4.145	0.539	4.085	0.470	4.137	0.278	4.387
atomistic free												
no charges	0.650	3.817	0.576	3.944	0.531	4.037	0.391	4.315	0.384	4.353	0.297	4.654
APT	0.650	3.817	0.576	3.944	0.531	4.037	0.391	4.315	0.384	4.353	0.297	4.654
Hirshfeld	0.646	3.818	0.574	3.944	0.533	4.035	0.393	4.312	0.384	4.352	0.294	4.656
Mulliken	0.656	3.816	0.595	3.937	0.579	4.011	0.439	4.279	0.417	4.332	0.296	4.657
Albertí	0.543	3.864	0.509	3.968	0.524	4.014	0.407	4.272	0.376	4.322	0.237	4.684
NPA	0.527	3.878	0.513	3.970	0.568	3.986	0.459	4.227	0.402	4.299	0.214	4.721
atomistic restricted												
no charges	0.458	3.935	0.457	3.968	0.466	3.988	0.382	4.169	0.417	4.155	0.345	4.434
APT	0.458	3.935	0.457	3.968	0.466	3.988	0.382	4.169	0.417	4.155	0.345	4.434
Hirshfeld	0.456	3.935	0.456	3.968	0.469	3.986	0.385	4.166	0.418	4.154	0.341	4.437
Mulliken	0.442	3.937	0.453	3.966	0.492	3.966	0.416	4.138	0.429	4.146	0.306	4.466
Albertí	0.430	3.939	0.450	3.965	0.512	3.949	0.443	4.115	0.439	4.140	0.277	4.491
NPA	0.409	3.942	0.445	3.962	0.548	3.921	0.491	4.078	0.455	4.130	0.231	4.537
other potentials												
TraPPE[a]	0.292	4.248	0.292	4.248	0.292	4.248	0.292	4.248	0.292	4.248	0.292	4.248
Stassen A[b]	0.296	4.251	0.296	4.251	0.296	4.251	0.296	4.251	0.296	4.251	0.296	4.251
Vela[c]	1.118	3.843	0.971	4.052	0.892	4.119	0.664	4.476	0.498	4.700	0.303	5.200
Stassen B[b]	0.543	3.670	0.475	3.871	0.470	3.933	0.320	4.297	0.267	4.500	0.157	5.000
Stassen C[b]	0.506	3.625	0.472	3.771	0.491	3.835	0.336	4.181	0.317	4.200	0.194	4.700
Amber[d]	0.422	3.729	0.420	3.848	0.499	3.858	0.367	4.183	0.268	4.158	0.136	4.900

[a] [159] [b] [65] [c] [41] [d] [178]

be expected to provide a cheap way for simulations of methane and more importantly, the model without charges, which is even cheaper, gives a very good average performance.

Switching to the atomistic approach, we do expect the intrinsic directionality of the model to be able to distinguish the six dimers. Indeed, the models with small charges (APT and Hirshfeld) overestimate the interaction energies only slightly by about 0.1 kcal mol^{-1}. The NPA charges give energies that are in good agreement, while having some trouble to separate the dimers that are close in energy in the same way that DFT does. Using Albertí's charges the energy ordering is reproduced completely as these charges are intermediate in size between the largest charges like NPA and the lower charges like APT, suggesting that intermediate charges perform best in this comparison. The intermolecular distances are still slightly overestimated, but the performance seems better than for the united-atom approach. Looking at the restricted atomistic potentials, it is seen that flexibility is lost in the model: the most stable dimer is underestimated, while the least stable is overestimated, thus reducing the energy interval predicted by these models. Furthermore, the correct ordering is lost by trying to regain some physics in the model and it is thus once again clear that mathematical accuracy is favored in this approach. The equilibrium distances seem to behave similarly: the distance for the most stable dimer is overstimated, while the distance for the least stable one is underestimated lowering the spread predicted by the model. This loss of ordering was rewon by introducing more restrictions (the very restricted parameters discussed in section 3.2.2), but since these potentials behaved completely off in subsequent tests explained below, they were discarded.

Finally, we have compared the performance of our newly developed ILJ potentials to established LJ potentials from the literature, all of which have been mentioned in the text before. We have recalculated the same six methane dimers with some selected potentials, more specifically Stassen A, B and C [65], the force field presented by Vela [41] and the widely used force fields TraPPE [159] and Amber [178]. This comparison can be seen as a validation of the ILJ potential over the LJ potential for the methane dimer and the results are given in table 3.6. Obviously, the united-atom approaches (TraPPE and Stassen A) are still not able to differentiate the different dimer orientations, but on average they predict an interaction energy that is about 0.1 kcal mol^{-1} lower than our potential and thus overestimate the interaction slightly more than our low charges (APT and Hirshfeld) models do. For the atomistic models, Vela et al. overestimate the interaction energy strongly by almost a factor of two, while the other atomistic potentials (Stassen B, Stassen C and Amber) perform reasonably well. Specifically, the Stassen B model performs exceptionally well, outperforming our models in some dimer geometries. However, it should be remembered that the main advantage of the ILJ potential is its flexibility to outperform the LJ potentials at short and medium to long distances.

Next, we want to benchmark the two models that were developed for the graphene-methane system by comparing the performance of the force fields to the coupled cluster results collected in table 3.5. Since it was shown that the specific adsorption site is not so important, we limited the benchmark to the three different geometries of the methane molecule above the centre of mass of the coronene (see figure 3.5). The results are shown in table 3.7 together with more data from the literature. The united-atom approach represents the CCSD(T) interaction energies to within 0.6 kcal mol^{-1} for the coronene-methane system, approaching closely the DFT interaction energies. Furthermore, the predicted energy is very close to the reported

TABLE 3.7: Interaction energies (D_e) in kcal mol^{-1} and intermolecular equilibrium distances (R_e) in Å of the representative configurations of the coronene-CH$_4$, naphthalene-CH$_4$ and benzene-CH$_4$ systems as calculated from the potential energy functions in table 3.5 and figure 3.5

	$C_{24}H_{12}$-CH_4		$C_{10}H_8$-CH_4		C_6H_6-CH_4	
	D_e	R_e	D_e	R_e	D_e	R_e
united-atom						
	2.930	3.502	-	-	1.293	3.673
atomistic						
H-up	3.295	3.404	2.109	3.501	1.497	3.562
2H-up	2.977	3.499	1.875	3.598	1.314	3.667
3H-up	2.384	3.675	1.388	3.787	0.970	3.912
CCSD(T)						
H-up	2.584	3.4	2.126 [172]	-	1.23 [179]	3.6 [179]
2H-up	2.312	3.4	1.86 [177] 2.088 [172]	3.6 [177]	1.32 [179]	3.6 [179]
3H-up	2.018	3.6	-	-	1.45 [179]	3.8 [179]
experimental						
	3.00 ± 0.23[a] [176]	3.45[a] [176]	-	-	1.321 - 1.421[b] [180]	-

---

[a] graphite-CH$_4$, best estimate

[b] Mass analyzed treshold ionization (MATI) technique on the benzene-methane cluster. Values corrected with zero-point energies (ZPE=0.291 kcal mol^{-1}).

experimental interaction energy for the graphite-methane system and the same goes for the predicted equilibrium distance. Obviously, the model is again not capable of including any orientation dependence of the methane molecule, but this picture changes when switching to the atomistic model. The stability sequence is now correctly reproduced although all energies are slightly overestimated between 0.4 kcal mol^{-1} and 0.7 kcal mol^{-1}. Compared to the experimental value, the comparison is very good considering that the lowest energy geometries contribute stronger to the experimental value. Also the equilibrium distances reproduce well the CCSD(T) and experimental values.

Although our potentials were designed specifically for large PAHs, we tested their performance on smaller molecules like naphthalene as well, whereby the major expected problem is the influence of dangling hydrogen atoms becoming larger for smaller molecules. However, the results for naphthalene are good for both the interaction energies and the equilibrium distances and both qualitatively and quantitatively. For the benzene-methane system, however, our potentials show the exact opposite behavior as CCSD(T). Our potentials show the same stability sequence as for the PAHs with the H-up geometry being the most stable, while CCSD(T) predicts the 3H-up to be more stable. However, Tsuzuki et al. have shown that there is a different behavior for the interaction with methane between benzene and PAHs [177]: while the interaction with benzene is stabilized via the weak electrostatic interaction of one hydrogen atom with the negative charge concentration in the benzene ring, this effect is countered by a larger dispersive contribution from different carbons in the PAH with as many hydrogen atoms as possible, i.c. three. Our potentials were not trained to capture the electrostatic effect stabilizing the 3H-up geometry for the benzene molecule and are therefore not able to well describe this interaction. Note, however that the average interaction energy agrees well with CCSD(T) and experiment.

3.2.4 Diffusion Coefficient of Methane

After benchmarking the obtained potentials at the molecular level, we want to further thest their performance by analyzing their ability to reproduce macroscopic properties that imply progagating the system through time. We have thus calculated the diffusion coefficient of a methane gas at room conditions using our different potentials which is directly comparable to the experimental value of 1.880 10^{-5} m^2/s, results are shown in table 3.8. As a first general conclusion, there is no systematic better behavior of the united-atom approach over the atomistic approach or the other way around, nor is there a systematic better performance of one or more of the charge schemes over both the united-atom and atomistic approaches. Overall, the best performing potential is the atomistic approach without charges, deviating only 0.004 10^{-5} m^2/s from the experimental value and in general, it is seen that for the atomistic approach, the best results are obtained using small charges, demonstrated by the Hirshfeld charges potential which only deviates by 0.06 10^{-5} m^2/s from the experimental value. Also, the restricted atomistic potentials perform well when combined with small charges. Larger charges, such as the charges by Albertí, albeit performing well during the CCSD(T) benchmark, now only give a qualitative description. Most striking is that, once again, the NPA charges, although very popular, perform the worst of all the considered charge schemes for all three model types. Looking at the united-atom approach, the Hirshfeld charge scheme performs the best with a deviation from the experimental value of 0.05 10^{-5} m^2/s. Furthermore, the united-atom model without charges, by far the cheapest of all the considered models, performs still reasonably well with an absolute error or 0.18 10^{-5} m^2/s, making this model of interest for large systems needing a high computational efficiency. It is noteworthy that, although the Hirshfeld charges do not provide the best picture for all three models (united-atom, atomistic free and atomistic restricted), it is the only scheme that performs well consistently over all three model types.

With all this, we can now decide on what force field to use for what purpose. For fast and efficient calculations, a united-atom approach is proposed, potentially using the Hirshfeld charges to add some directionality into the interaction. For more

TABLE 3.8: Diffusion coefficients calculated using the respective potentials for the methane dimer compared to the experimental value

	$10^5 . D\,(\mathrm{m}^2/\mathrm{s})$					
	no charges	APT	Hirshfeld	Mulliken	Albertí	NPA
united-atom	1.699	1.683	1.831	1.643	1.552	1.157
atomistic free	1.876	2.041	1.937	1.571	1.541	1.232
atomistic restricted	-	1.963	1.999	1.785	1.619	1.280
experimental	1.880					

accuracy, the atomistic potentials are suggested, whereby the model without charges seems to outperform the others.

3.3 Nitrogen and Graphene-Nitrogen Interactions

In the literature, the nitrogen molecule has been represented using a united-atom and an atomistic approach, whereby, since the molecule is not spherical and can be expected to have directional interactions, the atomistic approach should in principle behave better. For most united-atom models, no electrostatic part is included in the potential, while for the atomistic approach two main charge models exist, either assigning three or four partial charges to the molecule. The three-site model assigns negative charges to the nitrogen atoms and a positive charge, double the size, to the centre of mass. Although this model contradicts chemical intuition, expecting a negative charge in the middle of the triple bond, it accurately reproduces the quadrupole if charges are chosen appropriately. The four-site charge scheme assigns both a positive and a negative charge on either side of the molecule on the axis connecting the nitrogen atoms whereby the positive charges are separated by 1.694 Å and the negative charges are separated by 2.088 Å . The different models are represented in figure 3.7 and the parameters for the models described in the next paragraphs are given in table 3.9.

Ravikovitch et al. have represented the nitrogen molecule as a united-atom without consideration of any electrostatic interaction [182]. Wongkoblap et al. used this model to study the pore size distribution of carbon [1], while Do et al. used it to characterize both nongraphitized and graphitized carbon [57, 186]. A similar model was proposed by Takaba et al. [181] and used by Du et al. to study the separation of hydrogen and nitrogen by a porous graphene membrane [187].

Murthy et al. developed the MOM model, an atomistic three-site model, by studying properties in solid, liquid and gas phase [184]. Shao et al. used the model to study the adsorption of gases on activated carbon beads [111]. The popularly used TraPPE force field describes the nitrogen molecule in a similar fashion, atomistically and with a three-site charge scheme [183]. It was used by Patt et al. to study nitrogen

TABLE 3.9: Parameters for different nitrogen force fields from the literature. Cm refers to an interaction centre placed on the centre of mass and N to an interaction centre positioned on the nitrogen atom.

	interaction	ϵ (kcal mol^{-1})	r_0 (Å)	β	q^- (e)	q^+ (e)
united-atom						
Takaba [181]	CmCm	0.142	4.263	-	-	-
Ravikovitch [182]	CmCm	0.202	4.058	-	-	-
atomistic three-sites						
TraPPE [183]	NN	0.072	3.715	-	-0.482	0.964
MOM [184]	NN	0.072	3.724	-	-0.405	0.810
Bramastiya [185]	NN	0.081	3.770	9.000	-0.52	1.04
atomistic four-sites						
Sweatman [168]	NN	0.069	3.749	-	-0.373	0.373
Cracknell [167]	NN	0.075	3.724	-	-0.373	0.373

and carbon monoxide clathrates [188], while Bahamon et al. used it in their study on MOFs and zeolites for the separation of CO_2 from gas mixtures [189].

Sweatman et al. have developed an atomistic, four-site model by comparing Gibbs ensemble simulations to experiment and used it to characterize porous materials [168]. A similar model was developed by Cracknell et al. by fitting to dispersive and repulsive potentials and then used for the study of adsorption in slit-shaped carbonaceaous micropores [167]. The latter model was also used by Ohba et al. to estimate the number of graphene layers from nitrogen adsorption [94].

As for methane, most of the potentials in the literature use the LJ potential as indicated by the overview in the previous paragraphs. Bramastiya et al., however,

three-site model

four-site model

FIGURE 3.7: Different model types for nitrogen as discussed in the text. Partial charges are located on three (left) or four (right) sites as shown.

have proposed a potential for nitrogen based on the ILJ potential and used it to study sieving capabilities of graphynes [185].

Makrodimitris et al. have compared the performance of the MOM model to a four-site model and an atomistic model without charges for the permeation through silicalite [12]. They found that the cheap atomistic model without charges performed suprisingly well, while the MOM model performed the best of the three considered models. Do et al compared the atomistic, three-site MOM model by Potoff and Siepman with the united-atom model proposed by Ravikovitch and found that the cheaper united-atom model describes the adsorption on graphitized carbon black as well as the atomistic model [90]. In general, it seems that nitrogen does not need a complicated description for accurate simulation of adsorption phenomena.

3.3.1 Force Field for N_2 and C-N_2 Interactions

In our work, we have adapted both the united-atom and the atomistic approach and have tried for both of them the inclusion of no charges, three charges and four charges to study the influence on the ILJ potential. In the case of three charges, we have used the partial charges proposed by the MOM model, the TraPPE model and by Stone [190], while for the four-site model, we have used the charges proposed by Cracknell et al. Aside from this, we have also optimized our own charges.

As for methane, these potentials were fit to DFT interaction energies calculated on the nitrogen dimer and the circumcoronene-nitrogen stystem. 99 different, randomly generated, nitrogen dimers were scanned over a distance between 3.4 Å and 20 Å at 44 distances, leading to a total of 4356 calculations at the B97-D/TZV2P level. For the circumcoronene, 10 geometries were generated and scanned between 2.4 Å and 20 Å at 30 different distances leading to a total of 300 calculations at the same level of theory.

The parameters for the united-atom approach are given in table 3.10 for both the no-charge, three-charge and four-charge model. It is seen that for both charge models, only the inclusion of large partial charges substantially influences the interaction parameters, but the observed trends are different. For the three-charge model, increase of the charges leads to a higher ϵ and lower r_0 and β. The four-charge model, on the other hand, leads to a lower ϵ and a higher r_0 and β. Ravikovich et al. have published LJ parameters for a united-atom model for nitrogen without charges where they reported values of 0.202 kcal mol^{-1} for ϵ and 4.058 Å for r_0 [182]. Although ϵ is slightly higher and r_0 slightly lower than our results for the no-charge model, the parameters are in reasonable agreement taking into account that they were obtained via completely different methods.

Atomistic parameters can also be found in table 3.10. The introduction of the partial charges, changes the parameters to a smaller extent than for the united-atom approach. For the three-charge model, ϵ and r_0 increase slightly, while β decreases with rising charge. For the four-charge model, ϵ decreases, while r_0 and β increase.

TABLE 3.10: Interaction parameters for the N_2 dimer using a united-atom and atomistic model with and without charges. Cm refers to an interaction centre on the centre of mass of nitrogen, while N refers to an interaction centre on the nitrogen atom.

	interaction	ϵ (kcal mol^{-1})	r_0 (Å)	β	q^-(e)
united-atom no charges					
	CmCm	0.193	4.314	8.431	-
united-atom three-sites					
MOM	CmCm	0.198	4.307	8.391	-0.405
TraPPE	CmCm	0.200	4.305	8.374	-0.482
Stone	CmCm	0.200	4.304	8.368	-0.510
optimized	CmCm	0.211	4.289	8.281	-0.788
united-atom four-sites					
Cracknell	CmCm	0.189	4.322	8.465	-0.373
atomistic no charges					
	NN	0.074	3.893	8.033	-
atomistic three-sites					
MOM	NN	0.077	3.895	7.869	-0.405
TraPPE	NN	0.078	3.896	7.802	-0.482
Stone	NN	0.078	3.897	7.775	-0.510
optimized	NN	0.079	3.897	7.720	-0.564
atomistic four-sites					
Cracknell	NN	0.072	3.902	8.051	-0.373

More atomistic than united-atom models have been suggested in the literature, giving us more opportunity to compare our parameters. The widely used TraPPE and MOM force fields, provide the same LJ parameters for the nitrogen molecule, namely 0.072 kcal mol^{-1} and 3.730 Å for ϵ and r_0 respectively. Bramastya et al. have proposed an ILJ model using three charges with following parameters: 0.081 kcal mol^{-1} for ϵ, 3.770 Å for r_0 and 9.000 for β and a negative charge of -0.52e. Cracknells own LJ parameters complementing his charge scheme are 0.075 kcal mol^{-1} and 3.724 Å for ϵ and r_0, respectively. All these parameters are in close agreement with each other and with ours with the exception of the β proposed by Bramastiya et al. which was fixed *ad hoc* in their work, while being fit in ours.

Table 3.11 collects the parameters for the graphene-nitrogen interaction using both the united-atom and the atomistic approaches for nitrogen. In the literature, these kinds of parameters are usually obtained via combination rules of the atomic or molecular nitrogen parameters and the atomic carbon parameters within graphene [91, 94]. As said before, we have explicitly avoided this and constructed our own potential via the same procedure used throughout this work. Bramastiya et al. on the other hand have provided atomistic ILJ parameters for the interaction of the nitrogen atom within the nitrogen molecule with a carbon within the graphene as follows: ϵ = 0.092 kcal mol^{-1}, r_0 = 3.828 Å, while β was fixed at 7.5. These parameters are in close agreement with ours, again considering that we allowed the β parameters to relax.

TABLE 3.11: Interaction parameters for the circumcoronene-nitrogen system comparing a united-atom and atomistic nitrogen. Cm refers to the centre of mass of nitrogen, C_g to a carbon atom in graphene and N to the nitrogen atom.

	ϵ (kcal mol^{-1})	r_0 (Å)	β
united-atom			
C_gCm	0.123	4.133	6.470
atomistic			
C_gN	0.087	3.808	7.861

3.3.2 Benchmark of Obtained Force Fields

Similar to the methane molecule, we have benchmarked the performance of our potentials for nitrogen to CCSD(T)/CBS calculations from the literature. In this case, the comparison was done for three highly symmetrical dimer orientations: a linear geometry, a parallel geometry and a T-shaped geometry as indicated in figure 3.8, while the results are shown in table 3.12. It can be seen that the different models are in general capable of well-reproducing the CCSD(T)/CBS results [191], specifically

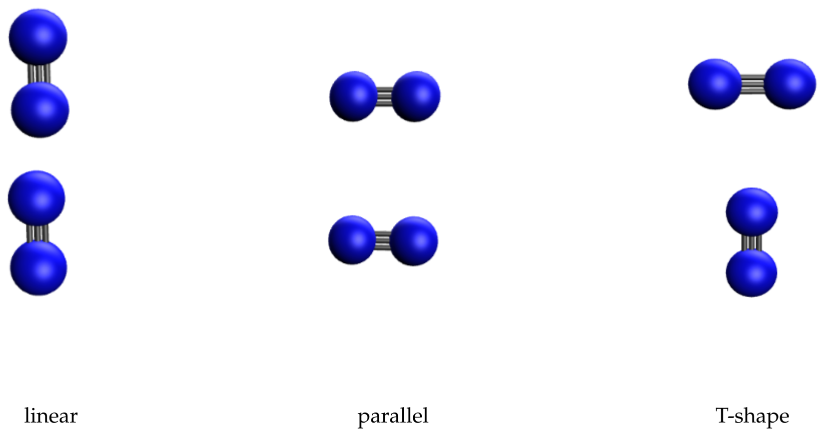

FIGURE 3.8: Different geometries for the nitrogen dimer used for benchmarking the obtained potentials.

TABLE 3.12: Interaction energies (D_e) and equilibrium distances (r_0) of the representative configurations of the N_2 dimer calculated by potential energy functions derived from B97-D/TZV2P calculations.

	linear		parallel		T-shape	
	D_e(kcal mol^{-1})	R_e(Å)	D_e(kcal mol^{-1})	R_e(Å)	D_e(kcal mol^{-1})	R_e(Å)
united-atom no charges[a]						
			0.199	4.270		
united-atom three-sites						
MOM	0.119	4.46	0.174	4.360	0.253	4.210
Stone	0.077	4.57	0.160	4.38	0.284	4.18
TraPPE	0.088	4.54	0.164	4.38	0.276	4.19
optimized	-	-	0.111	4.46	0.417	4.08
united-atom four-sites						
Cracknell	0.052	4.75	0.169	4.32	0.256	4.21
atomistic no charges						
	0.140	4.76	0.293	3.78	0.206	4.27
atomistic three-sites						
MOM	0.103	4.88	0.263	3.87	0.263	4.23
Stone	0.077	4.95	0.238	3.91	0.295	4.20
TraPPE	0.084	4.93	0.246	3.90	0.286	4.21
optimized	0.063	4.99	0.222	3.94	0.315	4.19
atomistic four-sites						
Cracknell	0.057	5.01	0.245	3.89	0.261	4.22
CCSD(T)						
[191]	0.006	4.74	0.205	3.57	0.277	4.03

[a] The united-atom no-charge model does not allow to differentiate the different conformations, instead, it provides an average over all configurations.

giving the correct stability sequence of T-shape > parallel > linear. They have a problem, however, at predicting the very low interaction energy for the linear structure, a recognized problematic geometry which is wrongly predicted by a number of DFT functionals — like M11, ωB97X-D and B3LYP-D3 among others — as antibonding [191]. For both the united-atom approach and the atomistic approach, the four-charge scheme outperforms the three-charge scheme while the united-atom no-charge scheme cannot distinguish the different geometries for obvious reasons. Furthermore, the atomistic appraoch in general, slightly outperforms the united-atom approach. The intermolecular distances for all model potentials are in general overestimated and deviate by an amount of about 0.25 Å .

To validate the graphene-nitrogen potentials, we have calculated the interaction energies for specific orientations of the circumcoronene-nitrogen and the benzene-nitrogen systems. More specifically, we placed the nitrogen molecule over the centre of mass of the circumcoronene and benzene molecules, respectively, both parallel and perpendicular to the plane of the molecule. Although the potential is specifically designed for PAHs, we look at the performance for benzene as well, the results are collected in table 3.13.

TABLE 3.13: Interaction energies (D_e) and equilibrium distances (r_0) for the representative configurations of the circumcoronene-nitrogen and benzene-nitrogen systems calculated by potential energy functions derived from B97-D/TZV2P calculations. C_g represent a carbon atom in graphene, Cm is the centre of mass of nitrogen and N represents a nitrogen atom.

	circumcoronene-N_2		benzene-N_2	
	D_e(kcal mol^{-1})	R_e(Å)	D_e(kcal mol^{-1})	R_e(Å)
united-atom				
C_gCm	2.189	3.630	0.741	3.888
atomistic				
C_gN/perpendicular	1.980	3.769	0.735	3.984
C_gN/parallel	2.593	3.391	1.024	3.554
RBDMC				
[192]	-	-	1.154	-
experimental[a]				
[176, 193, 194]	2.398	3.340	0.92 ± 0.07	-

[a] Experimental results for the graphene-N_2 system.

It is seen from the table that the united-atom approach provides consistently lower energies with respect to the experimental values. This approach is by construction not capable of distinguishing different orientations and therefore gives too low weights to the most stable geometries, underestimating the average interaction energy. The atomistic approach, on the other hand, reproduces well the interaction energies of the different orientations and provides an upper and a lower limit to the interaction energy enveloping the experimental interaction energy. The arithmic mean of 2.3 kcal mol^{-1} is close to the experimental value, certainly when taking into account that the experimental value will be closer to the lower bound of the interaction energy because more stable geometries will be favored in the system. Similar conclusions can be drawn for the equilibrium distance. Although not designed for a molecule like benzene, our potentials behave well and the performance is comparable to the circumcoronene case: the united-atom approach underestimates the interaction, while the atomistic potentials again present an upper and lower bound containing the experimental value. A reasonable agreement is also found with the value proposed by the rigid-body diffusion Monte Carlo (RBDMC) method.

3.3.3 Diffusion Coefficient of Nitrogen

Finally, we have tested the performance of the potentials by calculation of the diffusion coefficient at room conditions as shown in table 3.14. Neither the united-atom approach nor the atomistic approach perform consistently better than the other over all the different charge schemes. For the united-atom model, the performance worsens upon increasing the charges. The smallest charges of the MOM scheme, give already an absolute error of 0.341 $10^{-5}\,\mathrm{m^2/s}$ compared to the experimental value, while the four-charge model performs better, with a deviation of -0.081 $10^{-5}\,\mathrm{m}^2/s$ for the Cracknell charges. As the error becomes larger upon increasing the charges, it seems better not to include charges at all, leading to an absolute error of only 0.023 $10^{-5}\,\mathrm{m^2/s}$ for the model without charges. This result matters because for massive calculations, simplicity in the potential can lead to significant computational time savings. For the atomistic approach, a similar trend is seen: increasing the charges worsens the performance. However in this case, the four-charge model of Cracknell, with an error of -0.108 $10^{-5}\,\mathrm{m^2/s}$, is to be preferred over a model without charges with an error of -0.216 $10^{-5}\,\mathrm{m^2/s}$). In case of large simulations, however, leaving out the Coulombic sum altogether seems justified to save computing time. The difference in performance between the no-charge model and the best performing three-charge model (MOM) is a lot smaller than for the united-atom case, an error of -0.216 $10^{-5}\,\mathrm{m^2/s}$ versus 0.304 $10^{-5}\,\mathrm{m^2/s}$. As a comparison we calculated the diffusion coefficient using the parameters proposed by Bramastya et al. [74], where we obtained a result of 0.900 $10^{-5}\,\mathrm{m^2/s}$, corresponding to a large error of 0.650 $10^{-5}\,\mathrm{m^2/s}$, compared to experimental value.

TABLE 3.14: Diffusion coefficients calculated using the respective force fields compared to the experimental value (exp.).

	$10^5 . D\,(\mathrm{m^2/s})$					
	no charges	three-sites				four-sites
		MOM	TraPPE	Stone	optimized	Cracknell
united-atom	1.527	1.209	0.946	0.809	0.339	1.631
atomistic	1.766	1.246	0.910	0.899	0.750	1.658
experimental [195]		1.55				

Considering the performance of all proposed potentials, it seems that the Cracknell charge scheme performs best in all cases although for large, expensive calculations the united-atom model without charges performs well in an average fashion. Introducing the Cracknell charges on the united-atom model gives the potential the possibility to represent accurately the different dimer energies, while slightly worsening the calculation of the diffusion coefficient. For the atomistic approach it is advised to include Cracknell charges in the potential for accurate simulations.

3.4 Water and Graphene-Water Interactions

Despite the simple structure of water, it has been proven really hard to capture its versatile chemistry in one single model. Part of the reason why this is so, is because multiple interaction types are interfering with each other: aside from the dispersive interactions, there are very important electrostatic interactions among which the hydrogen bonds. The latter are hard to describe accurately since they are very directional in nature, a feature hard to catch in a simple and computationally efficient model. Different attempts have been proposed in the literature, but none have been able to describe all the facets of the behavior of water. The most simple model types assign a single interaction centre on the oxygen atom, reducing the molecule to a spherical united-atom. Furthermore, they assign three partial charges at the most logical — following chemical intuition — positions, a negative charge on the oxygen atom and positive ones on the hydrogen atoms and are referred to as three-site models from now on. More complicated charge schemes assign four (four-site models) or five (five-site models) interaction centres (one dispersive and, respectively, three or four electrostatic) to the molecule, while only a limited number of models follow an atomistic approach. The different charge schemes are shown in figure 3.9 and a representative overview of parameters from the literature is collected in table 3.15.

The simple point charge model (SPC) was developed by Berendsen et al. [196], for use with hydrated proteins specifically, by fitting to experimental pressure and

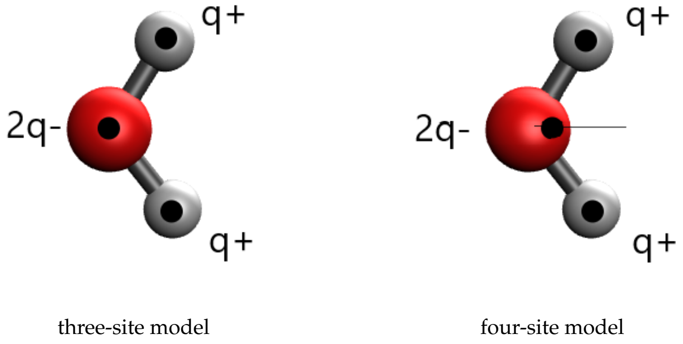

three-site model four-site model

FIGURE 3.9: The three- and four-site water models as discussed in the text. The negative charge in the four-site model is not centred on the oxygen atom, but positioned along the bisector of the H-O-H angle.

TABLE 3.15: Parameters for different water force fields from the literature, O refers to the oxygen atom and H to the hydrogen atom

	interaction	ϵ (kcal mol^{-1})	r_0 (Å)	β	q_O/q_M (e)	q_H (e)
united-atom three sites						
SPC [196]	OO	0.155	3.554	-	-0.820	0.410
SPC/E [197]	OO	0.155	3.554	-	-0.848	0.424
TIP3P [198]	OO	0.152	3.536	-	-0.834	0.417
TIP3P-Ew [199]	OO	0.102	3.578	-	-0.830	0.415
Costantini [200]	OO	0.209	3.730	7.5	-0.865	0.433
Albertí [101]	OO	0.209	3.730	6.6	-0.658	0.329
AMPF [201]	OO	0.209	3.730	6.6	-0.865	0.433
EM-AMPF [202]	OO	0.155	3.554	6.6	-0.848	0.424
united-atom four-sites						
TIP4P [198]	OO	0.155	3.540	-	-1.040	0.520
TIP4P-Ew [203]	OO	0.163	3.552	-	-1.048	0.524
TIP4P/2005 [204]	OO	0.185	3.546	-	-1.113	0.556
atomistic three-sites						
CHARMM27 [205]	OO	0.152	3.536	-	-0.834	0.417
	OH	0.084	1.987	-		
	HH	0.046	0.449	-		

potential energy. The same authors have extended this model to the expanded simple point charge model (SPC/E) by reparametrizing the SPC model after inclusion of a self-energy correction [197]. This model has proven its succes by studies on carbon nanotubes in water by Walther et al. [79], by a study on the interaction between a water drop and holey graphene by Wang et al. [105] and by a study on the separation of water from alcohol by Damasceno Borges et al. [102].

A whole set of potentials was developed for water with the specific aim to be transferable from one system to the other, a series called transferable intermolecular potential (TIP) functions whereby a number after the TIP indicates the amount of sites present in the charge scheme. The TIP3P model was developed by Jorgensen et al. [60] by fitting the behavior of gas-phase dimers and liquid water to experimental values. It was later adapted and reparametrized by Price et al. [199] to the TIP3P-Ew model for use with the Ewald summation. Jorgensen et al. [198] have developed the TIP4P model, evidently a four-site model, by fitting to experimental data of liquid water. These four-site models attempt to better describe the behavior of the water dipole by moving the negative charge from the oxygen inwards along the bisector of the H-O-H angle [206]. This popular model has proven its worth extensively via, for example, studies on the structural ordering of water and the adsorption on activated carbon and carbon black [92, 93]. The TIP4P/Ew model was developed by Horn et al. [203] as a reparametrization of the TIP4P model for use with Ewald techniques specifically. It was designed to reproduce accurately experimental bulk properties of water and has found application in the work by Jiao et al. [99] on the modeling of water incapsulated by graphene. Abascal et al. [204] have exploited the availability of stronger computational power, to redesign the TIP4P model by fitting to experimental data that was previously not accessible through theoretical methods, leading to the TIP4P/2005 model. This model has found popular use, for example, in studies by Zhao et al. [100] on the fountain effect of water in carbon nanotubes and by Bahamon et al. [97, 103] on the removal of ibuprofen from water and the evaluation of new materials for post-combustion CO_2 removal, while Ma et al. [51] used it for the study of water diffusion on graphene sheets. Mahoney et al. [207] developed the TIP5P model by representing the water molecule as an assymetric tetrahedron, with two hydrogens on their usual positions and two negative charges on the remaining two vortices of the tetrahedron. The model was then again fit to experimental data and it was used by Fingerhut et al. [208], among others, for studying the interaction of water with phosphates. MacKarell et al. [205] developed an atomistic model, specifically for use with proteins, by iterative fitting to experimental data that became part of the CHARMM27 force field. This model was used by Liu et al. [95] for the study of the effect of channel morphology on water adsorption in graphene bilayers and by Deshmukh et al. [52] for the study of water dynamics between static and free-standing, fully flexible graphene sheets. However, we have not further considered this model in our studies as it was found by Zielkiewicz to underperform compared to three- and four-site models [209].

All the above models were based on the Lennard-Jones potential for the dispersion interaction, yet, some ILJ models have been proposed as well. Costantini et al. [200] have developed a three site model for water based on the ILJ potential, whereby the ILJ parameters were derived via correlation formulae from the experimental molecular polarizability and the electrostatic charges were chosen such as to reproduce the experimental dipole moment [202]. This model was used in the same group by Albertí et al. [134] to study the influence of micelles on the formation of methane hydrates. Albertí et al. [201] afterwards developed the adapted molecular polarizability model for force fields (AMPF) model by lowering the β value of the model by Costantini et al. in order to better reproduce experimental data. Although they used a slightly lower dipole moment in another work by making the partial charges smaller [101]. The model was further developed in the same group by tuning of the electrostatic part, based on the SPC/E charge scheme, and reestimating the ILJ parameters from the molecular polarizability [202]. This model was further used to study the molecular stirrer catalytic effect on methane ice formation and the formation of carbon dioxide hydrates [101, 135].

Due to the permanent dipole of water, induction effects are to be expected as well and for this reason polarizable force fields have been developed that allow the molecule dipole to adapt to its environment. The most simple form adds Drude oscillators to the molecule, effectively a charge is attached to the oxygen molecule via a harmonic potential allowing the charge to adjust its position to the environment [157]. However, Ho et al. [210] have found the inclusion of this model to have very little effect on the behavior of the graphene-water interface and suggested they are only necessary for the interactions with ions. Another approach recalculates the dipole when the environment changes by introducing the polarizability and fitting to experimental data [156]. Although these models can be expected to give good results, they are computationally too demanding for the fast and reliable force fields that are the goal of this work. We would like to stress that by fitting to theoretical calculations these effects are implicitly and in an averaged way taken into account in our potentials.

3.4.1 CCSD(T) and DFT Interaction Energies

As in the previous cases, we benchmarked the performance of the B97-D/TZV2P level against the CCSD(T) level to validate its performance for the water molecule. Again the same three adsorption sites (over the centre of mass of coronene, C site, over the centre of a CH bond of the inner benzene ring, B site, and over a carbon atom of the same ring, T site) were calculated. Three orientations were considered as well: two where the molecule is perpendicular to the coronene plane — one with the oxygen atom up (O-up) and one with the oxygen atom down (O-down) — and one where the molecule is positioned parallel to the plane (side) as shown in figure 3.10. Table 3.16 gives a comparison for the interaction energies between the used

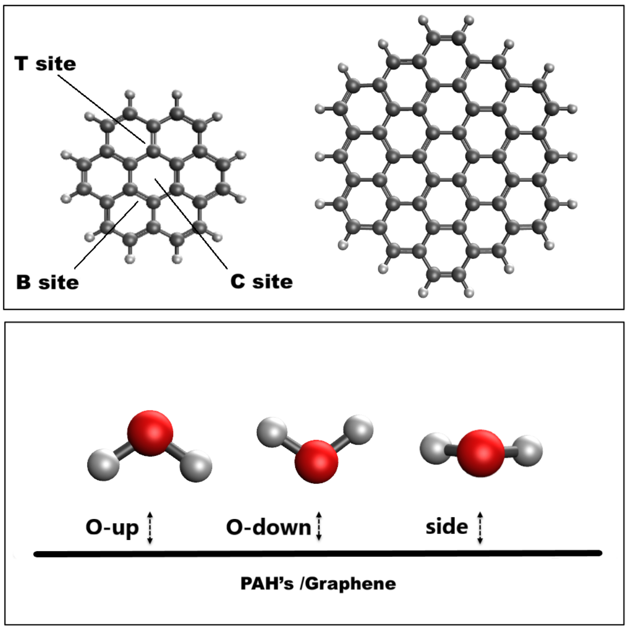

FIGURE 3.10: Structures of the coronene and circumcoronene molecules used as graphene models showing the different interaction sites of H_2O on coronene considered for *ab initio* calculations (top). The three different orientations of H_2O relative to the graphene plane (bottom).

TABLE 3.16: A comparison between the interaction energies at CCSD(T) and B97D DFT level for the coronene-water system.

		D_e (kcal mol^{-1})		R_e (Å)
site	orientation	DFT	CCSD(T)	DFT
C	O-down	0.808	1.290	3.2
	O-up	3.909	3.119	3.2
	side	1.839	2.115	3.2
T	O-down	0.540	0.747	3.4
	O-up	3.613	2.840	3.3
	side	1.474	1.547	3.3
B	O-down	0.633	0.948	3.3
	O-up	3.767	3.018	3.3
	side	1.620	1.613	3.3
other work		3.55[a], 3.35[b]		3.20[a],3.30[b]
experimental		3.71[c]		-

[a] site C O-up DFT/CC [173]
[b] site C O-up CCSD(T) [211]
[c] [176]

B97-D functional and the CCSD(T) results for the coronene-water system since circumcoronene is not feasible for calculation at the CCSD(T) level [147]. The equilibrium distance at DFT level was obtained by a scan over the distance and this equilibrium geometry was then used for calculation of the CCSD(T) interaction energy. Comparing DFT to CCSD(T), we see that DFT overestimates the most stable orientation (O-up) by about 0.7 kcal mol^{-1}, but underestimates the least stable orientation (O-down) by about 0.3 kcal mol^{-1}. Furthermore, the intermediate orientation (side) is especially well described, particularly for the T and B sites. More importantly, DFT is clearly capable of separating the different adsorption positions and attacking geometries and gives the correct order of stabilities.

Using these results, we can also draw some conclusions on adsorption preferences of water on graphene. It seems that the C site is slightly favored across all attacking geometries, followed by the B site and then the T site as the least stable adsorption site, although differences are not larger than 0.3 kcal mol^{-1}. There is, however, a clear dependence on the orientation of the water molecule. The O-up configuration is strongly favored across all adsorption sites reaching an interaction energy close to 4 kcal mol^{-1}. The side orientation follows with an interaction just below half the interaction energy of the O-up geometry, while by far the least stable attacking orientation is the O-down having interaction energies below 1 kcal mol^{-1}. The equilibrium distance is influenced very little by the adsorption site or the attacking orientation, which can be understood by keeping in mind that within the water molecule, the size of the hydrogen atoms is small compared to the size of the oxygen atom and thus has little influence on the equilibrium distance of different orientations. In a sense, these very similar equibrium distances are a justification for the use of a single interaction centre for dispersion interactions on the oxygen atom, thus treating the water molecule as a sphere.

The most stable geometry was thus found to be the O-up geometry, which is confirmed by both Rubes et al. [173] and Kysilka et al. [211] who found this geometry as the global minimum on the potential energy surface. They have reported interaction energies of 3.55 kcal mol^{-1} and 3.35 kcal mol^{-1}, respectively, which falls in the middle between our DFT and CCSD(T) results of 3.909 kcal mol^{-1} and 3.119 kcal mol^{-1}, respectively. The comparison with the experimental value of 3.71 kcal mol^{-1} is also very good, considering that the experimental value always has some influence from less stable geometries. Rubes et al. and Kysilka et al. have also reported equilibrium distances of 3.20 Å and 3.30 Å, respectively, in excellent agreement with our results [173, 211].

The benchmarking of the B97-D potential for use on the water dimer was done by considering 10 stationary points on the potential energy surface of the water dimer as proposed by Tschumper et al. [212] (see figure 3.11). The DFT calculations were

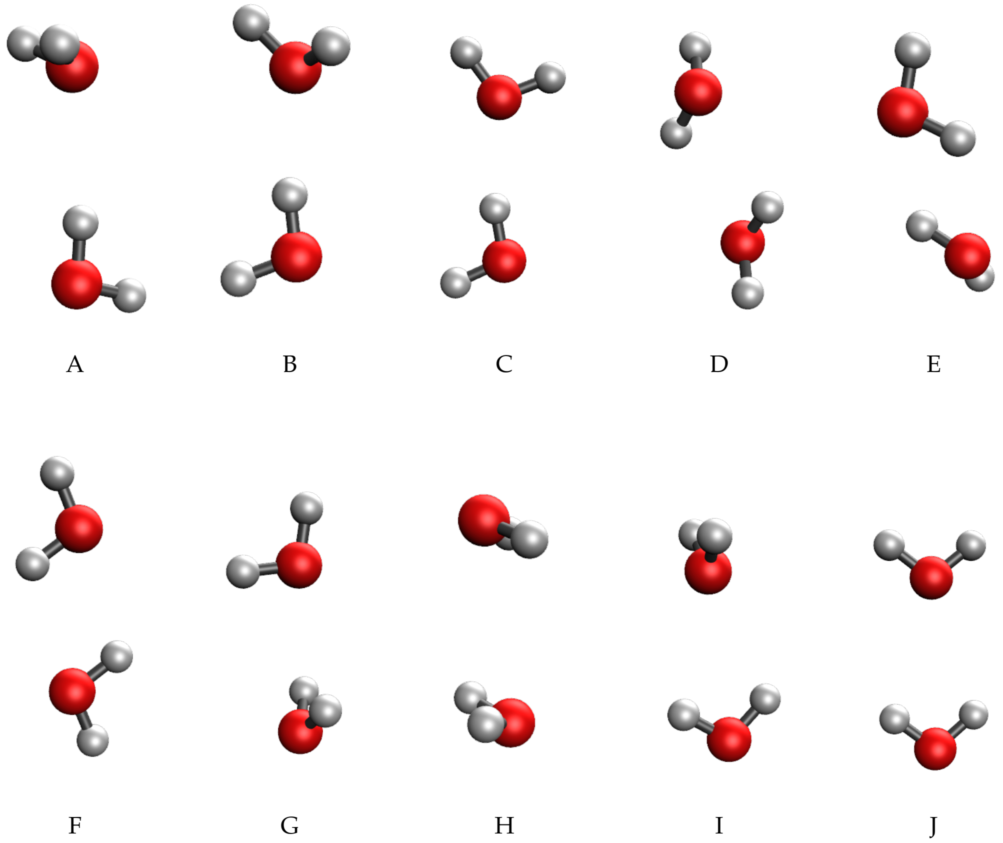

FIGURE 3.11: 10 stationary points on the water potential energy surface used for the benchmarking of the DFT level against CCSD(T) [212]

compared with the CCSD(T) interaction energies provided on those dimers in the same paper by Tschumper et al. as shown in table 3.17. In all cases, we started from the equilibrium geometry provided in the paper and then did a scan over the distance at both the DFT and CCSD(T) level to find the respective equilibrium distances and energies. In general, the DFT calculations underestimate the CCSD(T) interaction energies by about 0.5 kcal mol^{-1} for the more stable dimers. For the less stable dimers, our calculations overestimate the interaction energy by a small 0.1 kcal mol^{-1}. The equilibrium distances are generally overestimated by about 0.1 Å . The basis set used previously for the circumcoronene-water system is of double zeta type and, although augmented with suitable midbond functions, one may argue that this is too small a basis set. We have, therefore, recalculated the interaction energies of three selected water dimers at this double zeta basis set to compare with the triple zeta basis set that was used throughout for the water dimers. The results for water dimers A, H and J are 4.840 kcal mol^{-1}, 1.453 kcal mol^{-1} and 2.319 kcal mol^{-1}, respectively for the interaction energy, comparing very well with the triple zeta results of 5.043 kcal mol^{-1}, 1.453 kcal mol^{-1} and 2.321 kcal mol^{-1}, respectively. For the equilibrium distance, the double zeta basis set predicts the exact same values as the triple zeta basis set.

TABLE 3.17: The interaction energies and equilibrium distances for ten selected geometries of the water dimer at B97-D DFT level and CCSD(T) level.

	D_e (kcal mol^{-1})		R_e (Å)	
orientation	DFT	CCSD(T)	DFT	CCSD(T)
A non-planar open C_s	4.452	5.043	2.91	2.91
B open C_1	3.841	4.524	3.03	2.92
C planar open C_s	3.728	4.474	3.03	2.93
D cyclic C_1	4.049	4.340	2.92	2.82
E cyclic C_2	3.668	4.088	2.89	2.79
F cyclic C_{2h}	3.481	4.045	2.96	2.76
G triply hydrogen conded C_s	3.065	3.221	3.04	2.94
H doubly bifurcated C_{2h}	1.555	1.457	3.29	3.29
I non-planar bifurcated C_{2v}	3.138	3.248	3.11	3.01
J planar bifurcated C_{2v}	2.312	2.321	3.18	3.18

3.4.2 Force Field for H_2O

Following our protocol, we have calculated the B97-D interaction energies for 99 randomly generated water dimers at distances between 2 Å and 20 Å, at 51 distances leading to a total of 5049 calculations. For the circumcoronene-water system, we generated 10 different geometries and calculated the interaction energies between 2.5 Å and 20 Å at 35 distances for a total of 350 calculations. In all cases, we sampled more distances around the equilibrium region. Figure 3.12 shows the calculated DFT

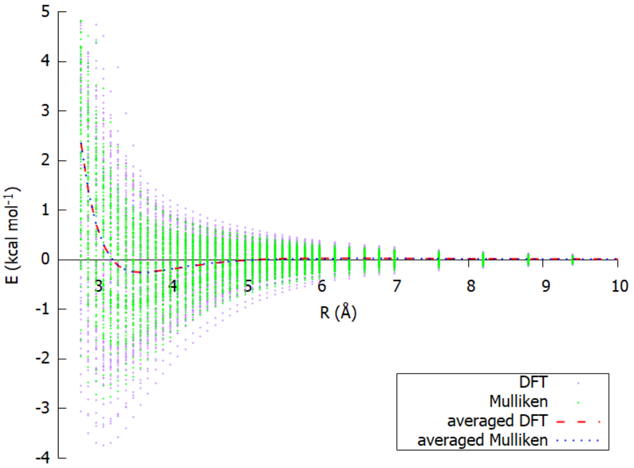

FIGURE 3.12: Interaction energies for 99 randomly generated water dimers calculated at DFT level and recalculated with a fitted potential. The average per considered distance is also given for both types of interaction energies.

energies of the water dimers together with the mean energy per intermolecular distance and the recalculated energies using one of the fitted potentials explained later on. A first important observation is the spread of the interaction energies which is very large for a given distance with some geometries never even becoming attractive, behavior that is hard to catch in a simple model.

As in the other cases studied, we have tried a united-atom model and an atomistic model using different charge schemes to fit to the interaction energies. More specifically, we have tried following three-site charge schemes: SPC [196], TIP3P [198], SPC/E [198], charges obtained from Mulliken and NPA population analysis and lastly, the charge scheme introduced by Albertí et al. [101]. Furhtermore, we have also optimized the charges ourselves by introducing the negative charge on oxygen as a parameter in the fitting. For the four-site charge schemes, we have used the partial charges from the TIP4P [198], TIP4P-Ew [203] and the TIP4P/2005 [204] models.

Firstly, we discuss the parameters for the united-atom three-site models for wich the interaction parameters are given in table 3.18. We can see that increase of the charges leads to the increase of ϵ and the decrease of r_0 and β. Furthermore, it is seen that the values for β are substantially lower than the ones for the united-atom methane and nitrogen molecules as a compensation for the influence of the important electrostatic interactions in water, as was indicated by Faginas Lago et al. [202]. Optimization of the charge suggests an ideal value of -0.753e on the oxygen atom, representing a situation in between the values predicted by Albertí and the SPC model. Mayo et al. [213] have given an experimental partial charge on the hydrogen atom of 0.33, which coincides quite well with our optimized hydrogen charge of 0.377. For the atomistic model (see below), the optimized value is slightly closer with a partial charge of 0.366 on the hydrogen atom. From this experimental value, the

TABLE 3.18: Interaction parameters for the H_2O dimer using the three-site charge model for the united-atom and atomistic approaches. Charges are indicated in the table between brackets in e. The values indicated as 0.000 are not exactly 0.

	parameters	no charges	Mulliken (-0.610)	Albertí (-0.658)	SPC (-0.820)	TIP3P (-0.834)	SPC/E (-0.848)	NPA (-0.904)	opt. (-0.753)
united-atom									
OO	ϵ (kcal mol^{-1})	0.231	0.451	0.488	0.632	0.646	0.659	0.718	0.568
	r_0 (Å)	3.622	3.545	3.538	3.516	3.514	3.512	3.506	3.524
	β	8.687	6.605	6.317	5.319	5.230	5.145	4.791	5.740
atomistic free									(-0.731)
OO	ϵ (kcal mol^{-1})	0.179	0.393	0.357	0.363	0.366	0.368	0.385	0.356
	r_0 (Å)	3.612	3.568	3.626	3.727	3.733	3.739	3.744	3.673
	β	8.546	6.135	5.790	4.688	4.592	4.495	4.134	5.295
OH	ϵ (kcal mol^{-1})	0.000	0.000	0.069	0.211	0.224	0.238	0.263	0.129
	r_0 (Å)	2.800	2.638	2.501	2.502	2.502	2.504	2.546	2.501
	β	6.970	6.028	4.016	4.016	4.017	4.018	4.020	4.013
HH	ϵ (kcal mol^{-1})	0.045	0.064	0.066	0.094	0.086	0.079	0.046	0.082
	r_0 (Å)	2.684	2.363	2.302	2.002	2.002	2.001	2.001	2.16
	β	4.001	4.002	4.003	4.006	4.007	4.007	4.013	4.004
atomistic restricted									(-0.731)
OO	ϵ (kcal mol^{-1})	0.251	0.444	0.475	0.455	0.458	0.460	0.473	0.459
	r_0 (Å)	3.559	3.528	3.522	3.552	3.550	3.548	3.540	3.541
	β	8.239	6.200	6.082	6.013	6.012	6.011	6.008	6.025
OH	ϵ (kcal mol^{-1})	0.000	0.000	0.000	0.129	0.139	0.150	0.192	0.060
	r_0 (Å)	6.000	2.646	2.601	2.501	2.501	2.501	2.505	2.501
	β	8.999	7.168	7.063	6.015	6.014	6.014	6.013	6.022
HH	ϵ (kcal mol^{-1})	0.001	0.008	0.010	0.036	0.033	0.030	0.016	0.018
	r_0 (Å)	3.804	2.750	2.601	2.005	2.004	2.003	2.003	2.321
	β	6.001	6.004	6.005	6.011	6.012	6.001	6.03	6.007

Albertí charge scheme is suggested to behave the best with a positive partial charge of 0.329, but we will see in the upcoming discussion that the good performance is rather unexpected.

Further in table 3.18, we report the parameters for an atomistic approach for the three-site model given as "atomistic free". With rising charges, ϵ and r_0 increase steadily for the O-O interaction, while the β parameter lowers. The O-H interaction parameters behave very different on the other hand: the ϵ is very low, even close to 0, for models with small charges, reaching meaningful values only for the models with larger charges. It seems the charges of Mulliken and Albertí are inadequate to reproduce the electrostatic interaction between the oxygen and hydrogen atoms, let alone the hydrogen bonds that are formed in some orientations of the water molecules, causing problems with the fitting of the potential. Only when the charge scheme has a value of -0.731e for the oxygen, which coincides with the charge scheme optimized to *ab initio* data, the ϵ for O-H reaches higher values more in line with other models suggested in the literature [205]. For larger charges as in the SPC, TIP3P and NPA charge schemes, the ϵ results are very similar to each other as are the β values for all schemes but Mulliken's. The intermolecular distance, r_0, has a different behavior, whereby the smallest values are obtained for oxygen charges around -0.7e, reaching a value of about 2.5 Å. Finally, the H-H ϵ rises at first with increasing charge, but lowers after reaching a maximum at a negative charge between -0.731e and -0.820e on the oxygen atom. For the lowest charges, this gives a situation where the H-H interaction has a stronger impact than the O-H interaction contradicting chemical intuition which would expect atoms with larger polarizabilities to have a stronger attraction. As for the O-H interaction, the values only behave as expected when the negative charge on oxygen reaches a value aroun -0.7e. It is thus even more clear that the smaller charge schemes are not capable of capturing the correct interactions thus disrupting the remainder of the potential. While the ϵ reaches a maximum in this intermediate charge range, the r_0 stabilizes above -0.731e. The β values for the H-H interaction, once again, change only slightly for most of the charge schemes.

In a similar fashion to the methane molecule, we have calculated a second set of atomistic models where we tried to retain the physical meaning of the β parameter. As said previously, the original authors advise to keep the β between 7 and 9, but have later suggested to lower this when strong electrostatic interactions are involved [70, 202]. More specifically, for the water molecule, they have advised a value as low as 6.6 and we have, therefore, refitted the atomistic parameters restricting the β values for the three interaction types between 6 and 9. These parameters are given in the third part of table 3.18 for the three-site models and are labeled "atomistic restricted". It is seen that upon restriction of the βs, the interaction is more strongly reproduced by the O-O interaction which is higher than for the free atomistic potentials, while the equilibrium distances become shorter. For the O-H interaction, the same trend is maintained as for the free parameters whereby for a smaller negative charge, the interaction is very close to zero. Going to larger charges, the O-H interaction slowly gains importance, although never reaching the same height as in the free parameters. The same goes for the ϵ of the H-H interaction, the trend from the free parameters is maintained albeit at smaller values.

Table 3.19 gives the parameters for the united-atom approach using the four-site charge schemes. These schemes not only differ in the size of the charges, but also on the exact position of the negative charge along the bisector of H-O-H angle. It is thus hard to draw direct conclusions about the systematic influence of the size of the charges on the ILJ parameters. Nevertheless, it is clear that the parameters are quite similar for the different charge schemes considered, while also being in the range of the optimized three-sites united-atom model discussed previously. Particularly very close are the parameters obtained for the TIP4P/2005 model, which is one of the most popularly used models in the recent literature, for which the ϵ is almost identical, r defers by only 0.02 Å and the β by only 0.2.

Table 3.19: Interaction parameters for the H_2O dimer using the four-site charge model for the united-atom and atomistic approaches. Charges are indicated in the table between brackets in e, together with the distance between the charge and the oxygen atom in Å .

	parameters	no charges	TIP4P (-1.040, 0.15)	TIP4P/Ew (-1.048, 0.125)	TIP4P/2005 (-1.113, 0.1546)
united-atom					
OO	ϵ (kcal mol^{-1})	0.231	0.533	0.589	0.567
	r_0 (Å)	3.622	3.549	3.538	3.547
	β	8.687	5.810	5.457	5.552
atomistic free					
OO	ϵ (kcal mol^{-1})	0.179	0.212	0.212	0.228
	r_0 (Å)	3.612	3.829	3.830	3.813
	β	8.546	5.160	5.109	4.674
OH	ϵ (kcal mol^{-1})	0.000	0.210	0.212	0.215
	r_0 (Å)	2.800	2.728	2.733	2.776
	β	6.970	4.033	4.035	4.059
HH	ϵ (kcal mol^{-1})	0.045	0.024	0.019	0.000
	r_0 (Å)	2.684	2.007	2.007	2.380
	β	4.001	4.045	4.056	6.539
atomistic restricted					
OO	ϵ (kcal mol^{-1})	0.251	0.313	0.316	0.343
	r_0 (Å)	3.559	3.624	3.618	3.556
	β	8.239	6.019	6.018	6.016
OH	ϵ (kcal mol^{-1})	0.000	0.134	0.134	0.112
	r_0 (Å)	6.000	2.697	2.706	2.854
	β	8.999	6.015	6.014	6.012
HH	ϵ (kcal mol^{-1})	0.001	0.008	0.006	0.000
	r_0 (Å)	3.804	2.019	2.020	5.991
	β	6.001	6.100	6.140	6.647

The parameters for the atomistic approach using the four-site charge model are given in table 3.19 as "atomistic free". It is visible that the parameters do not change a lot between the different charge schemes: it seems that the change of the charge size together with the moving of the negative charge, conserves the size of the electrostatic part of the energy. Indeed, the parameters for the TIP4P and the TIP4P/Ew are near identical. Although the quantitative differences are small, there is a qualitative difference between these two models and the TIP4P/2005 charge scheme where the ϵ for the O-O interaction is slightly higer than in the other models, while the β is slightly lower. This is compensated by a very small ϵ and a higher β for the H-H interaction. For all free four-site charge schemes, the parameters, once again, contradict chemical intuition by indicating that the O-H interaction has a dispersive interaction that is almost as important as the O-O interaction with almost equal ϵ values for all three charge schemes. The r_0 values on the other hand differ by about 1 Å.

Finally, in the third part of table 3.19, the parameters for the restricted atomistic four-site models are found. At first sight, the ordering of the ϵs for the O-O, O-H and H-H seems to make more sense, with the strongest interaction for O-O, a lower one for O-H and a very small one for H-H. Compared to the free parameters, the O-O ϵ is about 50% larger, while the O-H ϵ is about 50 % lower, the H-H ϵ drops significantly for the TIP4P and the TIP4P/Ew charge schemes. Also the r_0 change slightly, but only to a less extent: the O-O r_0 becomes slightly smaller as well as the O-H r_0. However, the qualitative trends are very similar as for the free parameters in the sense that the TIP4P and the TIP4P/Ew have very similar parameters. The TIP4P/2005 has, again, slightly different parameters with the O-O ϵ slightly higher, the O-H ϵ slightly lower and the H-H ϵ very close to 0. Most notable is the very high r_0 value for the H-H interaction, but given the very low contribution in energy, this is probably due to a very low fitting surface.

3.4.3 Benchmark of Obtained Force Fields

In the previous systems, where the dispersion interactions are the major source of the intermolecular attraction, we have sufficed to benchmark the obtained force fields via comparison of dimer energies to DFT and CCSD(T). Water, however, is a molecule with complex behavior exhibiting hydrogen bonds leading to cluster formation at different thermodynamic conditions. For this reason, we will not content ourselves with benchmarking our potentials against dimer interaction energies, but include a set of hexamer energies in the comparison as well.

3.4.3.1 Water Dimers

The proposed force fields were tested by calculating the interaction energies of 10 stationary points on the H_2O-H_2O potential energy surface as used in section 3.4.1. In this benchmark, all the previously discussed force fields have been included: the three-site united-atom, free atomistic and restricted atomistic models as well as the four-site united-atom, free atomistic and restricted atomistic models.

For the united-atom models with three sites, a comparison between their performance for the dimer interaction energies on one hand and the CCSD(T) and DFT energies on the other is shown in table 3.20. First of all, we have excluded the united-atom model without charges from this and following tables since it is totally uncapable to produce reasonable results; not only does it not differentiate the different orientations, but the average energy over all dimers (0.230 kcal mol^{-1}) is an order of magnitude lower than the average interaction energy predicted by DFT, while the equilibrium distance (3.62 Å) is off by about 0.5 Å. It is clear that the interaction between the water dimer is dominated by electrostatic interactions, which can not be replaced by a simple ILJ potential in an average fashion. As expected, a united-atom model without charges is unsuitable for representing the water molecule.

TABLE 3.20: Interaction energies (D_e) in kcal mol^{-1} and intermolecular equilibrium distances (R_e) in Å, of the representative configurations of the water dimer (see figure 3.11) as determined from the united-atom models with three charges given in table 3.18

		CCSD(T)	DFT	Mulliken (-0.610)	Albertí (-0.658)	SPC (-0.820)	TIP3P (-0.834)	SPC/E (-0.848)	NPA (-0.904)	opt. (-0.753)
A	D_e	5.043	4.452	2.747	3.262	5.588	5.844	6.113	7.293	4.503
	R_e	2.91	2.91	3.09	3.04	2.86	2.84	2.82	2.75	2.939
B	D_e	4.524	3.841	2.425	2.872	4.883	5.104	5.335	6.346	3.948
	R_e	2.92	3.03	3.11	3.06	2.89	2.875	2.85	2.78	2.96
C	D_e	4.474	3.728	2.707	3.211	5.479	5.728	5.989	7.128	4.424
	R_e	2.93	3.03	3.10	3.05	2.87	2.85	2.84	2.76	2.95
D	D_e	4.340	4.049	2.145	2.522	4.168	4.344	4.526	5.310	3.412
	R_e	2.82	2.92	3.16	3.12	2.97	2.962	2.94	2.88	3.03
E	D_e	4.088	3.668	1.875	2.195	3.584	3.731	3.882	4.537	2.948
	R_e	2.79	2.89	3.19	3.15	3.01	3.00	2.98	2.93	3.074
F	D_e	4.045	3.841	2.047	2.398	3.912	4.071	4.236	4.940	3.221
	R_e	2.76	2.96	3.19	3.15	3.01	3.00	2.98	2.93	3.07
G	D_e	3.221	3.065	2.238	2.612	4.189	4.351	4.518	5.224	3.476
	R_e	2.94	3.04	3.21	3.17	3.05	3.04	3.02	2.98	3.10
H	D_e	1.457	1.555	1.343	1.545	2.382	2.467	2.553	2.918	2.006
	R_e	3.29	3.29	3.31	3.28	3.18	3.184	3.17	3.134	3.22
I	D_e	3.248	3.138	2.537	2.967	4.774	4.959	5.150	5.957	3.958
	R_e	3.01	3.11	3.19	3.15	3.03	3.02	3.01	2.96	3.08
J	D_e	2.321	2.312	2.384	2.780	4.428	4.596	4.768	5.495	3.686
	R_e	3.18	3.18	3.21	3.18	3.07	3.05	3.04	3.00	3.11
av	D_e	3.676	3.365	2.245	2.636	4.339	4.520	4.707	5.515	3.558
	R_e	2.96	3.04	3.18	3.14	2.99	2.98	2.97	2.91	3.05

Upon introducing charges, the potentials become able to distinguish the different conformations in the same way as was the case with DFT: the extremes are separated, while issues arise with the correct ordering of the intermediate dimers. From a quantitative point of view, the different charge schemes show varying levels of success. More specifically, the models with a lower negative charge between -0.61e and -0.66e (Albertí and Mulliken) underestimate the interaction energies, 2.245 kcal mol^{-1} and 2.636 kcal mol^{-1}, respectively compared to the CCSD(T) and DFT interaction energies of 3.676 kcal mol^{-1} and 3.365 kcal mol^{-1}, respectively. Charge schemes with larger negative charges (SPC, TIP3P, SPC/E and NPA) between -0.820e and -0.904e overestimate the interaction energies with values of up to 2 kcal mol^{-1} for certain geometries, while the average interaction energy is increasingly overestimated with increasing charges, from 1.1 kcal mol^{-1} for the SPC charge scheme, to 2.3 kcal mol^{-1} for the NPA charges. The optimized charge scheme, with an intermediate negative charge of -0.75e, slightly underestimates the most stable conformations, while overestimating the least stable conformations. The average interaction energy, however, is good lying in between the DFT and CCSD(T) average interaction energy. The same conclusion can be drawn for the intermolecular distance.

In table 3.21, the same comparison is made for the free atomistic three-site models. Even though the no charge model now shows some signs of directionality, the energy values are still an order of magnitude too low and the energy sequence is not correctly reproduced. Even for an atomistic model, charges are clearly needed to describe the strong, directional interactions in the water dimer. Given that the dispersion interaction is clearly of minor importance in the water dimer, it is no surprise that the free atomistic three-site model performs quite similar to the united-atom model. However, it does seem like the performance is slightly better for the atomistic model by about 0.2 kcal mol^{-1} for the average dimer interaction energy. As such, the optimized charge scheme still performs the best, with an average interaction energy and intermolecular distance very close to the DFT results. This is an interesting results, since the atomistic model does not imply an extra computational

TABLE 3.21: Interaction energies (D_e) in kcal mol^{-1} and intermolecular equilibrium distances (R_e) in Å, of the representative configurations of the water dimer (see figure 3.11) as determined from the free atomistic models with three charges given in table 3.18

		CCSD(T)	DFT	Mulliken (-0.610)	Albertí (-0.658)	SPC (-0.820)	TIP3P (-0.834)	SPC/E (-0.848)	NPA (-0.904)	opt. (-0.753)
A	D_e	5.043	4.452	2.863	3.191	5.03	5.212	5.394	6.112	4.000
	R_e	2.91	2.91	3.03	3.06	3.00	3.00	2.99	2.98	3.02
B	D_e	4.524	3.841	2.511	2.792	4.392	4.549	4.709	5.34	3.492
	R_e	2.92	3.03	3.055	3.09	3.02	3.02	3.02	3.00	3.04
C	D_e	4.474	3.728	2.795	3.115	4.923	5.101	5.282	6.00	3.905
	R_e	2.93	3.03	3.04	3.07	3.00	3.00	3.00	2.98	3.03
D	D_e	4.340	4.049	2.207	2.564	4.342	4.521	4.712	5.49	3.316
	R_e	2.82	2.92	3.122	3.10	2.94	2.93	2.91	2.87	3.02
E	D_e	4.088	3.668	1.921	2.219	3.720	3.873	4.037	4.705	2.853
	R_e	2.79	2.89	3.15	3.13	2.97	2.96	2.954	2.90	3.05
F	D_e	4.045	3.841	2.089	2.413	4.036	4.203	4.381	5.115	3.097
	R_e	2.76	2.96	3.15	3.13	2.97	2.95	2.94	2.89	3.04
G	D_e	3.221	3.065	2.279	2.638	4.357	4.536	4.273	5.518	3.360
	R_e	2.94	3.04	3.16	3.14	2.98	2.97	2.96	2.91	3.06
H	D_e	1.457	1.555	1.399	1.599	2.552	2.651	2.760	3.218	2.001
	R_e	3.29	3.29	3.26	3.24	3.09	3.08	3.06	3.01	3.16
I	D_e	3.248	3.138	2.561	2.966	4.875	5.072	5.280	6.138	3.770
	R_e	3.01	3.11	3.15	3.13	2.99	2.98	2.97	2.92	3.06
J	D_e	2.321	2.312	2.401	2.775	4.512	4.690	4.878	5.652	3.509
	R_e	3.18	3.18	3.17	3.16	3.03	3.02	3.00	2.97	3.09
av	D_e	3.676	3.376	2.303	2.627	4.274	4.441	4.571	5.329	3.330
	R_e	2.96	3.03	3.13	3.13	3.00	2.99	2.98	2.94	3.06

cost for this specific case as the interatomic distances are needed anyway to calculate the electrostatic interactions.

The three-site restricted atomistic potentials are given in table 3.22, where we can see that the optimized charge schemes almost perfectly predicts the average interaction energy and intermolecular distance deviating only 0.003 kcal mol^{-1} and 0.01 Å, respectively. Looking at the different dimers, though, the energy range is still diminished compared to the DFT and the CCSD(T) results: the more stable geometries are underestimated, while the least stable geometries are overestimated. Looking at the different charge schemes, the restricted parameters predict slightly higher interaction energies than the free parameters, especially for charge schemes with large charges (SPC, TIP3P, SPC/E and NPA) with the exception of the H dimer where the restricted parameters predict slightly lower interaction energies. However, the results are quite similar and the lower charges still underestimate the interaction energies, while the larger charge schemes overestimate them. The equilibrium distances,

TABLE 3.22: Interaction energies (D_e) in kcal mol^{-1} and intermolecular equilibrium distances (R_e) in Å, of the representative configurations of the water dimer (see figure 3.11) as determined from the restricted atomistic models with three charges given in table 3.18

		CCSD(T)	DFT	Mulliken (-0.610)	Albertí (-0.658)	SPC (-0.820)	TIP3P (-0.834)	SPC/E (-0.848)	NPA (-0.904)	opt. (-0.753)
A	D_e	5.043	4.452	2.852	3.379	5.140	5.324	5.510	6.276	4.109
	R_e	2.91	2.91	3.04	3.00	3.01	3.01	3.01	3.01	3.01
B	D_e	4.524	3.841	2.518	2.974	4.522	4.684	4.850	5.528	3.615
	R_e	2.92	3.03	3.065	3.02	3.03	3.03	3.02	3.02	3.03
C	D_e	4.474	3.728	2.809	3.322	5.060	5.243	5.428	6.189	4.041
	R_e	2.93	3.03	3.05	3.00	3.01	3.01	3.01	3.01	3.01
D	D_e	4.340	4.049	2.199	2.586	4.360	4.544	4.736	5.530	3.317
	R_e	2.82	2.92	3.13	3.09	2.962	2.95	2.94	2.91	3.02
E	D_e	4.088	3.668	1.924	2.251	3.759	3.917	4.083	4.772	2.869
	R_e	2.79	2.89	3.16	3.12	2.99	2.98	2.97	2.93	3.05
F	D_e	4.045	3.841	2.100	2.457	4.082	4.253	4.432	5.177	3.123
	R_e	2.76	2.96	3.15	3.11	2.98	2.97	2.96	2.93	3.05
G	D_e	3.221	3.065	2.296	2.671	4.380	4.560	4.748	5.535	3.372
	R_e	2.94	3.04	3.17	3.13	3.01	3.00	2.98	2.95	3.07
H	D_e	1.457	1.555	1.384	1.584	2.535	2.637	2.744	3.196	1.972
	R_e	3.29	3.29	3.27	3.25	3.11	3.10	3.09	3.05	3.18
I	D_e	3.248	3.138	2.599	3.028	4.937	5.136	5.344	6.209	3.815
	R_e	3.01	3.11	3.15	3.12	3.00	2.99	2.98	2.95	3.06
J	D_e	2.321	2.312	2.437	2.832	4.577	4.759	4.949	5.738	3.552
	R_e	3.18	3.18	3.18	3.14	3.03	3.02	3.02	2.98	3.09
av	D_e	3.676	3.376	2.312	2.708	4.335	4.506	4.682	5.415	3.379
	R_e	2.96	3.03	3.137	3.10	3.013	3.01	3.00	2.97	3.06

on the other hand, are very similar to the ones predicted by the free parameters.

Similar benchmarks were done for the four-site charge schemes, starting with the united-atom model in table 3.23. It is immediately clear that all charge schemes overestimate the interaction energies for the different dimers and, consequently, also the average interaction energy. The TIP4P charge scheme performs best, overestimating the DFT interaction energy by 0.8 kcal mol^{-1}, while the TIP4P/Ew and TIP4P/2005 charge schemes overestimate the DFT interaction energy by almost 1.5 kcal mol^{-1}. As such, the performance of the four-site charge scheme is in the same range as the three-site SPC, TIP3P and SPC/E charge schemes. Despite the rather poor representation of the interaction energy, the equilibrium distance is very well described, especially the average value is between the CCSD(T) and DFT reference values for all four-site charge schemes.

Just as for the three-site charge scheme, the performance of the atomistic model is slightly better than the united-atom one for the four-site charge model (see table

TABLE 3.23: Interaction energies (D_e) in kcal mol^{-1} and intermolecular equilibrium distances (R_e) in Å, of the representative configurations of the water dimer (see figure 3.11) as determined from the united-atom models with four charges given in table 3.19

		CCSD(T)	DFT	TIP4P (-1.040)	TIP4P/Ew (-1.048)	TIP4P/2005 (-1.113)
A	D_e	5.043	4.452	5.688	6.496	6.693
	R_e	2.91	2.91	2.85	2.80	2.78
B	D_e	4.524	3.841	5.013	5.697	5.872
	R_e	2.92	3.03	2.89	2.84	2.82
C	D_e	4.474	3.728	5.280	6.055	6.160
	R_e	2.93	3.03	2.89	2.84	2.83
D	D_e	4.340	4.049	4.241	4.791	4.923
	R_e	2.82	2.92	2.95	2.91	2.90
E	D_e	4.088	3.668	3.136	3.514	3.610
	R_e	2.79	2.89	3.04	3.01	3.00
F	D_e	4.045	3.841	3.863	4.361	4.448
	R_e	2.76	2.96	3.01	2.97	2.96
G	D_e	3.221	3.065	3.644	4.199	4.125
	R_e	2.94	3.04	3.09	3.05	3.06
H	D_e	1.457	1.343	2.104	2.421	2.345
	R_e	3.29	3.31	3.25	3.21	3.234
I	D_e	3.248	2.537	4.014	4.655	4.535
	R_e	3.01	3.19	3.09	3.05	3.06
J	D_e	2.321	2.384	3.527	4.127	3.955
	R_e	3.18	3.21	3.15	3.11	3.13
av	D_e	3.676	3.291	4.051	4.632	4.667
	R_e	2.96	3.05	3.02	2.98	2.98

3.24). Again the average interaction energies are bettered by about 0.2 kcal mol^{-1}, making the performance just acceptable. However, the question rises whether the slight improvement justifies the extra computational cost that is in this case present as extra interatomic distances need to be calculated. Furthermore, the optimized three-sites model performs better and is cheaper as it needs less distances to be calculated. As for most models, the equilibrium distance is very well predicted on average, deviating only slightly from the DFT value.

Finally the restricted atomistic four-site charge scheme dimer interaction energies are given in 3.25. The more realistic parameters do not lead to better predictions and, indeed, the performance is even slightly worse than the free atomistic parameters, but still slightly better than the united-atom model. Although, some of the dimers seem to be predicted very good (e.g. dimers C and F for the TIP4P model), the fact that some other results are completely off (e.g. dimers I and J for the same model), suggests that this results is merely by coincidence. As was the case for the

TABLE 3.24: Interaction energies (D_e) in kcal mol^{-1} and intermolecular equilibrium distances (R_e) in Å, of the representative configurations of the water dimer (see figure 3.11) as determined from the free atomistic models with four charges given in table 3.19

		CCSD(T)	no charges	TIP4P (-1.040)	TIP4P/Ew (-1.048)	TIP4P/2005 (-1.113)
A	D_e	5.043	4.452	4.571	5.083	5.149
	R_e	2.91	2.91	3.09	3.06	3.08
B	D_e	4.524	3.841	4.054	4.486	4.569
	R_e	2.92	3.0.	3.11	3.09	3.10
C	D_e	4.474	3.728	4.311	4.821	4.854
	R_e	2.93	3.03	3.11	3.08	3.10
D	D_e	4.340	4.049	4.307	4.779	4.964
	R_e	2.82	2.92	2.95	2.92	2.91
E	D_e	4.088	3.668	3.215	3.530	3.697
	R_e	2.79	2.89	3.03	3.00	2.99
F	D_e	4.045	3.841	3.966	4.409	4.580
	R_e	2.76	2.96	2.98	2.95	2.94
G	D_e	3.221	3.065	3.866	4.319	4.420
	R_e	2.94	3.04	3.03	2.99	2.99
H	D_e	1.457	1.343	2.372	2.673	2.693
	R_e	3.29	3.31	3.13	3.09	3.10
I	D_e	3.248	2.537	4.121	4.715	4.681
	R_e	3.01	3.19	3.06	3.02	3.03
J	D_e	2.321	2.384	3.617	4.170	4.079
	R_e	3.18	3.21	3.13	3.08	3.10
av	D_e	3.676	3.291	3.840	4.299	4.369
	R_e	2.96	3.05	3.06	3.03	3.03

three-site charge scheme, the restricted parameters predicts slightly higher interaction energies for all dimers except for the H dimer. These differences are especially clear for the TIP4P and TIP4P/Ew charge schemes in dimer A, B and C, while for the TIP4P/2005 charge scheme, with larger charges, the most important differences between the restricted and the free parameters appear in the intermedia energy range for dimer D, E, F, G and I with differences around 0.5 kcal mol^{-1}.

For a better overview, we have compared the best performing potentials for each model type (united-atom - three sites, united-atom - four sites, restricted atomistic - three sites and restricted atomistic - four sites) with the DFT and CCSD(T) interaction energies in figure 3.13. It is now visually clear that the optimized three-site charge scheme outperforms the other schemes. It is the only one that consistently stays close to the dimer interaction energies although it does still overestimate the least stable geometries, while it underestimates some of the intermediate stability geometries. The other charge schemes seem to be capable of just representing one

TABLE 3.25: Interaction energies (D_e) in kcal mol^{-1} and intermolecular equilibrium distances (R_e) in Å, of the representative configurations of the water dimer (see figure 3.11) as determined from the restricted atomistic models with four charges given in table 3.19

		CCSD(T)	no charges	TIP4P (-1.040)	TIP4P/Ew (-1.048)	TIP4P/2005 (-1.113)
A	D_e	5.043	4.452	4.717	5.227	5.281
	R_e	2.91	3.60	2.91	3.07	3.07
B	D_e	4.524	3.841	4.213	4.647	4.714
	R_e	2.92	3.03	3.11	3.09	3.08
C	D_e	4.474	3.728	4.478	4.989	5.012
	R_e	2.93	3.03	3.11	3.08	3.08
D	D_e	4.340	4.049	4.393	4.868	5.546
	R_e	2.82	2.92	2.95	2.932	2.80
E	D_e	4.088	3.668	3.297	3.620	4.153
	R_e	2.79	2.89	3.02	2.99	2.86
F	D_e	4.045	3.841	4.051	4.498	5.177
	R_e	2.76	2.96	2.98	2.95	2.80
G	D_e	3.221	3.065	3.887	4.416	4.847
	R_e	2.94	3.04	3.03	3.00	2.85
H	D_e	1.457	1.343	2.312	2.615	2.869
	R_e	3.29	3.31	3.14	3.10	2.96
I	D_e	3.248	2.537	4.186	4.787	5.04
	R_e	3.01	3.19	3.05	3.02	2.91
J	D_e	2.321	2.384	3.671	4.234	4.329
	R_e	3.18	3.21	3.11	3.07	2.99
av	D_e	3.676	3.291	3.921	4.390	4.697
	R_e	2.96	3.05	3.06	3.03	2.94

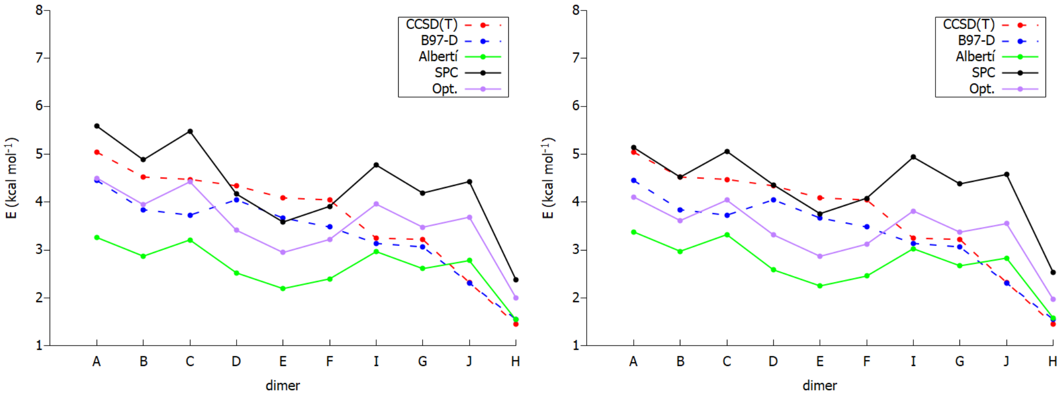

united-atom three-sites

atomistic three-sites

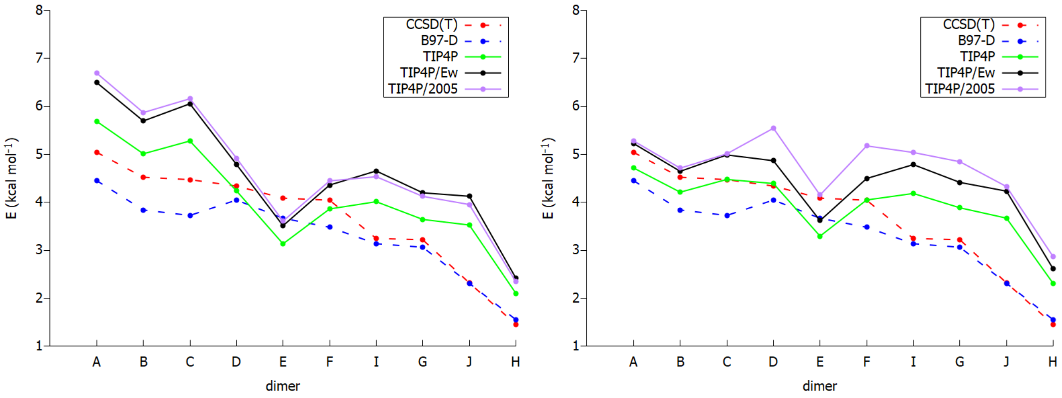

united-atom four-sites

atomistic four-sites

FIGURE 3.13: Comparison of selected potentials with CCSD(T) and DFT interaction energies for the ten water dimers considered. Four types of potentials are represented: united-atom models with three and four charges and restricted atomistic model with three and four charges.

part of the energy range: the lower charge schemes well describe the least stable dimers, while the larger charge schemes well describe the most stable geometries. The atomistic model does make the description better for the charge schemes by Albertí and SPC, making the interaction energies approaching closer to the DFT and CCSD(T) values. For the united-atom four-site models, all dimer energies are overestimated, with the striking exception of the E dimer which is underestimated for no clear apparent reason. The atomistic model represents the interaction energies better than the united-atom model as found previously for the dimers A to F, especially for the TIP4P charge scheme which gives interaction energies in between CCSD(T) and DFT. However, the the less bound dimers I to H are not better described and are overestimated by about 1 kcal mol^{-1}.

Taking into account the performance of all the proposed potentials for water, the atomistic potential with the optimized charge scheme performs best for the description of the water dimers in both the free and restricted varieties. It describes correctly the most stable and least stable isomers from the 10 studied dimers, while for the remaining dimers the interaction energies oscillate around the DFT and CCSD(T) results in such a way that, although the energy ordering is not correctly described, the sum of the errors never exceeds 0.25 kcal mol^{-1} For this reason, we expect that this potential describes with good accuracy the behavior of a set of water molecules which is the end goal of this work.

Looking back at figure 3.12, one may think that, perhaps, due to the very wide spread in interaction energies, too many configurations are included in the fitting that are too repulsive to ever play a role in actual systems. These, sometimes strongly repulsive dimer geometries, might include effects that are not present in data that is based on equilibrium bulk water data. In an attempt to better this situation, we have redone the fitting after introducing the DFT interaction energies of the ten geometries from figure 3.11 in the training data. Since these dimers represent special points on the potential energy surface, some of which minima, it might be expected that they are particularly important in bulk water. Unfortunately, this new fitting did not further improve the performance. In a last attempt, we tried to fit the potentials to the DFT interaction energies of these 10 stationary points only, but again without improvement.

3.4.3.2 Water Hexamers

One of the main difficulties in the description of water molecules are the hydrogen bonds that are present and cause the formation of clusters of molecules, especially at high pressures. It is therefore not sufficient to test the performance of the force field on dimers alone. The smallest clusters that are typically considered to evaluate the performance of a force field for hydrogen bonds are the hexamers [214], since they already give rise to a large amount of hydrogen bonds and they are the smallest cluster adopting three-dimensional shapes. We have taken six hexamers, optimized at the MP2 level with a cc-pVTZ basis set for the hydrogen atoms and a aug-cc-pVTZ basis set for oxygen (see figure 3.14), — called the prism, bag, boat, book, cage and ring structures after the original papers — for which the interaction energies have been calculated at different levels of theory [215, 216], and recalculated them with the potentials described in the previous sections. Absolute interaction energy results can be found in table 3.26, while relative interaction energies can be found in table 3.27. The level of the CCSD(T) energy predicts an energy ordering of prism < cage < book < bag < ring < boat with a range of 2.8 kcal mol^{-1}. Multiple DFT methods predict a different energy ordering of the different conformations and are incapable of predicting correctly the most stable conformation [215]. However, the DFT approximation used in this work, the B97-D/TZV2P level, ís capable of reproducing correctly the mentioned energy order, although the energy range is as large as 4.6 kcal mol^{-1}. The fields including three and four charges, for both the atomistic and the restricted atomistic models, underestimate the energies of the hexamers for all charge schemes with the exception of NPA. Errors of the order of the interaction energy itself are found for the schemes with smaller charges, while the NPA scheme

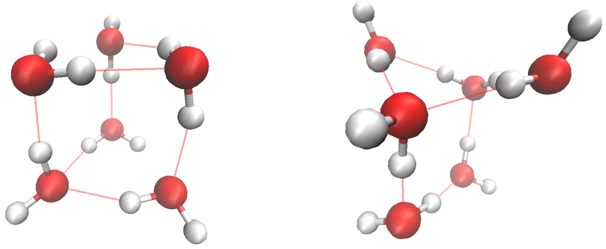

prism bag boat

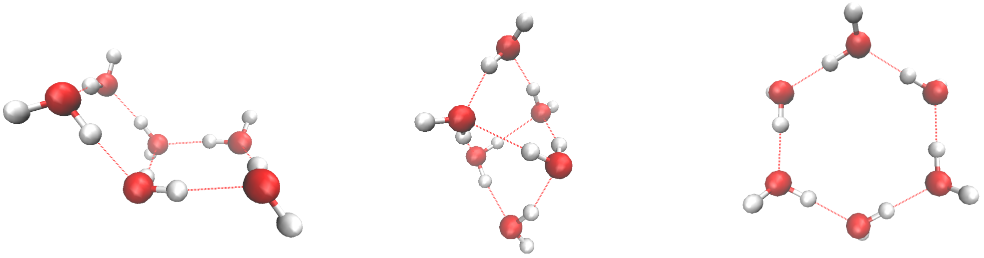

book cage ring

FIGURE 3.14: The hexamers considered in this work as taken from the literature [215, 216]

overestimates some isomers and underestimates others. In all charge schemes and models, the relative energies between the different isomers are overestimated, especially for schemes with large charges, although the relative order of stability of the different isomers is respected compared to the CCSD(T) benchmark. The large differences in relative energies related to large charges, make the schemes with four charges especially unsuitable for the description of these hexamers and they will further be dismissed for this reason.

Clearly, the models proposed previously, based on the ILJ potentials and a Coulombic sum, are not capable to reproduce these types of interactions for these hexamers and it is therefore necessary to introduce explicit terms for the evaluation of hydrogen bonds. The Dreiding force field [213], which is available in the DL_POLY program suit, uses a term for hydrogen bonds, specifically for the description of the interaction of the hydrogen atom with the strongly electronegative atoms, such as oxygen, asociated with a hydrogen bond

$$U\left(\theta_{jik}\right) = D_{\mathrm{hb}}\cos^4\left(\theta_{jik}\right)\left(5\left(\frac{R_{\mathrm{hb}}}{r_{jk}}\right)^{12} - 6\left(\frac{R_{\mathrm{hb}}}{r_{jk}}\right)^{10}\right) \tag{3.4}$$

where θ_{jik} is the bond angle between the oxygen donating the hydrogen, j, the hydrogen, i, and the oxygen accepting the hydrogen, k. r_{jk} is the distance between the

TABLE 3.26: Interaction energies in kcal mol^{-1} for the representative configurations of the water hexamer as determined from the three- and four-site atomistic models and adding explicitly hydrogen bond terms (HB) as described in the text.

method	charge scheme	q^- (e)	prism	cage	book	bag	ring	boat
CCSD(T) [216]	-	-	46.7	46.5	46.0	45.1	44.9	43.9
DFT	-	-	45.4	45	43.9	43.4	41.9	40.9
ILJ + 3q	Mulliken	-0.610	20.1	19.3	18.8	18.6	18.5	17.6
	Albertí	-0.658	21.6	20.2	19.2	18.8	18.5	17.6
	optimized	-0.731	29.6	27.7	26.1	25.6	25.1	24.0
	SPC	-0.820	38.8	36.2	33.9	33.1	32.6	31.1
	TIP3P	-0.834	40.3	37.6	35.3	34.4	33.9	32.3
	SPC/E	-0.848	41.9	39.1	36.6	35.7	35.2	33.6
	NPA	-0.904	48.3	45.0	42.1	41.0	40.5	38.6
ILJ + 4q	TIP4P	-1.040	32.1	28.9	24.2	24.0	20.0	19.5
	TIP4P/Ew	-1.048	37.3	34.0	29.5	29.0	25.6	24.8
	TIP4P/2005	-1.113	37.7	34.2	28.9	28.7	24.2	23.6
ILJ + 3q + HB	Mulliken	-0.610	44.7	46.4	47.5	46.4	46.7	45.9
	Albertí	-0.658	42.4	43.1	43.4	42.3	42.3	41.4
	optimized	-0.731	44.4	44.0	43.4	42.4	42.2	41.0
	SPC	-0.820	45.2	43.3	41.5	40.4	40.0	38.5
	TIP3P	-0.834	45.4	43.2	41.2	40.2	39.8	38.2
	SPC/E	-0.848	45.6	43.1	40.9	39.9	39.4	37.8
	NPA	-0.904	50.7	47.6	44.9	43.7	43.3	41.4

donor and the acceptor atoms in Angstrom, while D_{hb} and R_{hb} are are calculated from the chosen charge scheme [213]. The values used for D_{hb} and R_{hb} are given in table 3.28. For calculation of the interaction energies using these potentials, the hydrogen bond term was only included for bonds for which the $\cos(\theta_{jik})$ was smaller than -0.70, coinciding with bond angles, θ_{jik}, between 134° and 226°.

By including the hydrogen bond in the potential, the range of energies for the different isomers is significantly diminished for all charge schemes leading to a much better agreement with the CCSD(T) results, see tables 3.26 and 3.27 and figure 3.15. However, the schemes with smaller charges have a different ordering of the isomer energies. Most striking is the prism structure becoming the least stable isomer when using the Mulliken and Albertí charge schemes. The remaining charge schemes, however, give the correct order with the optimized charge scheme giving relative energies very close to the *ab-initio* results.

A comparison with CCSD(T) and DFT is shown in figure 3.16. The optimized atomistic force field gives a good description of the energies in the right order, with the relative energy difference close to the CCSD(T) results assuring a good description of small clusters in different conformations with hydrogen bonds. The absolute and relative energies obtained are intermediate between the DFT and CCSD(T) results obtained before and can thus be considered a good approximation of the system. This scheme was also found to perform the best for the dimers although at that point without the hydrogen bond term. We have tried to include the hydrogen bond term in the calculation of the dimer thereby also reoptimizing the ILJ parameters,

TABLE 3.27: Relative electronic energies in kcal mol^{-1} of the representative configurations of the water hexamers as determined from the three-site charge schemes with and without hydrogen bond term and the four-site charge scheme.

method	charge scheme	q^- (e)	prism	cage	book	bag	ring	boat
CCSD(T) [216]	-	-	0.0	-0.2	-0.7	-1.6	-1.8	-2.8
DFT	-	-	0.0	-0.4	-1.5	-2.0	-3.5	-4.6
ILJ + 3q	Mulliken	-0.610	0.0	-0.8	-1.3	-1.5	-1.6	-2.5
	Albertí	-0.658	0.0	-1.4	-2.4	-2.7	-3.1	-4.0
	optimized	-0.731	0.0	-1.9	-3.5	-4.0	-4.4	-5.6
	SPC	-0.820	0.0	-2.6	-4.8	-5.6	-6.2	-7.7
	TIP3P	-0.834	0.0	-2.7	-5.0	-5.9	-6.4	-8.0
	SPC/E	-0.848	0.0	-2.8	-5.3	-6.2	-6.7	-8.4
	NPA	-0.904	0.0	-3.3	-6.2	-7.3	-7.8	-9.7
ILJ + 4q	TIP4P	-1.040	0.0	-3.2	-7.9	-8.1	-12.1	-12.6
	TIP4P/Ew	-1.048	0.0	-3.3	-7.8	-8.3	-11.7	-12.5
	TIP4P/2005	-1.113	0.0	-3.5	-8.8	-9.1	-13.6	-14.1
ILJ + 3q + HB	Mulliken	-0.610	0.0	1.7	2.7	1.7	2.0	1.1
	Albertí	-0.658	0.0	0.7	1.0	0.0	-0.1	-1.0
	optimized	-0.731	0.0	-0.4	-1.0	-2.1	-2.3	-3.4
	SPC	-0.820	0.0	-1.9	-3.7	-4.8	-5.2	-6.7
	TIP3P	-0.834	0.0	-2.2	-4.2	-5.2	-5.7	-7.2
	SPC/E	-0.848	0.0	-2.5	-4.7	-5.7	-6.2	-7.8
	NPA	-0.904	0.0	-3.1	-5.8	-7.0	-7.5	-9.3

the charges and the dipole moments, but the description of the different dimers was not improved compared to the ILJ potentials and the previously proposed charge schemes. We may thus in general recommend the optimized restricteed atomistic potential for use on the water molecule whereby inclusion of the hydrogen bond term depends on the pressure on the system. The low amount of hydrogen bonds

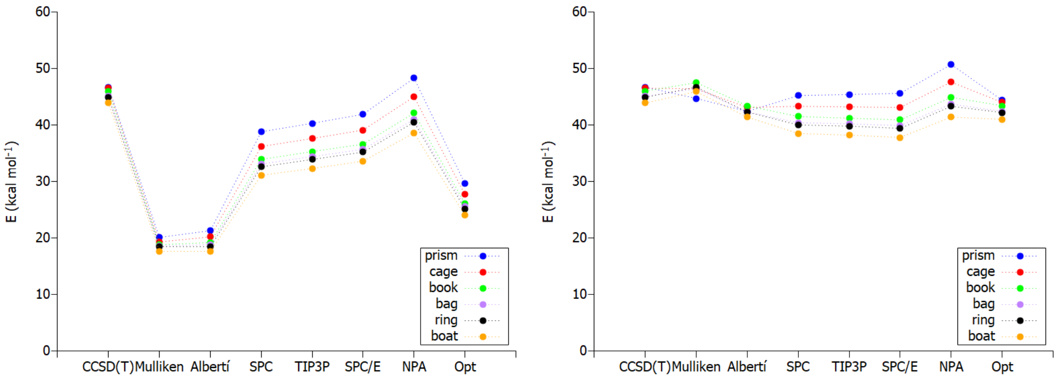

ILJ + 3q

ILJ + 3q + HB

FIGURE 3.15: Comparison of selected potentials with CCSD(T) and DFT interaction energies for the ten water dimers considered. Four types of potentials are represented: united-atom models with three and four charges and restricted atomistic model with three and four charges.

TABLE 3.28: D_{hb} and R_{hb} values for the different charge schemes used.

Charge scheme	q^-	D_{hb}	R_{hb}
Mulliken	-0.610	4.740	2.75
Albertí	-0.658	4.000	2.75
optimized	-0.731	2.854	2.75
SPC	-0.820	1.250	2.75
TIP3P	-0.834	0.980	2.75
SPC/E	-0.848	0.707	2.75
NPA	-0.904	0.470	2.75

in the water dimers (low pressure) needs no specific hydrogen bond since the potential, optimized to DFT results, has enough flexibility to reproduce the different isomer energies. When more hydrogen bonds are formed (high pressure) as in the hexamers, the hydrogen bond term is needed to well describe the different isomer energies.

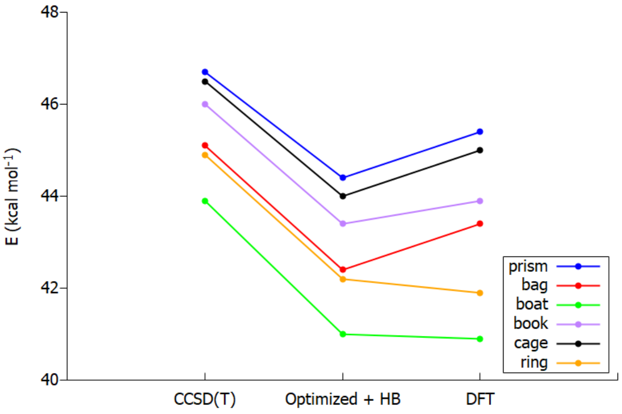

FIGURE 3.16: A comparison of the interaction energies for the different hexamers obtained from CCSD(T), the optimized charge scheme with inclusion of the hydrogen bond term and DFT.

3.5 Carbon Monoxide

Carbon monoxide is composed of one oxygen atom and one carbon atom and is far from spherical. In fact, the molecule is linear like nitrogen, studied previously, but, unlike nitrogen, contains a dipole moment and therefore electrostatic interactions are expected to be important. Furthermore, these traits will give rise to directional effects both within the CO-CO dimer and the graphene-CO system. Indeed, previous benchmarking calculations at CCSD(T) and DFT level have shown that the orientation of the CO molecule is very important for the interaction within the graphene-CO system with differences of up to 1 kcal mol^{-1} in interaction energy and up to 0.8 Å for the equilibrium distance [146]. For nitrogen, these differences were limited to about 0.6 kcal mol^{-1} and 0.2 Å, while for water, also exhibiting large directional electrostatic contributions, these interactions with graphene differed by as much as 2 kcal mol^{-1}, although the equilibrium distance was almost invariant. The maximum interaction energy between graphene and CO is 2.5 kcal mol^{-1}, which is intermediate between methane and nitrogen and substantially lower than water. Because of this, the use of a united-atom model has been discarded for this molecule and only an atomistic potential has been used.

Carbon monoxide has proven difficult to describe theoretically, because of its unexpected electronic density. Indeed, many methods, including MP2/TZV and SCF/TZVP, either give an incorrect sign for the dipole moment or largely overestimate it. B97-D/TZV2P on the other hand, overestimates the experimental dipole only slightly (0.164 D vs 0.122 D, respectively), while the CCSD(T)/aug-cc-pVDZ predicts a theoretical dipole of 0.149 D. In order to capture this behavior in a force field, three different charge schemes were considered for representation of the electrostatic part of the interaction [146]. The first one assigns a negative charge to the oxygen atom and a positive one to the carbon atom according to chemical intuition and based on the electronaffinity of the involved atoms. However, it has been found that the dipole present in the molecule, actually contradicts this. Therefore, a second charge scheme was considered assigning slightly different negative charges to both the carbon and the oxygen atom and a positive charge at the centre of mass of the molecule. The third charge scheme adds a negative charge outside the molecule on the carbon side compared to the first charge scheme. After careful consideration of the performance of the different charge schemes through comparison of their energy predictions for two CO-CO geometries to DFT and CCSD(T) data, the second charge scheme was selected as the best using charges of -0.620274, 1.248588, and -0.628314 for the carbon atom, the centre of mass and the oxygen atom, respectively. The resulting ILJ parameters are given table 3.29.

TABLE 3.29: Interaction parameters for the CO dimer using an atomistic model. C represents the carbon atom and O the oxygen in carbon monoxide, while C_g represents the carbon atom in graphene.

interaction	ϵ (kcal mol^{-1})	r_0 (Å)	β
CO-CO			
CC	0.126	3.797	9.33
CO	0.109	3.641	9.84
OO	0.090	3.656	9.58
graphene-CO			
C_gC	0.082	3.770	9.26
C_gO	0.087	3.819	7.37

3.6 Gas Mixtures

Usually, in the literature, potentials are developed for pure gases. When a combination of gas molecules is required, the parameters are obtained by applying some combination rules, very often the Lorentz-Berthelot rules:

$$\epsilon_{\mathrm{AB}} = \sqrt{\epsilon_{\mathrm{AA}}\epsilon_{\mathrm{BB}}} \tag{3.5}$$

for ϵ and

$$\sigma_{\mathrm{AB}} = \frac{1}{2}\left(\sigma_{\mathrm{AA}} + \sigma_{\mathrm{BB}}\right) \tag{3.6}$$

for the σ parameter in the LJ potential.

These rules are only applicable for molecules that are very similar in nature and it is unclear how they behave when the molecules are not similar enough. Furthermore, since we are using the ILJ potential, there is no rule defined for determining the β parameter. For these reasons, we have chosen to obtain the parameters directly using the same method as for the single species parameters. More specifically, for both the CH_4-H_2 and CH_4-N_2 systems, we did a scan over the distance between 2.6 Å and 20 Å over 36 different distances for 99 randomly created dimers and calculated their interaction energies at the B97-D/TZV2P level. We then selected the model that we found to perform best for the single species potential and used this to do a fitting to the newly obtained DFT data. For the CH_4 molecule, we used the Hirshfeld charges united-atom and the no charge atomistic models (see section 3.2.2), while for nitrogen, the Cracknell charge scheme was used for both the united-atom and atomistic model (see section 3.3.1). For the H_2 model, on the other hand, we used the united-atom model without charges that was previously developed by Yeamin et al. [56] using the same approach as described in this work. This way, we have obtained united-atom parameters for the CH_4-H_2 interaction and both united-atom and atomistic parameters for the CH_4-N_2 interaction as shown in table 3.30.

TABLE 3.30: Interaction parameters for the ILJ potential used in this work to represent the intermolecular potentials in a united-atom or fully atomistic representation for the CH_4-H_2 and CH_4-N_2. Cm represents the centre of mass of the respective molecules, C represents the carbon and H the hydrogen in methane, while N represents the nitrogen atom.

	ϵ (kcal mol^{-1})	r_0 (Å)	β
united-atom			
$\mathrm{Cm_{CH_4}Cm_{N_2}}$	0.288	4.243	7.698
$\mathrm{Cm_{CH_4}Cm_{H_2}}$	0.180	3.816	5.618
atomistic			
CN	0.428	3.527	7.923
HN	0.002	5.274	6.186

The interactions thus obtained were used in the subsequent chapter for simulations of the methane/nitrogen and the methane/hdyrogen mixtures. For the methane/nitrogen system, the development of both a united-atom and atomistic force field, allows comparison of the performance of both. This is of interest because a united-atom approach is computationally cheaper than the atomistic approach and might thus be more convenient for use in large-scale simulations. However, it must be clearly known what is sacrificed in accuracy in that case. For the methane/hydrogen mixture, only the united-atom model was used for computational reasons without inclusion of electrostatic charges. Although methane and hydrogen are not spherical, their highly symmetrical structures, together with the fact that their interaction is clearly dominated by dispersion forces, justify such description.

3.7 Intramolecular Potential for Graphene

Until now we have studied the intermolecular graphene-gas interaction potentials considering the graphene as an ideal surface whereby the interactions and the structure are unchanged. However, it is known that the graphene structure is not rigid, but exhibits carbon atoms moving in and out of the graphene plane. The most important point of interest in the MD studies in the next chapter is studying the influence of introducing flexibility in the graphene sheet on the adsorption of small gases. In this section, we introduce the intramolecular potentials that were used for a more realistic description of the graphene sheet.

Indeed, we have taken three force fields from the literature, two of which include stretch, bend and torsional terms, while the third only includes stretch and bend terms. The first intramolecular force fields that we used was developed by Walther et al. for the study of carbon nanotubes [79]. The fact that a carbon nanotube is nothing more than a rolled up graphene sheet suggests that this force field is transferable from one system to the other. The force field has following form

$$\begin{aligned} U_1(r_{ij}, \theta_{ijk}, \phi_{ijkl}) = {} & K_{Cr1}(e^{-\gamma_1(r_{ij}-r_{C1})} - 1)^2 \\ & + \frac{1}{2}K_{C\theta 1}(\cos\theta_{ijk} - \cos\theta_{C1})^2 \\ & + \frac{1}{2}K_{C\phi 1}(1 - \cos(2\phi_{ijkl})) \ , \end{aligned} \tag{3.7}$$

with K_{Cr1} = 114.46 kcal mol^{-1}, γ_1 = 2.1867 Å^{-1}, r_{C1} = 1.418 Å , $K_{C\theta 1}$ = 134.369 kcal mol^{-1} rad^{-2}, θ_{C1} = 120° and $K_{C\phi 1}$ = 6.004 kcal mol^{-1}. Kalosakas et al. have developed a force field specifically for graphene containing stretching and bending terms [80]

$$\begin{aligned} U_2(r_{ij},\theta_{ijk}) &= K_{Cr2}(e^{-\gamma_2(r_{ij}-r_{C2})}-1)^2 \\ &+\frac{1}{2}K_{C\theta 2}(\cos\theta_{ijk}-\frac{2\pi}{3})^2 \\ &+\frac{1}{2}K'_{C\theta 2}(\cos\theta_{ijk}-\frac{2\pi}{3})^3 \ , \end{aligned} \tag{3.8}$$

with K_{Cr2} = 131.429 kcal mol^{-1}, γ_2 = 1.960 Å^{-1}, r_{C2} = 1.420 Å , $K_{C\theta 2}$ = 161.401 kcal mol^{-1} rad^{-2} and $K'_{C\theta 2}$ = 92.232 kcal mol^{-1} rad^{-3}. The same group have extended this force field with torsional terms to give a more complete picture leading to [81]

$$\begin{aligned} U_2(r_{ij},\theta_{ijk},\phi_{ijkl}) &= K_{Cr2}(e^{-\gamma_2(r_{ij}-r_{C2})}-1)^2 \\ &+\frac{1}{2}K_{C\theta 2}(\cos\theta_{ijk}-\frac{2\pi}{3})^2 \\ &+\frac{1}{2}K'_{C\theta 2}(cos\theta_{ijk}-\frac{2\pi}{3})^3 \\ &+\frac{1}{2}K_{C\phi 2}(1-\cos(2\phi_{ijkl})) \ , \end{aligned} \tag{3.9}$$

containing only one extra parameter compared to the first version of the force field: $K_{C\phi 2}$ = 5.304 kcal mol^{-1}.

These three force fields will from now on be denoted as field 1, field 2 and field 2m, respectively, whereby the m stands for modified. The implementation of these three force fields in the DL_POLY v2.2 input allows for comparison with simulations whereby the graphene sheet is just completely rigid through time, the latter will be referred to as field 0 for consistency.

3.8 Correlation Formulae

To conclude this chapter on force fields, an alternative way of obtaining parameters for a LJ type potential is determined whereby formulae are used that give a semi-empirical relation between the polarizability and the well depth and its position. This allows parameters to be estimated from one single calculation of a molecule of interest [217, 218]. United-atom parameters can be obtained from the molecular polarizabitility, while atomistic parameters can be obtained by decomposing the molecular polarizability in atomic polarizabilities.

3.8.1 Mathematical Procedure

For the equilibrium distance, the following formula was encountered

$$r_0 = 1.767\frac{\alpha_i^{\frac{1}{3}}+\alpha_j^{\frac{1}{3}}}{(\alpha_i\alpha_j)^{\gamma}} \ , \tag{3.10}$$

where γ is an empirical parameter controlling the dependence on the long-range attraction and has been determined to be 0.095. It is, together with the value 1.767, obtained via a fit to very accurate calculations on reference systems like Ne-Ne, He-Ne and others.

To understand this relation, two observations should be made: firstly, the polarizability depends mainly on the size of the outer electronic orbitals of the molecule and can therefore be seen as a measure for the size-size repulsion between two interacting bodies. This is especially true in the equilibrium region where the interacting particles maintain their individual character which is the range where the parameters of a LJ-type potential are deduced. The numerator of equation 3.10 can then be read as a summation of the respective sizes of the involved interacting partners via their polarizability. Secondly, it is well known that the polarizability is responsible for long-range attraction and that this attraction can be described via multiplication of the polarizabilities of both interacting partners as is done in the denominator of equation 3.10. Since the equilibrium distance itself is the result of a competition between attractive and repulsive forces, both must be present in the formula.

Taking into account the definition of the dispersion interaction energy by Eisenschitz and London as a truncation of the power series of the inverse of R [190]

$$V(R) = \frac{C_6}{R_{ij}} \ , \tag{3.11}$$

the well depth can be calculated as

$$\epsilon = \frac{C_6}{r_0} \ , \tag{3.12}$$

using r_0 as defined in equation 3.10 and where C_6 is defined as

$$C_6 = \frac{3}{\pi} \int \alpha_i(i\omega)\alpha_j(i\omega)d\omega \ , \tag{3.13}$$

where α_i is the dynamics polarizability of interacting partner i and ω the frequency. It should be noted that in reference [217], ϵ was obtained via inclusion of an empirical scaling factor of 0.72. However the C_6 coefficient was calculated via the Kirkwood-Slater equation from experiment, meaning that higher order terms, such as C_8, C_{10} and so on, were included from the multipole series. We, on the other hand, used the correct Casimir-Polder relation including only the first C_6 term and we found that the scaling factor is not necessary in our calculations.

These formulae now allow us to determine the parameters of LJ-type potentials from just the dynamic polarizability. The polarizability at imaginary frequency is defined according to

$$\alpha(i\omega) = \sum_k \frac{f_{0k}}{E_{0k}^2 + \omega^2} \ , \tag{3.14}$$

where f_{0k} and E_{0k} are the oscillator strength and the excitation energy for excitation k, respectively. The infinite sum can be directly calculated through a damped response function, as implemented in the Dalton package for HF and DFT wave functions. However, at the coupled cluster level, this procedure is not implemented and we therefore used an alternative approach by defining the polarizability at imaginary frequencies as a series of Cauchy moments according to

$$\alpha(iy) = \sum_k S_k(-y^2)^k \ , \tag{3.15}$$

where S_k are the Cauchy moments, which can now be calculated by the Dalton program suit [219]. Unfortunately this summation only converges below the first transition and it was suggested to solve this by defining upper and lower bounds to the polarizability using Padé approximants [220]

$$\alpha(iy) \simeq [n,m]_\alpha = \frac{P_m(iy)}{Q_n(iy)} \ . \tag{3.16}$$

In particular, it can be proven [220] that

$$[n,n-1]_\alpha \leq \alpha \leq [n,n]_\alpha \ , \tag{3.17}$$

leading to a lower bound for the polarizability

$$[5,4]_\alpha = \frac{P_4(iy)}{Q_5(iy)} \simeq \alpha(iy) \ , \tag{3.18}$$

whereby we used the $[5,4]$ Padé approximant since it has been shown that it leads to results within ±1% of the actual value [219]. This can be rearranged to

$$\alpha(iy)Q_5(iy) - P_4(iy) = 0 \ . \tag{3.19}$$

Taking into account the definition of P_4,

$$P_4 = a_0 + a_1(-y^2) + a_2(-y^2)^2 + a_3(-y^2)^3 + a_4(-y^2)^4 \ , \tag{3.20}$$

Q_5,

$$Q_5 = 1 + b_1(-y^2) + b_2(-y^2)^2 + b_3(-y^2)^3 + b_4(-y^2)^4 + b_5(-y^2)^5 \tag{3.21}$$

and equation 3.15, we obtain a set of equations in terms of powers of $-y^2$

$$\begin{cases} a_0 - S_0 = 0 \\ -a_1 + b_1 S_0 + S_1 = 0 \\ \ldots \end{cases} \ . \tag{3.22}$$

From this, the a- and b-coefficients can be calculated and reinserted in equation 3.19 together with the Cauchy moments, which were calculated on beforehand, leading to a lower bound for the dynamic polarizability. In order to get an upper bound, it is not possible to use the Padé approximant $[n,n]_\alpha$ since its substitution in the integral

3.13 would make the latter diverge. Therefore, it is convenient to define the auxiliary function

$$\beta(iy) = N - y^2\alpha(iy) \ , \tag{3.23}$$

which can again be sandwiched between Padé approximants

$$[n, n-1]_\beta \leq \beta \leq [n]_\beta \ . \tag{3.24}$$

So we find

$$N - y^2\alpha(iy) = \beta \geq [n, n-1]_\beta \ , \tag{3.25}$$

leading to

$$\alpha(iy) \leq \frac{N - [n, n-1]_\beta}{y^2} \tag{3.26}$$

By making use again of [5,4] Padé approximants, the same procedure as before leads to a system of equations similar to equation 3.22

$$\begin{cases} -N + a_0 - S_0 = 0 \\ -a_1 + Nb_1S_0 + S_1 = 0 \\ \dots \end{cases} \ . \tag{3.27}$$

Again the a- and b- coefficients can be obtained and used together with the Cauchy moments to define an upper bound to the polarizability and the final prolarizability is then taken to be the arithmetic average between upper and lower bound. From the polarizability, the C_6 dispersion coefficient can then be calculated as the integral over the polarizability of the molecules involved: the so-called Casimir-Polder equation

$$C_6 = \frac{3}{\pi} \int_0^\infty \alpha_A(i\omega)\, \alpha_B(i\omega)\, d\omega \ . \tag{3.28}$$

This infinite integral is hard to calculate and we will therefore use the Gauss-Legendre approximation to make calculation feasible. The boundaries of the integral can be changed by transforming the integrand in the following way

$$y = y_0 \left(\frac{t-1}{t+1} \right) \ , \tag{3.29}$$

leading to a new integral

$$C_6 = 2y_0 \int_{-1}^{1} \alpha_A(t)\, \alpha_B(t)\, \frac{dt}{(1+t)^2} t \ , \tag{3.30}$$

which can be represented as a truncated summation

$$C_6 = 2y_0 \sum_{1}^{6} w_i \alpha_{\mathrm{A}}(t)\, \alpha_{\mathrm{B}}(t) \quad , \tag{3.31}$$

where w_i is a weight value that can be looked up in tables, together with the corresponding values for t. The dynamic polarizabilities at frequencies t, specified by mentioned tables, were calculated using Dalton at CC2 and CCSD level. From tese C_6 was calculated and used to find ϵ as described in equation 3.12.

The previously described method was used to calculate molecular polarizabilities allowing the deduction of united-atom models. For the development of atomistic potentials, atomic polarizabilities are needed and we used the CamCASP program suit to provide these [221]. Unfortunately, CamCASP is only capable of providing atomic polarizabilities at DFT level as it relies on the iterated stockholder method to separate the molecular electron density into atomic components [222]. In this method, each atom is assigned a spherically-symmetrical weight function $w_{\mathrm{a}}(R)$ and the electron density is divided over the atoms in proportion to this weight function at each point in space

$$\rho_{\mathrm{a}}(R) = \rho(r) \frac{w_{\mathrm{a}}(R)}{\sum_{\mathrm{b}} w_{\mathrm{b}}(R)} \quad , \tag{3.32}$$

whereby the weight functions statisfy

$$w_{\mathrm{a}}(R) = \langle \rho_{\mathrm{a}}(R) \rangle \quad , \tag{3.33}$$

where ρ_{a} is the total electron density and the angle brackets denote a spherical average. This equation is solved iteratively, to statisfy both equations such that the weight function equals the spherical weight of the corresponding atom density. The sum of the weight functions is then the best possible approximation to the molecular density as a sum of spherical densities.

3.8.2 Parameters for CH_4 and N_2

Table 3.31 collects the parameters that were calculated this way for the methane and the nitrogen molecule for both a united-atom and an atomistic approach and compares them to selected force fields from the literature as presented previously in table 3.1. For the methane molecule, the united-atom approach behaves quite differently from the TraPPE force field commonly used in the literature. It should be noted however, that the TraPPE force fields includes no charges on the molecule. The method we developed here, explicitly only takes into account the dispersion interaction meaning that other interactions, like the electrostatic one, are to be included explicitly. Comparing to the force field proposed by Albertí et al., which does include a specific electrostatic part, the comparison is a lot better [59]. For the atomistic approach, comparison is again better with models that include an explicit electrostatic part, although our ϵ values are substantially higher than the values proposed by Sun et al., while the r_0 values are lower [169].

TABLE 3.31: Parameters calculated from the correlation formulae for the methane and nitrogen molecule compared to selected force fields from the literature. C, H and N refer to the carbon, hydrogen and nitrogen atoms, respectively, while Cm refers to the centre of mass of the respective molecules.

	method	ϵ (kcal mol^{-1})	r_0 (Å)
united-atom methane			
$Cm_{CH_4}Cm_{CH_4}$	DFT	0.405	4.050
	CC2	0.411	4.032
	CCSD	0.402	4.019
	Albertí [59]	0.335	4.06
	TraPPE [159]	0.294	4.187
united-atom nitrogen			
$Cm_{N_2}Cm_{N_2}$	DFT	0.320	3.770
	CC2	0.323	3.822
	CCSD	0.328	3.824
	Ravikovitch [182]	0.202	4.058
atomistic methane			
CC	DFT	0.155	3.574
	Sun et al. [169]	0.109	3.816
CH	DFT	0.075	3.370
	Sun et al. [169]	0.041	3.395
HH	DFT	0.043	3.085
	Sun et al. [169]	0.016	2.974
atomistic nitrogen			
NN	DFT	0.092	3.770
	Cracknell [223]	0.075	3.724

Concerning the nitrogen molecule, our values for the united-atom approach are quite different from the ones proposed in the literature, with the same remark as for methane: the united-atom models from the literature usually do not consider an electrostatic part explicitly. Looking at the atomistic parameters, both our ϵ and r_0 are higher than the ones proposed by Cracknell et al.

Comparing these parameters to the ones that were obtained in the previous sections through fitting to DFT interaction energies, we see that especially the united-atom models of methane are very similar, while the other potentials are not. This can be justified by what was said in the introduction of this chapter: while the fitting procedure was an attempt to obtain as much information into a simple analytical expression without worrying too much about physical meaning, this second approach is explicitly an attempt to obtain dispersive interaction only. The model that can be expected to be most purely based on dispersion interaction, the united-atom methane model without charges, shows indeed the best comparison. For the other models, it will be important to include accurate electrostatic interactions to obtain comparable final interaction energies. As such we have validated the potentials obtained in this section indirectly by comparison to the potentials from the fitted procedure.

Chapter 4

Molecular Dynamics

In this chapter, a selection of the potentials developed in chapter 3 will be used in MD simulations to assess their performance for the simulation of gas adsorption on graphene. In a first section (section 4.1) the adsorption of methane and nitrogen gases will be studied separately as well as in mixture and in the second section (section 4.2) the adsorption of carbon monoxide will be studied. We have simulated a single graphene layer in all cases as it has been shown that the interaction energies between small molecules and a single graphene layer is about 10% higher than for few-layered graphene [149].

4.1 Methane and Nitrogen Adsorption on Flexible Graphene

In this study we want to investigate the influence of the flexibility introduced in the graphene sheet on the adsorption of methane, nitrogen and their mixture. For the implementation of the flexibility in the graphene sheet, we have used three intramolecular force fields from the literature containing stretching, bending and torsional terms as indicated in chapter 2. One of them was originally developed for carbon nanotubes, but given that a carbon nanotube is nothing more than a rolled up graphene sheet, the force field is expected to be transferable to graphene. The two remaining fields were developed specifically for graphene, whereby they differ in that one of them contains a torsional term, while the other does not. Furthermore, in this study, the performance of a united-atom and an atomistic model will be compared and for this, the best performing potential of either type was selected from chapter 3. More specifically, the Hirshfeld charge scheme was used for united-atom methane, while no charges were used for the atomistic methane model. For nitrogen, on the other hand, the Cracknell charge scheme was used for both the united-atom and atomistic models.

4.1.1 Methodology

All MD simulations were performed using an in-house version of the DL_POLY v2.2 software [136], which has the ILJ potential implemented. The graphene sheet was modeled by placing a single graphene sheet of 840 carbon atoms in their usual honeycomb pattern in the middle of the simulation box with an average C-C distance of 1.42 Å. The box was adjusted in size as to just envelop the graphene sheet in the x- and y-direction while making sure that no defects were introduced upon applying the boundary conditions. In the z-direction, 20 Å of space was left on either side of the graphene sheet as to avoid interactions of the graphene sheet with its copies after application of periodic boundary conditions [11]. The vacuum is also needed to allow the gas molecules to escape the adsorbed phase and enter a gas phase, while the applied boundary conditions prevent the gas molecules from escaping the simulation box. This led to a box size of 51.65 Å x 42.6 Å x 40 Å . The simulations were carried out in either the NVE and NVT ensemble, using a Hoover thermostat with a relaxation constant of 0.5 ps in the latter case. Timesteps of 1 fs were simulated while all interactions were cut off at 18 Å and simulations were done at 300 K. The gas molecules were modeled using the geometries from chapter 3 and assumed rigid throughout the simulation.

An important feature of a molecular dynamics simulation is the equilibration time that is set to allow the system to relax to a realistic configuration. During equilibration, the excess energy is taken away from the system after every couple of time steps by rescaling the velocities of the involved particles, leading to a lower energy conformation and preventing the system to gain more configurational energy. For adsorption, however, this means that the system will automatically evolve to a state with lowest configurational energy. In casu, all molecules will be adsorbed on the graphene sheet, a situation which is by no means physical since kinetic energy forces molecules out of the adsorption layers in reality. Since the equilibration time is set and the simulation goes towards adsorption of all molecules when equilibration is left unbound, this means that the amount of molecules is in fact artificially decided upon by setting the equilibration time. To avoid this and in order to obtain a reasonable criterion upon which to base the equilibration time, we have performed some preliminary studies varying the equilibration times between 50,000 time steps and 500,000 time steps for a constant total run time of 2,000,000 time steps. For all these different simulations, we then looked at the gas phase that was present in the system and calculated its pressure. We compared this to the pressure of a bulk gas at the same conditions and retained the equilibration times that lead to realistic pressures of the gas phase within the simulation box. This lead us to decide to run the simulations for 2,000,000 time steps, 150,000 of which for equilibration.

At all times, convergence was checked via monitoring of properties like temperature and pressure. The simulations were then always run in the NVE ensemble to allow relaxation after which an NVT simulation was performed as a production run. As a criterion for adsorption, it was decided that all molecules that were located closer than 4.6 Å from the graphene sheet, were considered adsorbed. This is justified by the z-density plots of all investigated systems where it is visible that the first adsorption layer ends at about this distance as can be verified in figures shown below.

The pressure, P, was calculated from the amount of molecules in the gas phase that was present within a known volume by the Peng-Robinson equation of state

$$P = \frac{RT}{V_\mathrm{m} - b} - \frac{a\alpha}{V_\mathrm{m}^2 + 2bV_\mathrm{m} - b^2} \quad , \tag{4.1}$$

where

$$a \approx 0.45724 \frac{R^2 T_\mathrm{c}^2}{P_\mathrm{c}} \quad , \tag{4.2}$$

$$b \approx 0.07780 \frac{R T_\mathrm{c}}{P_\mathrm{c}} \quad , \tag{4.3}$$

$$\alpha = \left(1 + \kappa \left(1 - T_\mathrm{r}^{\frac{1}{2}}\right)\right) \quad , \tag{4.4}$$

$\kappa \approx 0.37464 + 1.54226\omega - 0.26992\omega^2$ and $T_\mathrm{r} = \frac{T}{T_\mathrm{c}}$. R is the gas constant, T the temperature, V_m the molar volume, T_c and P_c the critical temperature and pressure, respectively, while ω is the acentric factor of the species of interest. For methane, the used constants were T_c = 190.4 K, P_c = 45.40 atm and ω = 0.011, while for nitrogen we used T_c = 126.2 K, P_c = 33.46 atm and ω = 0.039 [224].

Z-density profiles were calculated for the different gases on the different graphene sheets by slicing up the simulation box in the z-direction every 0.049 Å. The amount of molecules that was present in each slice was then calculated as an average over the simulation time, giving a clear picture of the distribution of the molecules within the simulation box.

A final property that is calculated, only for the adsorption of the gas mixture, is the selectivity. This property is a measure of the preference of the graphene sheet to adsorb one molecule type over another and thus gives an indication of the separating capacity of the graphene sheet for the specific gas mixture. The selectivity, S_AB, is calculated as

$$S_\mathrm{AB} = \frac{\left(\frac{x_\mathrm{A}}{x_\mathrm{B}}\right)_\mathrm{ads}}{\left(\frac{y_\mathrm{A}}{y_\mathrm{B}}\right)_\mathrm{bulk}} \quad , \tag{4.5}$$

where x is the mole fraction of the specified molecule adsorbed, while y is the mole fraction in the bulk of the specified molecule.

4.1.2 Saturating the Graphene Sheet

In a first protocol, 100 gas molecules were randomly distributed over the simulation box whereby care was taken to leave a distance of at least 5 Å between the different gas molecules, the box edges and the graphene sheet in order to avoid very high repulsions at the start of the simulation. At the end of the simulation, the resulting system was investigated and for all individual molecules was checked whether they were adsorbed or not. The ones that were not adsorbed were then deleted from the system and 100 new molecules were randomly added for a subsequent simulation containing the adsorbed molecules from the previous simulation together with the 100 newly added molecules. This procedure was then repeated until convergence of the amount of molecules that was adsorbed on the sheet. Effectively, this means that upon addition of 100 new molecules at the beginning of a new simulation, no extra molecules were adsorbed. This protocol allows studying how the adsorption advances when extra molecules are added to already adsorbed ones and allows for an estimation of the maximum amount of molecules that can be adsorbed under the given conditions. Thereby, it is important to consider that, given the dynamical nature of molecular dynamics simulations, the amount of molecules adsorbed from one simulation to the next fluctuates about the equilibrium value in the same way as experimental results.

Table 4.1 shows the results for the united-atom model using the first protocol on the pure methane gas for the four different fields under study. The results for the subsequent simulations are found indicating the amount of molecules that was present in the simulation box, the mole fraction that was adsorbed and the corresponding uptake in mmol (gas)/g (of graphene). For all four fields, the first 100 molecules are almost all adsorbed, while less and less molecules adsorb after every subsequent simulation. Furthermore, it takes five or six simulations to converge the

TABLE 4.1: First set of simulation results for the pure methane gas using a united-atom approach for the four intramolecular force fields considered in this work. X_{ads} stands for the adsorbed mole fraction.

field	simulation	molecules	X_{ads}	uptake (mmol/g)
field 0	1	100	0.99	9.82
	2	199	0.67	13.19
	3	233	0.65	15.08
	4	252	0.62	15.48
	5	256	0.58	14.68
	6	248	0.53	13.00
field 1	1	100	0.99	9.82
	2	199	0.91	17.96
	3	281	0.73	19.64
	4	298	0.74	21.63
	5	318	0.73	22.92
	6	331	0.67	22.12
field 2	1	100	0.98	9.72
	2	198	0.89	17.46
	3	276	0.73	19.94
	4	301	0.70	21.03
	5	312	0.67	20.73
field 2m	1	100	0.99	9.82
	2	199	0.72	14.19
	3	243	0.86	20.63
	4	308	0.74	22.52
	5	327	0.69	22.42

amount of molecules that is adsorbed on the different sheets considered. After convergence, the percentage of molecules that is effectively adsorbed is considerably different for the flexible graphene sheets than for the rigid one. Whereas the rigid one adsorbs 53 % of the molecules present, the flexible ones adsorb up to 69 % for field 2m and 67 % for field 1 and field 2.

The same results using an atomistic model are shown in table 4.2 and the picture is quite different. The rigid sheet shows a very fast convergence leading to 90 % of the molecules adsorbing, while the flexible sheets adsorb around 70 %. This is a reversed situation compared to the united-atom model where the rigid sheet showed a lower percentage of molecules adsorbed. The combination of the atomistic model with the most flexible graphene sheet (field 2m) gives the most realistic description and agrees well with the experimental values. The united-atom model combined with the rigid graphene sheet, on the other hand, performs badly. However, the introduction of flexibility in the graphene sheet allows to overcome a substantial part of the shortcomings of the united-atom model leading to a reasonable accuracy at a cheap computational cost.

TABLE 4.2: A first set of simulation results for the pure methane gas using an atomistic approach for the four intramolecular force fields considered in this work. X_{ads} stands for the adsorbed mole fraction.

field	simulation	molecules	X_{ads}	uptake (mmol/g)
field 0	1	100	0.99	9.82
	2	199	0.99	19.54
	3	297	0.89	26.09
	4	363	0.89	26.69
field 1	1	100	1.00	9.92
	2	200	0.98	19.35
	3	295	0.89	26.09
	4	363	0.78	27.98
	5	382	0.71	26.79
	6	370	0.73	26.79
field 2	1	100	1.00	9.92
	2	200	1.00	19.74
	3	299	0.85	25.30
	4	355	0.75	26.29
	5	365	0.73	26.39
field 2m	1	100	0.97	9.62
	2	197	0.99	19.44
	3	296	0.96	28.17
	4	384	0.74	28.27
	5	385	0.70	26.69

Table 4.3 shows the results of protocol 1 for the adsorption of nitrogen in the same way as they were presented for methane. It is immediately clear that far fewer nitrogen molecules are adsorbed (adsorption percentages below 50 %) than methane molecules as is confirmed by Shao et al. [111]. In general it seems that the rigid sheet adsorbs slightly more nitrogen molecules than the flexible ones which is the opposite behavior than for the methane molecule.

TABLE 4.3: A first set of simulation results for the pure nitrogen gas using a united-atom approach for the four intramolecular force fields considered in this work. X_{ads} stands for the adsorbed mole fraction.

field	simulation	molecules	X_{ads}	uptake (mmol/g)
field 0	1	100	0.59	5.85
	2	159	0.55	8.73
	3	188	0.50	9.33
	4	194	0.52	9.92
	5	200	0.52	10.22
	6	203	0.46	9.23
field 1	1	100	0.55	5.46
	2	155	0.52	8.04
	3	181	0.44	7.94
field 2	1	100	0.54	5.36
	2	154	0.55	8.33
	3	184	0.50	9.13
	4	192	0.45	8.53
field 2m	1	100	0.54	5.36
	2	154	0.49	7.54
	3	176	0.51	8.93
	4	190	0.49	9.33
	5	194	0.49	9.52
	6	196	0.46	8.93

The atomistic approach, for which the results are shown in table 4.4, shows very similar results for all four graphene sheets as was the case for the atomistic methane adsorption. Unlike the methane case, for nitrogen the atomistic model does not predict a stronger adsorption on the graphene sheets than the united-atom model, which coincides with the comparison done by Do et al. on a united-atom and atomistic model for nitrogen adsorption on graphitized carbon black [90].

While going over these results, it is important to reconsider the origin of the used intramolecular force fields. Whereas field 2m can be considered a fully developed intramolecular force field specifically for graphene, field 2 is not due to the lack of a torsional term. Field 1, on the other hand, was designed for carbon nanotubes and, although their internal behavior can be assumed to be similar to graphene, that does not guarantee an absolute equivalence and therefore it is necessary to stress the comparison between the rigid graphene sheet and field 2m. Considering this, we see that the methane uptake rises quite strongly with adding flexibility for the united-atom methane. For nitrogen and atomistic methane, on the other hand, a slight decrease is seen in adsorption capacity, although the trend is less pronounced than for the united-atom methane. These differences, however, are small and it thus seems that fexibility has less of an influence on the adsorption of nitrogen as opposed to methane.

The information discussed in the previous paragraphs was used for the estimation of adsorption isotherms for the respective molecules and their molecular models. To do this, we integrated the surface area under the first adsorption layer of the

TABLE 4.4: A first set of simulation results for the pure nitrogen gas using an atomistic approach for the four intramolecular force fields considered in this work. X_{ads} stands for the adsorbed mole fraction.

field	simulation	molecules	X_{ads}	uptake (mmol/g)
field 0	1	100	0.7	5.65
	2	157	0.56	8.73
	3	188	0.54	10.02
	4	201	0.53	10.52
	5	206	0.53	10.81
field 1	1	100	0.62	6.15
	2	162	0.54	8.73
	3	188	0.54	10.12
	4	202	0.51	10.12
	5	202	0.52	10.42
field 2	1	100	0.62	6.15
	2	162	0.46	7.44
	3	175	0.54	9.42
	4	195	0.53	10.32
	5	204	0.50	10.22
field 2m	1	100	0.59	5.85
	2	159	0.50	7.84
	3	179	0.61	10.81
	4	209	0.53	10.91
	5	210	0.52	10.91

previous simulations and calculated the pressure — via the Peng-Robinson equation of state — from the amount of molecules that was present in the gas phase. The points thus obtained were then fitted using the Langmuir equation

$$q = q_{\mathrm{m}} \frac{kP}{1 + kP} \, , \tag{4.6}$$

where q is the saturated equilibrium adsorption capacity, q_{m} is the adsorption capacity at saturation of the sheet and k is the Langmuir equilibrium constant.

The adsorption isotherms for methane, for both the united-atom and atomistic model, are shown in figure 4.1. The behavior of the isotherm is as expected, whereby the uptake increases at first, but converges as the graphene sheet is saturated with methane molecules. Since the atomistic model predicts more adsorption for methane than the united-atom, the convergence of the adsorption isotherm happens at higher utakes. The adsorption isotherms for nitrogen, in figure 4.2, on the other hand, show a much slower increase very similar as what was found by Apriliyanto et al. [185]. This indicates that the graphene sheet is never completely saturated with nitrogen molecules within the conditions investigated in this work.

More importantly, the behavioral difference between the rigid graphene sheet and the different flexible sheets is clear, mostly so for the adsorption of the united-atom methane. The rigid sheet adsorbs substantially less than the flexible sheets, resulting in a lower lying and more linear adsorption isotherm, converging slower,

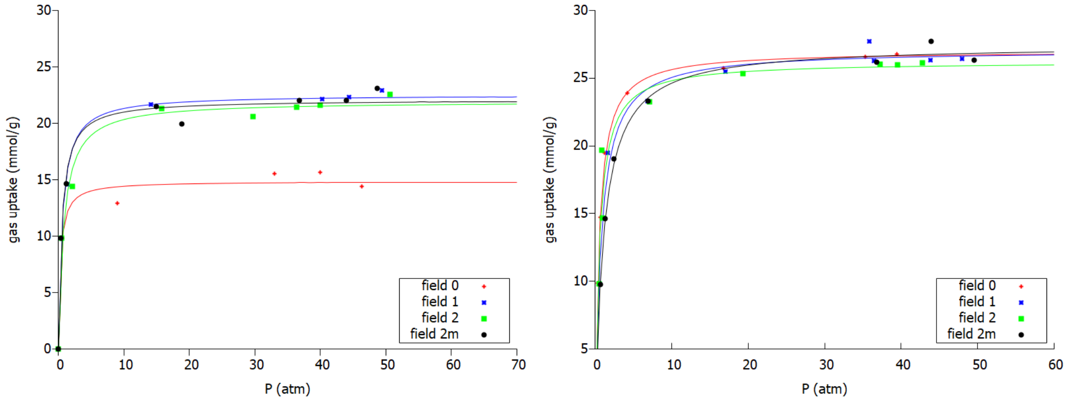

united-atom atomistic

FIGURE 4.1: Adsorption isotherms using the united-atom model (left) and the atomistic model (right) for the pure methane adsorption on the four different graphene sheets

while the differences between the flexible sheets themselves are much smaller. Although the atomistic methane and united-atom and atomistic nitrogen models, show some slight differences in their respective adsorption isotherms, the differences are less pronounced. We may conclude that the introduction of the flexibility in the graphene sheet can counteract the deficiencies of the united-atom model, especially for molecules such as methane in which orientation of the adsorbed molecule plays an important role. In fact, the clear different responses of the different models for methane and nitrogen, both apolar molecules, on the introduced flexibility in the graphene sheet, indicates that the directionality of the methane molecule is more important than for nitrogen in the adsorption process. Indeed, in chapter 3, it was found that the different gas orientations compared to the graphene sheet lead to differences in the interaction energies of up to 1 kcal mol^{-1}. For nitrogen, we found differences of at most 0.6 kcal mol^{-1}.

From the adsorption isotherms, we can then obtain a converged uptake and as such we found an uptake of 14.9 mmol/g for the united-atom methane molecule on the rigid graphene sheet and 22.4 mmol/g, 21.7 mmol/g and 21.9 mmol/g on field 1, field 2 and field 2m, respectively. Aside from the stronger adsorption of the flexible sheets as found before, we see that field 1 and field 2m adsorb slightly more than field 2. It should be noted that field 1 and field 2m include a torsional term in the intramolecular force field for graphene, while field 2 does not. The extra flexibility seems thus to allow extra methane molecules to adsorb onto the graphene sheet. For the atomistic model, a less pronounced influence of the flexibility is seen: uptakes of 26.8 mmol/g, 26.8 mmol/g, 26.0 mmol/g and 27.0 mmol/g are found for field 0, field 1, field 2 and field 2m, respectively.

The current target for methane adsorption was set at 0.5 gram(CH_4) per gram(sorbent) by the US Department of Energy (DoE) [36]. We found an amount that varies between 0.24 gram(CH_4) per gram(sorbent), equalling 14.9 mmol/g, for

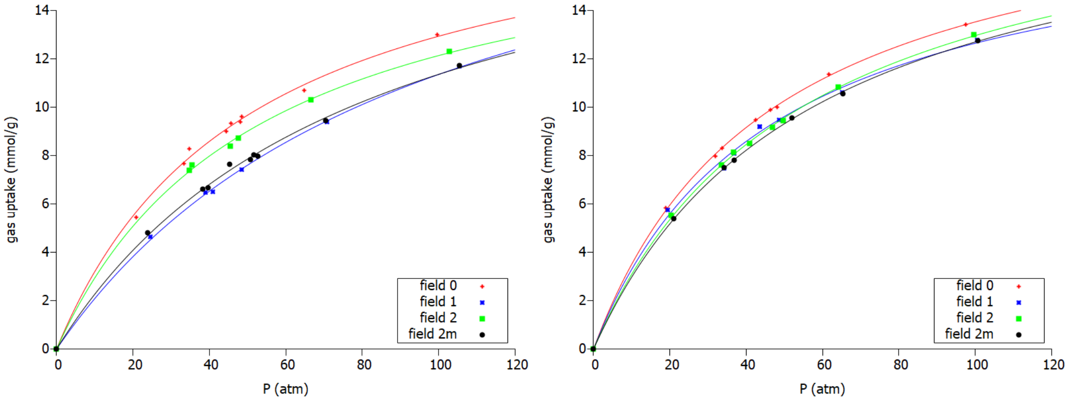

united-atom

atomistic

FIGURE 4.2: Adsorption isotherms using the united-atom model (left) and the atomistic model (right) for the pure nitrogen adsorption on the four different graphene sheets

the rigid sheet using the united-atom model and 0.43 gram(CH_4) per gram(sorbent), equalling 27.0 mmol/g for field 2m using the atomistic model, confirming the status of graphene as promising material for methane adsorption. Furthermore, comparison can be made with the work by Gadipelli et al. [39], where an uptake of 14.5 mmol/g was measured experimentally on one hand and an uptake of 30 mmol/g on a differently prepared graphene sheet. These ranges coincide once again rather well with our results.

The adsorption isotherms for nitrogen predict a much lower adsorption capacity of the graphene sheet for nitrogen than for methane. Indeed, the maximum uptake of nitrogen we found, using the atomistic model in combination with the rigid sheet, was 11.9 mmol/g, which is much lower than the minimal uptake of 14.9 mmol/g found for methane, using the united-atom model in combination with the rigid sheet. Furthermore, the latter was shown to strongly underestimate the amount of methane adsorbed in comparison with the remaining results. For the united-atom model, the rigid sheet predicts an uptake of 11.3 mmol/g of nitrogen, while the flexible sheets predict a lower uptake of 9.4 mmol/g, 10.6 mmol/g and 9.5 mmol/g for field 1, field 2 and field 2m, indicating once again a correlation between the resulting uptake and the inherent flexibility built in the force field. For the atomistic nitrogen, the differences found are much smaller while the trend is preserved with the rigid sheet adsorbing 11.9 mmol/g and the flexible sheets adsorbing 11.1 mmol/g, 11.3 mmol/g and 11.0 mmol/g for field 1, field 2 and field 2m, respectively. These results compare well with previous calculations by Apriliyanto et al. [185] who predicted, although on a different graphene-based graphtryine membrane, an uptake of 7.6 mmol/g.

4.1.3 Adsorption Behavior

In a second protocol, we just simulated a fixed amount of gas molecules in contact with the graphene sheet. 150 (14.9 mmol/g), 250 (24.8 mmol/g) or 350 (34.7 mmol/g) molecules were, in separate simulations, distributed randomly over the simulation box whereby again care was taken to leave 5 Å between the involved molecules, the simulation box edges and the graphene sheet. Given the size of our simulation box, these numbers of molecules amount to 1.7 10^{-3} molecules/$Å^3$, 2.8 10 $^{-3}$ molecules/$Å^3$ and 4.0 10^{-3} molecules/$Å^3$. The systematic increase allows for monitoring how the gas behaves for different amounts of molecules in the simulation box while the simulations are totally uncorrelated from each other. Screenshots of the simulations with 350 methane molecules in contact with the four different graphene sheets are shown in figure 4.3. In the screenshots, it is first of all possible to see the different behavior of the sheets themselves. Whereas the rigid sheet is completely straight, there is curving and bending in the three flexible sheets. In the fields with a torsional term, field 1 and field 2m, the movements look more like regular waves through the graphene sheet, while for field 2, the movements appear more irregular.

Figure 4.4 shows the z-density profiles for the united-atom methane adsorption on the four graphene sheets. It is seen that the four different graphene sheets all show a large first adsorption peak at about 3.5 Å on both sides of the graphene sheet. All fields show a single adsorption layer only, without presence of gas molecules or a gas phase in the first simulation with 150 methane molecules. This indicates that all the 150 methane molecules are accomodated in the first adsorption layer, which is supported by the results of the first protocol whereby up to 156 molecules were adsorbed for the rigid graphene sheet and up to 231 molecules were adsorbed for the flexible sheets. The rigid sheet, however, shows a very slight second adsorption layer meaning that accomodating 150 molecules in the first adsorption layer is not as easy as for the flexible sheets. In the simulation of 250 methane molecules, the first adsorption layer is higher for the flexible sheets than for the rigid one, which could be expected from the previously mentioned results of the first protocol. The excess amount of molecules that cannot be accomodated in the first adsorption layer for the rigid sheet is divided over a second adsorption layer and a small gas phase. The flexible sheets also have a second adsorption layer and a small gas phase, but to a smaller extent than the rigid sheet since they can accomodate more of the molecules in the first adsorption layer. When 350 molecules are adsorbed, something interesting is seen, the first adsorption layers of the flexible sheets do not grow in size anymore, while the rigid one does. It seems like the flexible sheets already reached full loading in the first layer with less molecules, while for the rigid sheet more molecules are needed in the box to force the same loading. The first protocol did indeed show, that no graphene sheets adsorbed more than 250 molecules and therefore a small amount of molecules is left for a second adsorption layer and a small gas phase. Furthermore, the rigid sheet shows a slightly lower second adsorption peak and slightly more molecules in the gas phase than the flexible sheets.

Two things are noteworthy on the adsorption peaks itself, firstly the peaks are broader for the flexible graphene sheets. This makes sense since there is intrinsic movement in the sheet which will be followed slightly by the adsorbed molecules leading to a larger spread over the z-coordinate. Secondly, the peaks for the flexible sheets are slightly shifting along the z-coordinate. This is an artefact of the simulation whereby, in the case of the rigid graphene, the carbon molecules of the graphene sheet were completely frozen in space. In the flexible sheets, however, they were left free to allow for the vibrations of the intramolecular force field, causing a slight drift in the z-direction of the sheet as a whole. The drift is limited to a about 0.2 Å only and

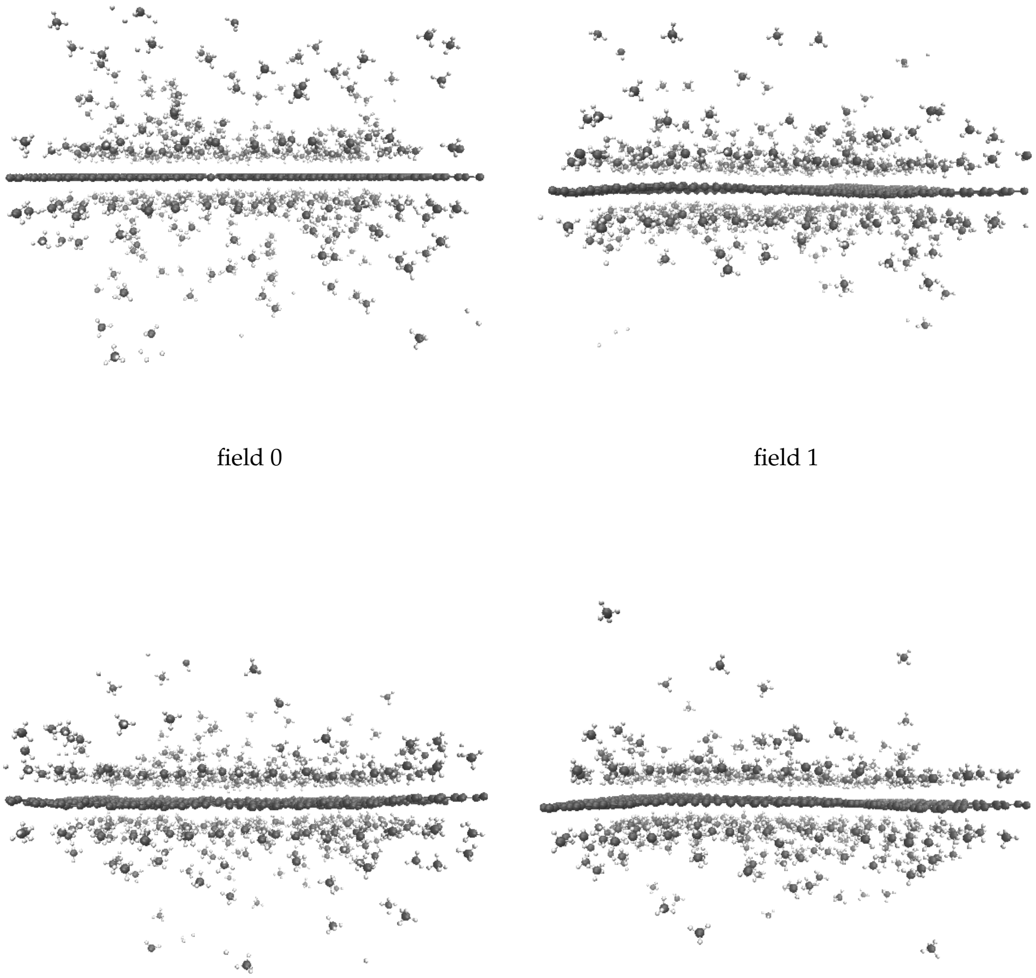

field 0 field 1

field 2 field 2m

FIGURE 4.3: Screenshots of the simulations of methane gas on the four graphene sheets using the united-atom model for 350 methane molecules.

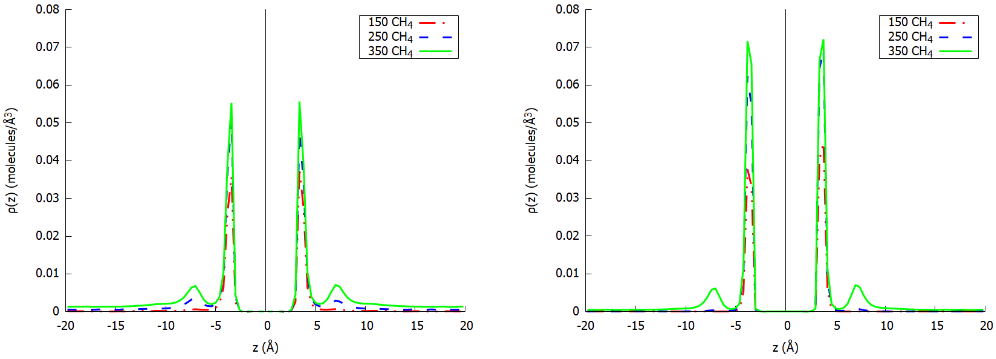

united-atom

field 0

atomistic

field 0

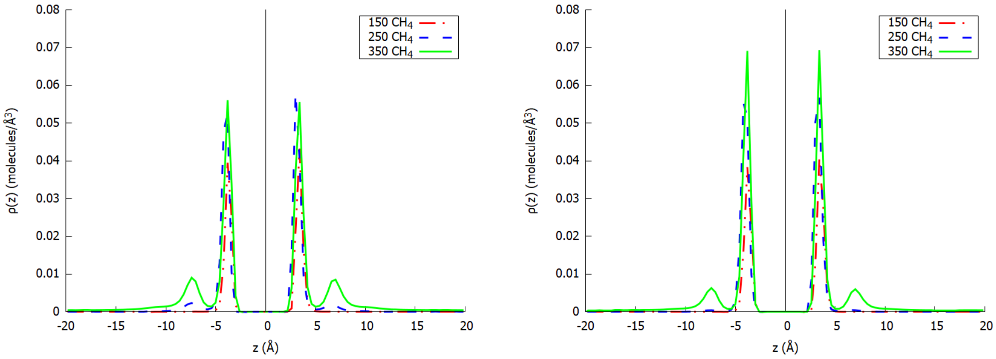

united-atom

field 1

atomistic

field 1

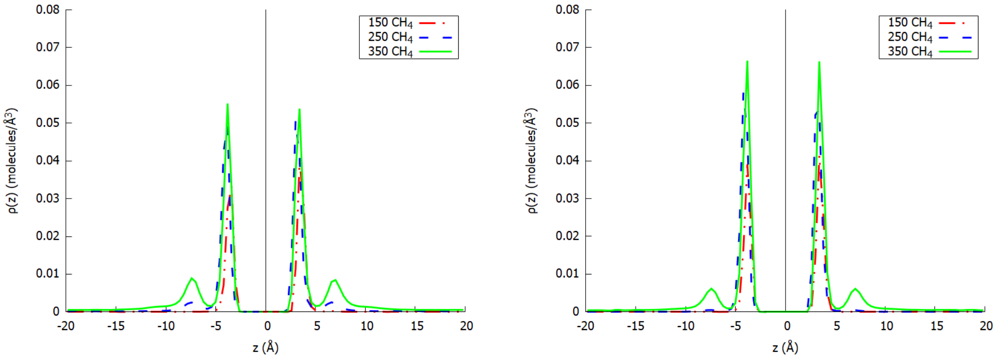

united-atom

field 2

atomistic

field 2

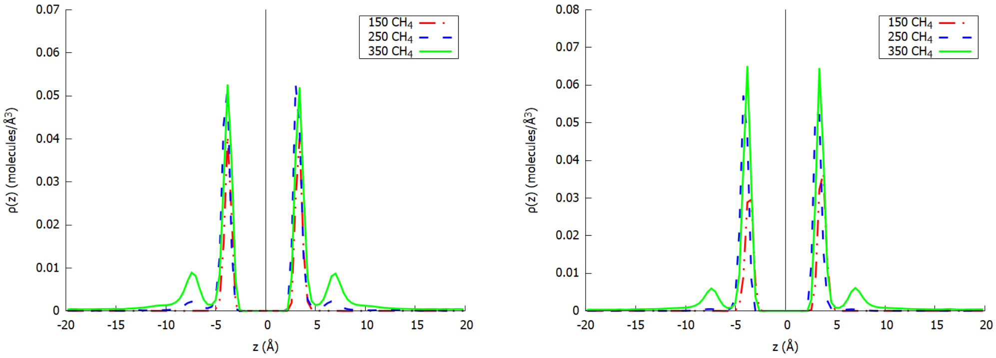

united-atom

field 2m

atomistic

field 2m

FIGURE 4.4: Absolute z-density plots for the four fields considered using the united-atom model (left) and atomistic model (right) for methane for simulations with 150, 250 and 350 methane molecules.

to make sure this did not influence the results, we did some test simulations whereby one carbon atom of the graphene sheet was frozen. This allowed the intramolecular force field to create the necessary vibrations, while preventing the graphene sheet from drifting. No significant influence on the results was found.

The same second protocol was also used for the pure methane adsorption on graphene using an atomistic model for methane, the z-density profiles are given in figure 4.4. As was found in the first protocol, the atomistic model shows very little difference in behavior between the rigid and the flexible graphene sheets. For all four sheets, the first simulation of 150 molecules shows all molecules adsorbed in the first adsorption layer which is consistent with protocol 1 where it was found that all sheets adsorb about 270 molecules. For the same reason, there appears only one adsorption layer for the simulation with 250 methane molecules. Again, all of them are easily accomodated in the first adsorption layer. Only in the final simulation with 350 methane molecules, then, is the amount of 270 molecules that can be accomodated in the first layer exceeded and do we see the formation of a substantial second adsorption layer.

One last interesting thing to note about the reported z-density profiles is the fact that the peak of the first adsorption layer is always located at about 3.5 Å from the graphene sheet, while the equilibrium distance of the force field is 3.938 Å. Most of the molecules are concentrated within the adsorption layer, while very little molecules are outside this layer. This clustering of the molecules pulls the layer slightly closer to the sheet than could be expected based on the force field.

For nitrogen, the same protocol was applied and 150, 250 and 350 molecules were simulated in contact with the four different graphene sheets under study. From the snapshots in figure 4.5, it is visible that a lot less molecules are adsorbed than methane molecules were as was suggested as well in the previous section. There is a gas phase consisting of many more molecules for nitrogen than there was for methane. Although, there is still a clear first adsorption layer visible, it is less populated than was the case for methane.

The z-density profiles for the adsorption of the united-atom and atomistic nitrogen models on the four different graphene sheets is shown in figure 4.6. As previously seen, there is very little difference between the performance of the united-atom and the atomistic model. There is, however, a difference between the behavior on the different graphene sheets. As observed before, the rigid sheet adsorbs more nitrogen molecules than the flexible ones as seen from the first adsorption layer. Furthermore, field 2 has an adsorption layer that is higher than the one for field 1 and field 2m, indicating that the extra flexibility introduced into the sheets limits the amount of molecules adsorbed. Furthermore, in all simulations and as suggested by the snapshots shown previously, there is a substantial gas phase present in the simulation box. These observations agree with the results from the previous section where it was suggested that the graphene sheet is saturated with nitrogen after adsorption of about 100 nitrogen molecules. The remaining molecules stay either in the gas

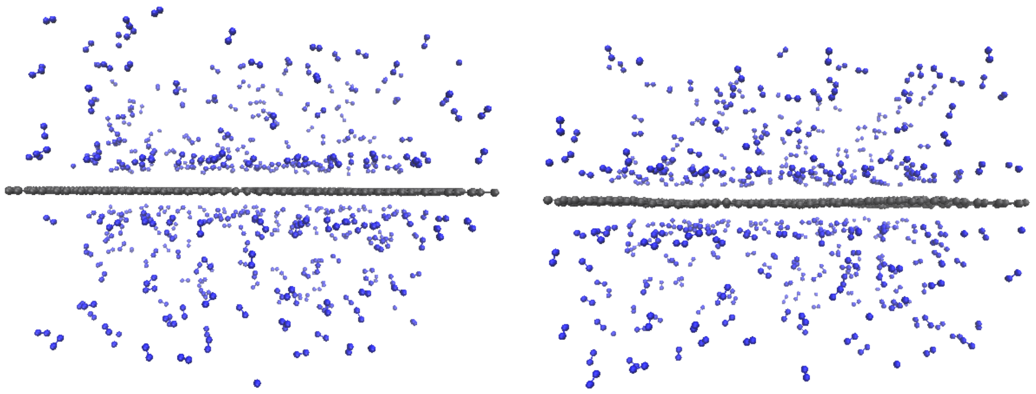

field 0 field 1

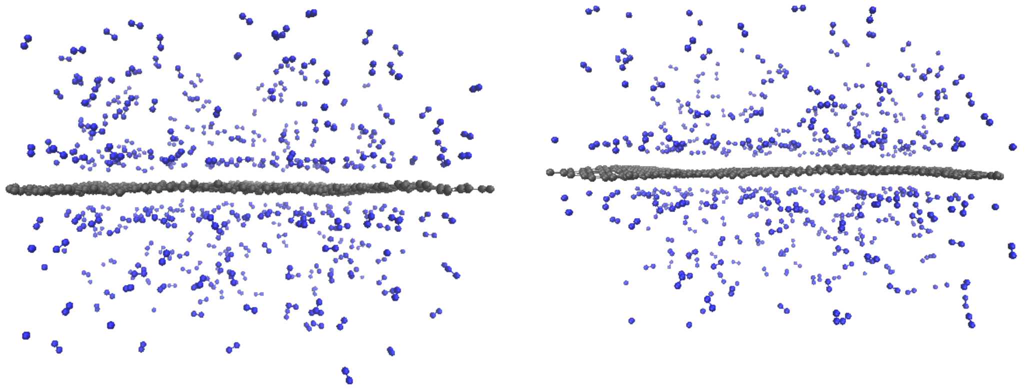

field 2 field 2m

FIGURE 4.5: Screenshots of the simulations of nitrogen gas on the four graphene sheets using the atomistic model for 350 nitrogen molecules.

phase or start forming a substantial second adsorption layer. Upon addition of more molecules, the extra molecules are divided over the first and second adsorption layer and the gas phase. For methane, the molecules all tried to enter the first adsorption layer and only when more space was left available, were molecules forced to populate the second adsorption layer or the gas phase. For nitrogen, however, there is always a dynamic equilibrium between the the first and second adsorption layer and the gas phase, which makes sense since nitrogen is known to form multilayers.

4.1.4 Methane/Nitrogen Mixture

The stronger affinity of graphene, either rigid or flexible, for methane compared to nitrogen has been clearly demonstrated in the previous section. Therefore, the simulation of the methane/nitrogen mixture is of interest to, first of all, verify that methane and nitrogen can be separated by graphene as expected and, secondly, to

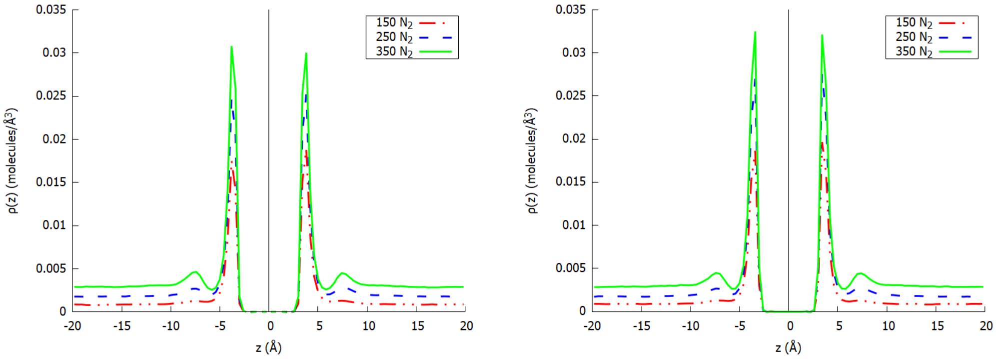

united-atom

field 0

atomistic

field 0

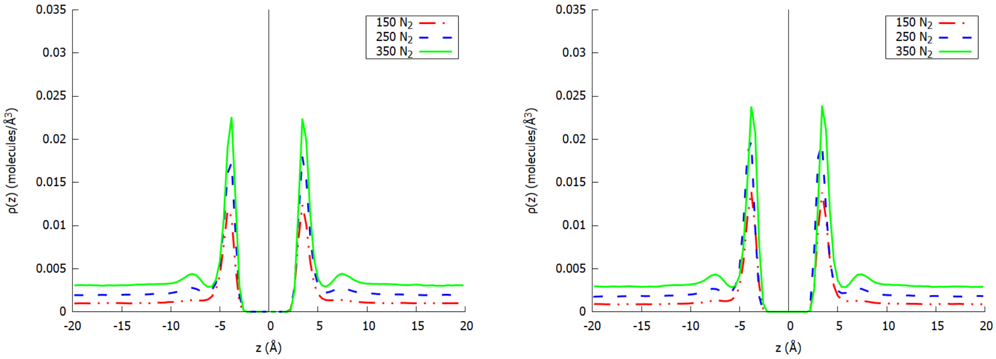

united-atom

field 1

atomistic

field 1

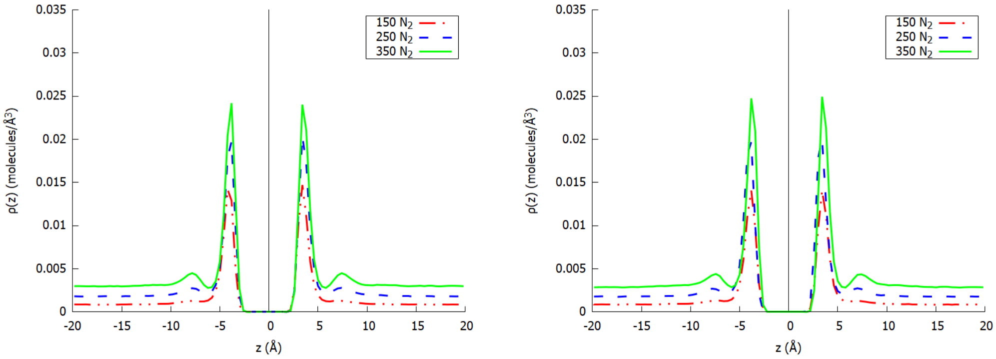

united-atom

field 2

atomistic

field 2

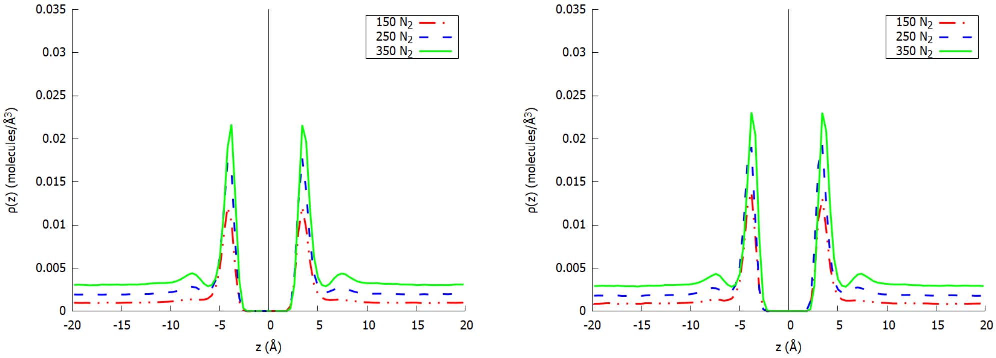

united-atom

field 2m

atomistic

field 2m

FIGURE 4.6: Absolute z-density plots for the four fields considered using the united-atom model (left) and the atomistic model (right) for nitrogen for simulations with 150, 250 and 350 methane molecules.

study the influence of the flexibility of the graphene sheet on this process. The protocols used for the methane/nitrogen mixture are in essence the same as the ones described for the pure methane and nitrogen gases, previously. For the first protocol — the deletion of non-adsorbed molecules and randomly adding 100 new ones — the total amount of molecules was equally divided between the two molecule types and, thus, 50 methane and 50 nitrogen molecules were always added.

The results for the united-atom model are given in table 4.5 whereby the results for the total amount of molecules on one hand and the results for the methane and nitrogen within the mixture are given on the other. More specifically, the total amount of molecules (methane and nitrogen combined) in the simulation box is given together with the total adsorbed mole fraction. Subsequently, the initial mole fraction of methane within the mixture is given as are the mole fractions of methane and nitrogen adsorbed onto the graphene sheet at the end of the simulation. A first observation is that the amount of simulations needed to reach convergence was a lot larger than for the pure gases. This is mainly caused by the fact that the mixture composition changes with every subsequent simulation, leading to different equilibria every time. The mixture composition changes with every simulation because more and more methane molecules enter the system, while nitrogen molecules are being pushed out. Indeed, it can be seen from the mole fractions that with every simulation a larger proportion of methane molecules is adsorbed than nitrogen molecules. The total amount of molecules that is adsorbed is initially very high, with percentages of 76 % for the rigid sheet, 84 % for field 1 and field 2 and 89 % for field 2m, while this percentage drops fast in subsequent simulations. Since the non-adsorbed molecules are eliminated, more nitrogen molecules disappear from the system than methane molecules leading to a larger proportion of methane molecules in the next, leading to even more methane molecules adsorbing and more nitrogen molecules being pushed out and so on. Indeed, in the initial simulations, 66 % of the nitrogen was adsorbed for the rigid sheet, 70 % for field 1 and field 2 and 78 % for field 2m, while this percentage drops much faster than for the total amount of molecules in the following simulations. Initially, the low amount of methane molecules leaves space for the nitrogen molecules, but as more and more methane molecules are introduced into the box, less space remains available for nitrogen. This process stabilizes at a situation where about 70 % of the total molecules are methane and only 30 % is nitrogen, consistently over the four different graphene sheets considered. Combining this with the much larger mole fraction of methane molecules adsorbed, we can indeed conclude that the united-atom model predicts the graphene sheet to be very effective separating methane from nitrogen.

Looking at the total amount of molecules that is adsorbed, it is seen that the rigid sheet adsorbs about 60 % of the total amount of molecules, while the flexible sheets all adsorb around 65 % of the total amount of molecules. This could be expected from the pure gas results, since this behavior follows the trend of the methane results which constitutes the larger part of the molecules in the mixture after a number of

TABLE 4.5: Simulation results for the methane/nitrogen mixture using a united-atom approach for the four intramolecular force fields considered in this work. Results are represented for the total amount of molecules (methane + nitrogen) and the separate methane and nitrogen adsorption within the mixture.

	total		CH_4		N_2
field	molecules	$X_{adsorbed}$	$X_{initial}$	$X_{adsorbed}$	$X_{adsorbed}$
field 0	100	0.76	0.5	0.86	0.66
	176	0.65	0.53	0.80	0.48
	214	0.63	0.56	0.81	0.39
	236	0.58	0.64	0.68	0.40
	237	0.61	0.64	0.73	0.39
	245	0.65	0.66	0.74	0.47
	259	0.61	0.65	0.74	0.36
	259	0.58	0.68	0.70	0.32
	250	0.57	0.70	0.71	0.25
field 1	100	0.84	0.50	0.98	0.70
	184	0.70	0.54	0.89	0.47
	228	0.67	0.60	0.85	0.40
	253	0.63	0.66	0.77	0.36
	260	0.63	0.69	0.76	0.33
	264	0.67	0.71	0.81	0.31
field 2	100	0.84	0.50	0.98	0.70
	184	0.73	0.54	0.90	0.53
	235	0.68	0.60	0.82	0.46
	259	0.65	0.64	0.83	0.33
	268	0.65	0.70	0.78	0.32
	274	0.67	0.72	0.80	0.33
field 2m	100	0.89	0.50	1.00	0.78
	189	0.71	0.53	0.89	0.52
	235	0.66	0.60	0.80	0.46
	255	0.65	0.63	0.77	0.44
	266	0.66	0.66	0.83	0.32
	275	0.67	0.71	0.83	0.30

subsequent simulations. Indeed, for methane, keeping in mind that the initial mole fraction of methane is similar for all four fields, the rigid sheet adsorbs about 70 % of the available methane molecules, while the flexible sheets adsorb about 80 %. The differences for nitrogen are less pronounced and less influential on the total amount of molecules given their much lower initial mole fractions.

Looking at the results in table 4.6 using the atomistic models for both methane and nitrogen, we see that the seperation is predicted to be even more efficient. Methane reaches a mole fraction of up to 0.80 for the rigid sheet and 0.85 for the flexible ones, while the amounts of methane adsorbing are so high, that effectively all nitrogen molecules are forced into gas phase, leaving adsorbed mole fractions of 0.00 for the flexible sheet and 0.07 for the rigid one. This is not surprising when keeping in mind the results of the pure gases, the atomistic methane was predicted to adsorb very strongly to graphene and thus poses a much stronger competition to

TABLE 4.6: Simulation results for the methane/nitrogen mixture using an atomistic approach for the four intramolecular force fields considered in this work. Results are represented for the total amount of molecules (methane + nitrogen) and the separate methane and nitrogen adsorption within the mixture.

	total		$\mathrm{CH}_{scriptscriptstyle4}$		$\mathrm{N}_{scriptscriptstyle2}$
field	molecules	X_{adsorbed}	X_{initial}	X_{adsorbed}	X_{adsorbed}
field 0	100	0.83	0.50	1.00	0.66
	183	0.74	0.55	1.00	0.42
	235	0.73	0.64	1.00	0.26
	272	0.74	0.74	0.97	0.09
	300	0.79	0.81	0.96	0.07
field 1	100	0.75	0.5	1.00	1.00
	175	0.75	0.57	0.99	0.44
	232	0.72	0.64	0.99	0.23
	267	0.74	0.54	0.97	0.19
	305	0.78	0.79	0.98	0.02
	337	0.78	0.85	0.92	0.00
field 2	100	0.80	0.50	1.00	0.60
	180	0.72	0.56	0.99	0.38
	229	0.76	0.65	0.98	0.34
	268	0.74	0.73	0.98	0.08
	298	0.78	0.81	0.98	0.00
	333	0.76	0.85	0.89	0.02
field 2m	100	0.80	0.50	1.00	0.60
	180	0.69	0.56	0.99	0.33
	225	0.75	0.66	0.99	0.28
	269	0.75	0.74	0.98	0.10
	302	0.79	0.81	0.97	0.02
	338	0.78	0.85	0.92	0.02

nitrogen. Indeed, after only 5 or 6 simulations, the nitrogen is (almost) completely removed from the graphene sheet. Once nitrogen is completely removed from the first adsorption layer, the adsorption numbers for methane are very simular to the ones for the pure methane gas with around 260 molecules adsorbed. The total amount of molecules behaves very similar for all sheets as it is dictated by the adsorption of methane, which, for the atomistic model, predicted little difference between the rigid and the flexible sheets.

Following up on these results, we have then, as for the pure methane and nitrogen gases, simulated the adsorption of 150 (75 CH_4 + 75 N_2), 250 (125 CH_4 + 125 N_2) and 350 (175 CH_4 + N_2) molecules in total. The screenshots for 350 molecules using the atomistic model are shown in figure 4.7. The expected separation of the methane and nitrogen is immediately visible: methane molecules are grouped together in a first adsorption layer close to the graphene sheet, while the nitrogen molecules mainly stay in gas phase, further away from the graphene. Altough there is some exchange of the two molecules, visually it looks quite limited.

The z-density plots for these simulations, together with the ones from the simulations with the united-atom model are shown in figure 4.8. The united-atom model

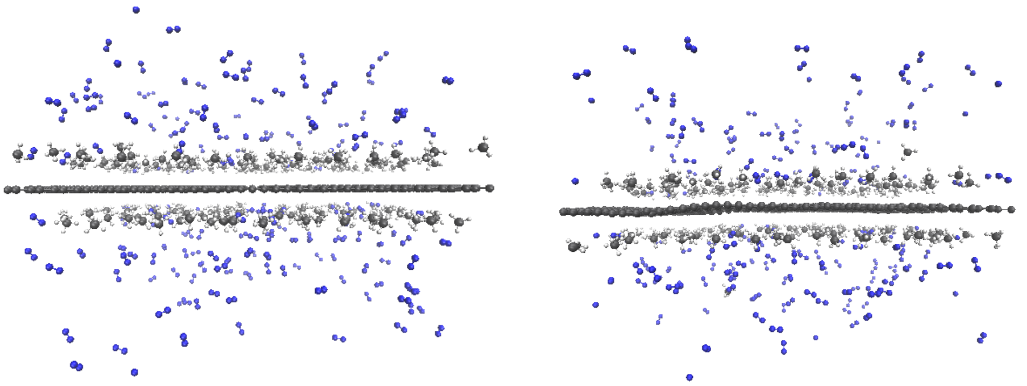

field 0 field 1

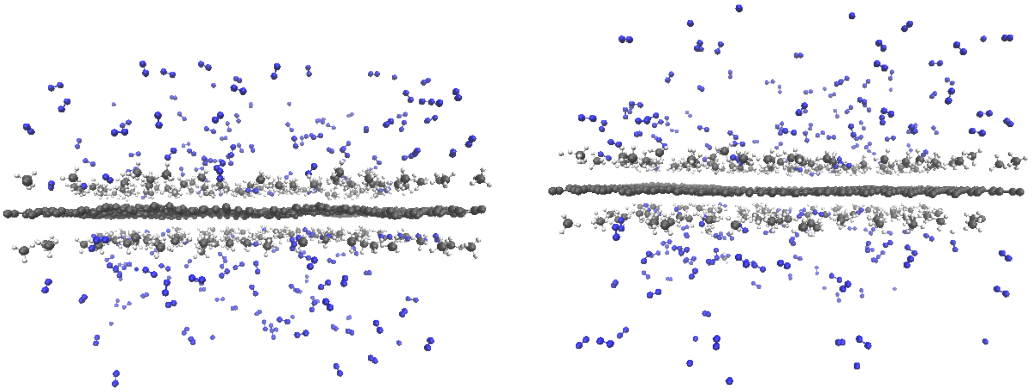

field 2 field 2m

FIGURE 4.7: Screenshots of the simulations of the methane/nitrogen mixture on the four graphene sheets using the atomistic model for 175 methane and 175 nitrogen molecules

predicts a lower methane adsorption than the flexible sheets in accordance with the results for the pure methane gas. Although the adsorption peaks of the flexible sheets reach less heigth, the larger broadness of the peaks as compared to the rigid case, makes up for that leading to a larger area. Apart from the omnipresent strong first adsorption layer, we also see the appearance of a second adsorption layer in the simulation with 350 molecule. For the simulations with 150 and 250 molecules, 75 and 125 methane molecules respectively, all methane was able to enter the first adsorption layer which is no surprise given the previously found saturation values for the respective graphene sheets. For the atomistic model, it is seen that in all three simulations, all methane molecules are located within the first adsorption layer which can be understood by taking into account that only 75, 150 and 175 methane molecules are present in the three simulations respectively. This is an amount that can be accomodated easily within the first adsorption layer of all four graphene sheets when using the atomistic model for methane as was shown earlier. Again, we find that the atomistic methane model is predicted to have a larger uptake than the united-atom model.

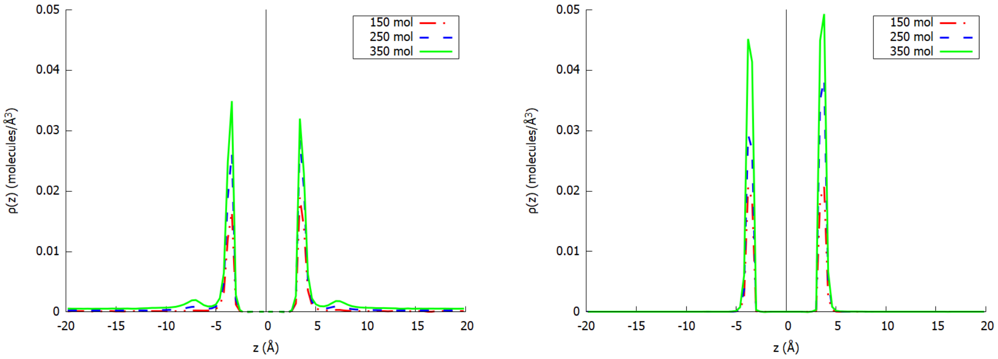

united-atom

field 0

atomistic

field 0

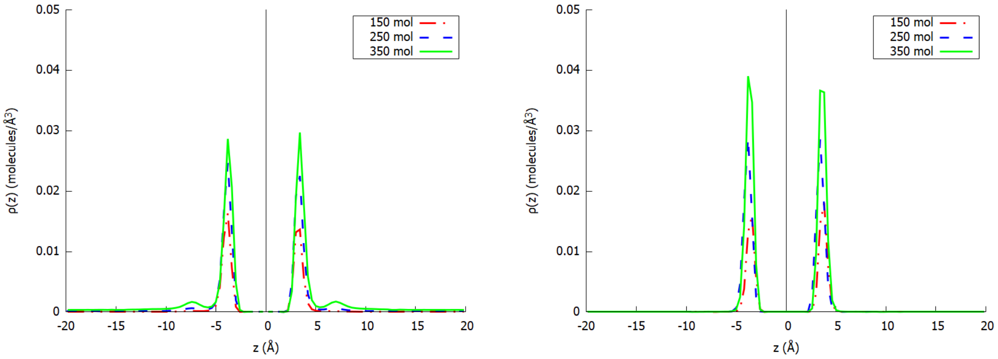

united-atom

field 1

atomistic

field 1

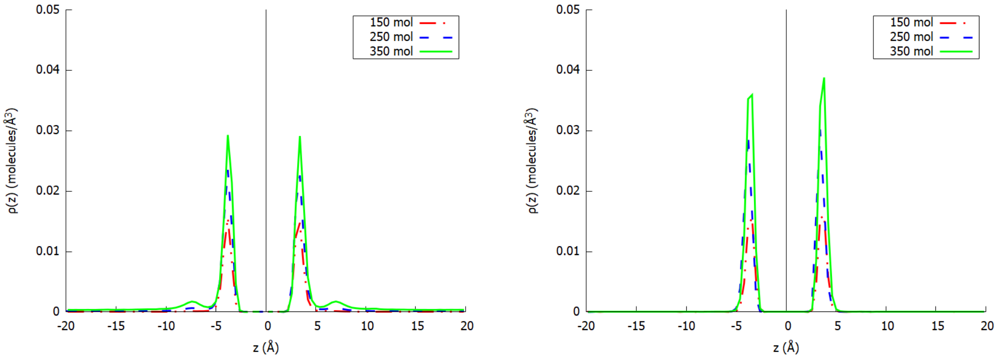

united-atom

field 2

atomistic

field 2

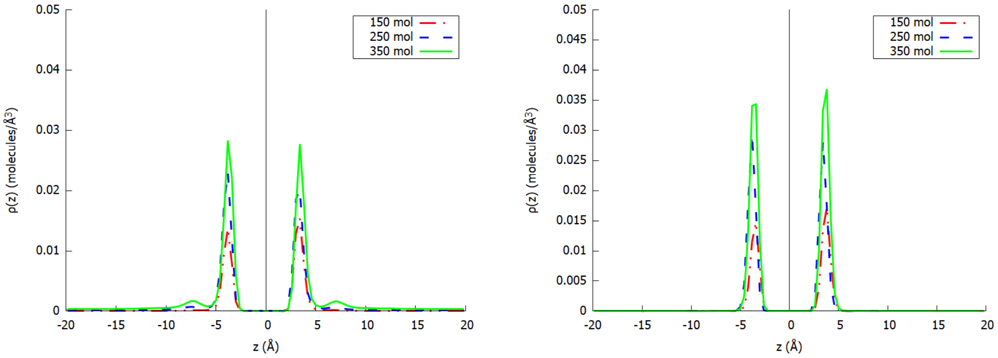

united-atom

field 2m

atomistic

field 2m

FIGURE 4.8: Absolute z-density plots for the four fields considered using the united-atom (left) and the atomistic (right) models for methane within the methane/nitrogen mixture

The z-density profiles of the nitrogen within the same mixture is shown in figure 4.9. As expected, a lot less nitrogen molecules are adsorbed in the first adsorption layer than was the case for the pure nitrogen gas. Clearly, the nitrogen molecules take up the space that is left by the methane molecules in the first adsorption layer, while the remaining nitrogen molecules start forming a relatively strong second adsorption layer and gas phase. For the united-atom model, the first adsorption layer does not grow much more after the first simulation. For the simulation with 150 molecules, most nitrogen that does not enter the first adsorption layer stays in gas phase. In the subsequent simulations with 250 and 350 molecules, we see, however, the formation of a strong second adsorption layer whereby, once again, the rigid sheet adsorbs slightly more nitrogen molecules. The behavior for the atomistic model is quite different as the first adsorption layer for the simulations with the most (350) molecules, has the lowest peak compared to the other two simulations (150 and 250 molecules). Clearly this is caused by the methane and not by nitrogen itself. The atomistic methane has been shown to adsorb very strongly to the graphene and to allow a large amount of molecules in the first adsorption layer. This leads to a very strong competition with the nitrogen molecules whereby the latter are denied entrance to the first adsorption layer. In the first simulation with 150 molecules, the first adsorption layer is not completely saturated yet by methane molecules and thus nitrogen molecules are allowed to enter. When more methane molecules are present, less space remains available and nitrogen is forced into a second adsorption layer and the gas phase. Here too, there is a difference between the behavior of the rigid sheet and the flexible graphene since the former allows almost twice as much nitrogen molecules in the first adsorption layer for the simulation with 150 molecules.

Figures 4.10 and 4.11 show the adsorption isotherms of the methane and nitrogen within their equimolar mixture. These adsorption isotherms allow for a better comparison of the uptakes of the different systems as compared to the z-density profiles discussed in previous paragraphs. As seen before, there is a different behavior between the united-atom and the atomistic models for the methane molecules. The previous observation that the uptake for the rigid sheet is substantially lower than for the flexible ones for the united-atom model is confirmed. For the atomistic sheet, on the other hand, there is again little difference found, although the rigid sheet does seem to adsorb slightly more than the flexible sheets. In general, the atomistic model again predicts a much larger uptake than the united-atom model.

The united-atom nitrogen shows a converged adsorption isotherm within the investigated pressure range. The rigid sheet adsorbs slightly less than the flexible sheets and converges somewhat slower as well. For the atomistic case, it is striking that the uptake diminishes strongly when going to the simulation with 350 molecules. This can be appreciated by considering the very strong methane uptake predicted by the atomistic model. The large amount of methane molecules that enter the first adsorption layer allow very little space for the nitrogen molecules to

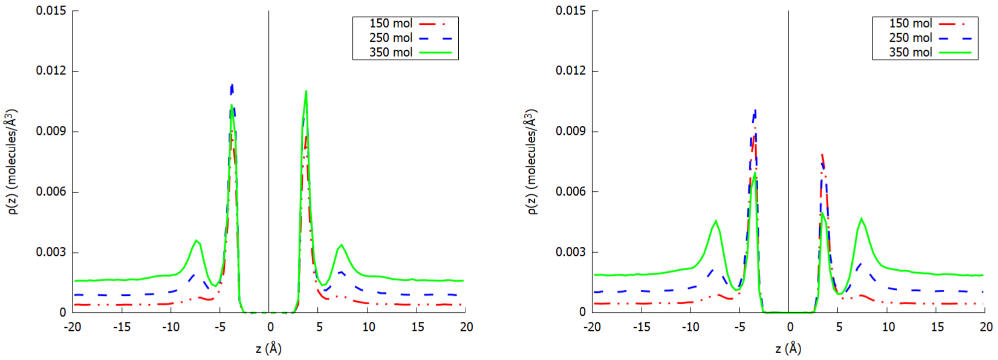

united-atom

field 0

atomistic

field 0

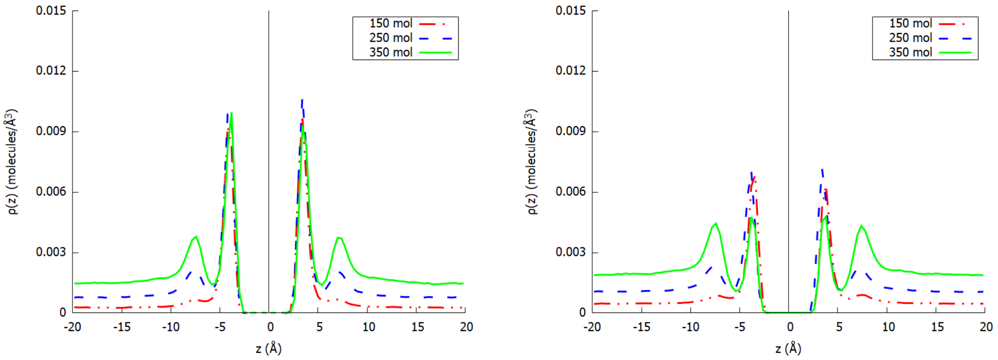

united-atom

field 1

atomistic

field 1

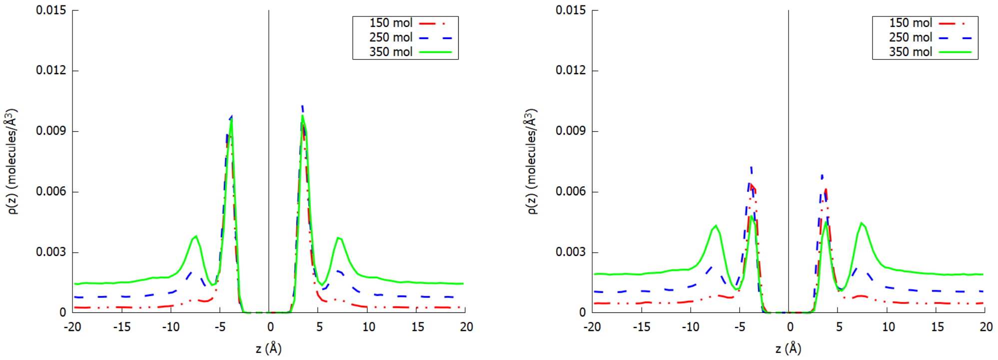

united-atom

field 2

atomistic

field 2

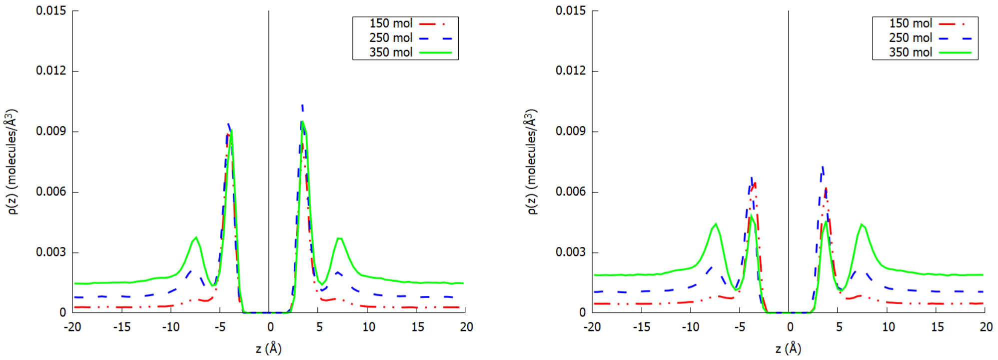

united-atom

field 2m

atomistic

field 2m

FIGURE 4.9: Absolute z-density plots for the four fields considered using the united-atom (left) and the atomistic (right) models for nitrogen within the methane/nitrogen mixture

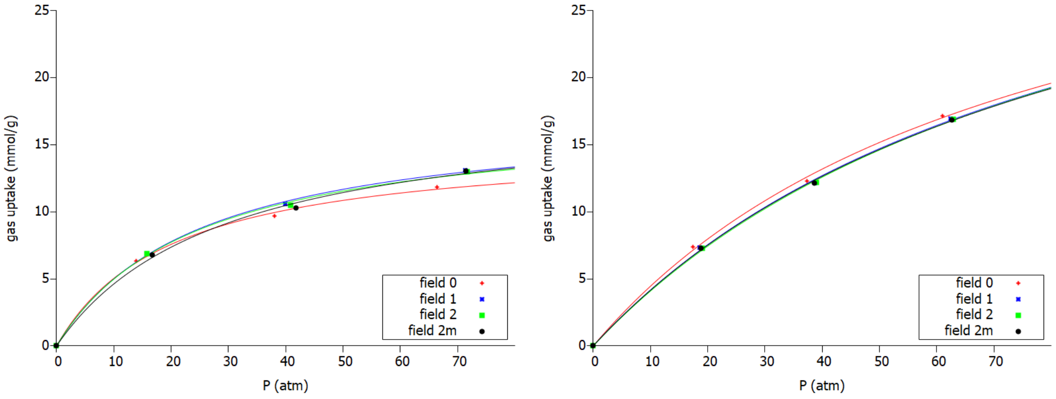

united-atom

atomistic

FIGURE 4.10: Adsorption isotherms using the united-atom model (left) and the atomistic model (right) for the methane adsorption on the four different graphene sheets within the methane/nitrogen mixture

enter. Because of this, we have only used the first two simulations to fit the adsorption isotherm as the Langmuir equation is not intended to deal with such a drop in the uptake, but more importantly, this drop is not caused by nitrogen itself, but by methane instead. A similar reasoning explains the higher nitrogen uptake in the united-atom model: the united-atom methane adsorbs less strongly to the graphene sheet and thus allows more nitrogen to adsorb than the atomistic methane does.

Finally, the selectivity of methane over nitrogen was calculated, using equation 4.5, via the uptakes predicted by the adsorption isotherms at the three different pressures coinciding with the three simulations that were done as presented in figure 4.12. For the united-atom model, the rigid sheet behaves again somewhat different than the flexible ones. The flexible sheets show a linear rise of the selectivity

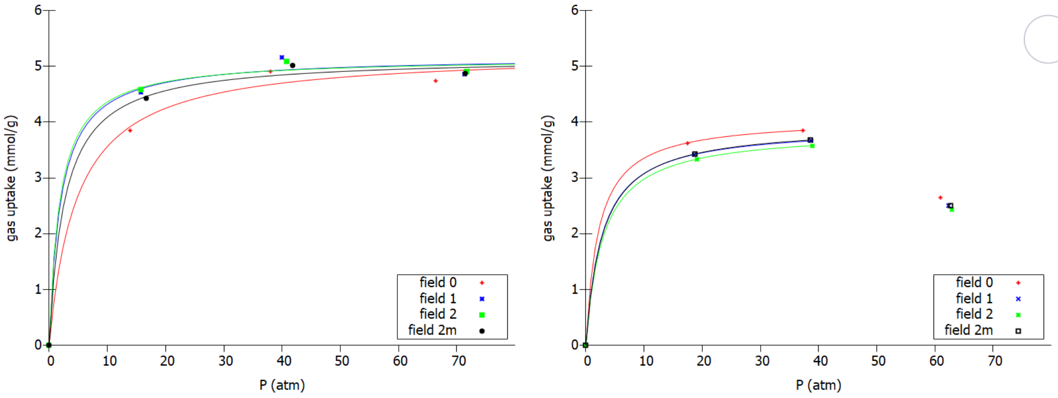

united-atom

atomistic

FIGURE 4.11: Adsorption isotherms using the united-atom model (left) and the atomistic model (right) for the nitrogen adsorption on the four different graphene sheets within the methane/nitrogen mixture

witin the pressure range investigated, while the rigid sheet shows a slightly curved increase crossing the flexible curves at around 35 atm. The atomistic model, on the other hand, shows little influence of the flexibility on the selectivity which rises exponentially with increasing pressure. The stronger attraction of the atomistic methane favors the methane adsorption leading to an ever higher selectivity. In all cases, however, the selectivity is good and rises with rising pressure.

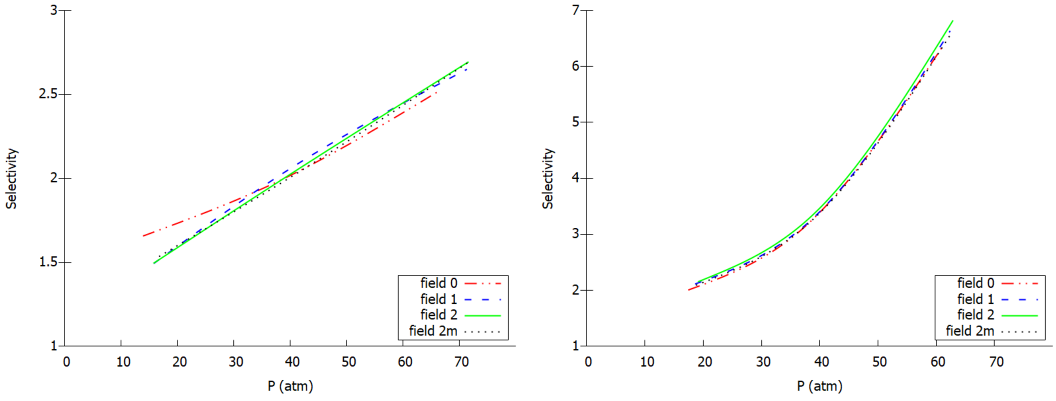

united-atom

atomistic

FIGURE 4.12: Selectivities for the methane/nitrogen mixture on the four different fields using a united-atom (top) and atomistic (bottom) model for the gas molecules

4.2 Adsorption of Carbon Monoxide on Flexible Graphene

In the previous section, we have considered graphene sheets exhibiting movements in and out of the plane, yet with idealized carbon-carbon distances. However, realistic graphene can represent different structural defects leading to variations in the length of the involved carbon-carbon bonds with consequences for the adsorption behavior. This effect is taken into account for the adsorption of carbon monoxide on graphene by simulating graphene sheets with initial carbon-carbon distances between 1.39 Å and 1.42 Å. Furthermore, we want to investigate the temperature dependence of such systems by running simulations at different temperatures, namely 77 K, 150 K, 200 K and 300 K. The methodology of this section is the same as described in section 4.1.1, except that somewhat less time steps were simulated: 1,300,000 time steps, 300,000 of which for equilibration. Obviously, the simulation box was adapted in the x- and y-direction to the new dimensions of the graphene sheet according to the chosen carbon-carbon distance to avoid defects at the edges. The flexibility was modeled via the same intramolecular potentials that were presented in the previous section with the remark that, at the moment that this study was conducted, the field 2m article had not been published yet. For this reason, only field 1 and field 2 will be compared in this section.

4.2.1 Simulation Results

To study the behavior of the CO molecule on the different graphene sheets during adsorption, different simulations were performed with 100 and 200 carbon monoxide molecules positioned randomly in the simulation box. Figure 4.13 shows the absolute z-density profile for field 1 using the different initial carbon-carbon distances and 100 carbon monoxide molecules. For the 1.42 Å equilibrium carbon-carbon distances in the graphene sheet, we find two well-defined sharp adsorption peaks as for the systems considered previously in this work. However, upon shortening the initial carbon-carbon distances, we find that the adsorption pattern apparently changes its behavior. The 1.41 Å distances give rise to two smaller, but broadly smeared adsorption peaks, while for the 1.40 Å distances, the peak becomes even broader and two smaller subpeaks start to appear. Finally, for 1.39 Å distances, two clearly distinct subpeaks are observed, leading to a very broad adsorption layer. Carefull analysis of the data, shows that these subpeaks are not due to multilayer adsorption, instead the adsorption layer follows the very strong vibrations of the graphene sheet. These vibrations become stronger upon decreasing carbon-carbon distance, since the bonds are more stressed under the force field which strives to obtain equilibrium distances larger than the set initial carbon-carbon bond. In fact, the vibration become so broad that large pockets are formed in the graphene sheet leading to distinct adsorption locations on the sheet, giving rise to subpeaks in the z-density profile. As said, this variation of bond lengths may be important in local defects of a realistic graphene sheet, leading to specific behavior of the adsorption layer in these regions although the effect on the total adsorption seems to be rather weak.

Absolute and relative z-densities for the simulations with 100 carbon monoxide molecules on graphene sheets using initial carbon-carbon distances of 1.39 Å are shown in figure 4.14, comparing the behavior of the three different fields. As just

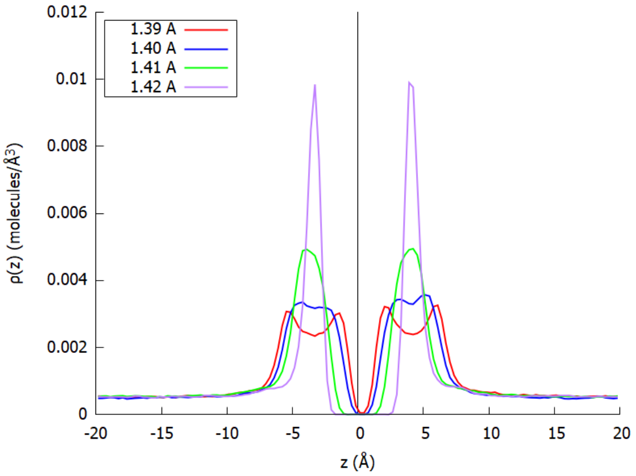

FIGURE 4.13: Influence of the initial C-C bond length in the graphene sheet on the absolute z-density plot using field 1.

described, we found the division into subpeaks for smaller carbon-carbon distances due tot the stress from the force field. Here, we can see that this is, not unexpectedly, depending on the flexibility that the force field introduces. Clearly, the rigid sheet (field 0) does not apply pressure on the carbon atoms to move, since all carbon atoms are fixed and we thus observe two large adsorption peaks on either side of the graphene sheet as found for all previous systems. However, we see that with increasing flexibility, remember the torsional term present in field 1 and not in field 2, we see that the peaks get lower and broader for field 2 and split in to subpeaks for field 1.

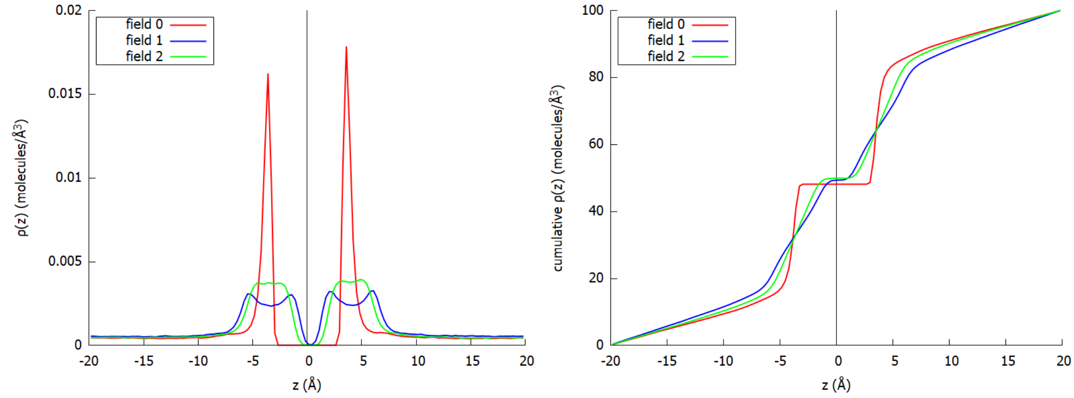

FIGURE 4.14: Absolute z-density profiles for the adsorption of CO on three different graphene sheets with a carbon-carbon distance of 1.39 Å (left). Cumulative z-density plot for the adsorption of CO on three different graphene sheets with a carbon-carbon distance of 1.39 Å (right).

From the cumulative density at the right side of figure 4.14, the slope of the z-density in the region of least density (gas phase) can be used to estimate the gas density in the simulation box. As with methane and nitrogen adsorption, it is seen that there is an influence of introducing flexibility in the graphene sheet. Furthermore, it is seen that the cumulative density behaves slightly different for the different fields. In the region of the first adsorption layer, the molecules are smeared out over a larger region for the flexible sheets because of the movement of the sheet itself as was explained before. Looking away from the adsorption layer, there is substantial gas phase present indicated by the increasing values with z. The gradient of this line in the gas phase region is a measure for the gas density in this area and is slightly different for the different sheets. In order to quantify this effect in further detail, the gas density was measured from the gradient and compared for different temperatures, different amount of CO molecules on the different fields.

As such, the densities for simulations at temperatures of 77K, 150K, 200K and 300K are compared in table 4.7. It is visible that an increase in temperature leads to an increased gas density. Indeed, the differences are quite high, going from around 1 g L^{-1} or below at 77 K for all fields and carbon-carbon distances to over 15 g L^{-1}

TABLE 4.7: Gas density and uptake results from MD simulations with 100 CO molecules at different temperatures using the different fields of study and different carbon-carbon distances.

	temperature (K)	gas density (g L^{-1})		mol. ads.	
		1.39 Å	1.42 Å	1.39 Å	1.42 Å
field 0	77	0.860	-	98.4	-
	150	1.712	1.590	96.9	97.1
	200	4.196	4.675	92.4	91.5
	300	15.727	16.664	71.5	69.8
field 1	77	1.366	1.314	97.5	97.6
	150	3.621	5.535	93.4	90.0
	200	7.446	9.986	86.5	81.9
	300	18.105	19.879	67.2	64.0
field 2	77	1.002	0.439	98.2	99.2
	150	1.602	1.767	91.7	69.8
	200	4.521	5.582	91.8	89.9
	300	16.274	17.904	70.5	67.5

and even up to 19.879 g L^{-1} for field 1 and carbon-carbon distances of 1.42 Å. The higher temperature gives more kinetic energy to the individual CO molecules allowing them to easier overcome the attraction of the graphene sheet to stay in gas phase and thus leading to lower adsorption rates.

Further in the table, we can compare in more detail the influence of the initial carbon-carbon distance on the adsorption process. We should make a clear difference here between the flexible sheets and the rigid one: in the latter, the carbon monoxide molecules are positioned closer to each other by definition of the set-up, while in the flexible sheets, the carbon monoxide molecules will move in and out of the plane in an attempt to find more comfortable positions. For the rigid sheet, at 150 K less carbon monoxide molecules are adsorbed for the shorter carbon-carbon distance, 96.9 vs. 97.1 adsorbed molecules, leading to a larger gas density, 1.712 g L^{-1} vs 1.590 g L^{-1}. At larger temperatures, however, the adsorption slightly diminishes for the longer carbon-carbon distances, leading to higher gas densities. For the flexible sheets, less molecules are adsorbed upon increasing the carbon-carbon distance at all temperatures with the exception of 77 K. At the latter temperature, both show an enhanced adsorption at large distances which is very different for field 2, 0.439 g L^{-1} vs. 1.002 g L^{-1}.

Comparing the different sheets (also seen in figure 4.15), where the variation of the gas density is seen in function of the temperature for the different fields, it is seen that field 1 adsorbs the least molecules, followed by field 2 and field 0. The more flexible graphene sheets show an enhanced gas density in the simulation box suggesting a decreased number of CO molecules adsorbed on the graphene sheet. As found for previous systems, the flexibility seems to have a clear influence on the adsorption of the carbon monoxide molecules. As for methane and nitrogen, carbon monoxide sees its adsorption reduced with increasing flexibility.

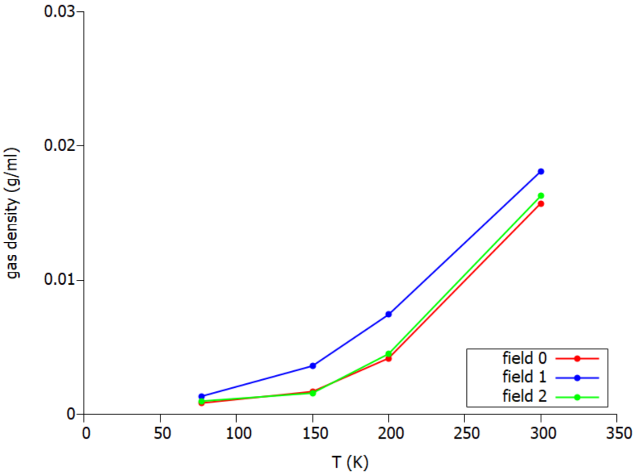

FIGURE 4.15: Gas density in function of temperature for 200 CO molecules on the three different graphene sheets considered in this study.

Chapter 5

Grand Canonical Monte Carlo Simulations

In this chapter, Grand Canonical Monte Carlo simulations will be discussed that were performed for the adsorption of methane, hydrogen and their mixture on graphene sheets. For these simulations, different pores were constructed existing out of two parallel graphene sheets whereby the interlayer distance was varied. More specifically, pores with interlayer distances of 5Å, 8 Å, 14 Å and 20 Å were simulated.

5.1 Methodolgy

The Grand Canonical Monte Carlo simulations were carried out using the potentials outlined in chapter 3 using the LAMMPS software package [225]. Since the standard LAMMPS package does not contain the ILJ potential, this was implemented by the author as will be discussed in more detail later on. The pores of study were represented by two parallel graphene sheets consisting of 1660 carbon atoms each, organized in the known honeycomb-like structure of graphene. Periodic boundary conditions were used in the x- and y-directions, while the z-direction was adjusted such that the two graphene sheets coincided with the simulation box sides. More specifically, this led to a simulation box size of 100.840 Å x 40.852 x z whereby z is equal to 5 Å, 8 Å, 14 Å or 20 Å depending on the specific pore that was simulated.

The volume, V, the temperature, T, and the chemical potential, μ, were the independent thermodynamic variables in the simulations whereby T was 300 K in all cases and μ was controlled via the pressure, P. For the Markov chain, three types of moves were considered with equal probability: particle deletion, particle insertion and particle displacement. 5 x 10^5 configurations were simulated with a cutoff distance of 14 Å and convergence was ensured via monitoring of properties like temperature and energy.

Concerning the result section, we will discuss both absolute and excess adsorption isotherms. The latter can be understood as plotting the amount of gas molecules, n_i^e, in function of the applied pressure that is present in the simulation box after subtracting the amount of molecules that would be present in bulk in the same volume at the same pressure, as it is obtained in experimental chemistry. This property can be calculated as

$$n_i^{\mathrm{e}} = n_i^{\mathrm{a}} - \rho_i V_{\mathrm{pore}} y_i \ , \tag{5.1}$$

where n_i^{a} is the total amount of molecules of compund i present in the simulation box after convergence, V_{pore} is the pore volume, y_i is the mole fraction of compound i and ρ_{b} is the bulk gas density of compound i at the specified temperature and pressure as calculated by the Soave-Redlich-Kwong equation of state [226]

$$P = \frac{RT}{V_{\mathrm{m}} - b} - \frac{a\alpha}{V_{\mathrm{m}}(V_{\mathrm{m}} + b)} \ . \tag{5.2}$$

Here

$$\alpha = \left(1 + (0.480 + 1.574\omega - 0.176\omega^2)\left(1 - \sqrt{T_{\mathrm{r}}}\right)\right)^2 \ , \tag{5.3}$$

$$a = 0.42748\frac{R^2 T_{\mathrm{c}}^2}{P_{\mathrm{c}}} \tag{5.4}$$

and

$$b = 0.08664\frac{RT_{\mathrm{c}}}{P_{\mathrm{c}}} \ , \tag{5.5}$$

while R is the gas constant, T the temperature, V_{m} the molar volume, ω the acentric factor (-0.216 for H_2 and 0.011 for CH_4), T_{c} the critical temperature (33.0 K for H_2 and 190.4 K for CH_4) and P_{c} the critical pressure (12.73 atm for H_2 and 45.40 atm for CH_4). The second term on the right hand side of equation 5.1, effectively equals the amount of molecules that would be present in the bulk in the same volume at the same pressure. The absolute adsorption isotherms that were thus obtained were fitted using the Langmuir equation (see equation 4.6).

For the adsorption of the pure gases in the pore, the isosteric heat is calculated indicating the energy released upon adsorption. It is calculated as

$$Q_{\mathrm{st}} = \frac{\langle U\rangle\langle N\rangle - \langle UN\rangle}{\langle N^2\rangle - \langle N\rangle\langle N\rangle} + k_{\mathrm{B}}T \ , \tag{5.6}$$

whereby the angle brackets denote the average of the specific property over the complete ensemble. U is the configurational energy of the system, N the number of particles adsorbed, T is the temperature of 300 K and k_{B} is the Boltzmann constant.

5.1.1 Implementation of the ILJ Potential in LAMMPS

The LAMMPS package is a program suit written in the C and C++ languages, divided in numerous packages. It is organised such that every single command of the program, constitutes a separate module that can be found independently in the source code. As such, it is quite straightforward to add an extra module and compile it into the main program. For the implementation of the ILJ potential into LAMMPS, we copied the already existing LJ module and used it as a starting point for the new implementation. Implementation of the ILJ potential itself posed no real problems, but the forces that need to be calculated from the potential proved more dificult as the forces are calculated as the derivative of the potential in R, leading to quite a complicated expression.

The implementation in LAMMPS of the forces as a derivative of R can be understood by looking at the form of the LJ potential

$$E_{ij}^{\mathrm{LJ}} = \epsilon \left(\left(\frac{r_0}{R_{ij}} \right)^{12} - 2 \left(\frac{r_0}{R_{ij}} \right)^{6} \right) \tag{5.7}$$

and recalling the description of the forces in equation 2.81

$$\vec{f}_{ij}^{\mathrm{LJ}} \left(R_{ij} \right) = - \left(\frac{1}{R_{ij}} \right) \left(\frac{d}{dR_{ij}} \Phi \left(R_{ij} \right) \right) \vec{R}_{ij} \ , \tag{5.8}$$

we find

$$f_{ij}^{\mathrm{LJ}} \left(R_{ij} \right) = -\epsilon \left(\frac{12 r_0^6}{R_{ij}^7} - \frac{12 r_0^{12}}{R_{ij}^{13}} \right) \tag{5.9}$$

which can be rearranged to

$$f_{ij}^{\mathrm{LJ}} \left(R_{ij} \right) = \frac{1}{R_{ij}^7} \left(\frac{12 \epsilon r_0^{12}}{R_{ij}^6} - 12 \epsilon r_0^6 \right) \quad . \tag{5.10}$$

This allows calculation of $12\epsilon r_0^6$ and $12\epsilon r_0^{12}$ once for every atom pair at the beginning of the simulation and their storage in a matrix. Given the large amount of interactions that are calculated throughout a simulation, this gives a considerable speed-up. Unfortunately, the complex expression of the derivative of the ILJ potential does not allow this

$$\begin{aligned} f_{ij}^{\mathrm{ILJ}} \left(R_{ij} \right) = -\, \epsilon \Bigg(& \frac{-8 m R_{ij} \left(\frac{r_0}{R_{ij}} \right)^{\frac{4R_{ij}^2}{r_0^2} + \beta}}{r_0^2 \left(-m + \frac{4R_{ij}^2}{r_0^2} + \beta \right)^2} + \frac{8 R_{ij} \left(\frac{r_0}{R_{ij}} \right)^m \left(\frac{4R_{ij}^2}{r_0^2} + \beta \right)}{r_0^2 \left(-m + \frac{4R_{ij}^2}{r_0^2} + \beta \right)^2} \\ & - \frac{8 R_{ij} \left(\frac{r_0}{R_{ij}} \right)^m}{r_0^2 \left(-m + \frac{4R_{ij}^2}{r_0^2} + \beta \right)} + \frac{m r_0 \left(\frac{r_0}{R_{ij}} \right)^{-1+m} \left(\frac{4R_{ij}^2}{r_0^2} + \beta \right)}{R_{ij}^2 \left(-m + \frac{4R_{ij}^2}{r_0^2} + \beta \right)} \\ & + \frac{m {\frac{r_0}{R_{ij}}}^{\frac{4R_{ij}^2}{r_0^2} + \beta} \left(- \frac{\frac{4R_{ij}^2}{r_0^2} + \beta}{R_{ij}} + \frac{8 R_{ij} \log\left(\frac{r_0}{R_{ij}} \right)}{r_0^2} \right)}{-m + \frac{4R_{ij}^2}{r_0^2} + \beta} \Bigg) \ . \end{aligned} \tag{5.11}$$

Aside from the added complexity of the equation, the whole derivative needs thus to be recalculated at every time step for every interaction present in the system, leading to a considerable extra computational cost over the LJ potential.

In figure 5.1, the comparison is made between the interaction energy predicted by the ILJ potential implemented in LAMMPS, printed out at predefined distances, and the analytical plot of the ILJ potential in Mathematica, the implementation proves to yield accurate energy results, a similar comparison was made for the forces and found equally good. For comparison, the energy values for the LJ as plotted by Mathematica is given as well, whereby it can be seen, as dicussed previously, that the behavior is different at intermediate range, while very similar at the equilibrium range. For this comparison, the parameters predicted by Albertí et al. for the methane molecule were used as indicated in chapter 3.

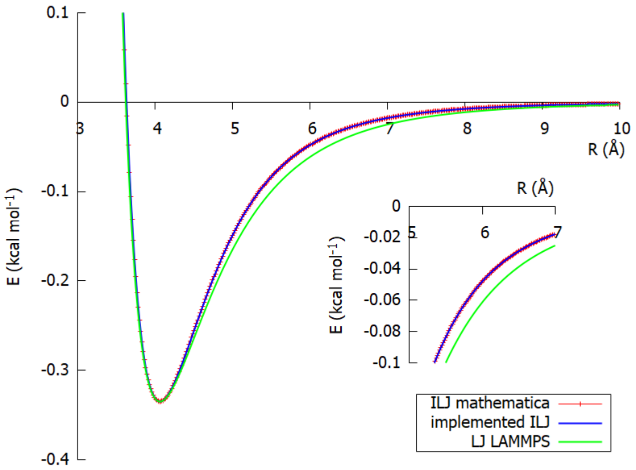

FIGURE 5.1: Comparison of the implemented ILJ potential in LAMMPS (red dots) with the analytical expression plotted in Mathematica (green), the agreement is maintained over all distances. The LJ potential is given as a reference (blue).

5.2 Adsorption of Methane and Hydrogen in a Slit-Shaped Graphene Pore

In this section, the results will be discussed of the performed GCMC simulations on the adsorption of pure methane, pure hydrogen and the equimolar mixture of both on graphene. As said, the pores that we have simulated range from a 5 Å pore to a 20 Å pore. Comparing these sizes to the Van der Waals radii of the gas molecules under study, 3.552 Å and 4.169 Å for hydrogen and methane respectively taken as the equilibrium distances from the force field, we simulated from very small pores to medium range pores. Figure 5.2 shows a schematic representation of the Van der Waals radii of the hydrogen and methane molecules within the four pores that were simulated. It can be seen that the molecules just barely fit into the smallest pore, while about five molecules could be put in the largest pore.

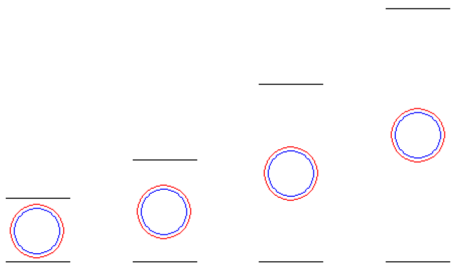

FIGURE 5.2: Van der Waals radii of methane (red) and hydrogen (blue) in comparison to the different pores under study, from left to right: 5 Å, 8 Å, 14 Å and 20 Å.

5.2.1 Pure Methane Gas

In figure 5.3 the absolute and excess adsorption isotherms for a pure methane gas are compared for the different pore sizes that were considered. To the absolute adsorption isotherms, the Langmuir adsorption model was fit and the parameters are given in table 5.1. It can be seen that the saturated adsorption capacity increases with increasing interlayer distance, while the Langmuir equilibrium constant decreases as was found by Lin et al. [35] for pore sizes between 20 Å and 110 Åand a pressure range of 9 atm to 350 atm. As the Langmuir equilibrium constant is a measure for the tendency of the molecules to adsorb onto the surface, it is suggested that methane will easier adsorb onto the smallest pores as is indeed observed from the adsorption isotherms.

Indeed, the 5 Å pore shows nearly no adsorption of methane gas as is seen by a near-zero absolute adsorption isotherm and a negative excess adsorption isotherm. The negative excess adsorption indicates that less molecules are adsorbed than there would be present in the same bulk volume. Looking at the equilibrium distance of the C_{graph}-CH_4 interaction, the methane molecule wants to maintain an ideal distance of 3.938 Å to either graphene sheet which is not possible in a pore of only 5 Å. Even stronger, the closeness of the methane to the graphene sheets forces the molecules out of the pore through repulsive interactions. From the three remaining pores, it is clear that all three of them have a higher molar density than the bulk phase as is evidenced by the strongly positive excess adsorption isotherms.

TABLE 5.1: The parameters for the Langmuir model, resulting from fitting to the absolute adsorption isotherm for the adsorption of pure methane on graphene

	q_m (mmol/cm^3)	k (atm^{-1})
5 Å	0.084	6.325
8 Å	11.405	0.909
14 Å	22.470	0.023
20 Å	31.178	0.008

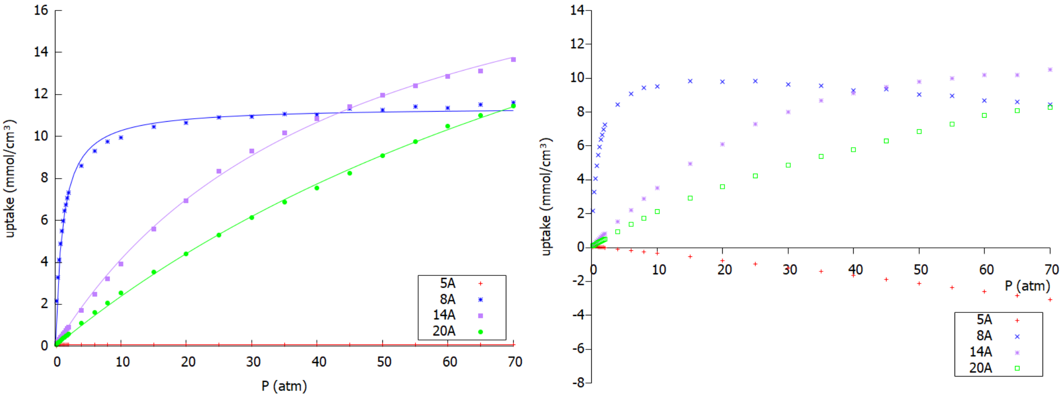

FIGURE 5.3: Absolute and excess adsorption isotherms for the pure methane gas in slit-pores with interlayer distances of 5 Å, 8 Å, 14 Å and 20 Å. For the absolute adsorption isotherms, the Langmuir fittings are shown by lines.

The behavior of the adsorption isotherm is different for the considered pore sizes. The 8 Å pore shows a very fast saturation to its maximum capacity around 15 atm and raising the pressure further does not accomodate many more molecules. Furhermore, at pressures higher than 15 atm, the excess adsorption isotherm shows a negative gradient, indicating that the density rises faster for the bulk volume than for the adsorbed methane gas. The higher the pressure, the lower the advantage of the graphene pore becomes compared to an empty container at the same pressure. Again, this behavior can be understood by looking at the equilibrium distance for the graphene-methane interaction, the pore of 8 Å allows methane molecules to enter the pore and sit in a position where the centre of mass is located more or less at the ideal distance from both graphene sheets feeling optimal attraction from both. There is, however, only a small region where this is possible and once this layer is saturated, the amount of molecules that further enter the system lowers. Newly entering molecules will now be forced to be placed closer to the graphene sheets, costing more energy.

For the larger pores of 14 Å and 20 Å, the convergence is a lot slower with rising pressure and no maximum is reached for the excess adsorption isotherm within the investigated pressure range. There are now two possible regions for the methane molecules to be at an ideal distance from a graphene sheet, one at either graphene sheet, allowing more molecules to enter the pore. However, the methane molecule feels a strong attraction from only one graphene sheet instead of both as in the 8 Å pore and therefore, higher pressures are needed to saturate the pore. Furthermore, there is more room for less ideal positions to be occupied by the methane molecules. The absolute adsorption isotherms of the 14 Å and the 20 Å pore cross the 8 Å pore at 40 atm and 70 atm respectively, adsorbing a larger amount of molecules above those pressures. From this, it seems that below 40 atm, the 8 Å pore is the most efficient one, while above 40 atm, the 14 Å becomes more efficient.

Mosher et al. [227] have simulated different pores using three-layered graphite slit-pores for pore sizes between 4 and 90 Å at 298 K while making use of a simple united-atom Lennard-Jones model. For a 10 Å pore at 298 K, they have calculated the adsorption isotherm in a pressure range between 0 atm and 200 atm. Looking at the the pressure of 70 atm, which is the highest pressure considered in this work, they report an absolute adsorption of about 15 mmol/cm^3 and an excess adsorption of about 12 mmol/cm^3. Although we did not calculate the exact same pore, our results are in the same range and, assuming that the adsorption of the 10 Å pore would lie in between the results for 8 Å and the 14 Å pores, we would expect slightly lower uptakes. Comparing the results for 20 Å pore, both our work and the work by Mosher et al. report an excess uptake of just below 7.5 mmol/cm^3. Furthermore, they report a maximum of the excess uptake at a pressure of 96.67 atm where an excess uptake of 7.50 mmol/cm^3 is reported. By extrapolating our results, we find again higher values with the maximum excess adsorption around 170 atm with an uptake of 10.39 mmol/cm^3. The flatness of the adsorption isotherm explains the large differences between the pressure of maximum uptakes as was also indicated in the work by Mosher et al., whereby, furthermore, the different simulation conditions should be taken into account. The largest difference with this work is that they report substantial adsorption already for a pore width of 4 Å, while using an r_0 value of 3.82 Å for the graphite-methane interaction. The small space in the pore would be expected to prohibit all adsorption in a pore with that size as we found in our work for the 5 Å pore and was also confirmed by Collins et al. [228].

The previously drawn conclusions are supported by the z-density profiles calculated at a pressure of 1 atm shown in figure 5.4 for the different pores whereby we have used reduced distance units to make direct comparison possible, the two graphene sheets are thus located at the 0 and 1 reduced distance coordinates. It is seen that, indeed, close to no molecules are adsorbed in the 5 Å pore, while a single, strong adsorption layer is present in the middle of the 8 Å pore. For the larger pores,

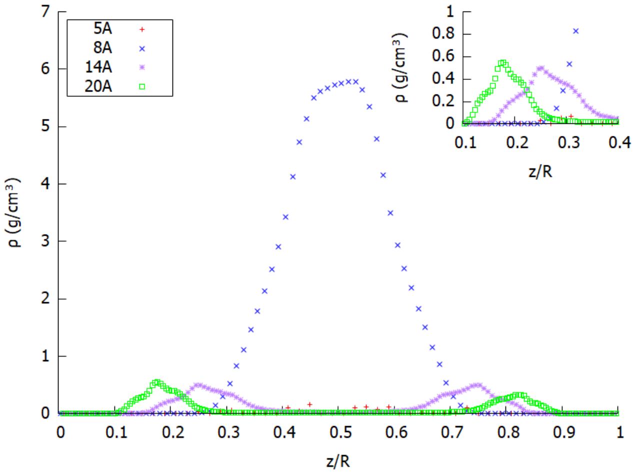

FIGURE 5.4: Z-density profiles for the pure methane gas in the different pores at a pressure of 1 atm.

two different adsorption layers are found, one on either graphene sheet. It is seen that the adsorption layers for the 14 Å pore are positioned slightly further from the graphene sheets than in the 20 Å pore. Presumably, this is caused by the opposing graphene sheet in the 14 Å pore being closer than in the 20 Å pore and pulling the adsorption layer slightly further from the ideal position to the closest graphene sheet. Collins et al. [228] report a strong, single adsorption layer in their 7 Å pore because of the combined interactions of both graphene sheets on the methane molecules. Considering their slightly smaller r_0 of 3.61 Å, this agrees well with our results. In their 11 Å pore, they report the formation of two weaker adsorption layers, one on each graphene sheet, while a very weak third adsorption layer in the middle of the pore is reported for a 14 Å pore. Although, this third adsorption layer is not visible in our Z-density profile because of the very high mobility of the involved methane molecules (as confirmed by Collins et al.), the snapshots of the simulation clearly show the presence of methane molecules in the middle of the pore that form the mentioned third adsorption layer (see below, figure 5.5).

Figure 5.5 shows snapshots of the simulation at 70 atm, whereby it can be seen

5 Å

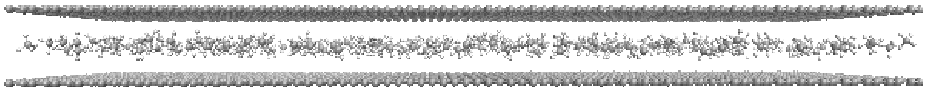

8 Å

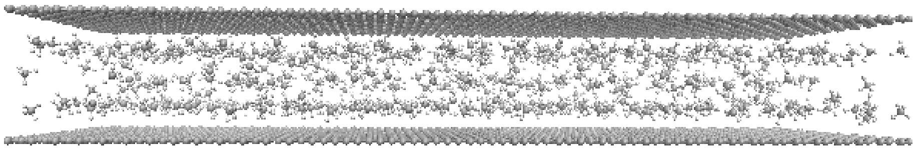

14 Å

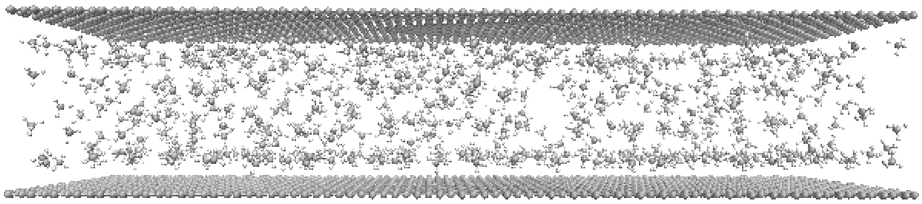

20 Å

FIGURE 5.5: Snapshots of the simulation of pure methane gas in the 5 Å, 8 Å, 14 Å and 20 Å pores at 70 atm.

that no molecules enter the 5 Å pore except for an occasional one for statistical reasons. In the 8 Å pore, we clearly see the single saturated adsorption layer in the middle of the box, while in the 14 Å pore, two adsorption layers are indeed observed, one on either graphene sheet. The high pressure has filled up the interlayer space with a third layer of adsorbed methane molecules. The same observation holds for the 20 Å pore, where the interlayer distance is now filled up with bulk methane because of the large amount of space that is left free.

Lin et al. have reported adsorption isotherms of methane on graphene slit pores with interlayer distances of 20 Å and beyond [35]. They report the same trend of lowering of the molar density with increasing pore size. They also find the Langmuir behavior indicating a single adsorption layer on every graphene sheet which is also reflected in our adsorption isotherms. The late convergence of the larger pores is also reflected in their adsorption isotherm which starts to converge around 250 atm.

Figure 5.6 shows the isosteric heat as a function of pressure for the pure methane gas for the 8 Å , 14 Å and 20 Å pores. The 5 Å pore is left out since the isosteric heat is very close to 0 as almost no methane gas is adsorbed in this pore. The 8 Å pore shows a high isosteric heat compared to the 14 Å and 20 Å pores indicating a stronger adsorption of the methane molecule in this pore as observed before. Interestingly, the isosteric heat is about twice the size of the larger pores which could be explained by the fact that in the 8 Å pore, the methane molecules are in ideal position to adsorb to both graphene sheets at the same time leading to an interaction that is twice as strong. For the larger pores, the molecules adsorb to only one sheet and feel a lower influence from the opposing graphene sheet. This is further confirmed by the observation that the 14 Å shows a slightly higher isosteric heat than the 20 Å pore. The closeness of the opposing graphene sheet, seems to clearly influence the isosteric heat. Lin et al. have reported the isosteric heat for a pure methane gas in a 20 Å slit-pore which showed a similar behavior as our system [35]. The isosteric decreases at first reaching a minimum, after wich it slightly goes up towards a value

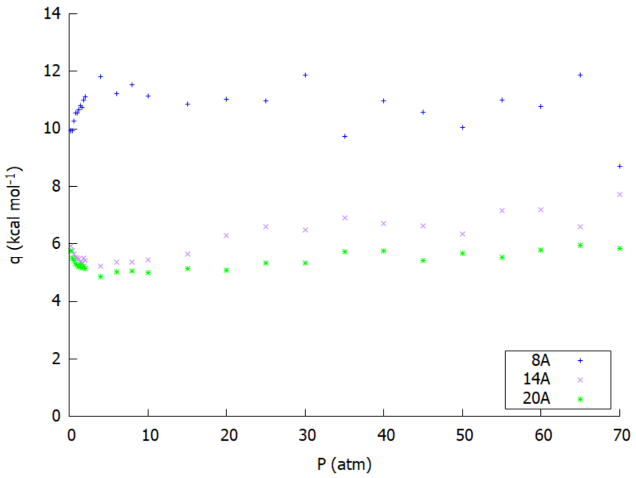

FIGURE 5.6: Isosteric heats in function of pressure for the pure methane gas in the 8 Å , 14 Å and 20 Å pore.

of 4.5 kcal mol^{-1} in their results and around 5 kcal mol^{-1} in ours.

5.2.2 Pure Hydrogen Gas

Figure 5.7 shows the absolute and excess adsorption isotherms for the pure hydrogen gas in the four pores under study. Again it is seen that the smallest pore adsorbs only a very limited amount of hydrogen, albeit almost double the amount of methane. Furthermore, the excess adsorption is strongly negative meaning that, although the pore does adsorb hydrogen, there is a lot less hydrogen present in the pore then there would be in the same volume of bulk hydrogen. Again the absolute adsorption isotherm was fitted with the Langmuir isotherm and the parameters are given in table 5.2.

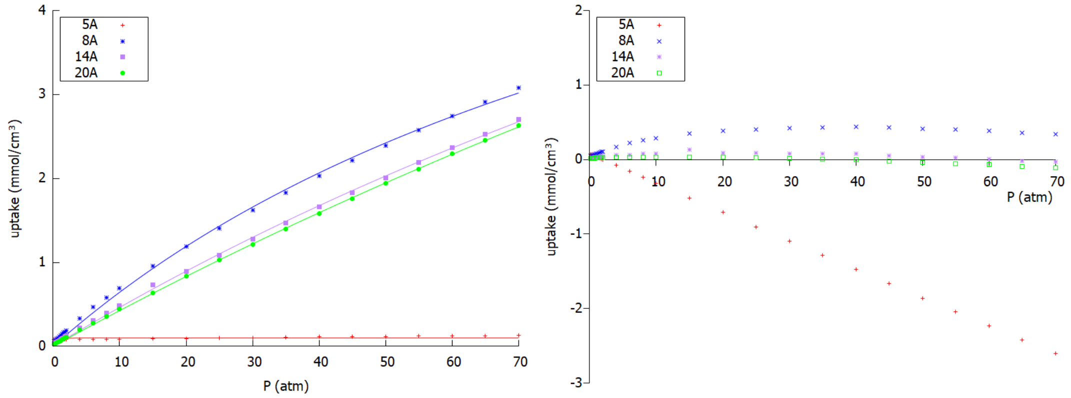

FIGURE 5.7: Absolute (left) and excess (right) adsorption isotherms for the pure hydrogen gas in the four different pores considered

The 8 Å pore shows a slight advantage compared to the bulk molar density, although this advantage is gained at smaller pressures and slowly dwindles at larger pressure as can be seen by the excess adsorption reaching a sort of plateau quite quickly. For the two larger pores, the adsorption isotherms are very close to the molar volume of the bulk as can be seen by the near-zero excess adsorption isotherms. It seems like the graphene barely influences the amount of hydrogen gas in the simulation box, as the large size of the pore compared to the hydrogen molecule, leaves

TABLE 5.2: The parameters for the Langmuir model, resulting from fitting to the absolute adsorption isotherm for the adsorption of pure hydrogen on graphene

	q_m (mmol/cm^3)	k (atm^{-1})
5 Å	0.103	5.828
8 Å	7.833	0.009
14 Å	13.094	0.004
20 Å	18.170	0.002

the hydrogen molecule as in bulk. Furthermore, the interaction between graphene and hydrogen is not strong enough to pull all hydrogen molecules present in the pore into the adsorption layers leaving bulk gas in the middle of the pore as can be seen in figure 5.8 where the z-density is shown for the pure hydrogen gas at 1 atm.

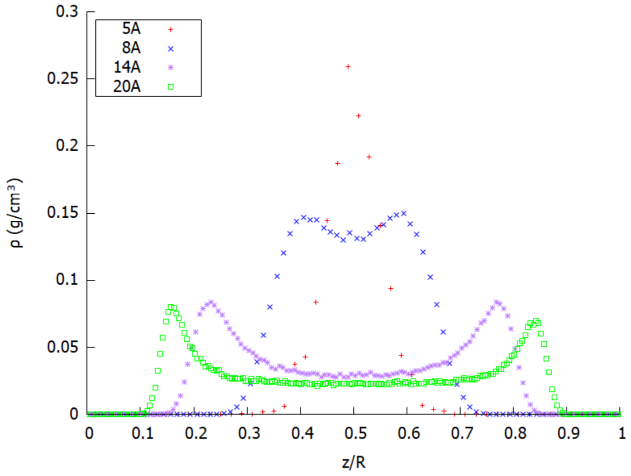

FIGURE 5.8: Z-density profiles for the adsorption of pure hydrogen gas in the different pores under study

For the 14 Å and the 20 Å pores, two adsorption layers are seen close to the graphene sheets, but there is a substantial gas phase in the middle, where gas molecules are free to behave as bulk hydrogen. This same observation is mentioned by Morales et al. for the adsorption of a pure H_2 gas in carbon cylindrical cavities [31]. This bulk phase is not present in the 8 Å pore because of a lack of space, the small size of the hydrogen molecule does allow for the presence of two overlapping adsorption layers. The 5 Å pore, on the other hand, shows one single adsorption layer in the middle of the pore.

Figure 5.9 shows snapshots of the simulations of the pure hydrogen gas in the different pores at 70 atm. It is immediately seen that the amount of adsorbed molecules is a lot smaller than for the methane gas. The low amount of molecules does not allow a clear visually identification of the adsorption layers on the graphene sheets. What is visible, though, is the hydrogen gas present in the middle of the pore as bulk gas.

Figure 5.10 gives the isosteric heat of adsorption for the pure hydrogen gas in the different pores where again, the results are not shown for the 5 Å pore. Although the adsorption isotherm showed adsorption, this adsorption is actually lower than the amount of molecules that would be present in bulk phase, leading to unphysical negative isosteric heats. Concerning the other pores, they all show a small diminishing at lower pressures, reaching a plateau at higher pressures. Again, the 8 Å has by far the highest isosteric heat, followed by the 14 Å and then the 20 Å pore. Although the adsorption isotherm showed little difference between these three pores, the difference is clear in the isosteric heat of adsorption.

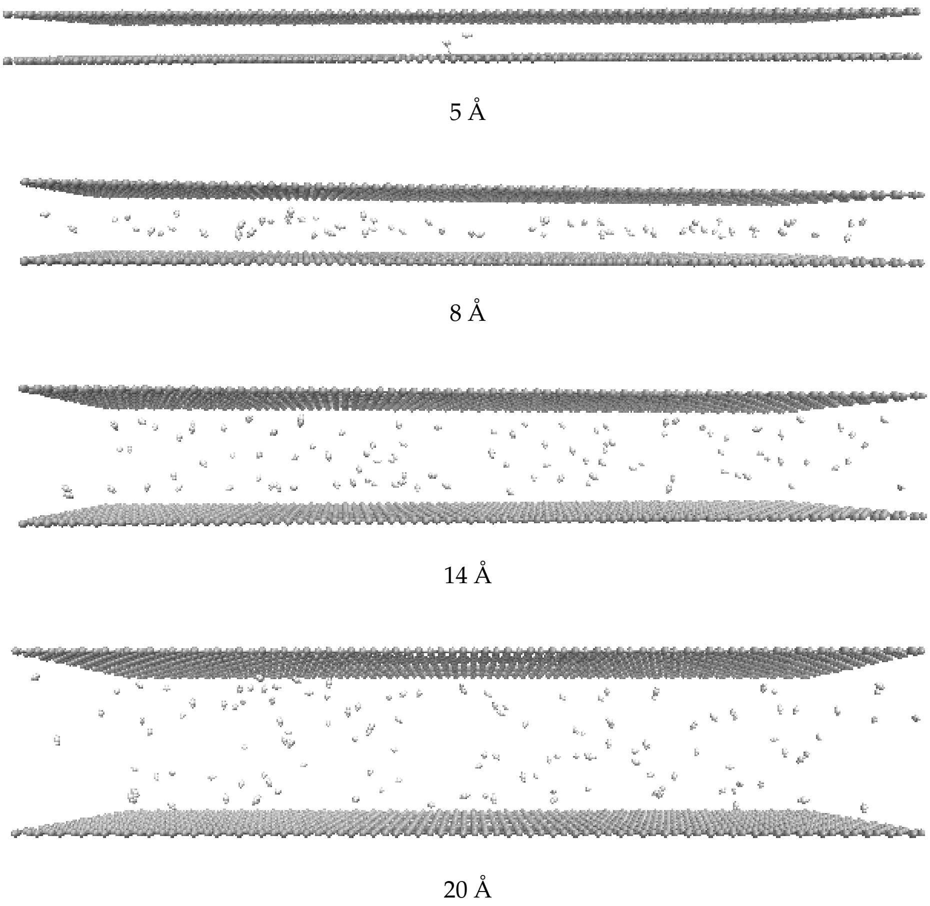

5 Å

8 Å

14 Å

20 Å

FIGURE 5.9: Snapshots of the simulation of pure hydrogen gas in the 5 Å, 8 Å, 14 Å and 20 Å pores.

Kowalczyk et al. have reported an interaction potential for hydrogen gas in slit-shaped graphite pores with different interlayer distances at 303K [229]. These interaction potentials can effectively be compared to the z-density profiles of this work, since one is in fact expected to be the opposite of the other. They have reported pores with interlayer distances of 1.8 σ up to 3 σ, coinciding with pores of 5.7 Å up to 9.5 Å . For the smaller pores, they observed one single peak as is found in our z-density profile. Increasing the pore size leads to splitting up of the peak into two overlapping peaks in the 3 σ pore, which is again in agreement with our z-density profiles.

5.2.3 Methane/Hydrogen Mixture

In figure 5.11, the absolute and excess adsorption isotherms for the different pores are shown for the methane adsorption within the equimolar CH_4/H_2 mixture. In the 5 Å pore, there is again, as expected, close to no adsorption of methane and the excess adsorption is therefore negative. The 8 Å pore shows very similar behavior as for the adsorption of the pure methane gas. Very little H_2 molecules are entering the pore and the CH_4 adsorption is thus hardly influenced, again we see a very fast

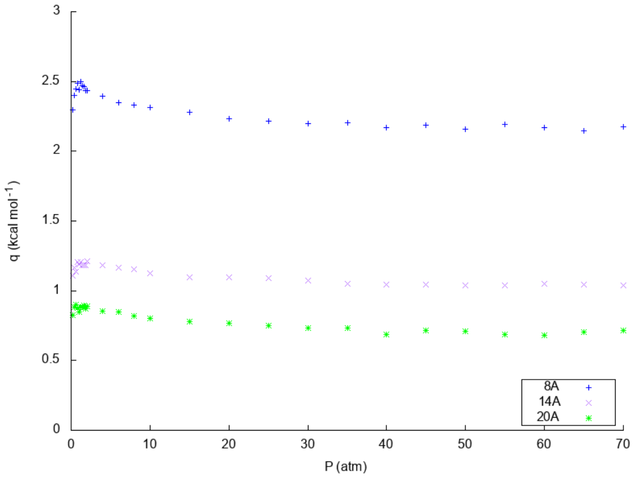

FIGURE 5.10: Isosteric heats in function of pressure for the pure hydrogen gas in the 8 Å 14 Å , and 20 Å pore.

convergence with pressure which stabilizes around the same molar density as for the pure methane gas. The larger pores behave slightly different upon adsorption of the mixture, as larger portions of H_2 molecules enter the pore lowering the amount of CH_4 molecules through competition. The methane adsorption isotherm on the 14 Å pore is no longer crossing the 8 Å isotherm at around 40 atm, but is set to do so just outside the pressure range simulated here. Also the 20 Å pore sees its adsorption of methane molecules shifted to higher pressures. The excess adsorption of the two largest pores are set to reach a maximum, something which is not visible for the adsorption of pure methane. The same tendency of less methane molecules adsorbing from a mixture of CH_4 and H_2 in larger pores was also reported in the work by Morales et al. [31] although their mixture was not equimolar.

The above observations are confirmed by the adsorption isotherms for the hydrogen adsorption within the methane/hydrogen mixture in figure 5.12, where it

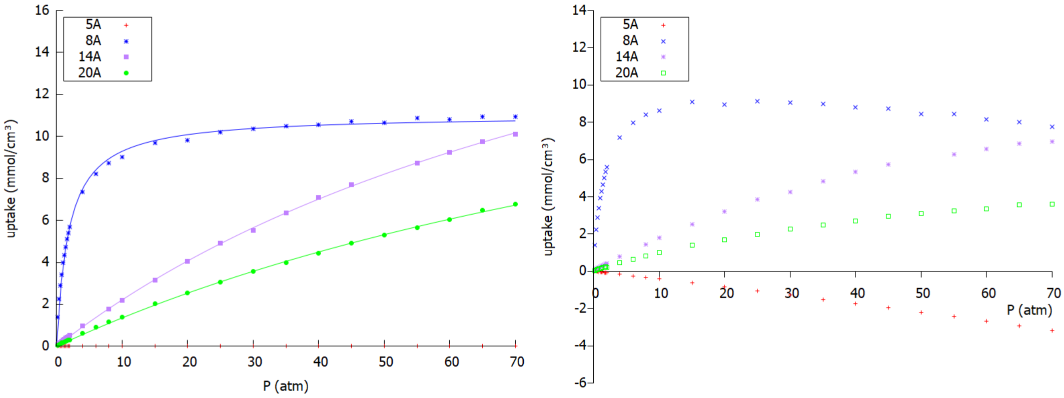

FIGURE 5.11: Absolute (left) and excess (right) adsorption isotherms for the methane gas within the methane/hydrogen equimolar mixture in the four pores under study.

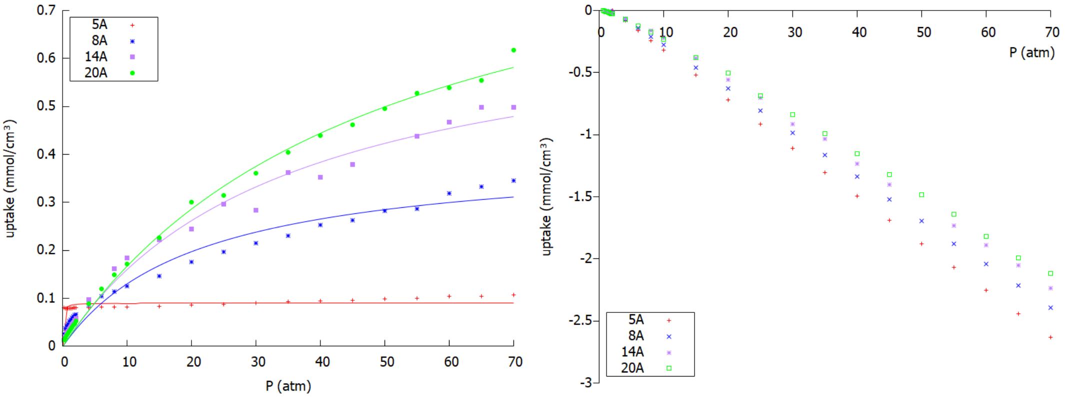

FIGURE 5.12: Absolute (left) and excess (right) adsorption isotherm for the hydrogen gas within the equimolar methane/hydrogen mixture in the four pores under study.

can be seen that indeed larger amounts of H_2 enter the pores with increasing pore size. The trend is now reversed compared to the pure H_2 adsorption in the sense that the 8 Å pore adsorbs less hydrogen molecules from the mixture because it is pushed out by the methane adsorption. With larger pores, more space is left available for the hydrogen molecules arising from the fact that the methane molecules tend to adsorb solely in a layer directly to the graphene surface, leaving space for hydrogen molecules to fill-up the intermediate range. In all pores with methane adsorption, however, there is little H_2 adsorption visible, indeed, Morales et al. [31] have reported non-zero adsorption for H_2 in pores as large as 26.6 Å and 41.6 Å for a 0.8/0.2 CH_4/H_2 mixture and in pores larger than 8.6 Å for a 0.2/0.8 CH_4/H_2 mixture. They also find larger amount of H_2 adsorption with increasing pore size, which can be explained by the lower selectivity for larger pores. The excess adsorption isotherms for hydrogen gas are negative for all cases where methane is competing with hydrogen adsorption as methane adsorption is stronger and prohibits the hydrogen density from approaching the bulk density. It shows once again that graphene preferentially adsorbs methane over hydrogen. Even in the smallest pore, where methane is prohibited to enter because of its size, hydrogen shows a negative excess adsorption isotherm. In fact, this is just the same result as was found for the pure hydrogen adsorption as methane is not an influence in this specific case.

For both the methane and the hydrogen absolute adsorption isotherms, a fitting was again done using the Langmuir isotherm, the parameters are given in table 5.3. It is seen that the presence of the other gas clearly influences the fitting parameters of the isotherm. For the methane gas, q_m behaves quite similar for the 8 Å and the 14 Å pores, while it is smaller in the mixture than in the pure gas for the 5 Å and 20 Å pores. In general, the equilibrium constants are lower indicating a less favorable adsorption for methane in the mixture. The 5 Å pore, however, shows an extremely high equilibrium constant, which is probably due to a mathematical artefact because

TABLE 5.3: The parameters for the Langmuir model, resulting from fitting to the absolute adsorption isotherm for the adsorption of methane and hydrogen from the mixture on graphene

	CH_4		H_2	
	q_m (mmol/cm^3)	k (atm^{-1})	q_m (mmol/cm^3)	k (atm^{-1})
5 Å	0.001	340834	0.090	16.065
8 Å	11.023	0.536	0.405	0.0476
14 Å	25.420	0.010	0.716	0.029
20 Å	19.898	0.007	0.989	0.020

of the near-zero adsorption. For the hydrogen molecule, the q_m parameters are an order of magnitude lower in the pure gas then in the mixture, while the equilibrium constants are an order of magnitude higher in most cases.

The above observations are supported by the snapshots of the simulations of the gas mixture within the four pores shown in figure 5.13. In all pores very little hydrogen molecules are present and it is only in the larger pores that hydrogen molecules

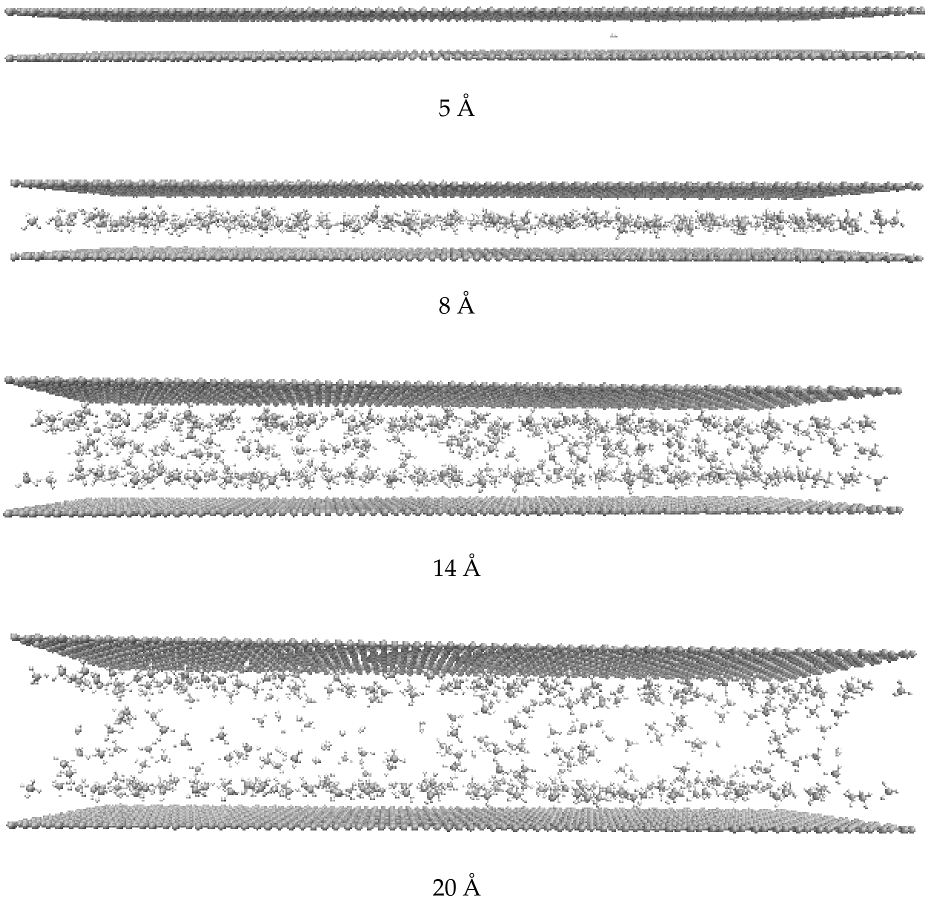

FIGURE 5.13: Snapshots of the simulation of the methane-hydrogen gas mixture in the 5 Å, 8 Å, 14 Å and 20 Å pores.

can easily be spotted in the middle of the pore where the methane density is substantially lower.

This is better observed in figure 5.14 where the z-density profiles for the methane and hydrogen molecules within the mixtures is given for the different pores at 1 atm. The 5 Å pore behaves quite similar as for the respective pure gases, there is barely any methane adsorption, while there is a single peak of hydrogen adsorption. The 8 Å pore shows very similar behavior for the methane gas only, there is one strong single adsorption layer although the amount of molecules in the layer is lowered from around 6 g/cm^3 to around 4.5 g/cm^3. This strongly affects the hydrogen adsorption, which is showing still two overlapping adsorption layers, but they are a lot less occupied than in the pure hydrogen gas. The density is lowered from around 0.15 g/cm^3 to around 0.07 g/cm^3. The same goes for the layers in the 14 Å and 20 Å pores, the size of the peaks is about half the size of the respective pure gases. The competition in the larger pore is stronger and more hydrogen is able to enter the pore compared to the 8 Å pore. Furthermore, it is clearly seen that in the middle of the pore, the space is occupied by hydrogen molecules, more than methane. This picture contradicts with the snapshots shown before, because they were taken at different pressures. At low pressure, hydrogen preferentially takes up the middle region of the pore, while at higher pressures, more methane is forced into the pore.

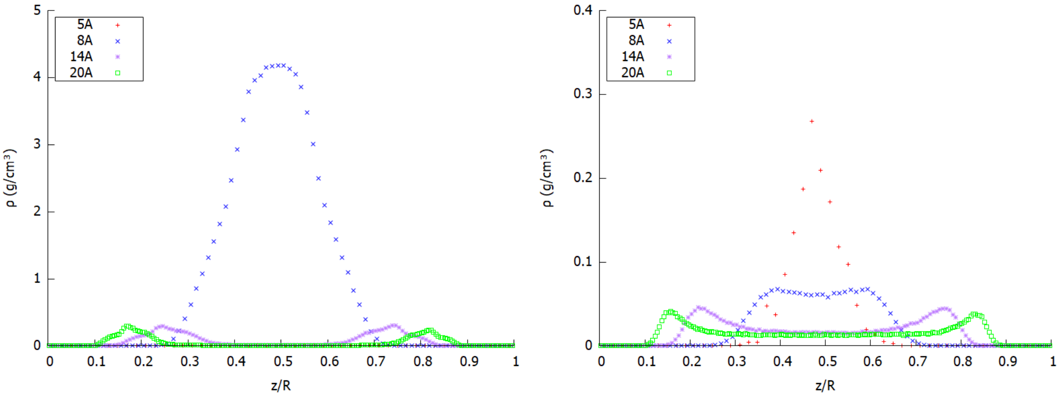

methane hydrogen

FIGURE 5.14: Z-densities for methane and hydrogen in the mixture in the different pores of study.

Figure 5.15 gives the selectivity of methane over hydrogen for the different pores considered. It is seen that the 8 Å gives by far the highest selectivity and that it shows a peak at around 2 atm. Furthermore, the selectivity at 1 atm is still very high at 76.68 thus suggesting again that a graphene slit pore of 8 Å is very suitable for methane separation from hydrogen. The larger pores also show lower selectivities without a maximum, where it is clear that larger pores show a smaller preference for methane over hydrogen. This confirms previous findings that larger pores allow easier entrance of the hydrogen molecules. The 5 Å pore is a special case which favors the adsorption of hydrogen over methane based on molecular size, thus giving

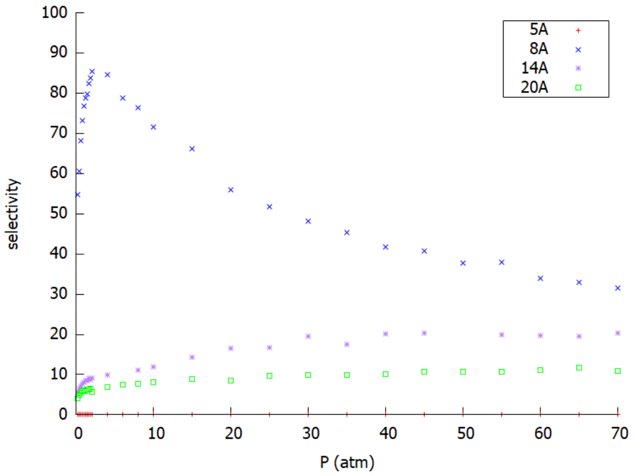

FIGURE 5.15: The selectivity as a function of the pressure for the methane/hydrogen mixture for the four pores under study.

a CH_4/H_2 selectivity very close to 0. Actually, the H_2/CH_4 selectivity of this pore is very high, although the small amount of H_2 molecules entering keeps it from being very useful, as mentioned before.

Kumar et al. have reported equimolar methane/hydrogen selectivities for different graphite slit-pore widths at 298K [116] and found the same trend of decreasing selectivity with increasing pore size. Furthermore, they too found an extremely high selectivity, around 250, for the methane molecule in a 7.3 Å pore, which is comparable to our 8 Å pore. This selectivity drops very fast when increasing the pore size, already below 20 for a 12 Å pore. Furthermore, they reported a selectivity of around 10 for the 15 Å pore and around 8 for the 19 Å pore. These results are in the same range as our 14 Å and 20 Å pore results.

Chapter 6

Conclusions

A set of force fields has been proposed for graphene and its interaction with several gases, as well as the interactions between those gases themselves. For all gases, multiple united-atom, describing the interactions in an average fashion, and fully atomistic, giving a full potential energy surface of the interaction, models were proposed and tested. The influence of different charge schemes was explored within these models and the relevance of the elcetrostatic interactions for the accurate fitting of these models was assessed. Furthermore, we have proposed a similar set of parameters obtained from fast calculations starting from atomic and molecular polarizabilities, thus avoiding the sometimes cumbersome fitting process.

Dimer interaction energies for the different gases and gas-graphene systems, were calculated at DFT level, using the B97-D funtional and benchmarked against CCSD(T) calculations. It was clearly shown that the B97-D functional gives thrustworthy results for the hard-to-describe non-covalently interacting systems of interest in this work. These interactions are mainly of dispersive type and thus related to electron correlation effects which are still today posing a major problem to the theoretical chemistry community for routine calculations. However, we have shown that these problems can be overcome, and accurate force fields can be constructed from this level of theory. For the gas adsorption on graphene, we found, for all gases, that the attacking orientation of the molecule is far more important than the exact position over the graphene sheet.

Specifically, for methane and nitrogen, the proposed potentials have been shows to reproduce well the interaction energies and equilibrium distances of selected dimers calculated at CCSD(T) levels and from experiment. The atomistic potentials were capable of reproducing the respective stability sequences of the dimers under consideration, while the united-atom models gave very good reproductions of the average interaction energies. For methane, small charges are advised for the atomistic potential (APT, Hirshfeld or Mulliken), while slightly larger charges, such as the ones by Albertí, also perform well. The atomistic model for graphene-methane reproduced very well the interaction with various PAHs, such as naphthalene and coronene and is thus expected to be useful for other extended carbon structures and nanotube sytems. In the same way, this atomistic potential is capable of reproducing experimental results on graphene-methane systems. Based on the diffusion coefficient and in agreement with the CCSD(T) results, we have selected the united-atom model with Hirshfeld charges and the atomistic potential without charges to be most thrustworthy in simulations, with the note that the cheapest model, united-atom without charges, also performs very reasonably. For the nitrogen molecule, it was found that the four-site Cracknell charge scheme reproduces with high accuracy the CCSD(T) interaction energies as well as the experimental diffusion coefficient for both the united-atom and full atomistic potentials. Besides, the atomistic model provides an average graphene-nitrogen interaction energy in excellent agreement with the experimental value.

For water, it is known that, despite its simple structure, its very complex interactions are hard to represent adequately. Nevertheless, we found that our atomistic potential with three optimized charges was well capable of reproducing the extremes of the 10 stationary points considered on the CCSD(T) potential energy surface. The intermediate energy range, with close-lying energies, is not described in the exact correct ordering, but the obtained energies are always close to the reference CCSD(T) and DFT energies. This gives us confidence to believe that our potentials well describe the behavior of a set of water molecules. In systems with higher pressures, where hydrogen bonds become more important, we have included an explicit term treating the hydrogen bonds present. Again, the potentials with three optimized charges were shown to perform best and were capable of describing the considered hexamers reasonably well. Nevertheless, it seems that the Coulombic representation of the electrostatic is not accurate enough to describe dimers and clusters with a single potential and a more advanced approach, explicitly including the dipole, might be needed. The electrostatic interactions are very directional and dominate the dispersive interactions, something wich our potentials are not flexible enough to account for.

We have also explored the possibility of determining the parameters that enter the LJ-like force fields by direct calculation of static polarizabilities and C_6 dispersion coefficients. This preliminary study shows the necessity of including very accurately the electrostatic contributions to the interaction and, moreover, illustrates the intrinsic arbitrariness in the distribution of the total electronic density, the only true quantum observable, into atomic components.

During MD simulations, we have studied the behavior of carbon monoxide, methane, nitrogen and the mixture of the latter two during adsorption on graphene whereby we paid particular attention to the influence of the intramolecular force field of graphene. Three different intramolecular force fields were taken from the literature for the modeling of the graphene and compared to the traditional rigid model of graphene. We found that the adsorption of methane and nitrogen is clearly influenced by the flexibility of the graphene sheet and the latter should thus be taken into consideration in future research. Specifically, for averaged interaction energies, such as the united-atom model, the flexibility seems to be be of major importance.

For the systems considered in this work, this effect was found most strongly for methane, with important directional effects, and nitrogen, although to a lesser extent. For these systems, introduction of the flexibility was capable of improving the description of the united-atom models to almost the level of the atomistic models. For the atomistic potentials, the effect seems less pronounced, being of little influence for the methane case and slightly decreasing the adsorption in the nitrogen case. Finally, in this study, a clear preference was shown for the adsorption of methane over nitrogen on graphene. Indeed, we saw that upon gradually increasing the amount of molecules in the system, all nitrogen was effectively removed from the first adsorption layer in favor of methane.

Finally, during the GCMC simulations, we have first of all delivered a proof of concept in the sense that we have for the first time, attempted GCMC simulations using the ILJ potentials leading to statisfying results comparable with existing literature, whereby the ILJ potential was implemented in the LAMMPS software package by the author. We studied different pores and identified their ability to adsorb methane, hydrogen and the separation of both these gases. It was found that the 8 Å pore is the ideal size to accomodate one layer of methane molecules and thus shows a strong preference for methane over hydrogen, leading to a very high selectivity. In general, methane is favored over hydrogen with the exception of the smallest pore of 5 Å which is too small to accomodate methane molecules. The larger pores have a lower preference for methane over hydrogen, because there is plenty of space in the middle of the pore to allow bulk hydrogen to enter.

Conclusiones

En este trabajo se ha propuesto una serie de campos de fuerza para describir la interacción entre el grafeno y distintos gases, así como las interacciones de los gases entre ellos. Para todos los gases, se propusieron y probaron un modelo de múltiples átomos unidos, que describen las interacciones de una manera promedio, y un modelo completamente atomistica, dando una superficie de energía potencial completa de la interacción. Se exploró la influencia de los diferentes esquemas de distribución de carga dentro de estos modelos y se evaluó la relevancia de las interacciones electrostáticas para el ajuste preciso de estos modelos.

Las energías de interacción del dímero para los diferentes gases y el sistema grafeno-gase se calcularon a nivel DFT, utilizando el funcional B97-D, compararondolo finalmente con cálculos CCSD(T). Se demostró claramente, que el funcional B97-D ofrece resultados de confianza para los sistemas dificiles de describir, que presentan interacción no covalente de interés en este trabajo. Estas interacciones son principalmente de tipo dispersivo y, por lo tanto, están relacionadas con los efectos de correlación entre electrones que todavía hoy plantean un problema para la comunidad de química teórica a la hora de llevar a cabo cálculos. Sin embargo, hemos demostrado que estos problemas pueden superarse y que se pueden construir campos de fuerza precisos a partir de este nivel de teoría. Para la adsorción de gas en el grafeno, encontramos, para todos los gases, que la orientación de ataque de la molécula es mucho más importante que la posición exacta sobre la hoja de grafeno.

Específicamente, para el metano y el nitrógeno, se ha demostrado que los potenciales propuestos reproducen bien las energías de interacción y las distancias de equilibrio de los dímeros seleccionados calculados a los niveles de CCSD(T) y obtenidos experimentalmente. Los potenciales atomísticos fueron capaces de reproducir las secuencias de estabilidad respectivas de los dímeros en consideración, mientras que los modelos de átomos unidos proporcionaron muy buenas estimaciones de las energías de interacción promedio. Para el metano, se recomiendan pequeñas cargas para el potencial atomístico (APT, Hirshfeld o Mulliken), mientras que las cargas ligeramente más grandes, como las de Albertí, también dan un buen comportamiento. El modelo atomístico para el grafeno-metano reproduce muy bien la interacción con varios PAH, como el naftaleno y el coroneno, y por lo tanto se espera que sea útil para otras estructuras de carbono extendidas y sistemas de nanotubos. De la misma manera, este potencial atomístico es capaz de reproducir resultados experimentales en sistemas de grafeno-metano. En base al coeficiente de difusión y de acuerdo con los resultados de CCSD(T), hemos seleccionado el modelo de átomo unido con cargas de Hirshfeld y el potencial atomístico sin carga como el más fiables en las simulaciones, con la nota de que el modelo más barato de átomo unido sin cargas, también se comporta muy razonablemente. Para la molécula de nitrógeno, se encontró que el esquema de carga de Cracknell de cuatro sitios reproduce con alta precisión las energías de interacción CCSD(T) así como el coeficiente de difusión experimental para ambos potenciales, el de átomo unido y el atómico completo. Además, el modelo atomístico proporciona una energía de interacción de grafeno-nitrógeno promedio en excelente acuerdo con el valor experimental.

Para el agua, se sabe que, a pesar de su estructura simple, sus complejas interacciones lo convierten en un sistema difícil de representar adecuadamente. Sin embargo, encontramos que nuestro potencial atomístico con tres cargas optimizadas era capaz de reproducir los extremos de los 10 puntos estacionarios considerados en la superficie de energía potencial CCSD(T). El rango de energía intermedio, con energías próximas, no se describe en el orden correcto exacto, pero las energías obtenidas siempre están cerca de las energías CCSD(T) y DFT de referencia. Esto nos da confianza para creer que nuestros potenciales describen bien el comportamiento de un conjunto de moléculas de agua. En sistemas a presiones más altas, donde los enlaces de hidrógeno se vuelven más importantes, hemos incluido un término explícito que trata los enlaces de hidrógeno presentes. Nuevamente, se mostró que los potenciales con tres cargas optimizadas se comportaban mejor y eran capaces de describir los hexámeros considerados razonablemente bien. Sin embargo, parece que la representación coulómbica de la interacción electrostática no es lo suficientemente precisa para describir con un unico potencial dimeros y "clusters" y podría ser necesario un enfoque más avanzado, que incluya explícitamente el dipolo. Las interacciones electrostáticas son muy direccionales y dominan las interacciones dispersivas, algo que nuestros potenciales no son lo suficientemente flexibles para tener en cuenta.

Hemos también explorado la posibilidad de determinar los parámetros que entran en los campos de fuerza tipo LJ mediante el cálculo directo de las polarizabilidades y coeficients de dispersión C_6. Este estudio preliminar muestra la necesidad de incluir con gran exactitud las contribuciones electrostáticas a la interacción y, además illustra la intrínsica arbitrariedad en la distribución de la densidad electrónica total, el único observable cuántico verdadero, en compononentes atómicas.

En las simulaciones MD, hemos estudiado el comportamiento del metano, el nitrógeno y su mezcla respecto a la adsorción en grafeno, prestando especial atención a la influencia del campo de fuerza intramolecular del grafeno. Se tomaron tres campos de fuerza intramoleculares diferentes de la literatura para el modelización del grafeno y se compararon con el modelo rígido tradicional de grafeno. Encontramos que la adsorción de metano y nitrógeno está claramente influenciada por la flexibilidad de la hoja de grafeno y, por lo tanto, esta última debe tomarse en consideración en futuras investigaciones. Específicamente, para las energías de interacción promediadas, como el modelo de átomo unido, la flexibilidad parece ser de gran importancia. Para los sistemas considerados en este trabajo, este efecto resultó ser más significativo para el metano, con importantes efectos direccionales, y nitrógeno, aunque en menor medida. Para estos sistemas, la introducción de la flexibilidad fue capaz de mejorar la descripción de los modelos de átomos unidos a casi al nivel de los modelos atomisticas. Para los potenciales atomísticos, el efecto parece menos pronunciado, siendo de poca influencia para el caso del metano y disminuyendo ligeramente la adsorción en el caso del nitrógeno, la misma tendencia se encuentra para la adsorción del carbon monoxido sobre grafeno. Finalmente, en este estudio, se mostró una clara preferencia por la adsorción de metano sobre nitrógeno en grafeno. De hecho, vimos que al aumentar gradualmente la cantidad de moléculas en el sistema, todo el nitrógeno se eliminó efectivamente de la primera capa de adsorción en favor del metano.

Finalmente, durante las simulaciones de GCMC, en primer lugar hemos realizado un "proof of concept" en el sentido de que por primera vez hemos intentado realizar simulaciones de GCMC utilizando los potenciales ILJ que conducen a resultados estadísticos comparables con la literatura existente, por lo que se implementó el potencial de ILJ en el paquete de software LAMMPS por el autor. Estudiamos diferentes poros e identificamos su capacidad para adsorber el metano, el hidrógeno y la separación de ambos gases. Se encontró que un poro de 8 Å es el tamaño ideal para acomodar una capa de moléculas de metano y, por lo tanto, muestra una fuerte preferencia por el metano sobre el hidrógeno, lo que lleva a una selectividad muy alta. En general, el metano se favorece sobre el hidrógeno, con la excepción del poro más pequeño de 5 AA que es demasiado pequeño para acomodar las moléculas de metano. Los poros más grandes tienen una menor preferencia por el metano sobre el hidrógeno, porque hay mucho espacio en el medio del poro para permitir que ingrese el hidrógeno molecular.

Conclusioni

Una serie di campi di forza è stato proposto per il grafene e la sua interazione con diversi gas, così come per le interazioni tra questi ultimi stessi. Per tutti i gas, sono stati proposti e testati diversi modelli ad atomo unito che descrivono le interazioni tramite medie pesate e modelli completamente atomistici in grado di produrre la completa superficie di energia potenziale dell'interazione. L'influenza di diversi schemi di carica è stata esplorata all'interno di questi modelli ed è stata valutata la rilevanza delle interazioni elettrostatiche per l'ottenimento di modelli accurati.

Le energie di interazione fra dimeri per i diversi gas ed i sistemi gas-grafene, sono state calcolate a livello DFT, utilizzando il funzionale B97-D, e successivamente confrontate con calcoli CCSD(T). È stato chiaramente dimostrato che il funzionale B97-D fornisce risultati affidabili per i difficili sistemi studiati in questo lavoro, che richiedono un'accurata descrizione delle interazioni non covalenti. Queste interazioni sono principalmente di tipo dispersivo e sono quindi dovute agli effetti di correlazione elettronica, che ancora oggi rappresentano un problema importante nei calcoli in ambito di chimica teorica. Tuttavia, abbiamo dimostrato che questi problemi possono essere superati, e campi di forza precisi possono essere costruiti a questo livello di teoria. Per l'assorbimento di gas sul grafene, abbiamo trovato, per tutti i gas, che l'orientamento di attacco della molecola è molto più importante della posizione esatta sulla superficie di grafene.

Nello specifico, per il metano e l'azoto, è stato dimostrato che i potenziali proposti riproducono bene le energie di interazione e le distanze di equilibrio dei dimeri selezionati ottenuti a livello CCSD(T) e sperimentale. I potenziali atomistici sono in grado di riprodurre l'ordine di stabilità dei dimeri presi in considerazione alla distanza di equilibrio, mentre i modelli ad atomo unito hanno riprodotto le energie di interazione medie in maniera accurata. Per il metano, si consigliano piccole cariche per il potenziale atomistico (APT, Hirshfeld o Mulliken), anche se cariche leggermente più grandi, come quelle di Albertí, si comportano bene. Il modello atomistico per il sistema grafene-metano riproduce molto bene l'interazione con vari IPA, come naftalene e coronene e dovrebbe quindi essere utilizzabile per altre strutture di carbonio estese e nanotubi. Allo stesso modo, questo potenziale atomistico è in grado di riprodurre risultati sperimentali su sistemi di grafene-metano. Sulla base del coefficiente di diffusione ed il confronto con i risultati CCSD(T), abbiamo selezionato il modello ad atomo unificato con le cariche di Hirshfeld ed il potenziale atomistico senza cariche, essendo questi i più affidabili, con la nota che il modello più economico, ad atomo unito senza cariche, risulta anche essere una buona scelta. Per la molecola di azoto, è stato riscontrato che lo schema di carica di Cracknell a quattro siti riproduce con elevata accuratezza le energie di interazione CCSD(T) ed il coefficiente di diffusione sperimentale sia per l'atomo unito che per i potenziali completamente atomistici. Inoltre, il modello atomistico fornisce un'energia di interazione media grafene-azoto in eccellente accordo con il valore sperimentale.

Per l'acqua, è noto che, nonostante la sua struttura sia semplice, le sue interazioni molto complesse sono difficili da rappresentare adeguatamente. Tuttavia, abbiamo scoperto che il nostro potenziale atomistico con tre cariche ottimizzate è in grado di riprodurre gli estremi dei 10 punti stazionari considerati sulla superficie di energia potenziale CCSD(T). Le energie a media distanza non sono descritte nell'ordine corretto, ma i valori ottenuti sono sempre vicini a quelli di riferimento CCSD(T) e DFT. Questo risultato ci dà fiducia nel credere che i nostri potenziali descrivono bene il comportamento di un insieme di molecole d'acqua. Nei sistemi a pressioni più elevate, dove i legami idrogeno diventano più importanti, abbiamo incluso un termine esplicito per trattare questi ultimi. Anche in questo caso, i potenziali con tre cariche ottimizzate hanno dimostrato essere i migliori ed in grado di descrivere gli esameri considerati ragionevolmente bene. Tuttavia, sembra che la rappresentazione Coulombiana degli effetti elettrostatici non sia sufficientemente accurata per descrivere dimeri e aggregati con un singolo potenziale e potrebbe essere necessario un approccio più avanzato, per esempio includendo esplicitamente il dipolo. Le interazioni elettrostatiche sono molto direzionali e dominano le interazioni di dispersione, un effeto questo, che i nostri potenziali non sono abbastanza flessibili da poter descrivere.

Abbiamo inoltre esplorato la possibilità di determinare i parametri dei campi di forza di tipo Lennard-Jones direttamente delle polarizzabilità statiche ed i coefficienti di dispersione C6 calcolati a livello ab initio. Questo studio preliminare mostra la necessità di includere nell'interazione contributi elettrostatici molto accurati, ed inoltre illustra l'arbitrarietà intrinseca nel distribuire la densità elettronica totale, l'unico vero osservabile quantomeccanico, in componenti atomici.

Durante le simulazioni di dinamica molecolare, abbiamo studiato il comportamento del metano, dell'azoto e della loro miscela durante l'adsorbimento sul grafene, nel quale abbiamo prestato particolare attenzione all'influenza del campo di forza intramolecolare del grafene. Tre diversi campi sono stati presi dalla letteratura per la modellizzazione del grafene e confrontati con il modello rigido tradizionale. Abbiamo riscontrato che l'adsorbimento di metano ed azoto è chiaramente influenzato dalla flessibilità della superficie di grafene e quest'ultima deve quindi essere presa in considerazione nelle ricerche future. Specificatamente, per le energie di interazione medie come il modello ad atomo unito, la flessibilità sembra essere di grande importanza. Per i sistemi considerati in questo lavoro, l'effetto maggiore è stato trovato per il metano, con importanti effetti direzionali, e per l'azoto, anche se in misura minore. Per questi sistemi, l'introduzione della flessibilità è in grado di migliorare la descrizione dei modelli ad atomo unito ad un livello quasi pari a quello dei modelli atomistici. Per i potenziali atomistici, l'effetto sembra meno pronunciato, essendo di scarsa influenza per il caso del metano e decrescente leggermente l'adsorbimento nel caso dell'azoto, quest'ultimo comportamento è osservato anche per il monossido di carbonio. Infine, in questo studio, è stata mostrata una chiara preferenza per l'adsorbimento sul grafene del metano rispetto all'azoto. Infatti, abbiamo visto che aumentando gradualmente la quantità di molecole nel sistema, tutto l'azoto è stato effettivamente rimosso dal primo strato di adsorbimento a favore del metano.

Infine abbiamo dimostrato per la prima volta l'uso del potenziale ILJ per simulazioni GCMC, reso possibile grazie alla sua implementazione nel pacchetto software LAMMPS da parte dell'autore di questa tesi, riscontrando risultati soddisfacenti e confrontabili con la letteratura esistente. Abbiamo studiato diversi pori e identificato la loro capacità di assorbire metano, idrogeno e la separazione di entrambi questi gas. È stato trovato che il poro di 8 Å costituisce la dimensione ideale per accogliere uno strato di molecole di metano e quindi mostra una forte preferenza per il metano rispetto all'idrogeno, portando ad una selettività molto elevata. In generale, il metano è favorito rispetto all'idrogeno ad eccezione del più piccolo poro di 5 Å che è troppo piccolo per accogliere le molecole di metano. I pori più grandi hanno una preferenza inferiore per il metano rispetto all'idrogeno, perché c'è molto spazio nel mezzo del poro per consentire l'ingresso di idrogeno sfuso.

Bibliography

(1) Wongkoblap, A.; Intomya, W.; Somrup, W.; Charoensuk, S.; Junpirom, S.; Tangsathitkulchai, C. *Eng. J.* **2010**, *14*, 45–56.

(2) Ohno, H.; Mukae, Y. *J. Phys. Chem. C* **2016**, *120*, 23968.

(3) Novoselov, K. S.; Geim, A. K.; Morozov, S. V.; Jiang, D.; Zhang, Y.; Dubonos, S. V.; Grigorieva, I. V.; Firsov, A. A. *Science (80-.).* **2004**, *306*, 666–669.

(4) Novoselov, K. S.; Jiang, D; Schedin, F; Booth, T. J.; Khotkevich, V. V.; Morozov, S. V.; Geim, A. K. *Proc. Natl. Acad. Sci. U. S. A.* **2005**, *102*, 10451–10453.

(5) Geim, A.; Novoselov, K. *Nat. Mater.* **2007**, *6*, 183–191.

(6) Slonczewski, J. C.; Weiss, P. R. *Pysical Rev.* **1958**, *109*, 2.

(7) Haldane, F. D. M. *Phys. Rev. Lett.* **1988**, *61*, 2015–2018.

(8) Fradkin, E. *Phys. Rev. B* **1986**, *33*, 3257–3262.

(9) Gómez-Gualdrón, D. A.; Wilmer, C. E.; Farha, O. K.; Hupp, J. T.; Snurr, R. Q. *J. Phys. Chem. C* **2014**, *118*, 6941–6951.

(10) Bianco, A.; Chen, Y.; Chen, Y.; Ghoshal, D.; Hurt, R. H.; Kim, Y. A.; Koratkar, N.; Meunier, V.; Terrones, M. *Carbon N. Y.* **2018**, *132*, 785–801.

(11) Pykal, M.; Jurečka, P.; Karlický, F.; Otyepka, M. *Phys. Chem. Chem. Phys.* **2016**, *18*, 6351–6372.

(12) Makrodimitris, K.; Papadopoulos, G. K.; Theodorou, D. N. *J. Phys. Chem. B* **2001**, *105*, 777–788.

(13) Momirlan, M.; Veziroglu, T. N. *Int. J. Hydrogen Energy* **2005**, *30*, 795–802.

(14) Johnston, B.; Mayo, M. C.; Khare, A. *Technovation* **2005**, *25*, 569–585.

(15) Düren, T.; Sarkisov, L.; Yaghi, O. M.; Snurr, R. Q. *Langmuir* **2004**, *20*, 2683–2689.

(16) Elyassi, M.; Rashidi, A.; Hantehzadeh, M. R.; Elahi, S. M. *Surf. Interface Anal.* **2017**, *49*, 230–237.

(17) Delgado, J. A.; Águeda, V. I.; Uguina, M. A.; Sotelo, J. L.; Brea, P.; Grande, C. A. *Ind. Eng. Chem. Res.* **2014**, *53*, 15414–15426.

(18) Schedin, F; Geim, A. K.; Morozov, S. V.; Hill, E. W.; Blake, P; Katsnelson, M. I.; Novoselov, K. S. *Nat. Mater.* **2007**, *6*, 652–655.

(19) Ao, Z. M.; Yang, J.; Li, S.; Jiang, Q. *Chem. Phys. Lett.* **2008**, *461*, 276–279.

(20) Morris, R. E.; Wheatley, P. S. *Angew. Chemie - Int. Ed.* **2008**, *47*, 4966–4981.

(21) Fischer, M.; Hoffmann, F.; Fröba, M. *RSC Adv.* **2012**, *2*, 4382.

(22) Getman, R. B.; Bae, Y.-s.; Wilmer, C. E.; Snurr, R. Q. *Chem. Rev.* **2012**, *112*, 703–23.

(23) Peng, Y.; Krungleviciute, V.; Eryazici, I.; Hupp, J. T.; Farha, O. K.; Yildirim, T. *J. Am. Chem. Soc.* **2013**, *135*, 11887–11894.

(24) Bichoutskaia, E.; Suyetin, M.; Bound, M.; Yan, Y.; Schröder, M. *J. Phys. Chem. C* **2014**, *118*, 15573–15580.

(25) Kim, J.; Maiti, A.; Lin, L.-C.; Stolaroff, J. K.; Smit, B.; Aines, R. D. *Nat. Commun.* **2013**, *4*, 1694–7.

(26) Cavenati, S.; Grande, C. A.; Rodrigues, A. E. *J. Chem. Eng. Data* **2004**, *49*, 1095–1101.

(27) Blanco, A. A.; de Oliveira, J. C.; López, R.; Moreno-Piraján, J. C.; Giraldo, L.; Zgrablich, G.; Sapag, K. *Colloids Surfaces A Physicochem. Eng. Asp.* **2010**, *357*, 74–83.

(28) Salehi, E.; Taghikhani, V.; Ghotbi, C.; Nemati Lay, E.; Shojaei, A. *J. Nat. Gas. Chem.* **2007**, *16*, 415–422.

(29) Albesa, A. G.; Llanos, J. L.; Vicente, J. L. *Langmuir* **2008**, *24*, 3836–3840.

(30) Razak, M. A.; Do, D. D.; Birkett, G. R. *Adsorption* **2011**, *17*, 385–394.

(31) Morales-cas, A. M.; Moya, C.; Coto, B.; Vega, L. F.; Calleja, G. *J. Phys. Chem. C* **2007**, *111*, 6473–6480.

(32) Raghavan, B.; Gupta, T. *J. Phys. Chem. C* **2017**, *121*, 1904–1909.

(33) Bartolomei, M.; Giorgi, G. *ACS Appl. Mater. Interfaces* **2016**, *8*, 27996–28003.

(34) Liu, L.; Nicholson, D.; Bhatia, S. K. *Chem. Eng. Sci.* **2015**, *121*, 268–278.

(35) Lin, K.; Yuan, Q.; Zhao, Y. P. *Comput. Mater. Sci.* **2017**, *133*, 99–107.

(36) Szczęśniak, B.; Choma, J.; Jaroniec, M. *Adv. Colloid Interface Sci.* **2017**, *243*, 46–59.

(37) Conti, S.; Cecchini, M. *Phys. Chem. Chem. Phys.* **2018**, *20*, 9770–9779.

(38) Choi, P.-S.; Jeong, J.-m.; Choi, Y.-k.; Kim, M.-s.; Shin, G.-j.; Park, S.-j. *Carbon Lett.* **2016**, *17*, 18–28.

(39) Gadipelli, S.; Guo, Z. X. *Prog. Mater. Sci.* **2015**, *69*, 1–60.

(40) Thierfelder, C.; Witte, M.; Blankenburg, S.; Rauls, E.; Schmidt, W. G. *Surf. Sci.* **2011**, *605*, 746–749.

(41) Vela, S.; Huarte-Larrañaga, F. *Carbon N. Y.* **2011**, *49*, 4544–4553.

(42) Terrones, H.; Lv, R.; Terrones, M.; Dresselhaus, M. S. *Reports Prog. Phys.* **2012**, *75*, 062501.

(43) Lechner, C.; Baranek, P.; Vach, H. *Carbon N. Y.* **2018**, *127*, 437–448.

(44) Dai, J.; Yuan, J.; Giannozzi, P. *Appl. Phys. Lett.* **2009**, *95*, 232105.

(45) Chen, J.-J.; Li, W.-W.; Li, X.-L.; Yu, H.-Q. *Environ. Sci. Technol.* **2012**, *46*, 10341–10348.

(46) Tonel, M. Z.; Lara, I. V.; Zanella, I.; Fagan, S. B. *Phys. Chem. Chem. Phys.* **2017**, *19*, 27374–27383.

(47) Chowdhury, S.; Balasubramanian, R. *Sci. Rep.* **2016**, *6*, 1–10.

(48) Zhang, T.; Xue, Q.; Zhang, S.; Dong, M. *Nano Today* **2012**, *7*, 180–200.

(49) Bartolomei, M.; Carmona-Novillo, E.; Giorgi, G. *Carbon N. Y.* **2015**, *95*, 1076–1081.

(50) Gordeev, E. G.; Polynski, M. V.; Ananikov, V. P. *Phys. Chem. Chem. Phys.* **2013**, *15*, 18815.

(51) Ma, M.; Tocci, G.; Michaelides, A.; Aeppli, G. *Nat. Mater.* **2016**, *15*, 66–71.

(52) Deshmukh, S. A.; Kamath, G.; Sankaranarayanan, S. K.R. S. *Soft Matter* **2014**, *10*, 4067–4083.

(53) Klimes, J.; Michaelides, A. *J. Chem. Phys.* **2012**, *137*, 120901.

(54) Bludský, O.; Rubeš, M.; Soldán, P.; Nachtigall, P. *J. Chem. Phys.* **2008**, *128*, 114102.

(55) Lucena, S. M.; Frutuoso, L. F.; Silvino, P. F.; Azevedo, D. C.; Toso, J. P.; Zgrablich, G.; Cavalcante, C. L. *Colloids Surfaces A Physicochem. Eng. Asp.* **2010**, *357*, 53–60.

(56) Bin Yeamin, M.; Faginas-Lago, N; Alberti, M; Cuesta, I. G.; Sanchez-Marin, J; Sanchez de Meras, A. M. J. *Rsc Adv.* **2014**, *4*, 54447–54453.

(57) Do, D. D.; Do, H. D. *Fluid Phase Equilib.* **2005**, *236*, 169–177.

(58) Rana, M. K.; Koh, H. S.; Zuberi, H.; Siegel, D. J. *J. Phys. Chem. C* **2014**, *118*, 2929–2942.

(59) Alberti, M; Aguilar, A; Lucas, J. M.; Pirani, F *J. Phys. Chem. A* **2012**, *116*, 5480–5490.

(60) Jorgensen, W. L. *J. Am. Chem. Soc.* **1981**, *103*, 335–340.

(61) Stuart, S. J.; Tutein, A. B.; Harrison, J. A. *J. Chem. Phys.* **2000**, *112*, 6472–6486.

(62) Grimme, S. *J. Comput. Chem.* **2006**, *27*, 1787–1799.

(63) Grimme, S. *J. Comput. Chem.* **2004**, *25*, 1463–1473.

(64) Peverati, R.; Baldridge, K. K. *J. Chem. Theory Comput.* **2008**, *4*, 2030–2048.

(65) Stassen, H. *J. Mol. Struct.* **1999**, *464*, 107–119.

(66) Wu, C.-D.; Fang, T.-H.; Lo, J.-Y.; Feng, Y.-L. *J. Mol. Model.* **2013**, *19*, 3813–3819.

(67) Dundar, E.; Boulet, P.; Wexler, C.; Firlej, L.; Llewellyn, P.; Kuchta, B. *J.* **2016**, *145*, 144704–7.

(68) Becker, T. M.; Heinen, J.; Dubbeldam, D.; Lin, L.-C.; Vlugt, T. J. H. *J. Phys. Chem. C* **2017**, *121*, 4659–4673.

(69) Pirani, F.; Albertí, M.; Castro, A.; Moix Teixidor, M.; Cappelletti, D. *Chem. Phys. Lett.* **2004**, *394*, 37–44.

(70) Pirani, F.; Brizi, S.; Roncaratti, L. F.; Casavecchia, P.; Cappelletti, D.; Vecchiocattivi, F. *Phys. Chem. Chem. Phys.* **2008**, *10*, 5489–5503.

(71) Bartolomei, M.; Carmona-Novillo, E.; Hernández, M. I.; Campos-Martínez, J.; Pirani, F. *J. Phys. Chem. C* **2013**, *117*, 10512–10522.

(72) Faginas-Lago, N.; Yeamin, M. B.; Sánchez-Marín, J.; Cuesta, I. G.; Albertí, M.; Sánchez de Merás, A. *Theor. Chem. Acc.* **2017**, *136*, 91.

(73) Faginas-Lago, N.; Yeni, D.; Huarte, F.; Wang, Y.; Alcamí, M.; Martin, F. *J. Phys. Chem. A* **2016**, *120*, 6451–6458.

(74) Bramastya, Y.; Faginas-lago, N.; Lombardi, A.; Evangelisti, S. *Carbon N. Y.* **2018**, *In press*.

(75) Vandenbrande, S.; Verstraelen, T.; Gutiérrez-Sevillano, J. J.; Waroquier, M.; Van Speybroeck, V. *J. Phys. Chem. C* **2017**, *121*, 25309–25322.

(76) Eggimann, B. L.; Sunnarborg, A. J.; Stern, H. D.; Bliss, A. P.; Siepmann, J. I. *Mol. Simul.* **2013**, *40*, 101–105.

(77) Qin, Z.; Taylor, M.; Hwang, M.; Bertoldi, K.; Buehler, M. J. *Nano Lett.* **2014**, *14*, 6520–6525.

(78) Kaiser, A.; Leidlmair, C.; Bartl, P.; Zöttl, S.; Denifl, S.; Mauracher, A.; Probst, M.; Scheier, P.; Echt, O. *J. Chem. Phys.* **2013**, *138*, 074311.

(79) Walther, J. H.; Jaffe, R; Halicioglu, T; Koumoutsakos, P *J. Phys. Chem. B* **2001**, *105*, 9980–9987.

(80) Kalosakas, G; Lathiotakis, N. N.; Galiotis, C; Papagelis, K *J. Appl. Phys.* **2013**, *113*, 134307.

(81) Fthenakis, Z.; Kalosakas, G.; Chatzidakis, G. D.; Galiotis, C.; Papagelis, K.; Lathiotakis, N. *Phys. Chem. Chem. Phys.* **2017**, *19*, 30925–30932.

(82) Zhang, L.; Wu, C.; Ding, X.; Fang, Y.; Sun, J. *Phys. Chem. Chem. Phys.* **2018**, *20*, 18192.

(83) Shindell, D. T.; Faluvegi, G.; Koch, D. M.; Schmidt, G. a.; Unger, N.; Bauer, S. E. *Science (80-.).* **2009**, *326*, 716–718.

(84) Afgan, N. H.; Pilavachi, P. A.; Carvalho, M. G. *Energy Policy* **2007**, *35*, 704–713.

(85) Harfoot, M. B.; Tittensor, D. P.; Knight, S.; Arnell, A. P.; Blyth, S.; Brooks, S.; Butchart, S. H.; Hutton, J.; Jones, M. I.; Kapos, V.; Scharlemann, J. P.; Burgess, N. D. *Conserv. Lett.* **2018**, *11*, 1–13.

(86) Menon, V. C.; Komarneni, S. *J. Porous Mater.* **1998**, *5*, 43–58.

(87) Rogelj, J. et al. *Nat. Clim. Chang.* **2018**, *8*, 325–332.

(88) Deutz, S.; Bongartz, D.; Heuser, B.; Kätelhön, A.; Schulze Langenhorst, L.; Omari, A.; Walters, M.; Klankermayer, J.; Leitner, W.; Mitsos, A.; Pischinger, S.; Bardow, A. *Energy Environ. Sci.* **2018**, *11*, 331–343.

(89) Marques, A. C.; Fuinhas, J. A.; Pereira, D. A. *Energy Policy* **2018**, *116*, 257–265.

(90) Do, D. D.; Do, H. D.; Nicholson, D *Adsorp. Sci. Technol.* **2007**, *25*, 347–364.

(91) Fan, C.; Do, D. D.; Nicholson, D.; Jagiello, J.; Kenvin, J.; Puzan, M. *Carbon N. Y.* **2013**, *52*, 158–170.

(92) Prosenjak, C; Nabais, J. M. V.; Laginhas, C. E.; Carrott, P. J. M.; Carrott, M. M.L. R. *Adsorpt. Sci. Technol.* **2010**, *28*, 797–806.

(93) Kaur, S. P.; Sujith, K. S.; Ramachandran, C. N. *Phys. Chem. Chem. Phys.* **2018**, *20*, 9157–9166.

(94) Ohba, T.; Takase, A.; Ohyama, Y.; Kanoh, H. *Carbon N. Y.* **2013**, *61*, 40–46.

(95) Liu, B.; Wu, R.; Law, A. W.-K.; Feng, X.-Q.; Bai, L.; Zhou, K. *Sci. Rep.* **2016**, *6*, 38583.

(96) Sumida, K.; Rogow, D. L.; Mason, J. A.; McDonald, T. M.; Bloch, E. D.; Herm, Z. R.; Bae, T. H.; Long, J. R. *Chem. Rev.* **2012**, *112*, 724–781.

(97) Bahamon, D.; Vega, L. F. *Chem. Eng. J.* **2016**, *284*, 438–447.

(98) Camden, A. N.; Barr, S. A.; Berry, R. J. *J. Phys. Chem. B* **2013**, *117*, 10691–10697.

(99) Jiao, S.; Duan, C.; Xu, Z. *Sci. Rep.* **2017**, *7*, 2646.

(100) Zhao, K.; Wu, H. *Phys. Chem. Chem. Phys.* **2017**, *19*, 28496–28501.

(101) Albertí, M.; Pirani, F.; Laganá, A. *J. Phys. Chem. A* **2013**, *117*, 6991–7000.

(102) Damasceno Borges, D.; Woellner, C. F.; Autreto, P. A.; Galvao, D. S. *Carbon N. Y.* **2018**, *127*, 280–286.

(103) Bahamon, D.; Carro, L.; Guri, S.; Vega, L. F. *J. Colloid Interface Sci.* **2017**, *498*, 323–334.

(104) Misra, R. P.; Blankschtein, D. *J Phys Chem C* **2017**, *121*, 28166–28179.

(105) Wang, Y.; Sinha, S.; Hu, L.; Das, S. *Phys. Chem. Chem. Phys.* **2017**, *19*, 27421–27434.

(106) Zhou, H.; Ganesh, P.; Presser, V.; Wander, M. C. F.; Fenter, P.; Kent, P. R. C.; Jiang, D. E.; Chialvo, A. A.; McDonough, J.; Shuford, K. L.; Gogotsi, Y. *Phys. Rev. B* **2012**, *85*, 035406.

(107) Wei, N.; Lv, C.; Xu, Z. *Langmuir* **2014**, *30*, 3572–3578.

(108) Jahangiri, H.; Bennett, J.; Mahjoubi, P.; Wilson, K.; Gu, S. *Catal. Sci. Technol.* **2014**, *4*, 2210–2229.

(109) Cheng, X.; Shi, Z.; Glass, N.; Zhang, L.; Zhang, J.; Song, D.; Liu, Z. S.; Wang, H.; Shen, J. *J. Power Sources* **2007**, *165*, 739–756.

(110) Cristancho, D.; Akkutlu, I. Y.; Criscenti, L. J.; Wang, Y. *SPE Eur. Featur. 78th EAGE Conf. Exhib.* **2016**, *MS*, 180142.

(111) Shao, X.; Feng, Z.; Xue, R.; Ma, C.; Wang, W.; Peng, X.; Cao, D. *AIChE J.* **2011**, *57*, 3042–3051.

(112) Lombardi, A.; Pirani, F.; Laganà, A.; Bartolomei, M. *J. Comput. Chem.* **2016**, *37*, 1463–1475.

(113) Lombardi, A.; Faginas-lago, N.; Gaia, G.; Palazzetti, F.; Aquilanti, V. *ICCSA 2016, Part I, LNCS 9786* **2016**, 246–257.

(114) Shah, N.; Panjala, D.; Huffman, G. P. *Energy and fuels* **2001**, *15*, 1528–1534.

(115) Kowalczyk, P.; Bhatia, S. K. *J. Phys. Chem. B* **2006**, *110*, 23770–23776.

(116) Kumar, K. V.; Müller, E. A.; Rodríguez-Reinoso, F. *J. Phys. Chem. C* **2012**, *116*, 11820–11829.

(117) Jensen, F., *Introduction to computational chemistry*; John Wiley & Sons Ltd.: West Sussex, 2007.

(118) Szabo, A.; Ostlund, N. S., *Modern quantum Chemistry Introduction to advanced electronic structure theory*; McGraw-Hill, Inc.: New York, 1989.

(119) Smith, W., *Elements of Molecular dynamics*, 2014.

(120) Landau, D. P.; Binder, K., *A guide to Monte-Carlo simulations in statistical physics*; Cambridge University Press: 2009.

(121) Cacheiro, J. L.; Pedersen, T. B.; Fernández, B.; De Merás, A. S.; Koch, H. *Int. J. Quant. Chem.* **2011**, *111*, 349–355.

(122) Hohenberg, P.; Kohn, W. *Phys. Rev.* **1964**, *136*, B864–B871.

(123) Perdew, J. P.; Tao, J.; Staroverov, V. N.; Scuseria, G. E. *J. Chem. Phys.* **2004**, *120*, 6898–6911.

(124) Becke, A. D. *J. Chem. Phys.* **1997**, *107*, 8554–8560.

(125) Perdew, J. P.; Wang, Y. *Phys. Rev. B* **1992**, *45*, 13244–13249.

(126) Becke, A. D. **1986**, *4524*.

(127) Schäfer, A.; Huber, C.; Ahlrichs, R. *J. Chem. Phys.* **1994**, *100*, 5829–5835.

(128) Boys, S.; Bernardi, F *Mol. Phys.* **1970**, *19*, 553–566.

(129) Tao, F.-M.; Pan, Y.-K. *Mol. Phys.* **1994**, *81*, 507–518.

(130) Sladek, V.; Ilcin, M.; Lukes, V. *Acta Chim. Slovaca* **2011**, *4*, 46–54.

(131) Mentel, Ł. M.; Baerends, E. J. *J. Chem. Theory Comput.* **2014**, *10*, 252–267.

(132) London, F *Trans. Faraday Soc.* **1937**, *33*, 8–26.

(133) Warshel, A.; Lifson, S. *J. Chem. Phys.* **1970**, *53*, 582–594.

(134) Albertí, M.; Costantini, A.; Laganá, A.; Pirani, F. *J. Phys. Chem. B* **2012**, *116*, 4220–4227.

(135) Faginas-lago, N.; Albertí, M.; Laganà, A.; Lombardi, A.; Pacifici, L.; Costantini, A. *ICSSA 2014, part I, LNCS* **2014**, *5879*, 585–600.

(136) Smith, W; Yong, C. W.; Rodger, P. M. *Mol. Simul.* **2002**, *28*, 385–471.

(137) Pirani, F.; Cappelletti, D.; Liuti, G. *Chem. Phys. Lett* **2001**, *350*, 286–296.

(138) Hermann, J.; DiStasio, R. A.; Tkatchenko, A. *Chem. Rev.* **2017**, *117*, 4714–4758.

(139) Becke, A. D. *J. Chem. Phys.* **1993**, *98*, 5648–5652.

(140) Hehre, W. J.; Ditchfield, R.; Pople, J. A. *J. Chem. Phys* **1972**, *56*, 2257–2261.

(141) Frisch, M. J. et al. Gaussian 09., Wallingford CT, 2016.

(142) Feller, D. *J. Comput. Chem* **1996**, *17*, 1571–1586.

(143) Schuchardt, K. L.; Didier, B. T.; Elsethagen, T.; Sun, L.; Gurumoorthi, V.; Chase, J.; Li, J.; Windus, T. L. *J. Chem. Inf. Model.* **2007**, *47*, 1045–1052.

(144) Dalton, a molecular electronic structure program., 2015.

(145) Aidas, K. et al. *WIREs Comput. Mol. Sci.* **2014**, *4*, 269–284.

(146) Wilson, J.; Faginas-lago, N.; Vekeman, J.; Cuesta, I. G.; Sánchez-Marín, J.; Sánchez de Merás, A. *ChemPhysChem* **2018**, *19*, 774–783.

(147) Janowski, T.; Ford, A. R.; Pulay, P. *Mol. Phys.* **2010**, *108*, 249–257.

(148) Rubeš, M.; Bludský, O. *ChemPhysChem* **2009**, *10*, 1868–1873.

(149) Lazar, P.; Karlický, F.; Jurecka, P.; Kocman, M.; Otyepková, E.; Safárová, K.; Otyepka, M. *J. Am. Chem. Soc.* **2013**, *135*, 6372–6377.

(150) Podeszwa, R. *J. Chem. Phys.* **2010**, *132*, 044704.

(151) Medeiros, P. V.; Gueorguiev, G. K.; Stafström, S. *Carbon N. Y.* **2015**, *81*, 620–628.

(152) Zhao, Y.; Truhlar, D. G. *J. Phys. Chem. C* **2008**, *112*, 4061–4067.

(153) Jenness, G. R.; Jordan, K. D. *J. Phys. Chem. C* **2009**, *113*, 10242–10248.

(154) Haldar, S.; Kolář, M.; Sedlák, R.; Hobza, P. *J. Phys. Chem. C* **2012**, *116*, 25328–25336.

(155) Gubbels, K. B.; Van De Meerakker, S. Y.; Groenenboom, G. C.; Meijer, G.; van der Avoird, A. *J. Chem. Phys* **2012**, *136*, 74301–15.

(156) Ren, P.; Ponder, J. W. *J. Phys. Chem. B* **2003**, *107*, 5933–5947.

(157) Lamoureux, G.; MacKerell, A.; Roux, B. *J. Chem. Phys.* **2003**, *119*, 5185–5197.

(158) Pranami, G.; Lamm, M. H. *J. Chem. Theory Comput.* **2015**, *11*, 4586–4592.

(159) Martin, J. M. L. In *Comput. Thermochem.* 1998.

(160) Gómez-Gualdrón, D. A.; Simon, C. M.; Lassman, W.; Chen, D.; Martin, R. L.; Haranczyk, M.; Farha, O. K.; Smit, B.; Snurr, R. Q. *Chem. Eng. Sci.* **2017**, *159*, 18–30.

(161) Liu, L.; Zhang, H.; Do, D. D.; Nicholson, D.; Liu, J. *Phys. Chem. Chem. Phys.* **2017**, *19*, 27105–27115.

(162) Martin, M. G. *Fluid Phase Equilib.* **2006**, *248*, 50–55.

(163) McDaniel, J. G.; Song, L.; Tylianakis, E.; Snurr, R. Q.; Schmidt, J. R. *J. Phys. Chem. C* **2015**, *119*, 3143–3152.

(164) Albesa, A. G.; Fertitta, E. a.; Vicente, J. L. *Langmuir* **2010**, *26*, 786–95.

(165) Heuchel, M; Davies, G. M.; Buss, E; Seaton, N. A. *Langmuir* **1999**, *15*, 8695–8705.

(166) Gatica, S. M.; Nekhai, A.; Scrivener, A. *Molecules* **2016**, *21*, 662.

(167) Cracknell, R. F.; Nicholson, D.; Tennison, S. R.; Bromhead, J. *Adsorption* **1996**, *2*, 193–203.

(168) Sweatman, M. B.; Quirke, N. *J. Phys. Chem. B* **2001**, *105*, 1403–1411.

(169) Sun, Y.; Spellmeyer, D.; Pearlman, D. A.; Kollman, P. *J. Am. Chem. Soc.* **1992**, *114*, 6798–6801.

(170) Yeganegi, S.; Gholampour, F. *Chem. Eng. Sci.* **2016**, *140*, 62–70.

(171) Yamamoto, T.; Kataoka, Y.; Okada, K. *J. Chem. Phys.* **1977**, *66*, 2701–2730.

(172) Smith, D. G.; Patkowski, K. *J. Chem. Theory Comput.* **2013**, *9*, 370–389.

(173) Rubeš, M.; Kysilka, J.; Nachtigall, P.; Bludský, O. *Phys. Chem. Chem. Phys.* **2010**, *12*, 6438–6444.

(174) Qiu, N. X.; Xue, Y.; Guo, Y.; Sun, W. J.; Chu, W. *Comput. Theor. Chem.* **2012**, *992*, 37–47.

(175) Umadevi, D; Sastry, G. N. *Curr. Sci.* **2014**, *106*, 1224–1234.

(176) Vidali, G.; Ihm, G.; Kim, H. Y.; Cole, M. W. *Surf. Sci. Rep.* **1991**, *12*, 133–181.

(177) Tsuzuki, S.; Honda, K.; Fujii, A.; Uchimarua, T.; Mikami, M. *Phys. Chem. Chem. Phys.* **2008**, *10*, 2860–2865.

(178) Hu, Z.; Zhang, L.; Jiang, J. *J. Chem. Phys.* **2012**, *136*, 244703.

(179) Tsuzuki, S.; Honda, K.; Uchimaru, T.; Mikami, M.; Tanabe, K. *J. Am. Chem. Soc.* **2000**, *122*, 3746–3753.

(180) Shibasaki, K.; Fujii, A.; Mikami, N.; Tsuzuki, S. *J. Phys. Chem. A* **2006**, *110*, 4397–4404.

(181) Takaba, H.; Matsuda, E.; Nair, B. N.; Nakao, S. I. *J. Chem. Eng. Japan* **2002**, *35*, 1312–1321.

(182) Ravikovitch, P. I.; Vishnyakov, A.; Neimark, A. V. *Phys. Rev. E* **2001**, *64*, 011602.

(183) Potoff, J. J.; Siepmann, J. I. *AIChE J.* **2001**, *47*, 1676–1682.

(184) Murthy, C. S.; Singer, K; Klein, M. L.; Mcdonald, I. R. *Mol. Phys.* **1980**, *41*, 1387–1399.

(185) Apriliyanto, Y. B.; Faginas Lago, N.; Lombardi, A.; Evangelisti, S.; Bartolomei, M.; Leininger, T.; Pirani, F. *J. Phys. Chem. C* **2018**, *122*, 16195–16208.

(186) Do, D. D.; Do, H. D. *J. Phys. Chem. B* **2006**, *110*, 17531–17538.

(187) Du, H.; Li, J.; Zhang, J.; Su, G.; Li, X.; Zhao, Y. *J. Phys. Chem. C* **2011**, *115*, 23261–23266.

(188) Patt, A.; Simon, J.-m.; Picaud, S.; Salazar, J. M. *J. Phys. Chem. C* **2018**, *122*, 18432–18444.

(189) Bahamon, D.; Vega, L. F. *Chem. Eng. J.* **2016**, *284*, 438–447.

(190) Stone, A., *The Theory of Intermolecular Forces*; Oxford University Press: 2013.

(191) Lu, T.; Chen, F. *J. Mol. Model.* **2013**, *19*, 5387–5395.

(192) Buch, V. *J. Chem. Phys.* **1992**, *97*, 726–729.

(193) Zhao, J.; Buldum, A.; Han, J.; Lu, J. P. *Nanotechnology* **2002**, *13*, 195–200.

(194) Ernstberger, B; Krause, H; Neusser, H. J. *Atoms, Mol. Clust.* **1991**, *20*, 189–192.

(195) Mostinsky, I. Diffusion coefficient.

(196) Berendsen, H. J. C.; Postma, P. M.; van Gunsteren, W. F.; Pullman, B *Intermol. forces* **1981**, 331–342.

(197) Berendsen, H. J.; Grigera, J. R.; Straatsma, T. P. *J. Phys. Chem.* **1987**, *91*, 6269–6271.

(198) Jorgensen, W. L.; Chandrasekhar, J.; Madura, J. D.; Impey, R. W.; Klein, M. L. *J. Chem. Phys.* **1983**, *79*, 926–935.

(199) Price, D. J.; Brooks, C. L. *J. Chem. Phys.* **2004**, *121*, 10096–10103.

(200) Costantini, A.; Albertí, M.; Pirani, F.; Laganà, A. *Int. J. Quantum Chem.* **2012**, *112*, 1810–1817.

(201) Albertí, M.; Aguilar, A.; Cappelletti, D.; Laganà, A.; Pirani, F. *Int. J. Mass Spectrom.* **2009**, *280*, 50–56.

(202) Faginas Lago, N.; Huarte Larranaga, F.; Alberti, M. *Eur. Phys. J. D* **2009**, *55*, 75–85.

(203) Horn, H. W.; Swope, W. C.; Pitera, J. W.; Madura, J. D.; Dick, T. J.; Hura, G. L.; Head-Gordon, T. *J. Chem. Phys.* **2004**, *120*, 9665–9678.

(204) Abascal, J. L.; Vega, C. *J. Chem. Phys.* **2005**, *123*, 234505.

(205) MacKerell, A. D. et al. *J. Phys. Chem. B* **1998**, *102*, 3586–3616.

(206) Bernal, J. D.; Fowler, R. H. *J. Chem. Phys.* **1933**, *1*, 515–548.

(207) Mahoney, M. W.; Jorgensen, W. L. *J. Chem. Phys.* **2000**, *112*, 8910–8922.

(208) Fingerhut, B. P.; Costard, R.; Elsaesser, T. *J. Chem. Phys.* **2016**, *145*, 115101.

(209) Phys, J. C.; Zielkiewicz, J. **2005**, *104501*.

(210) Ho, T. A.; Striolo, A. *J. Chem. Phys.* **2013**, *138*, 054117.

(211) Kysilka, J.; Rubeš, M.; Grajciar, L.; Nachtigall, P.; Bludský, O. *J. Phys. Chem. A* **2011**, *115*, 11387–11393.

(212) Tschumper, G. S.; Leininger, M. L.; Hoffman, B. C.; Valeev, E. F.; Schaefer, H. F.; Quack, M. *J. Chem. Phys.* **2002**, *116*, 690–701.

(213) Mayo, S. L.; Olafson, B. D.; Iii, W. A. G. **1990**, *91101*, 8897–8909.

(214) Gillan, M. J.; Alfè, D.; Michaelides, A. *J. Chem. Phys.* **2016**, *144*, 130901.

(215) Dahlke, E. E.; Olson, R. M.; Leverentz, H. R.; Truhlar, D. G. *J. Phys. Chem. A* **2008**, *112*, 3976–3984.

(216) Bates, D. M.; Tschumper, G. S. *J. Phys. Chem. A* **2009**, *113*, 3555–3559.

(217) Cambi, R.; Cappelletti, D.; Liuti, G.; Pirani, F. *J. Chem. Phys.* **1991**, *95*, 1852–1861.

(218) Liuti, G.; Pirani, F. *Chem. Phys. Lett.* **1985**, *122*, 245–250.

(219) Hättig, C; Christiansen, O; Jørgensen, P *J. Chem. Phys.* **1997**, *107*, 10592–10598.

(220) Langhoff, P. W.; Karplus, M. *J. Chem. Phys.* **1970**, *53*, 233.

(221) Misquitta, A. J.; Stone, A. J.; Fazeli, F. *J. Chem. Theory Comput.* **2014**, *10*, 5405–5418.

(222) Lillestolen, T. C.; Wheatley, R. J. *J. Chem. Phys.* **2009**, *131*, 144101.

(223) Cracknell, R. F.; Gordon, P.; Gubbins, K. E. *J. Phys. Chem.* **1993**, *97*, 494–499.

(224) Poling, B. E.; Prausnitz, J. M., *The properties of gases and liquids*.

(225) Plimpton, S. *J. Comput. Phys.* **1995**, *117*, 1–19.

(226) Redlich, O.; Kwong, J. N. *Chem. Rev.* **1949**, *44*, 233–244.

(227) Mosher, K.; He, J.; Liu, Y.; Rupp, E.; Wilcox, J. *Int. J. Coal Geol.* **2013**, *109-110*, 36–44.

(228) Collins, S. P.; Perim, E.; Daff, T. D.; Skaf, M. S.; Galvao, D. S.; Woo, T. K. *J. Phys. Chem. C* **2019**, *123*, 1050–1058.

(229) Kowalczyk, P.; Tanaka, H.; Hołyst, R.; Kaneko, K.; Ohmori, T.; Miyamoto, J. *J. Phys. Chem. B* **2005**, *109*, 17174–17183.